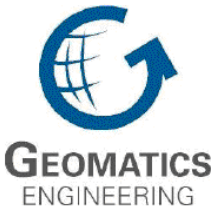

UCGE Reports

Number 20361

Department of Geomatics Engineering

Modeling the Impact of Equatorial Ionospheric Irregularities on GPS Receiver Performance

(URL: http://www.geomatics.ucalgary.ca/graduatetheses)

by

Fatemeh Ghafoori

September 2012

UNIVERSITY OF CALGARY

MODELING THE IMPACT OF EQUATORIAL IONOSPHERIC IRREGULARITIES ON GPS RECEIVER PERFORMANCE

by

Fatemeh Ghafoori

A THESIS

SUBMITTED TO THE FACULTY OF GRADUATE STUDIES

IN PARTIAL FULFILMENT OF THE REQUIREMENTS FOR THE

DEGREE OF DOCTOR OF PHILOSOPHY

DEPARTMENT OF GEOMATICS ENGINEERING

CALGARY, ALBERTA

SEPTEMBER, 2012

Abstract

The performance of a generic GPS receiver carrier tracking loop, subject to ionospheric scintillations, is studied in this thesis via theoretical analyses and simulation results. A physics-based simulation of equatorial scintillations has been employed to provide a full variety of test cases for the simulated carrier tracking loop to assess GPS receiver performance. This simulation tool is novel in allowing oblique signal propagation in an anisotropic medium for multiple frequencies. The scintillation simulation algorithm has been verified through comparison with real scintillation data collected in the equatorial region during the solar maximum of 2001. The utilization of the scintillation simulation tool is demonstrated through applying it to a GNSS signal, and evaluating the subsequent effects on a generic GPS tracking loop model. Theoretical predictions – from the derived equations – are verified through comparison with simulation results

According to the studies conducted in this thesis, the effect of phase scintillations on carrier tracking loop error variance is found to be considerably high, even for moderate scintillation levels. In the presence of strong intensity scintillation, the tracking loop's effective carrier-to-noise ratio can be much lower; as a result, the probability of loss of lock can increase and the mean time between cycle slips can decrease significantly. In regard to scintillation effects, the performance of the second-, and third-order carrier tracking loop are very similar. The first-order loop, however, is more fragile as it can lose phase lock at much lower level of scintillation strength. In the presence of scintillation, the choice of the pre-detection integration time does not significantly affect the carrier tracking error variance, provided that the signal's carrier-to-noise ratio level is not very low. The carrier tracking loop requires a relatively wide bandwidth to precisely track changes in the carrier phase due to ionospheric phase scintillation, while requires a narrow bandwidth in order to suppress the effect of signal fading and intensity scintillation. To meet this tradeoff, an optimum bandwidth for minimum tracking error can be determined for the carrier tracking loop in terms of scintillation and tracking loop parameters.

Acknowledgements

I express my gratitude and appreciation to all those who made this thesis possible. My utmost gratitude goes to my supervisor, Dr. Susan Skone for her expertise, kindness, and most of all, for her precious help and motivation.

I am very grateful to the academic members of the Department of Geomatics Engineering, in particular Dr. Mark Petovello and Dr. Kyle O'Keefe who in one way or another improved this work through their questions and comments. My sincere thanks also go to Dr. Theodore Beach of Air Force Research Laboratory for providing the real equatorial scintillation data which were crucial to this thesis. I also wish to acknowledge the Department of Geomatics Engineering and my fellow graduate students for creating a friendly and enjoyable working environment.

Lastly, and most importantly, I wish to thank my parents and my very patient husband for their understanding, endless love and encouragement when it was most required. To them I dedicate this thesis.

Table of Contents

List of Tables

List of Figures

List of Acronyms

ADC	Analog-to-Digital Converter
AFRL	Air Force Research Laboratory
C/A-Code	Coarse/Acquisition Code
CDMA	Code Division Multiple Access
CME	Coronal Mass Ejection
dB	Decibel
dBw	decibel watts
DFT	Discrete Fourier Transforms
DLL	Delay Lock Loop
DoD	Department of Defense
EM	Electromagnetic Wave
FFT	Fast Fourier Transform
FPE	Forward Propagation Equation
GDI	Gradient Drift Instability
GNSS	Global Navigation Satellite System
GPS	Global Positioning System
HOW	Handover Word
I	In-phase Signal
IF	Intermediate Frequency
IFFT	Inverse Fast Fourier Transform
LFSR	Linear Feedback Shift Registers
MCS	Master Control Station
NBP	Narrow Band Power
NCO	Numerically Controlled Oscillator
P(Y)-Code	The Encrypted Precision Code
P-Code	Precision Code
Pdf	Probability Density Function
PLL	Phase Lock Loop
PRN	Pseudorandom Noise
PSM	(Rino's) Phase Screen Model
PSSM	Phase Screen Scintillation Model
Q	Quadrature Signal
RMS	Root-Mean-Square
SBAS	Satellite-Based Augmentation System
SDF	Spectral Density Function
SNR	Signal-to-Noise Ratio
SMR	Signal-to-Multipath Ratio

SSE	Steady State Error
SSN	Sunspot Number
SSM	Statistical Scintillation Model
TEC	Total Electron Content
TECU	Total Electron Content Units
TLM	Telemetry
UV	Ultraviolet
VTEC	Vertical Total Electron Content
WBMOD	Wide Band Ionospheric Scintillation Model
WBP	Wide Band Power

Chapter One: Introduction

The Global Positioning System (GPS) is a satellite-based navigation system, consisting of a constellation of nominally 24 satellites operated by the U.S. Department of Defense (DoD). GPS satellites continuously broadcast ranging codes and navigation data on two L-band frequencies[1] (L_1 = 1575.42 MHz, and L_2 = 1227.60 MHz). Satellite positions can be calculated from the navigation message, and signal propagation time can be obtained from the ranging codes. Using this information, a GPS receiver can determine the satellite-to-receiver pseudorange[2]. Having at least four pseudorange measurements to four satellites, the receiver is able to estimate the user's positions in three dimensions and the time offset in the receiver clock [Kaplan, 1996].

The overall system comprises three main segments: the space segment, the ground control segment, and the user segment. The *space segment* consists of nominally 24 satellites arranged in six orbital planes, where each plane is inclined 55 degrees relative to the equator, has a radius of 26,560 km, and a period of 12 hours. The *control segment* currently consists of a master control station (MCS), twelve monitor stations, and four ground antennas. The monitor stations are responsible for tracking all the satellites in view, collecting their ranging data, and forwarding this information to the master control station. The navigation information is processed at the MCS in order to update each satellite's navigation message. Updated information is then transmitted back to each GPS satellite using the ground antennas [Misra and Enge, 2006]. All GPS user receivers and their support equipment are collectively referred to as the *user segment*.

---

[1] *At the time of writing, few GPS satellites also broadcast information on a third L-band frequency, L_5 = 1176.45 MHz.*

[2] *Pseudorange is the apparent measured range by the receiver which differs from the true range between the user and the satellite because of the receiver clock bias.*

Applications for GPS are vast and diverse, including military applications, aviation, marine and land navigation, surveying and asset tracking, to name a few. The performance of the GPS can be affected by a number of environmental elements including irregular atmospheric conditions (e.g. disturbed ionosphere and troposphere), electromagnetic interference, and multipath [Knight et al., 1998]. Among these factors - depending on the situation - the *disturbed ionosphere* and associated *ionospheric scintillation* can have the most significant impact on the GPS performance.

1.1 The Ionosphere

The ionosphere is a region of the Earth's atmosphere filled with electrons and electrically charged molecules and atoms. The density of electrons and ions are assumed to be equal in the ionosphere, with the density of ions to be less than 1 percent of the neutral density. The mixture of positively and negatively charged particles and neutral gas atoms is referred to as *plasma* [Vollath, 2007]. The ionosphere therefore is a weakly-ionized plasma. The lower and upper boundaries of this region are typically considered to be located around 50 km and 1000 km from the surface [Misra and Enge, 2006].

The ionosphere is formed by solar ionizing radiation. At ultraviolet (UV) and X-ray wavelengths (i.e. 0.01 to 400 nm), solar radiation is extremely energetic and therefore capable of freeing one or more electrons from neutral gas atoms or molecules (mostly N_2 and O_2 at lower altitudes, and H_2 and He at higher altitudes) [Misra and Enge, 2006]. In this process, known as ionization, the solar radiation energy is partly absorbed by a neutral gas atom, which, in turn, promotes the atom to a less stable configuration where it finally loses one of its outer electrons. At lower altitudes, plasma density increases and solar radiation become weaker; thus, the chance of positive ion-free electron recombination increases. The balance between these two opposite processes leads to the formation of several ionization layers, namely D, E, F_1, and F_2 as shown in Figure 1.1. The F_2 layer persists by night and day. The other three layers, however, are strongly tied to the UV radiation and disappear during nighttime [Klobuchar, 1996].

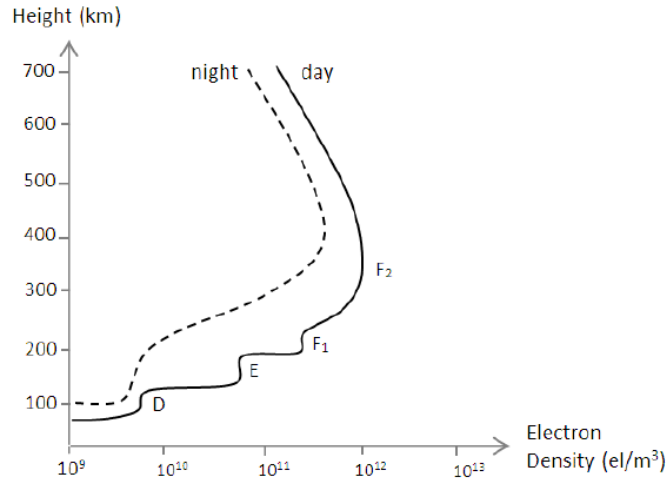

Figure 1.1: Electron density profile [modified after Klobuchar, 1996].

This research is principally focused on the behavior of the ionospheric F_2-region as radio signals are mainly refracted and perturbed at this region. The peak electron density of F_2 experiences both diurnal variations and annual fluctuations.

Equatorial anomaly:

The F_2-region daytime electron density peak occurs around 2:00 p.m. (local time) at about 350 km altitude. During the evening hours, the peak electron density is lower and it usually occurs at higher altitudes as compared with daytime [Klobuchar, 1996]. In the equatorial regions, for example, the F_2-layer evening height reaches up to 500-600 km from the surface. This is because of an upward E×B plasma drift of the equatorial F_2-layer formed by the northward Earth's magnetic field (B), and an eastward electric field (E) in the E-layer that is intensified around sunset. After elevating to high altitudes, the plasma starts to move downward along the magnetic field lines due to the effect of pressure gradient (∇p) from upper layers, and gravity (g). This phenomenon is known as the *Fountain Effect* (see Figure 1.2), and results in the formation of the *Equatorial Anomaly* [Fejer et al., 1999; de Rezende et al., 2007].

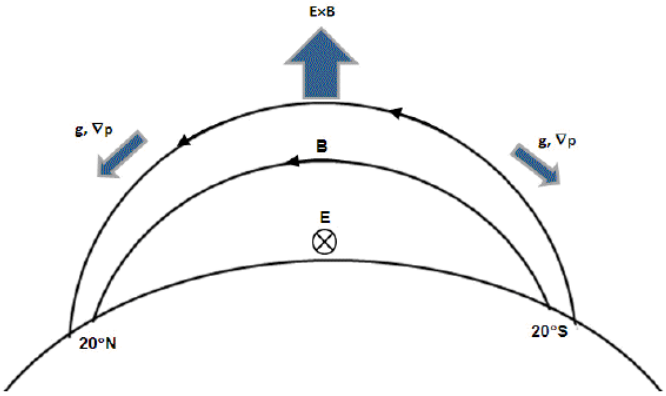

Figure 1.2: Equatorial Anomaly scheme [modified after de Rezende et al., 2007].

The Equatorial Anomaly consists of two ionospheric regions with high electron density peaks, around 20 degrees north and south of the magnetic equator, and is the main factor responsible for the generation of low-latitude plasma irregularities [de Rezende et al., 2007; Alfonsi et al., 2010].

Annual variation:

Both the electron concentration and the peak height of the F_2-region depend on solar cycle. The sun has an 11-year activity cycle, which is characterized by the number of sunspots (SSN) on the solar disk. Higher SSNs correspond to stronger solar activities. During the period of greatest solar activity (i.e. the solar maximum), the F_2 peak electron density usually increases by more than one order of magnitude, and its peak height rises by tens of kilometers as compared with solar minimum [Lühr et al., 2010].

The next solar maximum is predicted to occur in 2013. It is expected that during this period further solar radiation will increase the level of ionization in the ionosphere, with an increased impact on transionospheric radio wave propagation.

1.2 Ionospheric Effects on Global Positioning System

The GPS signals are affected by the propagation medium. More than 95 percent of their propagation path is located in free space and the rest is located within the Earth's atmosphere. Unlike the free space, the atmosphere changes the *speed* and *direction* of propagation of GPS signals. This phenomenon, known as *refraction*, increases the signal's travel time, which is a key measurement required for positioning and navigation [Misra and Enge, 2006].

To calculate the impact of propagation medium on GPS signals, the refractive index of the propagation medium needs to be determined first. The scale-free refractive index of a medium (n) is expressed as the ratio of the speed of propagation of the signal in free space (c) relative to that in the considered medium (v) [Misra and Enge, 2006]:

$$n = \frac{c}{v} \tag{1.1}$$

where c = 299,792,458 m/s. Since the ionosphere is not uniform in composition, the refractive index changes all along the path of a signal. At a given location in the ionosphere the phase refractive index (n_p) can be expressed using the Appleton-Hartree formula [Klobuchar, 1996].

$$n_p^2 = 1 - \frac{X}{1 - iZ - \frac{Y_T^2}{2(1 - X - iZ)} \pm \left[\frac{Y_T^4}{4(1 - X - iZ)^2} + Y_L^2 \right]^{1/2}} \tag{1.2}$$

where

$X = N_e e^2 / (\varepsilon_0 m \omega^2) = f_n^2 / f^2$,

$Y_L = f_H \cos\theta / f$,

$Y_T = f_H \sin\theta / f$,

$Z = \nu / \omega = f_\nu / f$,

$\omega = 2\pi f$,

f is the radio-wave frequency,

f_H is the electron gyro frequency (1.5 MHz),

f_n is the electron plasma frequency (20 MHz),

N_e is electron density (el/m^3),

e is electron charge (-1.602×10^{-19} Coulomb),

ε_0 is permittivity of free space (8.854×10^{-12} F/m),

θ is the angle between the wave direction and the Earth's magnetic field,

m is the electron rest mass (9.107×10^{-31} kg), and

ν is the electron-neutral collision frequency ($\nu = 2\pi f_\nu$, $f_\nu = 0.01$ MHz).

The higher order terms in Equation (1.2) are often neglected as they only contribute to a few centimeters of range error during solar maximum conditions [Brunner and Gu, 1991]. The refractive index of the ionosphere to first order can therefore be expressed as [Klobuchar, 1996]

$$n_p \approx 1 - \frac{X}{2} = 1 - \frac{N_e e^2}{2\varepsilon_0 m \omega^2} \tag{1.3}$$

Substituting the actual values of m (9.107×10^{-31} kg), ε_0 (8.854×10^{-12} F/m), and e (-1.602×10^{-19} Coulomb) in Equation (1.3), the phase refractive index becomes a function of radio-wave frequency and the ionosphere electron density at that specific location [Misra and Enge, 2006]

$$n_p = 1 - \frac{40.3\ N_e}{f^2}. \tag{1.4}$$

When the refractive index of a propagation medium is a function of propagating signal frequency, as in Equation (1.4), the medium is called *dispersive*. In a dispersive medium, signal velocity depends on frequency. The ionosphere is dispersive for the GPS signals. As a result, the GPS carrier wave propagation depends on phase refractive index (n_p) in the ionosphere while the modulating code signal experiences a different refractive index, called the group refractive index (n_g), as defined below [Misra and Enge, 2006].

$$n_g = n_p + f\frac{dn_p}{df} = 1 + \frac{40.3\ N_e}{f^2} \tag{1.5}$$

The simple fact that the ionospheric refractive index has a non-unit value results in some major effects on GPS signals including [Klobuchar, 1996]

1- Group delay of the modulating signals
2- Carrier wave phase advance
3- Doppler shift or range-rate error
4- Phase and amplitude scintillation
5- Angular refraction
6- Signal distortion

Knowing the refractive index, it is possible to quantify the impact of the ionosphere on radio-waves. The first four effects listed are explained in more detail in the following sections.

1.2.1 Carrier Phase Advance and Modulation Group Delay

In the estimation of GPS pseudorange, it is assumed that the speed of GPS signal within the propagation medium is equal to the speed of light in a vacuum (c = 299,792,458 m/s). Since the ionospheric refractive index differs from unity, this assumption is not correct.

Following Equations (1.1), (1.4) and (1.5), the phase velocity (v_p) is found to be slightly larger than the speed of light in a vacuum, causing the *phase advance* [Skone, 1998].

$$v_p = \frac{c}{n_p} = \frac{c}{1 - \frac{40.3\ N_e}{f^2}} \approx c\left(1 + \frac{40.3\ N_e}{f^2}\right) = c + \Delta v, \qquad (m/s) \tag{1.6}$$

The group velocity (v_g), on the other hand, is found to be slightly less than the speed of light, which causes the *group delay*.

$$v_g = \frac{c}{n_g} = \frac{c}{1 + \frac{40.3\ N_e}{f^2}} \approx c\left(1 - \frac{40.3\ N_e}{f^2}\right) = c - \Delta v, \qquad (m/s) \tag{1.7}$$

By subtracting the accurate phase and group velocities (v_p and v_g) from the speed of light (c) and multiplying the remainder ($\pm \Delta v$) by the signal travel time, one can calculate the amount of range delay caused by the ionosphere, in units of meters, via

$$\begin{aligned}\Delta R_p &= \int_R^S (c - v_p)\, dt \\ &= \int_R^S (n_p - 1)\, dl \\ &= -\frac{40.3}{f^2} \int_R^S N_e\, dl \\ &= -\frac{40.3}{f^2} \cdot TEC\end{aligned} \tag{1.8}$$

$$\begin{aligned}\Delta R_g &= \int_R^S (c - v_g)\, dt \\ &= \frac{40.3}{f^2} \int_R^S N_e\, dl \\ &= \frac{40.3}{f^2} \cdot TEC\end{aligned} \tag{1.9}$$

where S denotes satellite, and R denotes receiver.

As can be seen from the above two equations, the "magnitude" of ionospheric range delay is the same for the carrier phase and pseudorange measurements. The term $\int N_e\, dl$ is referred to as the *total electron content* (TEC), and represents the number of electrons in a column with the cross sectional area of 1 m^2 extending all the way from the receiver to the satellite [Misra and Enge, 2006]. Equations (1.8) and (1.9) indicate that the range delay caused by the ionosphere directly depends on the number of free electrons along the path of the signal. The total electron content is measured in units of TECU, where one TECU is equal to 10^{16} el/m^2.

Having the range delay (ΔR), the equivalent amount of time delay and phase shifts added to the signal by the ionosphere can be determined through [Skone, 2009]

$$t_{shift} = \frac{|\Delta R|}{c} = \frac{1.34\times10^{-7}\cdot TEC}{f^2} \tag{1.10}$$

$$\phi_{shift} = 2\pi\cdot\frac{|\Delta R|}{\lambda} = 2\pi f\cdot\frac{|\Delta R|}{c} = \frac{8.44\times10^{-7}\cdot TEC}{f} \tag{1.11}$$

where t_{shift} is in seconds, and ϕ_{shift} is in radians.

1.2.2 Ionospheric Doppler Shift

Due to the relative motion between a satellite and the GPS receiver, the frequency of the received signal deviates from the original frequency transmitted by the satellite. The difference between the true and the received frequency is referred to as the Doppler shift. In GPS context, there is a geometric Doppler shift due to relative motion between a GPS satellite and the user, and an *ionospheric Doppler shift* because of varying TEC [Klobuchar, 1996].

The Doppler shift added by the ionosphere is smaller than the geometric Doppler shift, and is calculated, in units of Hz, by [Skone, 2009]

$$\Delta f = \frac{1}{2\pi}\cdot\frac{d\phi_{shift}}{dt} = \frac{8.44\times10^{-7}}{2\pi f}\cdot\frac{dTEC}{dt} = \frac{1.34\times10^{-7}}{f}\cdot\frac{dTEC}{dt} \tag{1.12}$$

1.2.3 Ionospheric Scintillation

Scintillation refers to random fluctuations in the received wave field strength caused by the irregular structure of the propagation medium. Ionospheric scintillations are random rapid variations in the intensity and phase of received signals resulting from plasma density irregularities in the ionosphere [Conker et al., 2003]. Shown in Figure 1.3 are the areas highly prone to scintillation effects, namely the *equatorial regions* (about 20

degrees either side of the geomagnetic equator), and the *high-latitude regions* (including auroral and polar cap). The physics of the equatorial F-region irregularity patches are rather different from those in high-latitude regions, resulting in different scintillation behaviors [Aarons, 1982].

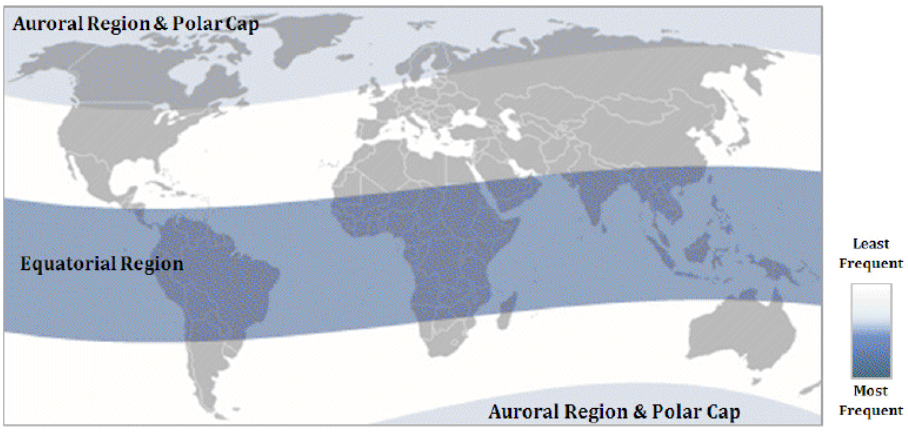

Figure 1.3: Regions of the world prone to strong scintillation effects [modified after Klobuchar, 1991].

1.2.3.1 High-latitude scintillations

High-latitude scintillations primarily result from geomagnetic storms, which, in turn, result from interactions between the solar coronal mass ejections (CME) and the Earth's magnetosphere. When a major CME takes place, an extremely huge amount of solar plasma is ejected from the sun into space. When part of this stream, known as solar wind, reaches the Earth (see Figure 1.4), it is deflected by the Earth's magnetic shield [Gopalswamy, 2009]. Strong solar wind pressures, however, are capable of compressing the magnetosphere to a point where the CME magnetic field can easily interact with the

Earth's magnetic field and, as a result, transmit a huge number of energetic particles into the magnetosphere and ionosphere.

Within the ionosphere, the charged particles precipitate along the Earth's magnetic field lines and create large patches of high electron density. The magnetosphere-solar wind interactions also generate electric fields which displace the plasma patches within the ionosphere. In this case, the movement of plasma patches with strong horizontal density gradients will result in another phenomenon called gradient drift instability (GDI), during which the patches break down into smaller regions of irregular plasma density. Electron precipitation and GDI are believed to be the main sources of scintillation at high latitudes at GPS frequencies [Sojka et al., 1998].

The intensity and frequency of geomagnetic storms are controlled by the solar cycle. Accordingly, the most severe and most common storms are associated with the solar cycle maximum.

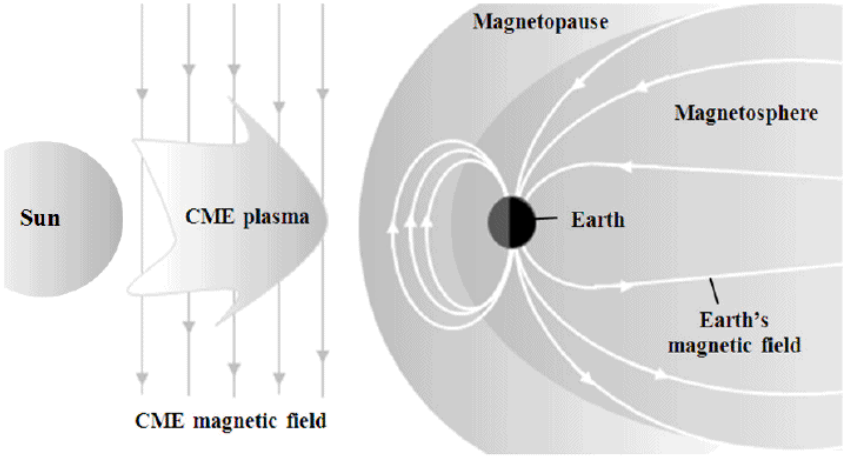

Figure 1.4: Solar-terrestrial interaction [modified after de Rezende et al., 2007]

1.2.3.2 Equatorial scintillations

The physics of the equatorial F-region irregularity patches are different from those at high-latitude regions. During daytime local time near the magnetic equator, the E-region dynamo electric field (E) is eastward. As the northward magnetic field (B) is nearly parallel to the Earth's surface, the resulting E×B drift lifts the F-region plasma upward. The elevated plasma then moves down along the magnetic field lines (see Figure 1.2), and creates the Equatorial Anomaly; two peaks in electron density roughly 20 degrees either side of the magnetic equator [de Rezende et al., 2007; Alfonsi et al., 2010].

Shortly after sunset, another dynamo is developed at higher altitudes in the F-region, which enhances the eastward electric field. The post-sunset electric field moves the ionospheric plasma upward, thus intensifying the Equatorial Anomaly peaks. The "post-sunset enhancement" of the eastward electric field is responsible for the creation of equatorial ionospheric irregularities [Alfonsi et al., 2010].

As the F-region plasma moves to higher altitudes, the density gradient between the top and bottom side of this region increases, which, in turn, results in the formation of plasma density depletion areas (plasma bubbles) in the lower F-region, as illustrated in Figure 1.5. When a bubble starts to grow or move upward, large electron density gradients on the bubble edges produce smaller irregularities. These small irregular regions with a size of the order of the first Fresnel zone radius[3] or less can cause strong scintillations of intensity and phase of GPS signals [Afraimovich et al., 2006; Alfonsi et al., 2010].

Around local midnight, the electric field starts turning westward and, thus, the plasma gradually moves to lower altitudes and the irregularities begin to fade [Alfonsi et al., 2010]. Equatorial scintillations are studied in this work as they affect larger number of navigation users, and tend to be more severe than high-latitude scintillations.

---

[3] *The radius of the first Fresnel zone is calculated via* $r \approx (H \cdot \lambda)^{1/2}$, *where H denotes the ionospheric electron density peak height, and* λ *denotes the signal wavelength. For H=350 km, and* λ_{L1}*=0.19 m, the Fresnel radius is about 260 m for the GPS* L_1 *signal.*

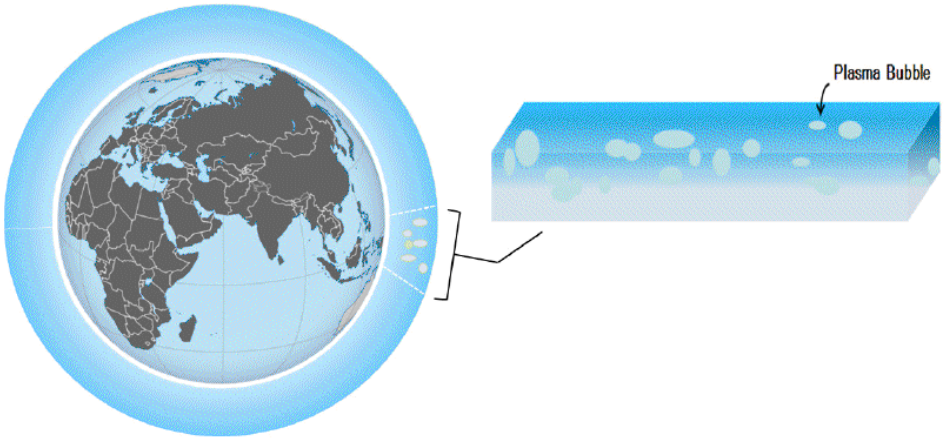

Figure 1.5: Formation of equatorial plasma bubbles.

1.3 Impact of Ionospheric Scintillation on GPS Receiver

Ionospheric plasma density irregularities and plasma bubbles can impair the performance of GPS receivers though introducing unexpected phase and intensity variations to the received signals. Propagation through randomly distributed irregularities changes the phase modulation of the propagating signal and produces complex diffraction patterns on the ground [Wernik et al., 2003].

Scintillation components affect GPS receivers mostly at the tracking loop stage and, therefore, have the capability to disturb all GPS systems, including stand-alone receivers and differential systems [Knight and Finn, 1996].

Phase scintillations induce a frequency shift in the received signal carrier wave. When the frequency shift exceeds the phase locked loop bandwidth, the signal may be lost and need to be reacquired. Intensity scintillations, on the other hand, cause signals to fade. During severe fading conditions, the signal strength may drop almost entirely below the receiver

lock threshold, and signal loss and cycle slips may occur. In general, scintillations can impair the performance of communication and navigation systems [Klobuchar, 1996].

1.4 Literature Review

Although the physics of ionospheric scintillation has been studied over the past several decades [e.g. Aarons, 1982; Fremouw and Ishimaru, 1992; Wernik et al., 2003], and scintillation effects on GPS applications are widely investigated for the equatorial regions and, to less extent, for high-latitude regions [Beniguel et al., 2004; Kintner et al., 2007; Seo et al., 2007; Hinks et al., 2008; Alfonsi et al., 2010; Prikryl et al., 2010], *predicting* the behavior of a GPS receiver under different ionospheric scintillation conditions is still a difficult task to accomplish.

This problem arises due to the following reasons: first, the dependence of ionospheric activity on the 11-year solar activity cycle, the difference in the physics of the high-latitude scintillation versus equatorial scintillation and, more importantly, the *random* nature of scintillation makes it difficult for researchers to develop a standard model to be applicable at any given location and time. Second, due to fast developments in technology of GPS receivers, especially in signal tracking algorithms [e.g. Alban et al., 2003; Kamel et al., 2010], extending the prediction results obtained for one specific type of receiver to all other types is not easily achievable.

1.4.1 Scintillation Models

WBMOD Model

The Wide Band ionospheric scintillation MODel (WBMOD), developed by researchers at Northwest Research Associates, Inc. (NWRA), is often used by researchers to determine the global distribution and behavior of ionospheric scintillation at a specified location and time. The model itself is a combination of an *environmental* model and a *propagation* model. The WBMOD environmental model characterizes the plasma density

irregularities within the ionosphere, and the propagation model determines their subsequent effects on radio wave propagation [Secan et al., 1995].

For a given set of environmental conditions (e.g. date, time, SSN, and geomagnetic activity levels), and system parameters (e.g. transmitter and receiver location, and carrier frequency), the WBMOD model calculates the intensity scintillation index (S_4), the phase scintillation index (σ_ϕ), the strength of the phase scintillation power spectral density (T_{scin}), and the power spectral index (ν), together with the statistics on the occurrence of each parameter. Since its development, the WBMOD model has been reviewed and revised several times using the latest space-based/ground-based observation data [Fremouw and Secan, 1984; Secan et al., 1995].

Phase Screen Scintillation Model

The phase screen scintillation model (PSSM), developed by a group of researchers at Cornell University [Psiaki et al., 2007], is a simple physics-based model used for the evaluation of single and dual-frequency GPS receiver tracking loops robustness in the presence of scintillation. The model assumes that the ionospheric irregularities are concentrated within a thin shell or screen at the typical height of maximum irregularities[4] (e.g. 350 km). At the screen height, it is also assumed that variations in the vertical total electron content - produced by ionospheric irregularities - are distributed perpendicular to the earth's magnetic field lines, as illustrated in Figure 1.6. Shown in the figure is the nominal magnetic field direction along the y-axis, the wave propagation direction along the z-axis, and the TEC profile along the x-axis.

For a given profile of vertical TEC (VTEC), the PSSM model generates the scintillation-induced phase fluctuations using the following equation [Psiaki et al., 2007].

---

[4] *According to Aarons [1982], the main disturbance region for equatorial irregularities is located between 250 and 400 km altitude.*

$$\phi_{sc}(x) = (2\pi)^2 \left[\frac{40.3 TEC(x)}{c\omega} \right] \tag{1.13}$$

where c is the speed of light in m/s, ω is the carrier frequency in rad/s, and *TEC(x)* has a unit of el/m^2.

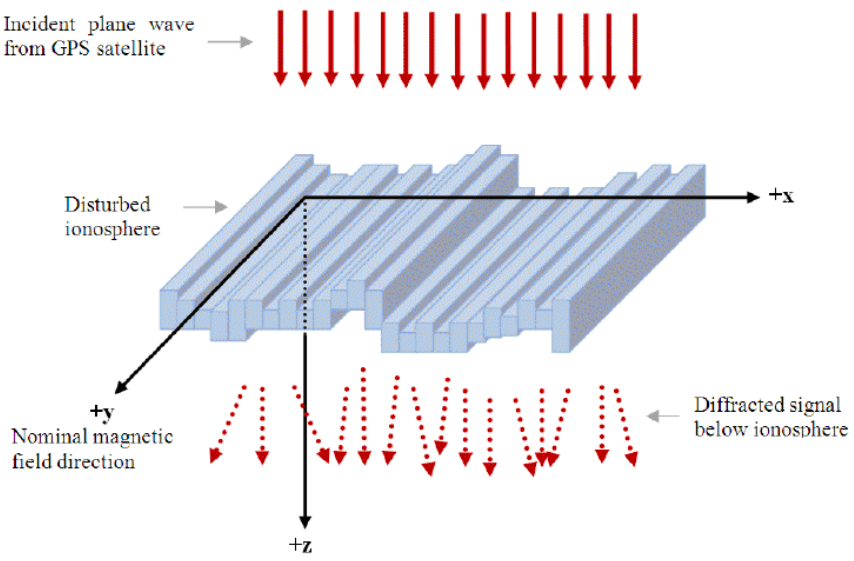

Figure 1.6: Geometry of the phase screen scintillation model [modified after Psiaki et al., 2007].

The phase perturbation effects are then propagated towards the receiver using the Huygens-Fresnel formulation for wave propagation [Psiaki et al., 2007]:

$$[\tilde{I}_{sc}(x,\omega)+j\tilde{Q}_{sc}(x,\omega)]e^{j\omega t}= A_0\sqrt{jk/2\pi z}\exp\{j(\omega t-kz)\}\int_{-\infty}^{\infty}\exp\left\{j\left(\phi_{sc}(x')-k(x-x')^2/2z\right)\right\}dx' \quad (1.14)$$

where A_0 is the signal's amplitude, $\tilde{I}_{sc}(x,\omega)$ and $\tilde{Q}_{sc}(x,\omega)$, respectively, represent the scintillation-induced in-phase and quadrature-phase signal fluctuations at the receiver, and $k=\omega/c$ is the signal's wavenumber in rad/m.

For the typical ionospheric drift velocity ($v_{drift}\approx 100-150$ m/s), the temporal variation of the in-phase and quadrature-phase scintillation perturbation can be obtained via [Psiaki et al., 2007]

$$\begin{aligned} I_{sc}(t) &= \tilde{I}_{sc}(x,\omega) \\ &= \tilde{I}_{sc}(v_{drift}\,t,\omega) \end{aligned} \quad (1.15)$$

and

$$\begin{aligned} Q_{sc}(t) &= \tilde{Q}_{sc}(x,\omega) \\ &= \tilde{Q}_{sc}(v_{drift}\,t,\omega). \end{aligned} \quad (1.16)$$

Considering the TEC variations as the seeding source of ionospheric scintillation and adopting the diffraction theory for signal propagation towards the receiver makes the PSSM model a reasonable candidate for studying the impact of scintillation on GPS receivers at the equatorial regions. The model, however, is based on the assumption that the wave propagation direction is normal to the phase screen (as shown in Figure 1.6). In other words, only transmissions from high elevation sources are considered. In reality, however, signals arrive from different directions; sometimes from very low elevation

angles. Moreover, it is shown by Rino [2011] that ionospheric scintillation effects are more severe during oblique signal propagation compared with that in normal propagation. Thus, oblique propagation should be included in the PSSM model if one decides to bring the results closer to reality.

Statistical Model

For the purpose of testing GPS receiver carrier tracking loops robustness in equatorial regions, a simple statistical scintillation model (SSM) for simulating equatorial trans-ionospheric radio wave scintillation is suggested by Humphreys et al. [2009]. The SSM model evaluates the scintillation signal in a complex form. Accordingly, the model generates a complex tracking channel response function in the form of

$$z(t) = \bar{z} + \xi(t) \tag{1.17}$$

with $\bar{z}$ being the direct component, and $\xi(t)$ being the fading process. The magnitude of $z(t)$ is assumed to follow a Rice distribution (similar to Nakagami-m distribution) with the Rician parameter $K = \sqrt{1 - S_4^2} \big/ (1 - \sqrt{1 - S_4^2})$, and the spectrum of $\xi(t)$ is assumed to follow that of a low-pass second-order Butterworth filter whose cutoff frequency is related to τ, the decorrelation time of $\xi(t)$, via $f_c = 1.24 \big/ (\sqrt{2}\pi\tau)$ [Humphreys et al., 2009].

The SSM model requires two input parameters (i.e. the fading processes decorrelation time τ, and intensity scintillation index S_4) to generate different scintillation time histories. The model has been validated by comparison with phase-screen-generated and empirical scintillation data in realistic tracking loop tests [Humphreys et al., 2009].

In terms of simplicity and number of input parameters, the statistical model is preferred over the more complicated WBMOD model, or even the phase screen scintillation model.

However, it does not provide any information regarding the seeding sources of irregularities, or the physical processes that lead to the often-observed scintillation disturbing effects.

1.4.2 A Review of Scintillation Effects on Tracking Loops

During the last two decades, a number of researchers have attempted to investigate the performance of GPS receiver tracking loops using tracking loop simulators, and real and/or simulated scintillation data:

Using code and carrier tracking loop simulators for GPS L_1 signal, Hegarty et al. [2001] have determined the tracking errors in terms of intensity scintillation index, and carrier-to-noise ratio. According to their results, unlike code tracking loops which are quite robust to phase and intensity scintillation, carrier tracking loops are very susceptible to scintillation, and for strong scintillation conditions, the required carrier-to-noise ratio for consistent carrier tracking often drops below the threshold, and loss of signal lock occurs. Their results on semi-codeless tracking of the L_2 carrier indicate that these types of receivers are very vulnerable to scintillation especially when signals are received at low elevation angles. Similar results have been demonstrated earlier by Nichols et al. [1999] for high-latitude scintillations.

Following the work of Rino [1979], and Knight and Finn [1998], and using a reasonable combination of the WBMOD model and tracking loop models, Conker et al. [2003] have determined the effects of scintillation on the availability of GPS and satellite-based augmentation systems (SBAS) for L_1 C/A and L_2 semi-codeless receivers. Their analyses suggest that during high solar activity periods, such as solar cycle peaks where scintillation is at a maximum level, in the equatorial regions, Hawaii, and far-northern reaches of Canada there could be a significant number of satellite signals lost for both full-code correlation and semi-codeless receivers. They did not, however, consider system dynamics as part of error sources (in terms of steady state error or transient error) in their calculations. As shown in Chapter six of this thesis, system dynamics, as one

important source of error, directly affect the choice of optimum loop bandwidth and loop order.

Using real scintillation data collected in the equatorial region (Cachoeira Paulista, Brazil, November 6-19, 1998) via multiple spaced receivers, Kintner et al. [2001] have investigated the impact of equatorial scintillations, in terms of fade depth and fade duration, on the performance of GPS receivers. According to their observations, the ionospheric scintillation fade duration is directly related to the difference between the ionospheric drift velocity, and the GPS signal penetration point velocity at 350 km altitude (considered as the typical height of maximum electron density). As shown in their results, for small velocity differences, the signal fade duration is lengthened, sometimes up to 15-16 seconds. During prolonged signal fadings, the loss of receiver lock on GPS signals is more likely when fade depth is near the tracking threshold.

Seo et al. [2008] have also analyzed the aviation navigation availability during a strong scintillation period based on real scintillation data collected at Ascension Island on March 18, 2001. According to their results, the aviation receivers do not generally provide high availability under severe scintillation conditions, and to overcome that, short signal reacquisition periods are required. None of these researchers, however, have provided the relationship between the scintillation-induced fade depth and duration, and the receiver performance parameters.

1.5 Research Objectives

Since GPS has found an enormous market in the civilian community in diverse areas, determining the accuracy and reliability of GPS receivers and predicting their behavior under different environmental conditions is of great importance. As one of the most important environmental factors, the disturbed ionosphere and associated ionospheric scintillation can significantly affect the performance of the GPS receivers through introducing unexpected variations in the phase and intensity of received signals. In addition, increased ionospheric activity in the years preceding the solar maximum of

2013 will likely have more severe impact on GPS in terms of navigation errors due to large-scale irregular structures and loss of signal lock due to scintillation.

The principle objective of this research is to develop tools to *investigate* the impact of low-latitude ionospheric scintillations on a generic GPS receiver carrier tracking loop, with the aim of developing a means to *quantify* the performance of GPS receivers as a function of different ionospheric conditions. The following tasks and sub-objectives are identified:

Tasks

1. Implement a physics-based model for characterizing ionospheric scintillation signals based on existing theory.
2. Develop scintillation simulator based on Task 1.
3. Develop a single-frequency GPS signal simulator.
4. Develop GPS receiver code and carrier tracking loop simulators.

Sub-objectives

1. Obtain expressions for the carrier phase tracking mean square error, and carrier velocity mean square error as a function of scintillation parameters (T_{scin}, S_4, ν) and tracking loop parameters (β, η, f_n, B_n) in the presence of thermal noise and system dynamics.
2. Determine the intensity and phase scintillation thresholds beyond which the carrier tracking loop is expected to lose phase lock, and the carrier velocity error is expected to exceed a preset level.
3. Determine the impact of scintillation-induced signal fade depth and fade duration on the probability of loss of phase lock, and the probability of cycle slips.
4. Obtain an expression for the optimum loop equivalent noise bandwidth for a minimum tracking error in the presence of ionospheric scintillation, thermal noise and system dynamics for both full-code correlation and semi-codeless receivers.
5. Determine the ionospheric scintillation effects on the correlation of different L-band signals transmitted by the GPS satellites on the same propagation path.

1.6 Thesis Outline

The current chapter contains an introduction to the ionosphere, the sources of ionospheric irregularities, their geographic dependence, and their impacts on GPS receivers.

Chapter two covers the general theory of scintillation. This includes electromagnetic wave propagation in homogeneous and weakly-inhomogeneous media, scattering and propagation theories as building blocks of scintillation theory, statistical characteristics of scintillations, and finally, wave oblique propagation in anisotropic media. In addition, the physics-based phase screen model and the scintillation simulator, used for generating different intensity and phase scintillation realizations, are described in detail.

A GPS signal simulator and a GPS receiver code and carrier tracking loop simulator is developed in this work for testing different algorithms and techniques throughout the thesis. GPS signal structure and signal simulator are described in Chapter three. The software receiver building blocks, together with signal acquisition and tracking algorithms, and GPS tracking loop simulators are given in Chapter four. Using the tracking loop simulators, the results of processing synthetic scintillated data are evaluated through comparison with real scintillation data collected at Ascension Island during the solar maximum of 2001.

In Chapter five, the ionospheric scintillation effects on the GPS receiver carrier tracking loop performance are investigated, and quantified through the definition of two receiver performance measures (i.e. the carrier phase tracking mean square error and carrier velocity mean square error), as a function of scintillation parameters (T_{scin}, S_4, ν) in the presence of thermal noise and system dynamics. Moreover, the intensity and phase scintillation thresholds beyond which the carrier tracking loop may lose lock are determined. The simulation results are used to validate theoretical outcomes, whenever applicable, and to determine where the theoretical predictions fail.

The impacts of scintillation on the probability of loss of lock and the probability of cycle slips are investigated in Chapter six. In addition, the optimum loop noise bandwidth for a

minimum tracking loop error is calculated as a function of scintillation parameters (T_{scin}, S_4, ν) and tracking loop parameters (β, η, f_n) in the presence of thermal noise and receiver-platform dynamics. Finally, the effects of scintillation on the correlation of different L-band signals employed by the GPS system are explored, and further used in the determination of carrier tracking error variance of L_2 semi-codeless receivers.

Chapter seven contains the main conclusions and recommendations for future studies on the methods developed within the thesis.

1.7 Methodology Flowchart

The methodology flowchart in Figure 1.7 provides an overview of the sequence of steps taken throughout the thesis to accomplish the tasks and achieve the final objectives. The work is summarized in five steps:

Step 1: Generate different scintillation realizations (i.e. scintillation time histories) by means of the phase screen model scintillation simulator in Chapter two.

Step 2: Generate GPS L_1 signal using the signal simulator developed in Chapter three, and modulate the GPS signal with scintillation signals via complex modulation technique.

Step 3: Process the scintillated GPS signal in the carrier tracking loop simulators in Chapter four.

Step 4: Employ the statistical properties of scintillation components, and the model of the conventional Costas-type carrier tracking loop to derive various loop measures as a function of scintillation and tracking loop parameters in Chapters five and six.

Step 5: Evaluate the theoretical predictions through comparison with simulation results, whenever applicable.

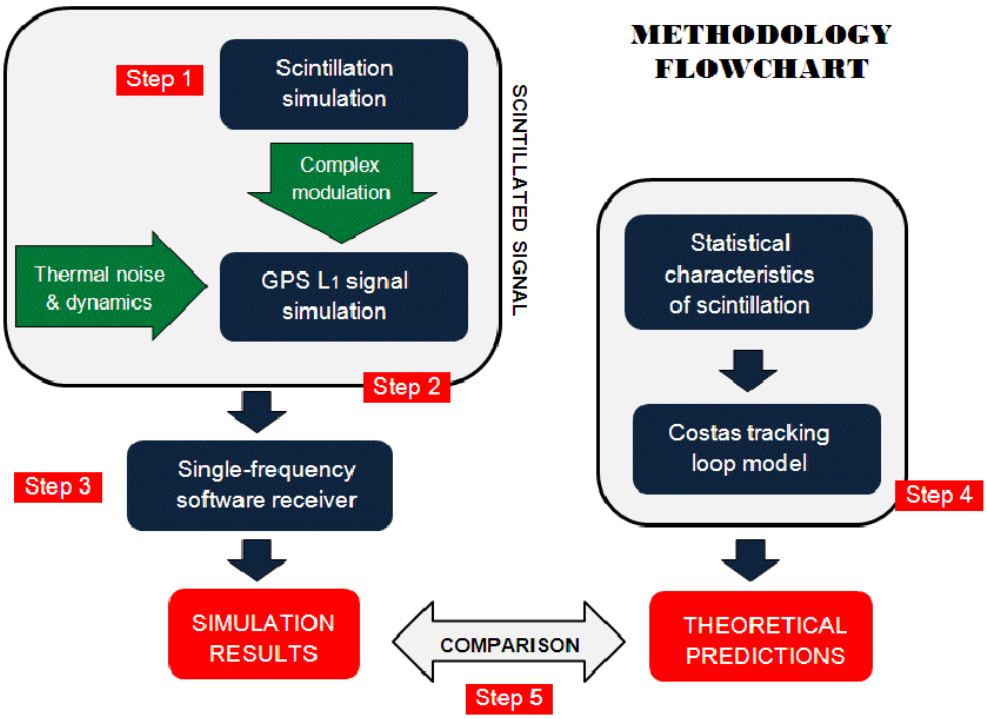

Figure 1.7: Simulation methodology flowchart.

Chapter Two: Theory of Scintillation

With a few adjustments, scintillation theory can be considered as a combination of *propagation theory* and *scattering theory*. Propagation theory defines the space and time progression of wave fields within a uniform or homogeneous medium. The physical properties of such media do not change at different points. Scattering theory, on the other hand, is mainly concerned with the wave propagation in an inhomogeneous medium. This theory defines the generation of scattered wave fields when the initial propagating wave experiences steep gradients in the material properties of the medium [Rino, 2011].

Following the propagation theory, the theory of scintillation assumes that the gradients in the material properties of the propagation medium are small enough that they can be neglected. The propagation medium, therefore, is assumed to be *weakly inhomogeneous*.

Similar to the scattering theory, the theory of scintillation accepts wave scatterers (here, plasma density depletion regions) throughout the propagation medium. However, unlike the scattering theory, only *forward* propagation is considered in scintillation theory and all backscatters induced by structured medium are neglected. According to this assumption, the energy propagating in the forward wave field is preserved [Rino, 2011].

Wave propagation theory and weak scattering approximation are reviewed in Section 2.1 as a means of developing scintillation theory. This forms a basis for further expansion and modification of scintillation theory in later sections to develop realistic simulation tools. This review is based on Chapters 1-4 of Rino [2011].

2.1 Electromagnetic Wave Propagation Theory

The transmission of electromagnetic (EM) waves is described by Maxwell's equations which define the mutual connection between the magnetic and electric field quantities. These equations are valid at any spatial location, and in any material including free space [Mitchell, 2008].

2.1.1 Propagation in Homogeneous Media

Maxwell's equations in time-harmonic form relate the wave fields to the material quantities of the propagation medium via the following two equations [Rino, 2011].

$$\nabla \times \mathrm{E} = -i\omega\mu \mathrm{H} \tag{2.1}$$

$$\nabla \times \mathrm{H} = i\omega\varepsilon \mathrm{E} + \mathrm{J} \tag{2.2}$$

where, "$\nabla\times$" represents the curl operator, the complex vectors *E* and *H* are electric (V/m) and magnetic (amp/m) fields, respectively. The complex vector *J* represents electric current density (amp/m^2), μ is permeability (H/m), ε is permittivity (F/m), and $\omega = 2\pi f$ is frequency (rad/s).

Using Maxwell's equations defined above, the general form of wave equation is obtained as follows [Rino, 2011].

$$\nabla^2 \mathrm{E} + \omega^2 \mu\varepsilon \mathrm{E} = -\nabla(\mathrm{E} \cdot \nabla \log \varepsilon) \tag{2.3}$$

Since in a homogeneous medium both the magnetic permeability (μ) and electric permittivity (ε) are constant, the right-hand side of Equation (2.3) equals zero. As a result, the solutions to equation

$$\nabla^2 \mathrm{E} + \omega^2 \mu\varepsilon \mathrm{E} = 0 \tag{2.4}$$

represents *freely propagating waves*. For a constant wavenumber value (k), where

$$k = |\bar{\mathrm{k}}| = \omega\sqrt{\mu\varepsilon} = \omega/c, \tag{2.5}$$

the plane waves of the form [Rino, 2011]

$$\mathrm{E}(\bar{\mathrm{r}}) = \hat{\mathrm{E}}(\bar{\mathrm{k}})\ \exp\{\mathrm{i}\bar{\mathrm{k}}\cdot\bar{\mathrm{r}}\} \tag{2.6}$$

can satisfy Equation (2.4), where $\bar{\mathrm{k}} = k_x\hat{a}_x + k_y\hat{a}_y + k_z\hat{a}_z$ is the spatial wavenumber vector, and $\bar{\mathrm{r}}$ is the position vector. Since k is constant, the components of the wave vector are dependent. Considering x as a reference propagation direction, and k_x as the magnitude of x-component of $\bar{\mathrm{k}}$, the relation between k_x, the transverse component κ, and k is defined as [Rino, 2011]

$$\begin{aligned} k_x &= k\sqrt{1-(\kappa/k)^2} \\ &= k\ g(\kappa). \end{aligned} \tag{2.7}$$

For $\kappa \le k$, the plane wave propagates without attenuation. The two-dimensional Fourier decomposition of an electric field in a plane perpendicular to the propagation direction, at $x = x_m$, can be expressed by [**after modification from** Rino, 2011]

$$\hat{\mathrm{E}}(\mathrm{x}_\mathrm{m};\bar{\kappa}) = \iint \mathrm{E}(\mathrm{x}_\mathrm{m},\bar{\varsigma})\exp\{-\mathrm{i}\bar{\kappa}\cdot\bar{\varsigma}\}\mathrm{d}\bar{\varsigma}, \tag{2.8}$$

where the integration range is from -∞ to ∞, and $\bar{\varsigma}$ is the transverse vector axis. Now at any point beyond the plane, the freely propagating wave field would be [Rino, 2011]

$$\mathrm{E}(\bar{\mathrm{r}}) = \iint \hat{\mathrm{E}}(\mathrm{x}_\mathrm{m};\bar{\kappa})\exp\{\mathrm{ik}_\mathrm{x}(\bar{\kappa})\,|\,\mathrm{x}-\mathrm{x}_\mathrm{m}\,|\}\times\exp\{\mathrm{i}\bar{\kappa}\cdot\bar{\varsigma}\}\frac{\mathrm{d}\bar{\kappa}}{(2\pi)^2}, \tag{2.9}$$

which satisfies Equation (2.4). The term $\exp\{\mathrm{ik}_\mathrm{x}(\bar{\kappa})\,|\,\mathrm{x}-\mathrm{x}_\mathrm{m}\,|\}$ is referred to as the *spatial transfer function*.

2.1.2 Propagation in Weakly Inhomogeneous Media

Similar to Equation (2.3), the general form of the wave equation for inhomogeneous media is given by [Rino, 2011]

$$\begin{aligned} \nabla^2 E + k^2 n^2 E &= -\nabla(E \cdot \nabla \log \varepsilon) \\ &\approx 0 \end{aligned} \tag{2.10}$$

The term $\omega^2 \mu\varepsilon$, in Equation (2.3), is substituted by its equivalent $k^2 n^2$ in Equation (2.10), where [**after modification from** Rino, 2011] $n = c_0 / c = c_0 \sqrt{\mu\varepsilon}$ is refractive index, and c_0 is the speed of light in free space. For a *weakly inhomogeneous* media, the right-hand side of Equation (2.10) can be approximated by zero.

Structures in a propagation medium are characterized by changes in the local refractive index: $n = 1 + \delta n$. Following this, the approximate form of Equation (2.10) for a weakly inhomogeneous media would be [Rino, 2011]

$$\begin{aligned} \nabla^2 E + k^2 E &= -k^2 (2\delta n + \delta n^2) E \\ &\approx -2k^2 \delta n E \end{aligned} \tag{2.11}$$

One method of solving Equation (2.11) would be via employing the scalar free-space Green function [Rino, 2011]:

$$G(\bar{r}, \bar{r}') = \frac{\exp\{ik\,|\,\bar{r} - \bar{r}'|\}}{2\pi\,|\,\bar{r} - \bar{r}'|}. \tag{2.12}$$

where $\bar{r}$ and $\bar{r}'$ denote two position vectors in space. Using Equation (2.12), the following scatter integral [**after modification from** Rino, 2011]

$$E(\bar{r}) = E_i(\bar{r}) + 2k\iiint G(\bar{r},\bar{r}')S(\bar{r}')E(\bar{r}')\,d\bar{r}' \\ = E_i(\bar{r}) + E_s(\bar{r}) \tag{2.13}$$

can be considered as the solution to Equation (2.11), where

$$S(\bar{r}) = k\delta n(\bar{r}) \tag{2.14}$$

is the structure source function. In Equation (2.13), the vector field $E_s(\bar{r})$ represents the scattered field, while $E_i(\bar{r})$ denotes the solution to the homogeneous equation, and can be obtained from Equation (2.9). The general solution to Equation (2.13) requires certain approximations in the structured medium as described in the next section.

2.1.3 Weakly Scattering Media

Finding solutions to $E(\bar{r})$ initiated by $E_i(\bar{r})$ is very complicated; however, by considering the propagation medium as a *weakly scattering* medium, $E(\bar{r}')$ in Equation (2.13) can be approximated by a freely propagating wave field as introduced in Equation (2.9), and the Green function can be expressed by [Rino, 2011]

$$G(k \mid \bar{r} - \bar{r}'|) = \iint \frac{i\exp\{ikg(\kappa) \mid x - x'|\}}{2kg(\kappa)} \exp\{i\bar{\kappa}\cdot\Delta\bar{\varsigma}\}\frac{d\bar{\kappa}}{(2\pi)^2} \tag{2.15}$$

By substituting Equation (2.15) in (2.13), the general solution to wave propagation equation for a weakly inhomogeneous medium is obtained as [Rino, 2011]

$$
\begin{aligned}
E(\bar{r}) &= E_i(\bar{r}) + E_s(\bar{r}) \\
&= E_i(\bar{r}) + i\iint\left[\iint S(\Delta\bar{\kappa}(\bar{\kappa},\bar{\kappa}'))\,E(0,\bar{\kappa}')\frac{d\bar{\kappa}'}{(2\pi)^2}\right] \\
&\quad\times\frac{\exp\{ikg(\kappa)x\}}{g(\kappa)}\exp\{i\bar{\kappa}\cdot\bar{\varsigma}\}\frac{d\bar{\kappa}}{(2\pi)^2}.
\end{aligned}
\tag{2.16}
$$

Equation (2.16) forms a linear integral relation between an observable scattered field $E_s(\bar{r})$ and the structure that is initiating the scatter or the propagation disturbance. Wave propagation theory along with weak scattering approximation is used to develop scintillation theory.

2.2 Scintillation Theory

Under the weak inhomogeneity restriction for the propagation medium, and considering x as the reference propagation direction, the wave field evolution in space can be expressed by [Rino, 2011]

$$
\frac{\partial E(x,\bar{\varsigma})}{\partial x} = ik\Theta E(x,\bar{\varsigma}) + ik\delta n(x,\bar{\varsigma})E(x,\bar{\varsigma}). \tag{2.17}
$$

Equation (2.17) is known as forward propagation equation (FPE) and consists of two terms: the *propagation operator* ($ik\Theta$), and the *media-interaction term* ($ik\delta n(x,\bar{\varsigma})$), where $\bar{\varsigma}$ denotes the propagation transverse axes, and Θ is the propagation operator defined by the Taylor series expansion of $g(\kappa)$ in Equation (2.7).

One general solution to this equation would be, first, determining Equation (2.17) in the absence of the propagation operator via

$$E(x_{n+1},\bar{\varsigma}) = E(x_n,\bar{\varsigma})\underbrace{\exp\left\{ik\int_{x_n}^{x_{n+1}}\delta n(x',\bar{\varsigma})\,dx'\right\}}_{phase\ \ perturbation} \tag{2.18}$$

and then using the *split-step* method (described in the following section), in which the wavefront is modulated by the phase perturbation in Equation (2.18) at the irregularity layer entrance, then the wave is propagated towards the next layer using the propagation operator.

2.2.1 Split-Step Solution to Forward Propagation Equation

Following Equation (2.17), the forward propagation equation in a two-dimensional medium, with x being the reference propagation direction, can be written as [Rino, 2011]

$$\frac{\partial\psi(x,z)}{\partial x} = ik\Theta\psi(x,z) + ik\delta n(x,z)\psi(x,z) \tag{2.19}$$

where $\psi(x,z)$ is the complex wave field intensity. The general solution to this equation consists of the *media-interaction solution* plus the *propagation solution*. Assuming $\Theta = 0$, the media-interaction solution to Equation (2.19) follows that of Equation (2.18) for a two-dimensional medium, and the propagation solution follows [Rino, 2011]

$$\psi(x,z) = \int\hat{\psi}(x_n,\kappa_z)\exp\{ikg(\kappa_z)(x-x_n)\}\exp\{i\kappa_z z\}\frac{d\kappa_z}{2\pi} \tag{2.20}$$

with

$$\hat{\psi}(x_n,\kappa_z) = \int\psi(x_n,z)\exp\{-i\kappa_z z\}\,dz. \tag{2.21}$$

The above two solutions can be combined in a single recursive method, known as the *split-step* algorithm. To apply this method, the propagation medium is divided into n consecutive layers with thickness Δx_n - each layer described by local homogeneous statistical properties - and the solution is determined by repeating continuously the *propagation* and the *media-interaction* calculations given in Equations (2.18) and (2.20). The split-step recursion method can be applied through [Rino, 2011]

$$\psi(x_n, m\Delta z) = \psi(x_{n-1}, m\Delta z)\exp\{ik\delta n(x_n, m\Delta z)\Delta x_n\} \tag{2.22}$$

$$\hat{\psi}(x_n, l\Delta\kappa_z) = \sum_{m=0}^{N-1}\psi(x_n, m\Delta z)\exp\{-2\pi ilm/N\} \tag{2.23}$$

$$\psi(x_{n+1}, m\Delta z) = \frac{1}{N}\sum_{l=0}^{N-1}\hat{\psi}(x_n, l\Delta\kappa_z)P_l^{\Delta x_n}\exp\{2\pi ilm/N\} \tag{2.24}$$

where Equations (2.23) and (2.24) are, respectively, forward and inverse discrete Fourier Transforms (DFT), and the spatial transfer function P_l is defined as [Rino, 2011]

$$P_l = \exp\{ikg(\kappa_z(l\Delta\kappa_z)\}, \tag{2.25}$$

at a set of spatial frequencies given by

$$\kappa_z(l\Delta\kappa_z) = [-N/2, -N/2+1, ..., -1, 0, 1, ..., N/2-1]\Delta\kappa_z; \quad l = 0, 1, ..., N-1 \tag{2.26}$$

The required parameters are the number of layers (n), the primary field $\psi(x_0)$, the sampling intervals Δz and Δx_n, and the DFT size N.

Equations (2.22) to (2.24) can simply be modified to accommodate wave propagations in three-dimensional media (e.g. replacing $\delta n(x_n, m\Delta z)$ by $\delta n(x_n; m_y\Delta y, m_z\Delta z)$).

2.3 Statistical Characteristics of Scintillations

Small-scale irregular structures in the propagation medium, from which scintillation originates, must be specified in the statistical theory. In this case, irregularity is principally shown as perturbations δn to the local refractive index, where [Rino, 2011]

$$\begin{aligned} \delta n &= -4\pi r_e \delta N_e c^2/\omega^2 \\ &= -4\pi r_e \delta N_e / k^2. \end{aligned} \tag{2.27}$$

In this equation, r_e denotes the classical electron radius (~ 2.8198×10^{-13} cm), and δN_e denotes the electron density perturbation.

The theory of stochastic processes determines the mathematical basis for statistical measurements that describe random structures. As ionospheric scintillation is the result of wave propagation in a randomly structured medium, *scintillation is a stochastic process*. Scintillation components (phase and intensity) can therefore be characterized using a set of statistical parameters such as *mean*, *variance*, *spectral density* and *probability distribution*. The following sections describe these parameters in some detail.

2.3.1 Scintillation Spectral Density

According to the Landau-Hopf theory of turbulence, a fluid (liquid, gas or plasma) develops Fourier modes as it flows. Under strong forcing conditions, the Fourier modes follow the *power-law distribution* of the general form C_s/q^p over the spatial wavenumber range $q_o << q << q_i$ [Rino, 2011]. The parameter C_s is the turbulent strength, p is the power-law index, q_o is the outer scale and corresponds to the largest irregularity in the propagation medium (where $q_o = 2\pi/l_0$, with l_0 being the outer scale

length), and q_i is the inner scale and represents the smallest irregularity. Following this theory, the spectral density function (SDF) of the refractive index fluctuation is defined as [Rino, 2011]

$$\begin{aligned}\Phi_{\delta n}(q) &= \frac{\left\langle \delta n^2 \right\rangle (4\pi)^{3/2}\,\Gamma(\nu+1/2)}{\Gamma(\nu-1)\,q_o^{-2\nu+2}\,(q_o^2+q^2)^{(\nu+1/2)}} \\ &= \frac{C_s}{(q_o^2+q^2)^{(\nu+1/2)}} \\ &\approx \frac{C_s}{q^{(2\nu+1)}}\ , \qquad (q >> q_0)\end{aligned} \tag{2.28}$$

which is characterized by the scale-free turbulent strength parameter (C_s), the scale-free spectral index (ν), and the outer scale (q_0). In this equation $\Gamma(.)$ represents the Gamma function, and $\left\langle \delta n^2 \right\rangle$ represents the mean square value of refractive index variation. From Equation (2.27), the mean square value of refractive index variation can be calculated as follows.

$$\begin{aligned}\left\langle \delta n^2 \right\rangle &= (4\pi)^2\, r_e^2 \left\langle \delta N_e^2 \right\rangle / k^4 \\ &= r_e^2 \lambda^4 \left\langle \delta N_e^2 \right\rangle / \pi^2 .\end{aligned} \tag{2.29}$$

Using Equation (2.28) and considering x as the principal propagation direction, the impact of the three-dimensional irregular propagation medium on the two-dimensional propagating plane wave can be mapped onto the wavefront phase through integration over a propagation layer with thickness l_p . As a result, the three-dimensional refractive index SDF is linked to the two-dimensional phase scintillation SDF via [Rino, 2011]

$$\Phi_{\delta\phi}(\bar{\kappa}) = k^2 l_p \Phi_{\delta n}(q)$$
$$= \frac{k^2 l_p C_s}{(q_o^2 + q^2)^{(\nu+1/2)}} \approx \frac{k^2 l_p C_s}{q^{2\nu+1}}. \qquad (2.30)$$

2.3.2 Scintillation Probability Density Function

Among all different probability density functions that have been proposed for scintillation components thus far, the *Gaussian* distribution (for phase scintillation), and both the *Rice* and the *Nakagami-m* distributions (for intensity scintillation) were found to provide the best fit based on the results of the chi-square tests conducted on a large set of real scintillation data [e.g. Humphreys et al., 2009].

Amplitude (A), intensity ($I = A^2$) and phase ($\delta\phi$) scintillation probability density functions are defined as [Knight and Finn, 1998; Hegarty et al., 2001]

$$p(A) = \frac{2u^u A^{2u-1}}{\Gamma(u) \langle A^2 \rangle^u} e^{-uA^2/\langle A^2 \rangle} \quad , \quad A \geq 0 \qquad (2.31)$$

$$p(I) = \frac{u^u I^{u-1}}{\Gamma(u) \langle I \rangle^u} e^{-uI/\langle I \rangle} \quad , \quad I \geq 0 \qquad (2.32)$$

$$p(\delta\phi) = \frac{1}{\sqrt{2\pi}\sigma_\phi} e^{-\delta\phi^2/2\sigma_\phi^2} \qquad (2.33)$$

where $\sigma_\phi^2 = \langle \delta\phi^2 \rangle$ is the phase scintillation mean square value[5], $\langle I \rangle$ is the average intensity scintillation, and u is a parameter that is related to intensity scintillation via

---

[5] *Since phase scintillation follows a zero-mean Gaussian distribution, its variance and mean square value are equal.*

$$u = \frac{\langle I \rangle^2}{\langle I^2 \rangle - \langle I \rangle^2}. \tag{2.34}$$

Probability density functions are used in Chapter six when determining the impact of scintillation on the probability of loss of phase lock.

2.3.3 Scintillation Indices

Intensity scintillation index (S_4), and phase scintillation variance (σ_ϕ^2) defined below are typically used to determine the strength of scintillation activity [Rino, 2011].

$$S_4 = \frac{\sqrt{\langle I^2 \rangle - \langle I \rangle^2}}{\langle I \rangle} = \left[k^2 l_p C_s \rho_F{}^{(2\nu-1)} \frac{\Gamma\left((2.5-\nu)/2\right)}{2^{\nu+1/2}\sqrt{\pi}\,(\nu-0.5)\;\Gamma\left((0.5+\nu)/2\right)} \right]^{1/2} \tag{2.35}$$

$$\sigma_\phi^2 = \langle \delta\phi^2 \rangle = k^2 l_p C_s \frac{\Gamma(\nu-1/2)}{4\pi\;\Gamma(\nu+1/2)\;q_o^{2\nu-1}} \tag{2.36}$$

From Equations (2.34) and (2.35), one can simply realize that $u = 1/S_4^2$. The scintillation indices with geometric and anisotropy corrections are given in Appendix V.

2.3.4 Frequency Dependence of Scintillation Indices

The ionosphere is dispersive for radio waves (including the GPS signals). The ionospheric index of refraction is inversely proportional to the frequency of the propagating signal, therefore, it causes lower frequency signals to bend more than higher frequency signals [Misra and Enge, 2006]. Since ionospheric scintillation results from random variation of index of refraction, one may expect to see greater scintillation impacts on radio waves with lower frequencies compared with higher frequencies.

The amount of frequency dependence of the intensity and phase scintillation can be obtained from Equations (2.35) and (2.36), respectively. The intensity scintillation index S_4 is proportional to the wavenumber k, the turbulent strength parameter C_s, and the Fresnel radius $\rho_F = \sqrt{x/k}$, via

$$S_4 \propto \sqrt{k^2 C_s \rho_F^{(2\nu-1)}} \tag{2.37}$$

in which $k \propto \omega$ (from the definition of wavenumber), $C_s \propto \omega^{-4}$ (from Equations (2.28) and (2.29)), and $\rho_F \propto \omega^{-1/2}$ (from the definition of Fresnel radius). Accordingly, S_4 is dependent on the carrier frequency ω by

$$S_4 \propto \sqrt{\omega^2\, \omega^{-4} \omega^{(1-2\nu)/2}} = \omega^{-(2\nu+3)/4} \tag{2.38}$$

Similarly, the root-mean-square (RMS) phase scintillation (σ_ϕ) is related to k and C_s via

$$\sigma_\phi \propto \sqrt{k^2 C_s} \propto \sqrt{\omega^2\, \omega^{-4}} = \omega^{-1} \tag{2.39}$$

Therefore, it is inversely proportional to the signal's frequency.

According to these results, for GPS L_1 and L_2 frequencies, and $\nu = 4/3$ (a common value for the equatorial scintillation), $S_{4(L_2)} \approx 1.4\, S_{4(L_1)}$ and $\sigma_{\phi(L_2)} \approx 1.3\, \sigma_{\phi(L_1)}$.

2.4 Electromagnetic Wave Oblique Propagation in Anisotropic Media

In a magnetized plasma (like Earth's ionosphere), charged particles tend to move along the magnetic field lines. This results in the formation of rod-shaped field-aligned anisotropic irregular regions, whose impact on propagating wave fields differs from isotropic media. The effect of anisotropic irregularities can be accommodated in the theory of scintillation by scaling and rotating the principal coordinates that initially describe isotropic structures [Rino, 2011]. To do this, the direction of geomagnetic field lines at any specific location within the propagation medium is required.

2.4.1 Geomagnetic Field

According to Dynamo theory, rotating, thermally convecting, and electrically conducting fluids (either liquid or gas) tend to create magnetic fields. The Earth's magnetic field is believed to be generated within its metal-rich liquid outer core (see Figure 2.1) by a combination of planetary rotation, thermal convection, and electrical forces within the core [Macmillan and Rycroft, 2010]. The geomagnetic field is roughly a magnetic dipole, with its north pole near the Earth's geographic south pole and its south pole near the Earth's geographic north pole, as shown in Figure 2.2.

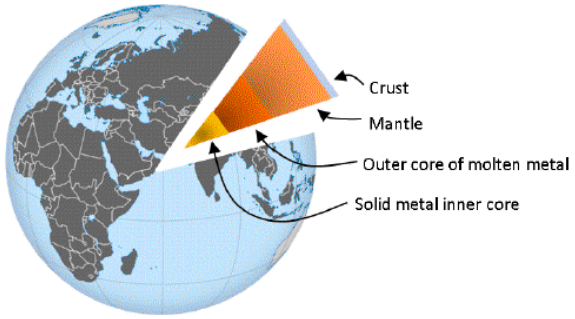

Figure 2.1: Earth's internal structure.

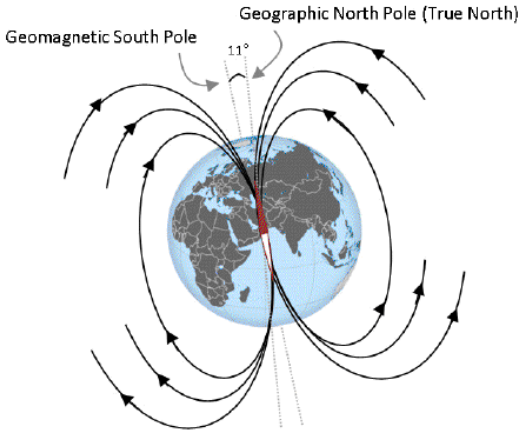

Figure 2.2: Earth's magnetic field. Axis of dipole is currently tilted about 11° with respect to spin axis.

2.4.1.1 Geomagnetic Components

The Earth's magnetic field is usually characterized (locally) in terms of one or a set of parameters defined below [Olsen et al., 2007]:

- **Total intensity (F):** the total strength of the magnetic field described in units of nanotesla (nT). It includes north component (X), east component (Y), and vertical component (Z), where Z is positive downwards.
- **Horizontal intensity (H):** the horizontal component of F, in nT. It includes north component (X) and east component (Y).
- **Declination angle (D):** the angle between the headings of magnetic north and geodetic north, in degrees. Declination angle is positive if magnetic north is east of geodetic north.
- **Inclination angle (I):** the angle of the magnetic field above or below the local horizontal plane, in degrees. Inclination angle is positive below the horizontal plane.

2.4.1.2 Geomagnetic Models

There are several geomagnetic field models available today to describe the local/global behavior of the Earth's main magnetic field. To name a few

- Crustal Geomagnetic Field Model, provided by National Geophysical Data Center (NGDC),
- POtsdam Magnetic Model of the Earth (POMME), provided by Deutsches GeoForschungsZentrum (GFZ), a German research center for geosciences, and
- International Geomagnetic Reference Field (IGRF).

Among these models, the International Geomagnetic Reference Field (IGRF) model is employed in this work. The IGRF is a global model that numerically determines the Earth's magnetic field vector at times between 1900.0 A.D. and present; the vector is defined anywhere, from the Earth's core out into space [Finlay et al., 2010].

Based on the IGRF model, the main geomagnetic field $B(r,\phi,\theta,t)$ is considered as the negative gradient of a scalar magnetic potential $V(r,\phi,\theta,t)$ at the Earth's surface and above. The magnetic potential $V(r,\phi,\theta,t)$ is generally represented by a series of spherical harmonics which can be calculated at any given location to determine the magnetic field vector and its direction. This is mathematically shown as [Finlay et al., 2010]

$$\begin{cases} B(r,\phi,\theta,t) = -\nabla V(r,\phi,\theta,t), \\ V(r,\phi,\theta,t) = R_e \sum_{n=1}^{N} \sum_{m=0}^{n} \left(\frac{R_e}{r}\right)^{n+1} (g_n^m(t)\cos m\phi + h_n^m(t)\sin m\phi) P_n^m(\cos\theta) \end{cases} \tag{2.40}$$

where r denotes the radial distance from the Earth's center in units of km, N is the maximum spherical harmonic degree of the expansion (e.g. $N=10$), ϕ and θ denote east longitude and colatitude (i.e. 90° - latitude) of the point where the magnetic field is of

interest, R_e is the Earth's radius, t is the time of interest in units of years, h_n^m and g_n^m are Gauss coefficients, and $P_n^m(\cos\theta)$ is the Schmidt normalized associated Legendre function of degree n and order m.

The magnetic potential $V(r,\phi,\theta,t)$ can be described by specifying the Gauss coefficients h_n^m and g_n^m. For the latest version of the IGRF model, the Gauss coefficients are available for each reference year (in 5-year increments) from 1900 to 2010, along with the predicted coefficients for 2010-2015 [e.g. Finlay et al., 2010]. Using Equation (2.40), the geomagnetic components of the magnetic field in the north, east and radially inwards directions (X',Y',Z') can be obtained from [Finlay et al., 2010]

$$X' = \frac{1}{r}\frac{\partial V}{\partial \theta}, \qquad Y' = -\frac{1}{r\sin\theta}\frac{\partial V}{\partial \phi}, \qquad Z' = \frac{\partial V}{\partial r} \tag{2.41}$$

Since geomagnetic parameters are usually defined in a local topocentric (geodetic) coordinate system, transformation from geocentric coordinate (X',Y',Z') to geodetic coordinate (X,Y,Z) is required [e.g. Olsen et al., 2007]. As shown in Figure 2.3, in the resulting geodetic coordinate system, the X and Y axes point toward geographic north and east, respectively, and the Z-axis points vertically down. Based on this arrangement, the geomagnetic field intensity and direction can be derived as [Finlay et al., 2010]

$$\begin{aligned} H &= \sqrt{X^2+Y^2}, && (nT)\\ F &= \sqrt{X^2+Y^2+Z^2}, && (nT)\\ D &= \arctan(Y/X), && (\text{deg})\\ I &= \arctan(Z/H). && (\text{deg}) \end{aligned} \tag{2.42}$$

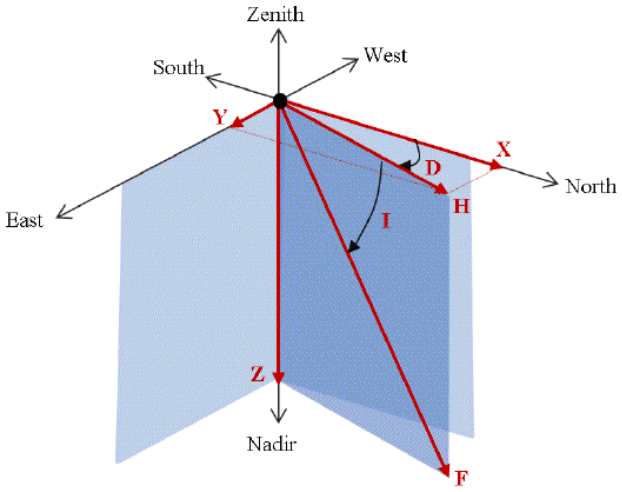

Figure 2.3: Geomagnetic elements in local topocentric system [modified after Olsen et al., 2007].

2.4.2 Oblique Propagation

The scintillation theory introduced in Section 2.2 is based on the assumption that the wave propagation direction is normal to the phase screen. In other words, only transmissions from high elevation sources were considered. In reality, however, most receivers - including GPS receivers - collect signals from different directions; sometimes at very low elevation angles. Thus, oblique propagation should be considered in the theory of scintillation if one decides to bring the results closer to reality. To this aim, a coordinate system with a continuously displaced measurement plane centered on the main propagation direction is used [Rino, 2011]. The continuously displaced coordinate system geometry is shown in Figure 2.4.

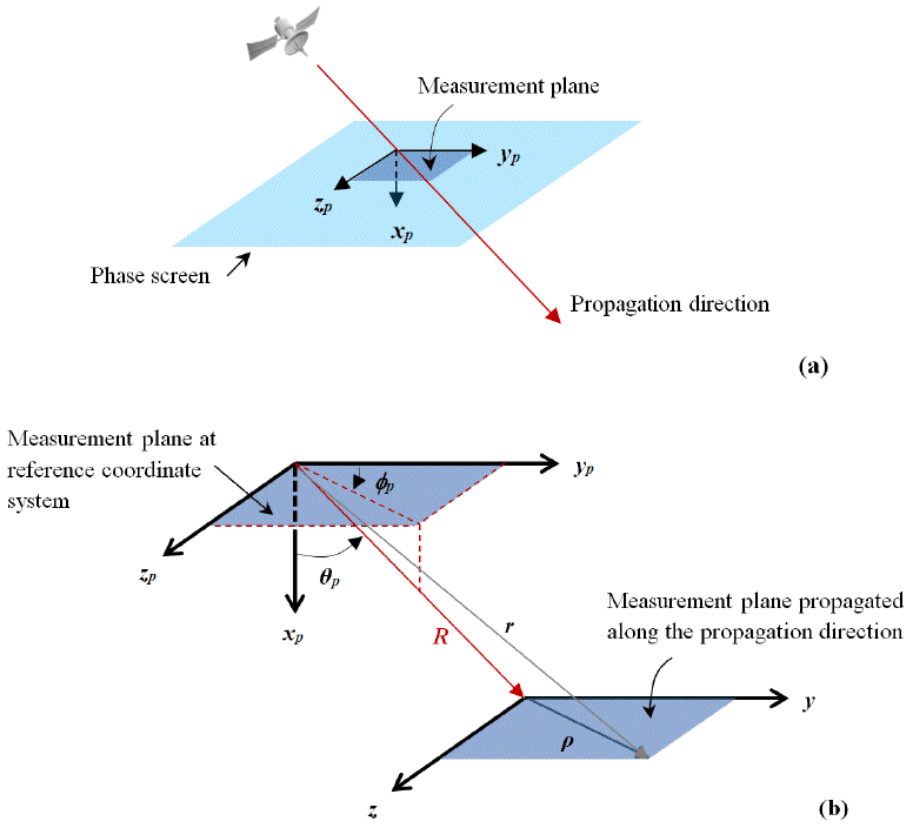

Figure 2.4: Oblique propagation reference coordinate system: (a) initial measurement plane, and (b) measurement plane along the propagation direction [modified after Rino, 2011].

In this figure, the propagation reference coordinate system is given by (x_p, y_p, z_p) with x_p downward, y_p eastward, and z_p southward. The origin of the coordinate system is chosen to be the point where the propagating wave intersects the phase screen. Propagation angle from x_p axis is denoted by θ_p, propagation azimuth angle from y_p axis is denoted by ϕ_p, and propagation distance along the principal propagation direction is given by *R*.

In order to solve the forward propagation equation in the continuously displaced coordinate system, the split-step solution (introduced in Section 2.2) needs to be adjusted to accommodate the oblique propagation. This starts by introducing the forward propagation equation [**after modification from** Rino, 2011]:

$$\frac{\partial \psi_{\bar{K}}(x,\bar{\rho})}{\partial x} = ik\,\Theta_{\bar{K}}\,\psi_{\bar{K}}(x,\bar{\rho}) + ik\,\delta n_{\bar{K}}(x,\bar{\rho})\psi_{\bar{K}}(x,\bar{\rho}) \tag{2.43}$$

where

$$\psi_{\bar{K}}(x;\bar{\rho}) = \iint \hat{\psi}_{\bar{K}}(x_0;\bar{\kappa})\exp\{i(kg(\bar{\kappa}+\bar{\mathrm{k}}_{\mathrm{T}}) - \tan\theta_p\,\hat{a}_{kT}\cdot\bar{\kappa})(x-x_0)\} \times\exp\{i\bar{\kappa}\cdot\bar{\rho}\}\frac{d\bar{\kappa}}{(2\pi)^2}, \tag{2.44}$$

and

$$\psi_{\bar{K}}(x,\bar{\varsigma}) = \psi_{\bar{K}}(x,\bar{\rho})\exp\{i\bar{\mathrm{k}}\cdot(x,\bar{\varsigma})\} \tag{2.45}$$

In Equations (2.43) to (2.45), $\bar{\rho}$ is the transverse coordinate in the displaced system, defined as [Rino, 2011]

$$\bar{\rho} = \bar{\varsigma} - \tan\theta_p\,\hat{a}_{kT}(x-x_0), \tag{2.46}$$

and $\bar{\mathrm{k}}$ is the constant wavenumber vector, where [**after modification from** Rino, 2011]

$$\bar{\mathrm{k}} = k\,[\cos\theta_p,\ \sin\theta_p\cos\phi_p,\ \ \sin\theta_p\sin\phi_p\,] = [k\ g(\bar{\mathrm{k}}),\ \bar{\mathrm{k}}_{\mathrm{T}}\,] \tag{2.47}$$

and $\hat{a}_{kT}$ is the unit vector along the transverse component, where [**after modification from** Rino, 2011]

$$\hat{a}_{kT} = \frac{\bar{\mathrm{k}}_{\mathrm{T}}}{k_T} = \frac{k[\sin\theta_p \cos\phi_p,\ \sin\theta_p \sin\phi_p]}{|\bar{\mathrm{k}}_{\mathrm{T}}|} = [\cos\phi_p, \sin\phi_p] \tag{2.48}$$

In this new system, phase fluctuation (the integral term in Equation (2.18)) is defined according to [Rino, 2011]

$$\delta\phi_{\bar{K}}(l_p, \bar{\rho}) = k \sec\theta_p \int_0^{l_p} \delta n(x, \bar{\rho} + \tan\theta_p\ \hat{a}_{kT}\ x)\, dx \tag{2.49}$$

The split-step solution to Equation (2.43) can be obtained by repeating continuously the propagation and the media-interaction calculations given in Equations (2.44) and (2.49).

2.4.3 Wave Field Spectral Density

Section 2.3.1 describes the SDF of the phase scintillation when the wave field propagates normal to the phase screen in an isotropic medium. This function needs to be rotated and scaled - via employing a series of rotating and scaling matrices - to accommodate oblique propagation in an anisotropic medium. Considering a and b as the principal and secondary anisotropy elongation factors, γ_B as the secondary anisotropy axis (non-zero for $b > 1$), and ϕ_B and θ_B as the magnetic field azimuth and dip angles in (x_p, y_p, z_p) system, the scaling matrix (D_{ab}), and the rotation matrices $(U_{\phi_B}, U_{\theta_B}, U_{\gamma_B})$ are defined as [Rino, 2011]

$$D_{ab} = \begin{bmatrix} 1 & 0 & 0 \\ 0 & a & 0 \\ 0 & 0 & b \end{bmatrix} \tag{2.50}$$

$$U_{\phi_B} = \begin{bmatrix} 1 & 0 & 0 \\ 0 & \cos\phi_B & \sin\phi_B \\ 0 & -\sin\phi_B & \cos\phi_B \end{bmatrix} \tag{2.51}$$

$$U_{\theta_B} = \begin{bmatrix} \cos\theta_B & \sin\theta_B & 0 \\ -\sin\theta_B & \cos\theta_B & 0 \\ 0 & 0 & 1 \end{bmatrix} \tag{2.52}$$

$$U_{\gamma_B} = \begin{bmatrix} \cos\gamma_B & 0 & \sin\gamma_B \\ 0 & 1 & 0 \\ -\sin\gamma_B & 0 & \cos\gamma_B \end{bmatrix} \tag{2.53}$$

The elements of the product matrix

$$D_{ab}^{-1} U_{\gamma_B} U_{\theta_B} U_{\phi_B} = \begin{bmatrix} c_{11} & c_{12} & c_{13} \\ c_{21}/a & c_{22}/a & c_{23}/a \\ c_{31}/b & c_{32}/b & c_{33}/b \end{bmatrix} \tag{2.54}$$

are used to define the anisotropy factors *A*, *B*, and *C*, via [Rino, 2011]

$$\begin{aligned} A &= m_{22} + m_{11}\tan^2\theta_p \cos^2\phi_p + 2m_{12}\tan\theta_p \cos\phi_p \\ B &= 2\,(m_{23} + m_{11}\tan^2\theta_p \sin\phi_p \cos\phi_p + \tan\theta_p\,(m_{12}\sin\phi_p + m_{13}\cos\phi_p)) \\ C &= m_{33} + m_{11}\tan^2\theta_p \sin^2\phi_p + 2m_{13}\tan\theta_p \sin\phi_p \end{aligned} \tag{2.55}$$

where

$$
\begin{aligned}
m_{11} &= {c_{11}}^2 + (c_{21}/a)^2 + (c_{31}/b)^2 \\
m_{22} &= {c_{12}}^2 + (c_{22}/a)^2 + (c_{32}/b)^2 \\
m_{33} &= {c_{13}}^2 + (c_{23}/a)^2 + (c_{33}/b)^2 \\
m_{12} &= m_{21} = c_{11}c_{12} + (c_{21}c_{22}/a^2) + (c_{31}c_{32}/b^2) \\
m_{13} &= m_{31} = c_{11}c_{13} + (c_{21}c_{23}/a^2) + (c_{31}c_{33}/b^2) \\
m_{23} &= m_{32} = c_{12}c_{13} + (c_{22}c_{23}/a^2) + (c_{32}c_{33}/b^2)
\end{aligned}
\tag{2.56}
$$

Using Equation (2.55), in an anisotropic continuously displaced coordinate system, the integrated phase SDF takes the form [**after modification from** Rino, 2011]

$$
\Phi_{\delta\phi}(\bar{\kappa}) = \frac{k^2 l_p abC_s \sec^2\theta_p}{(A\kappa_y^2 + B\kappa_y\kappa_z + C\kappa_z^2)^{(\nu+0.5)}}. \tag{2.57}
$$

In such system, the one-dimensional representation of the integrated phase scintillation SDF follows [Rino, 2011]

$$
\Phi(f) = \frac{T_{scin}}{(f_o^2 + f^2)^{\nu}} \tag{2.58}
$$

where f denotes the frequency of phase variations in Hz, and f_0 is related to the ionospheric outer scale q_0 via [Rino, 2011]

$$
f_0 = \frac{v_{eff}\, q_0}{2\pi}. \tag{2.59}
$$

In Equation (2.58), the power spectral strength (T_{scin}) is defined by [**after modification from** Rino, 2011]

$$T_{scin} = v_{eff}^{2\nu-1}\, ab\; C_p \sec^2\theta_p \; \frac{\sqrt{\pi}\;\Gamma(\nu)}{(2\pi)^{2\nu+1}\sqrt{(AC-B^2/4)}\;\;\Gamma(\nu+0.5)} \tag{2.60}$$

where $C_p = (2\pi/k)^2 r_e^2 l_p C_s$, and v_{eff} represents the effective velocity of the signal propagation path through the ionospheric irregularity layer, and is given by [Rino, 2011]

$$v_{eff} = f(v_k) = \sqrt{\frac{Cv_{ky}^2 - Bv_{ky}v_{kz} + Av_{kz}^2}{(AC-B^2/4)}}. \tag{2.61}$$

In the above equation, $v_k = v_d - v_I - \tan\theta_p\, \hat{a}_{kT} v_x$, where v_d denotes the irregularity drift velocity, v_I denotes the GPS signal penetration point velocity, and (*A*, *B*, *C*) are the anisotropy factors given in Equation (2.55).

The SDF of intensity scintillations has a similar power-law form to that of Equation (2.58), but it is significantly attenuated below a certain frequency (f_{cutoff}) determined by [Knight and Finn, 1998; Rino 2011]

$$f_{cutoff} = \frac{v_{eff}}{\sqrt{2}\,\rho_F} = \frac{v_{eff}}{\sqrt{2x\sec\theta_p/k}}. \tag{2.62}$$

2.5 Scintillation Simulator

In order to model the impact of equatorial scintillation on the performance of a GPS receiver carrier tracking loop, different records of phase and amplitude scintillations corresponding to weak, moderate, and severe ionospheric conditions are required. To accomplish this, following the theory of scintillation described above, a physics-based simulation of equatorial ionospheric scintillations has been developed as a means of providing a full variety of test cases for a simulated carrier tracking loop.

One major advantage of employing simulation over real data in this respect is that with real data, one never perfectly recognizes the real-world processes that result in a particular measured parameter value. With simulation, however, one can control the features defining the data and manipulate them methodically to observe directly how a certain change or assumption impacts the analysis [Trochim and Davis, 1996]. Simulation, on the other hand, does have its drawbacks. The most important one is simulation errors. This is due to the fact that the theories, based on which simulations are implemented, are never 100 percent correct, thus, simplifying assumptions - at different stages throughout the simulation algorithm - are usually applied. As a result, any incorrect implementation factor or inappropriate assumption has the potential to change the simulation results. In order for the simulation to be valid, its results should be compared against experimental results. The scintillation simulator introduced here is based on the phase screen formulation of Rino [1979, 1982, and 2011] – a model which is believed to have a reasonable level of validity for equatorial scintillations, as it has been adopted in the WBMOD model. The statistical characteristics of the intensity and phase scintillation time histories obtained from this model are evaluated through comparison with real scintillation data in Chapter four.

In general, when an electromagnetic wave field propagates in a structured medium, interference across the signal wavefront - which can occur at different points along the propagation path - produces complex diffraction patterns. In Rino's phase screen model (PSM), it is assumed that the entire ionospheric plasma density irregularities - which act

as wave field scatterers - are concentrated within a relatively thin diffracting screen at the F_2-layer peak height (e.g. 350 km). After passing through the screen, as the wave field propagates, the induced phase perturbations evolve and produce phase and intensity scintillations.

2.5.1 Propagation Coordinate System

The first step in implementing the PSM model is to define the wave field propagation coordinate system. Following the oblique propagation theory given in Section 2.4.2, a coordinate system with a continuously displaced measurement plane centered on the main propagation direction is used. The propagation reference coordinate system is shown as (x_p, y_p, z_p) with x_p downward, y_p eastward, and z_p southward in Figure 2.4 and Figure 2.5. The origin of the coordinate system is chosen to be the point where the propagating wave intersects the phase screen. This point is referred to as the *ionospheric pierce point* (IPP) or the *signal penetration point*. Propagation angle from x_p axis is denoted by θ_p, propagation azimuth angle from y_p axis is denoted by ϕ_p, and propagation distance along the principal propagation direction is given by *R*.

As the satellite moves in the sky, not only its position and velocity vectors, but all other propagation parameters, including the origin of the coordinate system (i.e. the IPP position), the propagation angles, the propagation distance, and the orientation of geomagnetic field lines with respect to the coordinate system axes, change as well.

Simulating phase and intensity scintillation data therefore requires a proper realization of the structured medium and satellite geometry with respect to the receiver and the irregular regions.

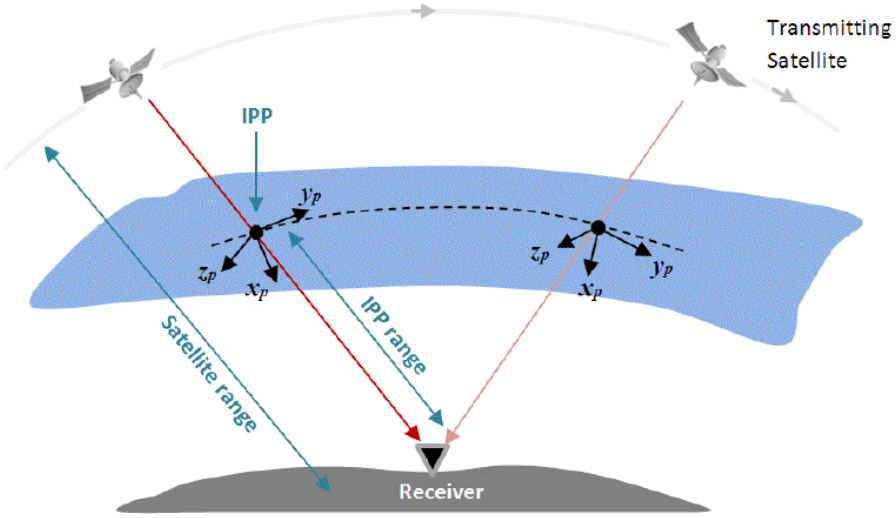

Figure 2.5: Reference coordinate system in scintillation simulator.

2.5.2 Satellite Propagation Geometry

The block diagram of the scintillation simulator employed in this thesis is illustrated in Figure 2.6. As shown in the diagram, the simulator uses the Simplified General Perturbation (SGP4) model to calculate the orbital state vectors of the GPS satellites [Vallado et al., 2006]. The SGP4 model consists of a set of modified Keplerian equations whose solution can be obtained by pseudo-orbital parameters achieved from high-precision orbital measurements[6] [Rino, 2011].

---

[6] *The original codes for the SGP4 model (in C++) are developed by David Vallado, and described in Vallado et al., [2006]. The modified version of the SGP4 model for MatLab is developed by Charles Rino, and is publically available at http://www.mathworks.com/matlabcentral/fileexchange/authors/80973.*

The standardized sets of two-line elements (TLE), specified by North American Aerospace Defense Command (NORAD), are required to run the SGP4 model[7]. A satellite's TLE is a set of orbital elements that can be used to calculate the state vector of that satellite at a particular epoch time [Kelecy et al., 2007]. The TLE format is described in Appendix I.

For given orbital information, the SGP4 model determines the satellite position $\bar{x}_{sat}(t)$ and velocity $\bar{v}_{sat}(t)$ vectors in the Earth Centered Fixed (ECF) coordinate system. Vector conversion from ECF system to geodetic (latitude, longitude, and height) and the Topocentric Coordinate System (TCS) can be performed through the available coordinate conversion algorithms [e.g. Vermeille, 2002; Misra and Enge, 2006]. Using the satellite position and velocity information, along with the ground station location and the phase screen height, the following propagation parameters can be obtained (details provided in Appendix IV).

- Satellite range, in m, and range rate, in m/s.
- Satellite elevation and azimuth angles, in degrees.
- IPP position and IPP range to the ground station, in m.
- Propagation angles θ_p and ϕ_p, in degrees.
- Signal penetration point velocities v_{px}, v_{py} and v_{pz}, in m/s.
- Apparent velocities in the measurement plane v_{k_east} and v_{k_south}, in m/s.
- Date and time

These propagation parameters are used in the split-step algorithm (details provided in Section 2.2.1) in order to generate two-dimensional complex scintillation realizations.

---

[7] *For each satellite, the TLE file can be obtained from* http://celestrak.com/NORAD/elements .

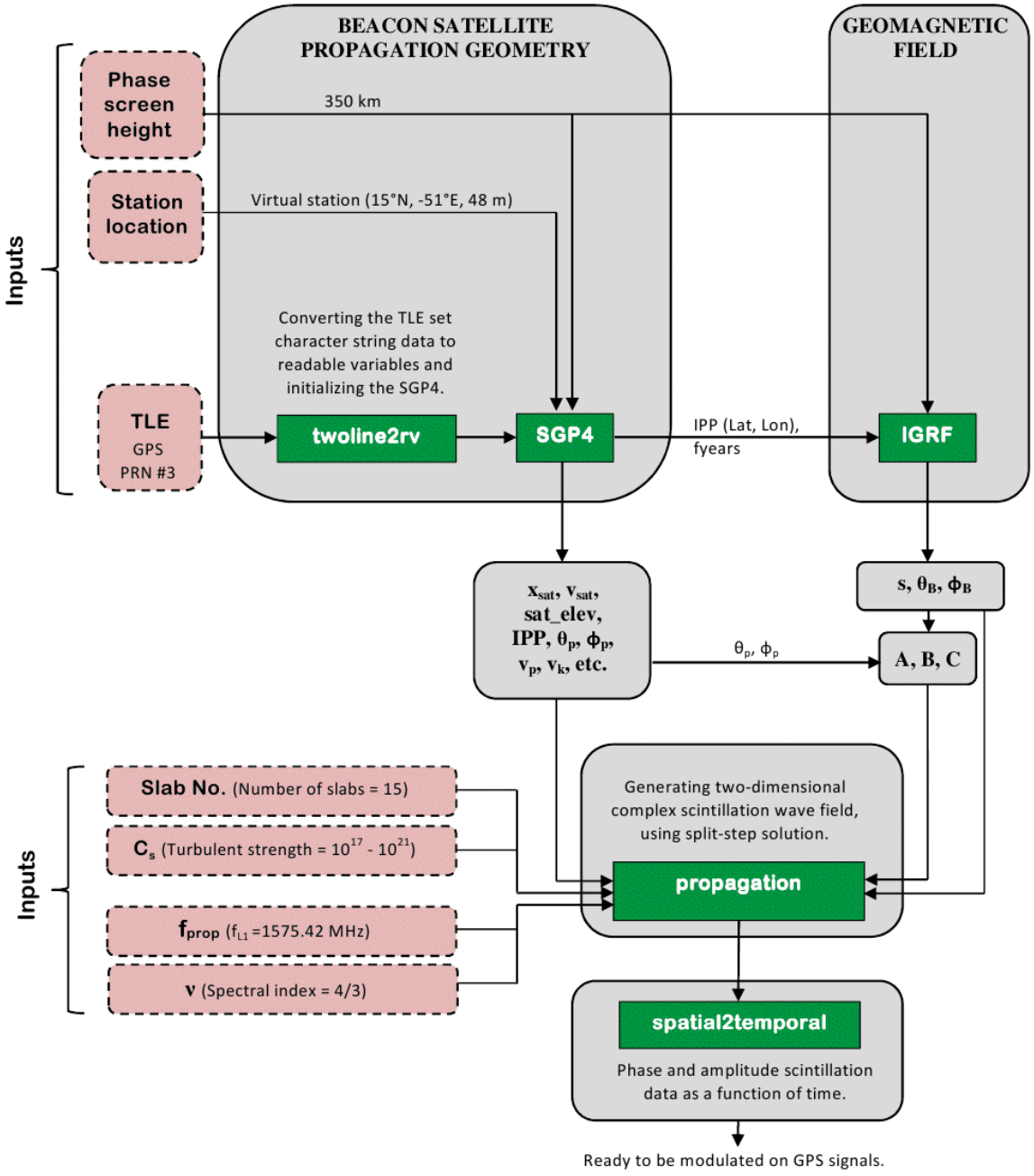

Figure 2.6: Block diagram of equatorial scintillation simulator based on PSM model.

In this thesis, the signal transmitter is considered to be the GPS satellite PRN3 (NORAD ID: 23833). For this satellite, the TLE corresponding to July 28, 2009 is obtained from NORAD website and provided as input to the simulator (the satellite PRN number and the date are selected arbitrarily). The phase screen is assumed at 350 km altitude, and a *virtual* ground station is considered in the equatorial region at 15°N, -51°E, and 48 m (altitude). Based on this information, part of the output from SGP4 model including the satellite trajectory, range to the ground station, rangerate, and elevation and propagation angles are plotted in Figure 2.7 to Figure 2.10, respectively. The GPS satellite PRN3 is visible to the ground station for a bit longer than eight hours. Figure 2.7 shows the satellite and the IPP trajectories.

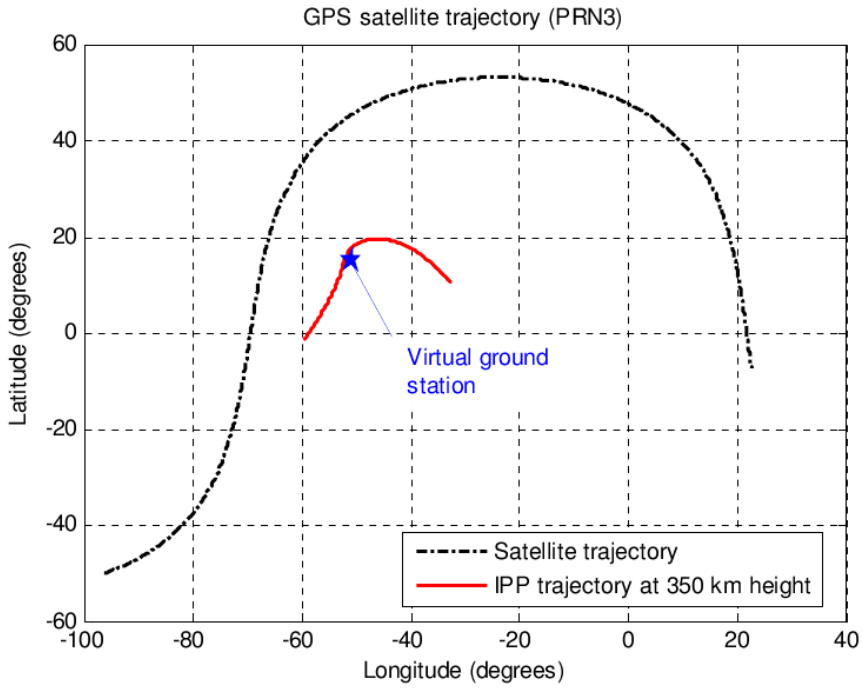

Figure 2.7: GPS satellite and its 350 km intersect point trajectory.

As shown below in Figure 2.8, the satellite distance from the ground station changes between 20,000 and 26,000 km. The largest possible distance is obtained when the satellite is at the horizon, corresponding to zero degrees elevation angle as illustrated in Figure 2.9. The shortest possible distance is obtained when the satellite is at the zenith. This is equivalent to 90 degrees elevation angle. For the example shown here, the satellite does not pass exactly above the station, and the maximum elevation angle obtained is about 70 degrees. The satellite rangerate is given, in km/s, in the lower panel of Figure 2.8. This is caused by the relative motion between the satellite and the ground station.

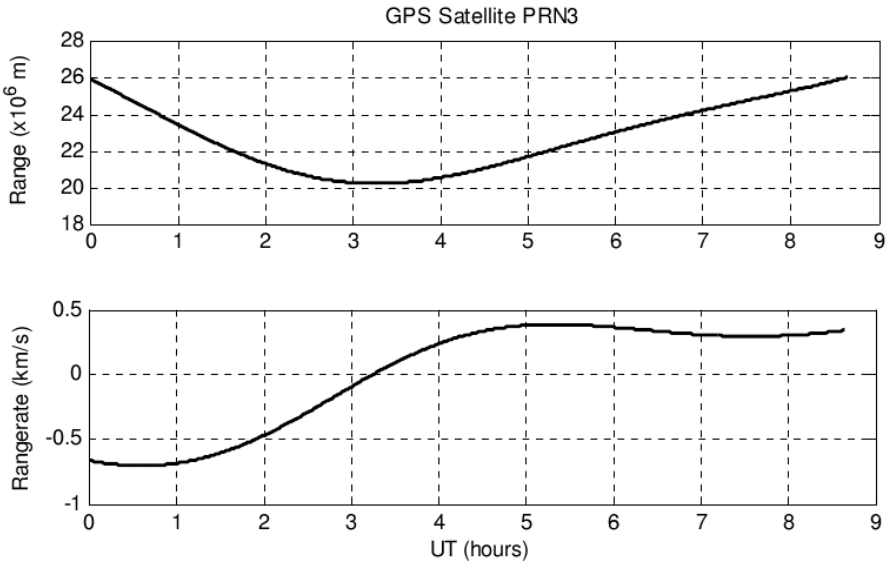

Figure 2.8: GPS satellite range to the ground station and rangerate.

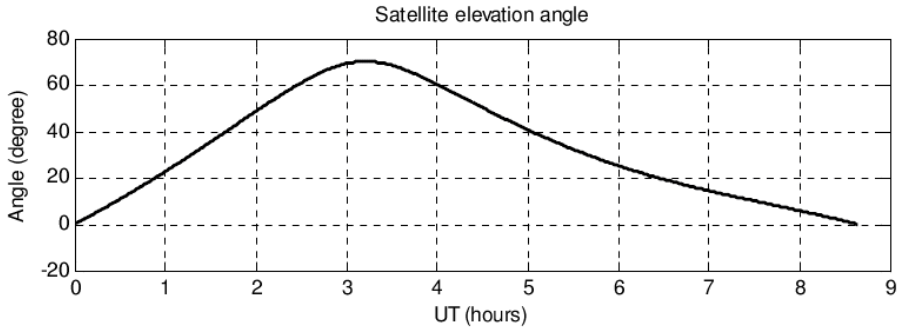

Figure 2.9: GPS satellite elevation angle.

The propagation angles θ_p and ϕ_p are defined in the (x_p, y_p, z_p) reference coordinate system. θ_p is measured with respect to x_p axis, and ϕ_p is measured with respect to y_p axis. For the satellite pass shown in Figure 2.7, the propagation angles, in degrees, are plotted in Figure 2.10.

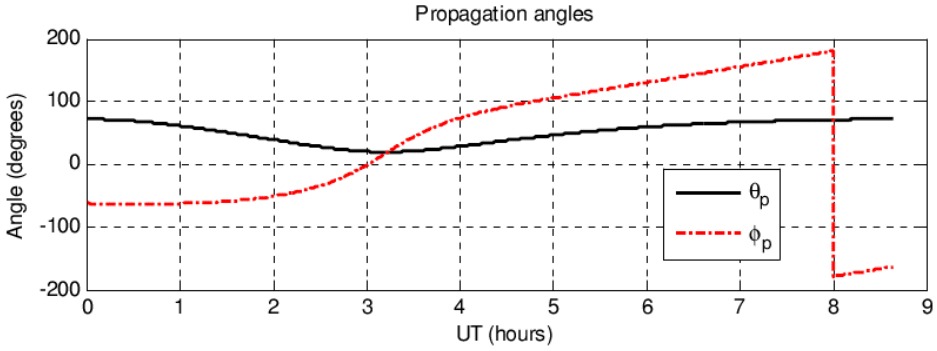

Figure 2.10: GPS signal propagation angles.

2.5.3 Geomagnetic Field Line Orientation

The IGRF model is used in this thesis to determine the orientation of the Earth's magnetic field lines in the propagation coordinate system[8] (details provided in Section 2.4.1). To run the model, the IGRF algorithm requires date, in decimal years, the latitude (positive North) and longitude (positive East), in degrees, of the position where geomagnetic field values are required, and the height, in km, above the WGS84 spheroid. The program then calculates the following geomagnetic field elements in nT:

- The north component of the field (B_{north}),
- The east component of the field (B_{east}),
- The vertical component of the field (B_{up}).

To calculate the field line orientation in the propagation coordinate system the following conversions are applied (see Figure 2.11)

$$B_{mag} = \sqrt{(B_{north})^2 + (B_{east})^2 + (B_{up})^2} \tag{2.63}$$

$$\begin{aligned} s_{px} &= \frac{-B_{up}}{B_{mag}} \\ s_{py} &= \frac{B_{east}}{B_{mag}} \\ s_{pz} &= \frac{-B_{north}}{B_{mag}} \end{aligned} \tag{2.64}$$

---

[8] *The IGRF MatLab codes (developed by Charles Rino) are publically available at* http://www.mathworks.com/matlabcentral/fileexchange/28874-igrf-magnetic-field

where s is the magnetic field unit vector in the propagation coordinate system. The geomagnetic line orientation in the (x_p, y_p, z_p) system can be expressed by

$$\theta_B = \tan^{-1}\left(\frac{s_{px}}{\sqrt{s_{py}^2 + s_{pz}^2}}\right) \tag{2.65}$$

$$\phi_B = \tan^{-1}\left(\frac{s_{pz}}{s_{py}}\right) \tag{2.66}$$

with θ_B and ϕ_B being the magnetic azimuth and dip angles, respectively.

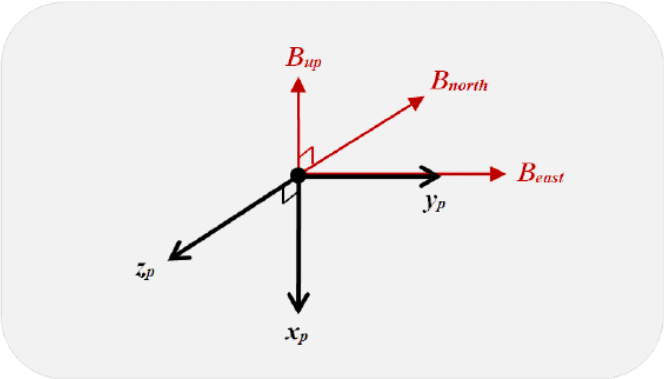

Figure 2.11: Geomagnetic field directions in geodetic versus propagation coordinate system.

To generate output from the IGRF model, the IPP locations corresponding to the phase screen height of 350 km are considered as the locations where geomagnetic field values are required, and the date, in fractional years, is provided via the SGP4 model. For these settings, the geomagnetic orientations (θ_B, ϕ_B) are calculated and plotted in Figure 2.12 for the satellite pass shown in Figure 2.7.

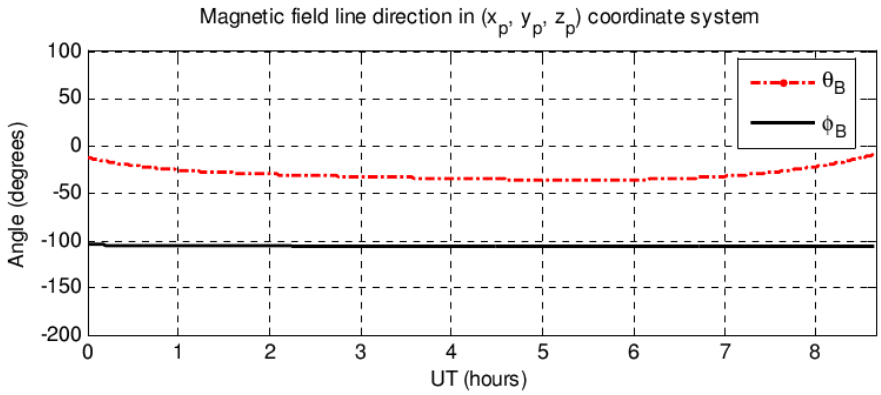

Figure 2.12: Geomagnetic orientation in the propagation coordinate system.

2.5.4 Generating Anisotropic Factors

Following the procedure described in Section 2.4.3, in order to accommodate oblique propagation in an anisotropic medium, the rotating and scaling matrices D_{ab}, U_{ϕ_B}, U_{θ_B} and U_{γ_B} are generated, using geomagnetic field angles (θ_B, ϕ_B) from IGRF model and propagation angles (θ_p, ϕ_p) from SGP4 model. In the simulation, the principal and secondary anisotropy elongation factors (a,b) are set to (10, 1), and the secondary anisotropy axis orientation angle (γ_B) is set to zero[9]. Based on these assumptions, for the satellite pass shown in Figure 2.7, the propagation medium anisotropy factors (*A*, *B*, *C*) are calculated and plotted in Figure 2.13.

---

[9] *According to the Singleton model described in Rino [2011], the secondary anisotropy axis orientation angle (γ_B) is non-zero only when b > 1, otherwise, it is set to zero.*

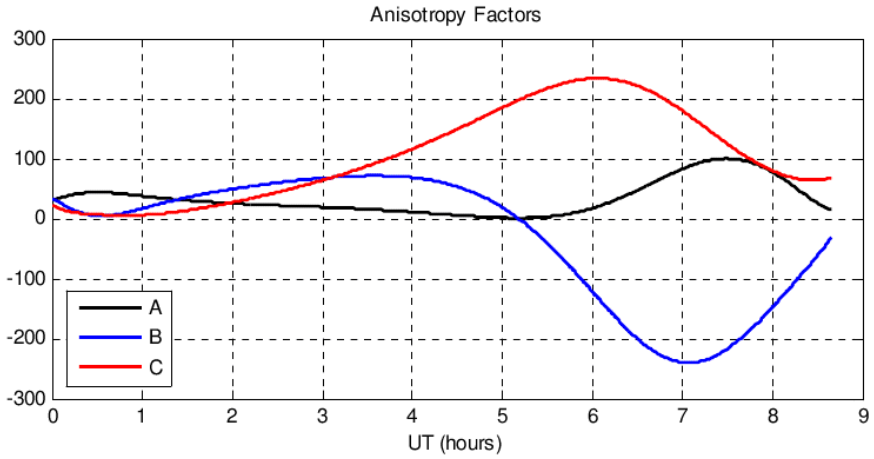

Figure 2.13: Propagation medium anisotropy factors.

The propagation medium anisotropy factors, along with the geomagnetic angles, and the satellite geometry parameters are used in the following sections to generate complex scintillation realizations.

2.5.5 Spatial Frequency Definition

To generate different phase and intensity scintillation realizations, the direct and inverse Fast Fourier Transform (FFT) algorithms are used at several points during the simulation process. In order to eliminate erroneous results that may arise due to the effect of frequency aliasing, a proper definition of spatial frequencies is essential. To accomplish this, as shown in Equation (2.26), the N signal samples are defined at the N equally spaced grid points

$$g_l = (-N/2 + l)\,\Delta\kappa; \qquad l = 0, 1, ..., N-1 \tag{2.67}$$

where $\Delta\kappa$ is the grid spacing in y_p and z_p directions. Since FFT requires an input sequence with a radix-2 length, that is 2^n, with n being a positive integer value, the number of samples N is assumed to be a power of 2. The spatial FFT of the signal profile is then a set of complex-valued numbers at the spatial frequencies [Psiaki et al., 2007]

$$\kappa_l = \begin{cases} \dfrac{2\pi l}{N \cdot \Delta\kappa} & l \le N/2 \\ \dfrac{2\pi (l-N)}{N \cdot \Delta\kappa} & l > N/2 \end{cases} \qquad (rad/m) \qquad (2.68)$$

where $l = 0, 1, ..., N-1$.

Following Equations (2.67) and (2.68), the scintillation simulator uses 1024-by-2048 point single phase perturbation screen realization with $\Delta\kappa = 10\lambda$ (m). The spatial sampling information is summarized in Table 2.1, and the measurement plane is shown in Figure 2.14.

Table 2.1: Measurement plane spatial sampling.

Signal frequency (f_{L1}) and wavelength (λ):	$f_{L1} = 1575.42 \quad [MHz], \quad c = 299{,}792{,}458 \quad [m/s]$ $\lambda = c/f = 0.19 \quad [m]$
Number of grid points:	$N_y = 2^{11} = 2048, \quad N_z = 2^{10} = 1024$
Grid spacing:	$\Delta\kappa_y = \Delta\kappa_z = 10\lambda \quad [m]$
Spatial frequency:	$\kappa_y = \left[\dfrac{-N_y}{2}, \dfrac{-N_y}{2}+1, ..., \dfrac{N_y}{2}-1\right]\dfrac{2\pi}{N_y \Delta\kappa_y}, \quad [rad/m]$ $\kappa_z = \left[\dfrac{-N_z}{2}, \dfrac{-N_z}{2}+1, ..., \dfrac{N_z}{2}-1\right]\dfrac{2\pi}{N_z \Delta\kappa_z}, \quad [rad/m]$

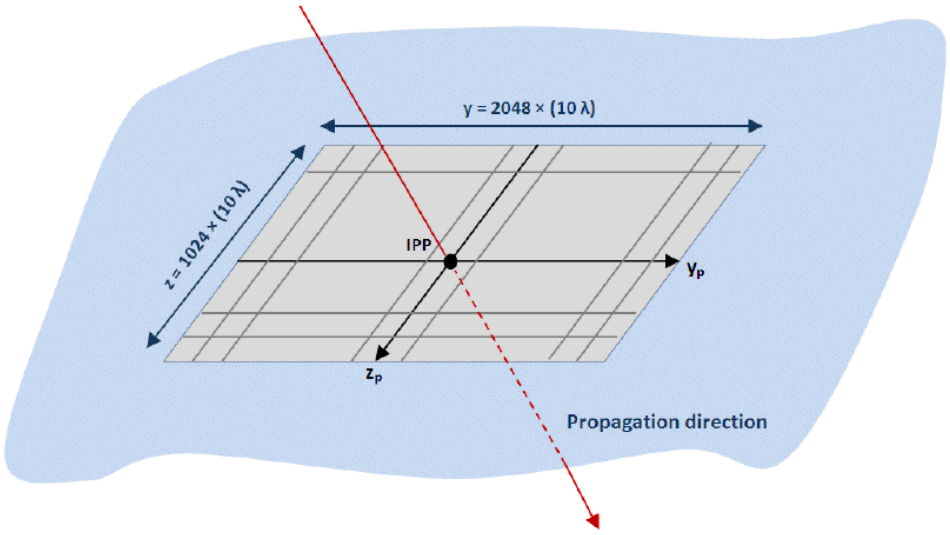

Figure 2.14: Measurement plane at phase screen. A two-dimensional measurement plane is considered at the phase screen height, symmetric about the IPP. The y_p axis is eastward and z_p is southward.

2.5.6 Scintillation Realization

After determining the propagation parameters ($\bar{x}_{sat}$, $\bar{v}_{sat}$, θ_p, ϕ_p, etc.), the geomagnetic field angles within the propagation coordinate system (θ_B, ϕ_B), and the anisotropic elements (A, B, C), the scintillation simulator generates a two-dimensional complex scintillation wave field $\psi_{(N_y \times N_z)}(y,z)$ at the phase screen height, and propagates the field towards the receiver by means of the split-step solution (details provided in Section 2.2.1). This is denoted as "propagation" in the simulator block diagram in Figure 2.6.

In reality, intensity and phase diffraction patterns would result from the effect of several small scale time-varying irregularities along the signal propagation path from the satellite to the receiver. In theory, however, it is assumed that the plasma density irregularities are concentrated within a thin layer or phase screen at 350 km altitude. In this thesis,

following the work of Rino [2011], a *single phase perturbation screen* followed by *several refraction layers* are considered in the simulation of different scintillation realizations. However, it is possible to use more than one phase perturbation layer in the simulation algorithm; for example, at 250 and 350 km altitudes for the case of two phase screens as considered by Humphreys et al. [2009]. Assuming a single phase screen at 350 km altitude, the scintillation simulator *initializes* the two-dimensional wave field $\psi_{(N_y \times N_z)}(x_0, y, z)$ with all-one values just before it passes through the phase screen; that is $\psi_{(N_y \times N_z)}(x_0, y, z) = \overline{1}_{(N_y \times N_z)}$. In the next step, the phase perturbation $\exp\{ik\Delta x_1 \, \delta n(x_1, y, z)\}$ is modulated on the wavefront at the screen height and, finally, the wave is refracted on its way to the receiver using r successive (usually log-spaced) refraction slabs or layers, as shown in Figure 2.15.

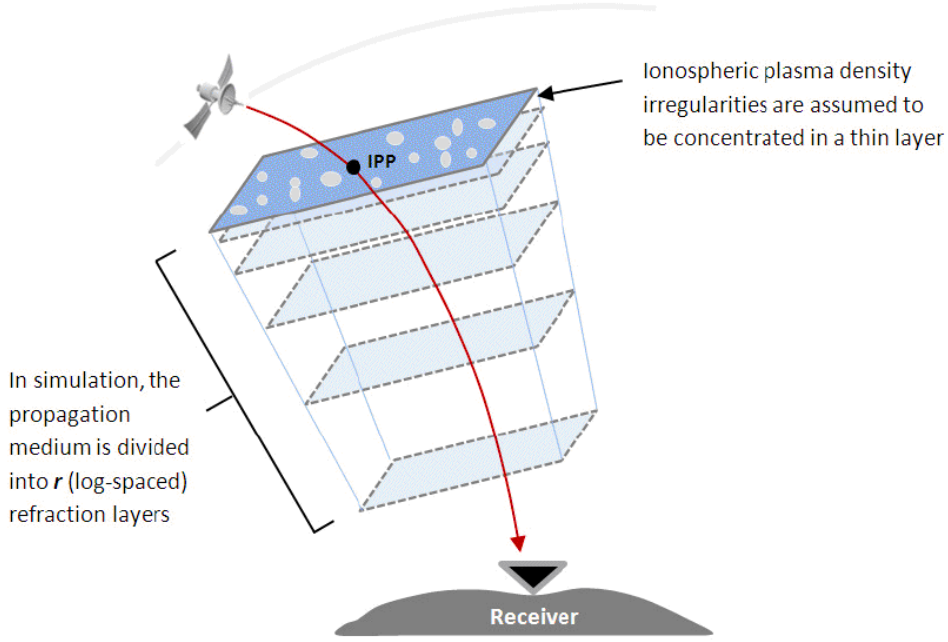

Figure 2.15: The representation of the split-step solution. The propagation medium is divided into a number of refraction layers.

2.5.6.1 Perturbation Simulation at the Phase Screen

In Section 2.1.2, the seeding source of phase perturbation ($\delta\phi$) is introduced as random variation of the local refractive index $n = 1 + \delta n$, where $\delta\phi \propto k\delta n$. For oblique wave propagations in anisotropic media, the power-law SDF of $\delta\phi$ and δn are related through [Rino, 2011]

$$\begin{aligned}\Phi_{\delta\phi}(\bar{\kappa}) &= \left(k^2 l_p ab \sec^2\theta_p\right)\Phi_{\delta n}(q)\\ &\approx \left(k^2 l_p ab \sec^2\theta_p\right)\frac{C_s}{q^{(2\nu+1)}}\\ &= \frac{k^2 l_p ab C_s \sec^2\theta_p}{(A\kappa_y^2 + B\kappa_y\kappa_z + C\kappa_z^2)^{(\nu+0.5)}}\end{aligned} \tag{2.69}$$

which can completely be characterized at each IPP point by the turbulent strength parameter (C_s), the spectral index (ν), and the irregularity spatial wavenumber q, where [Rino, 2011]

$$q^2 = A\kappa_y^2 + B\kappa_y\kappa_z + C\kappa_z^2. \tag{2.70}$$

In Equations (2.69) and (2.70), κ_y and κ_z are the spatial frequencies given in Table 2.1 and the coefficients *A*, *B*, and *C* are the anisotropic factors calculated in Section 2.5.4. Since $\delta\phi$ and δn are related, the perturbation simulation can be applied either through the generation of δn profile at the spatial grid points shown in Figure 2.14, or equivalently through the generation of $\delta\phi$ profile at the same grid points. The second approach is considered here.

Perturbation simulation begins with initializing the two-dimensional refractive index profile with all-one values at the phase screen height; that is $n_{0(N_y\times N_z)}(x_1, y, z) = \overline{1}_{(N_y\times N_z)}$.

Next, a two-dimensional perturbation profile is generated by means of a Gaussian random number generator, in the form of

$$X_{(N_y \times N_z)}(x_1, y, z) = \left[randn\ (N_y \times N_z) + i * randn\ (N_y \times N_z) \right] / \sqrt{2}. \tag{2.71}$$

The output from random number generator is denoted as $X_{(N_y \times N_z)}$ in Figure 2.16. The spatial filtering process takes the Fast Fourier Transform (FFT) of the $X_{(N_y \times N_z)}$ values after being re-scaled by the filter response amplitude corresponding to the phase perturbation SDF in Equation (2.69). The simulator then applies the scaling factor $2r_e / k$ to the resulting phase perturbation $\delta\phi_{(N_y \times N_z)}$ profile to obtain the profile of the refractive index perturbation $\delta n_{(N_y \times N_z)}$. Finally, the two-dimensional profile of the refractive index is calculated using

$$n_{(N_y \times N_z)}(x_1, y, z) = n_{0(N_y \times N_z)}(x_1, y, z) + \frac{2r_e}{k} \delta\phi_{(N_y \times N_z)}(x_1, y, z) \tag{2.72}$$

from which

$$\delta n_{(N_y \times N_z)}(x_1, y, z) \approx \left(n^2{}_{(N_y \times N_z)}(x_1, y, z) - \overline{1} \right) / 2 \tag{2.73}$$

After generating $\delta n_{(N_y \times N_z)}$ for the first layer (i.e. the phase screen), the phase perturbation $\exp\{ik\Delta x_1\, \delta n_{(N_y \times N_z)}(x_1, y, z)\}$ is modulated on the initial wavefront $\psi_{(N_y \times N_z)}(x_0, y, z)$. The resulting wave field would be

$$\psi_{(N_y \times N_z)}(x_1, y, z) = \psi_{(N_y \times N_z)}(x_0, y, z)\ \exp\{ik\Delta x_1\, \delta n_{(N_y \times N_z)}(x_1, y, z)\}. \tag{2.74}$$

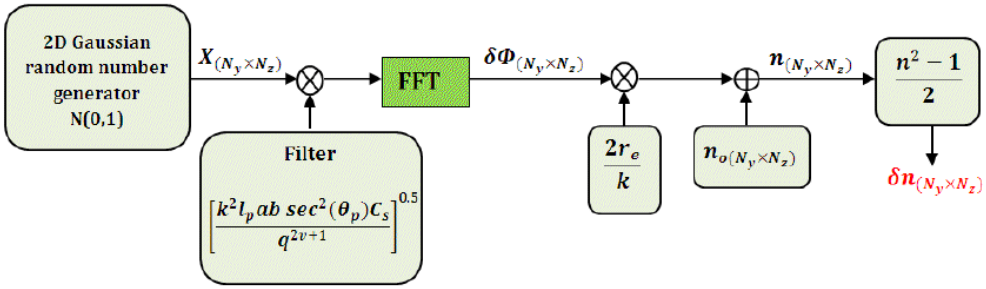

Figure 2.16: Generating the two-dimensional profile of index of refraction perturbation.

Next, according to Equations (2.23) and (2.24), the simulator takes the *spatial* Fourier transform of $\psi_{(N_y \times N_z)}(x_1, y, z)$ to produce $\hat{\psi}_{(N_y \times N_z)}(x_1, \kappa_y, \kappa_z)$, then moves the wave forward to the start of the next layer through multiplication with the propagation factor P_l (also known as spatial transfer function).

For a two-dimensional wave field $\hat{\psi}_{(N_y \times N_z)}(\kappa_y, \kappa_z)$ that propagates along x axis, the propagation factor $P_l = \exp(ik_x)$ is computed using Equation (2.7) in three-dimensional mode [Rino, 2011]:

$$k_x = k\sqrt{\bar{1}_{(N_y \times N_z)} - \left(\frac{\kappa_y + \hat{a}_{ky}}{k}\right)^2 - \left(\frac{\kappa_z + \hat{a}_{kz}}{k}\right)^2 - \kappa_y \hat{a}_{ky} \tan\theta_p - \kappa_z \hat{a}_{kz} \tan\theta_p} \qquad (2.75)$$

where $\bar{1}$ is a two-dimensional matrix with all values equal to one, $k = 2\pi/\lambda$ is the signal wavenumber, and [**after modification from** Rino, 2011]

$$\hat{a}_k = \frac{\bar{k}}{k} = [\cos\theta_p,\ \sin\theta_p \cos\phi_p,\ \sin\theta_p \sin\phi_p\ ]. \qquad (2.76)$$

The simulator takes the spatial Fourier transform of the P_l, and multiplies it by $\hat{\psi}_{(N_y \times N_z)}(x_1, \kappa_y, \kappa_z)$ and finally applies the spatial inverse Fourier transform to produce the wave field realization in the second layer, that is $\psi_{(N_y \times N_z)}(x_2, y, z)$.

Up to this point, the simulator has generated a two-dimensional complex wave field $\psi_{(N_y \times N_z)}(x_2, y, z)$ whose phase perturbation follows the SDF of Equation (2.69). In the case of *single phase screen*, all the ionospheric plasma density irregularities are assumed to be concentrated within the first refraction layer and thus no more turbulence will be added to the wave front in the following layers; instead, the signal is only refracted until it reaches the receiver's antenna on the ground. Accordingly, for the i^{th} layer, where $i = 2,3,...,r$, the refractive index $n_{(N_y \times N_z)}(x_i, y, z)$ in Equation (2.55) is replaced by

$$n_{(N_y \times N_z)}(x_i, y, z) = l_p \cdot \sec\theta_p \cdot n_{0(N_y \times N_z)}(x_1, y, z). \tag{2.77}$$

And the same procedure (Equations (2.72) to (2.76)) is repeated for the second, third, and also for the rest of the refractive layers until the wave field realization at the last layer is generated. In the case of *multiple phase screens*, more than one turbulent layer can be assumed within the propagation medium. In this case, the refractive index of the turbulent layers is determined from Equation (2.55), while for non-turbulent layers (i.e. simple refraction layer), it is determined from Equation (2.77).

To show an example, the geometry of the GPS satellite PRN3, which is visible from the ground station for more than eight hours, is segmented into about 750 paths separated by 40 seconds. The propagation along each path is simulated independently. Figure 2.17 shows the simulated measurement plane intensity in dB for one of these paths. The wave field is generated assuming a single phase screen at 350 km altitude with $\nu = 4/3$ and $C_s = 5\times10^{18}$, followed by 14 non-turbulent refraction layers (thus, $r = 15$).

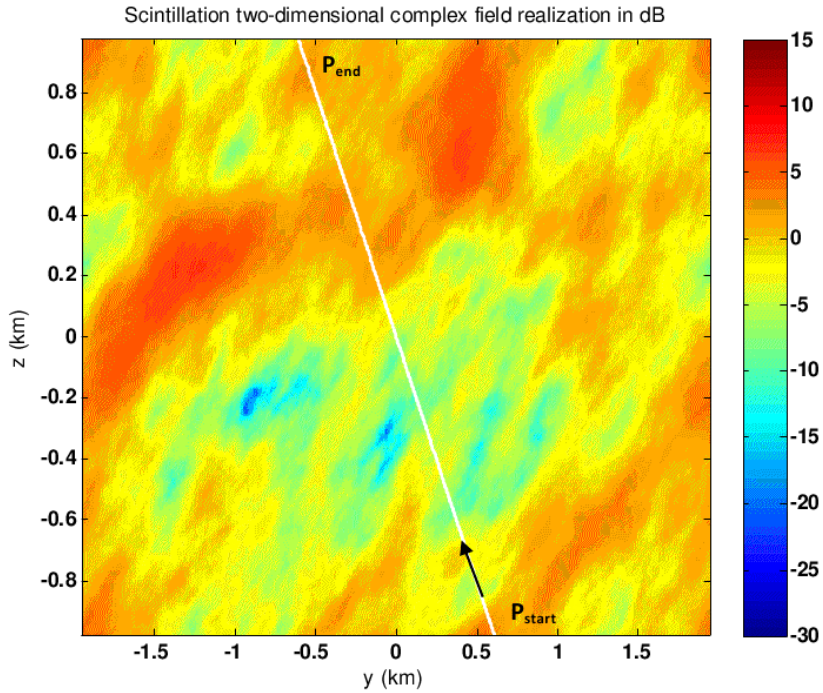

Figure 2.17: Scintillation complex wave field realization at the ground.

2.5.7 Conversion from Spatial to Temporal Variation

Since the software receiver requires phase and amplitude scintillation time histories, under the frozen-field assumption the spatial variation of the two-dimensional complex field $\psi(y,z) = A(y,z)e^{i\phi(y,z)}$ can be translated into a function of time using [Rino, 2011]

$$\begin{aligned} \rho_n &= v_k \cdot (n\Delta t) \\ &= (v_d - v_I - \tan\theta_p \, \hat{a}_{kT} v_x) \cdot (n\Delta t) \end{aligned} \tag{2.78}$$

where v_d is the drift velocity of the irregularities, v_I is the velocity of the ionospheric pierce point through the irregularity layer, ρ is defined in Equation (2.46), and $\hat{a}_{kT}$ is

given in Equation (2.48). The transit is from P_{start} to P_{end} along the highlighted path in Figure 2.17. The recorded phase, in radians, and intensity, in dB, is given in Figure 2.18. The resulting scintillation signal can be represented in the general form of $\sqrt{I_s(t)}\exp\{j\theta_s(t)\}$, with $I_s(t)$ and $\theta_s(t)$ being the intensity and phase scintillation signals, respectively.

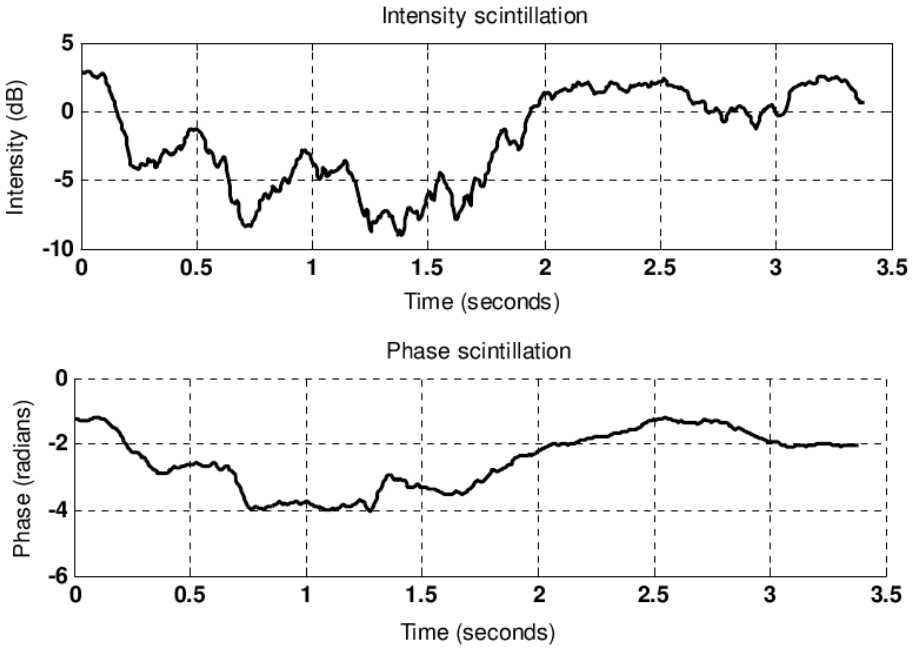

Figure 2.18: Intensity and phase scintillation record.

Referring to the methodology flowchart in Figure 1.7, these simulated phase and intensity scintillation records (and other similar examples) are modulated on the simulated GPS L_1 signal, using complex modulation method in Chapter three. The resulting *scintillated* GPS signal is then processed in the single-frequency software receiver in Chapter four. Outputs from software receiver (referred to as the simulation results) are used in Chapters five and six to evaluate theoretical predictions.

Chapter Three: GPS Signal Structure

In order to study the impact of ionospheric scintillation on GPS receiver carrier tracking loop performance, a software-defined single frequency GPS receiver is implemented in Chapter four of this thesis. Since software receiver design requires an in-depth knowledge of the characteristics of the signals and data transmitted from the GPS satellites, an overview of GPS signals generation structure and relevant properties are presented in this chapter. In addition, the GPS signal simulator, developed by the author, is described in some detail. The signal simulator is used throughout the work to generate two types of signals: (a) unperturbed GPS L_1 signal and, (b) disturbed signal after modulation with intensity and phase scintillation time histories. Both signals are processed in the software receiver to study the carrier tracking loop behavior in the absence/presence of ionospheric scintillations. It is important to note that even though the demonstration of this simulation capability is fairly specific (i.e. processing a scintillated GPS L_1 signal in a single-frequency GPS software receiver), the scintillation simulation procedure described in Chapter two can be applied for all other Global Navigation Satellite System (GNSS) signals, namely the GPS L_2 and L_5, as well as signals from other satellite constellations like the European Galileo and the Russian GLONASS.

3.1 GPS Signals

The GPS satellites transmit navigation information on at least two L-band signals: the L_1 signal centered at 1575.42 MHz, and the L_2 signal centered at 1227.60 MHz. The GPS L_1 signal is modulated by the navigation data message and two spread spectrum codes: the coarse acquisition code (C/A-code), and the precision code (P-code). The L_2 signal is modulated by P-code and the navigation data. Signals transmitted by a GPS satellite can be expressed as [Misra and Enge, 2006]

$$S_{L1}(t) = \sqrt{2P_C}\ X(t)\,D(t)\cos(2\pi f_{L1}t) + \sqrt{2P_{P_{L1}}}\ P(t)\,D(t)\sin(2\pi f_{L1}t) \quad (3.1)$$

$$S_{L2}(t) = \sqrt{2P_{P_{L2}}}\ P(t)\,D(t)\sin(2\pi f_{L2}t) \quad (3.2)$$

where P_C, $P_{P_{L1}}$, and $P_{P_{L2}}$ are the powers of signals with C/A or P-code, X and P are, respectively, the C/A-code and P-code sequences assigned to that specific satellite, and D is the navigation data sequence.

As part of the GPS modernization program, two new civilian signals have been added to the current system with the aim of improving its performance. A primary advantage of having a second civilian signal is the ability to directly determine and eliminate the ionospheric delay, which is a major source of error for non-authorized users [Walter et al., 2008]. The first of the two new civilian signals, known as the L2C, is transmitted on L_2 frequency by all block IIR-M and subsequent satellites [Fontana et al., 2001]. The other signal, set to be transmitted on the L_5 frequency (1176.45 MHz), is currently broadcast by only two of the GPS satellites (block IIF – PRN1 and PRN25).

Each GPS satellite is assigned a distinct spread spectrum code. Since the codes are chosen to have nearly zero cross-correlation values, all satellites transmit signals simultaneously without significant interference with each other. At the receiver, the code division multiple access (CDMA) technique is used to separate and detect each satellite signal. To track a particular satellite in view, a GPS receiver needs to replicate the carrier wave and the spread spectrum code for that specific satellite using code and carrier signal generators. Within the receiver, the incoming signal is *correlated* with the locally generated signal. Zero cross-correlation values remove the unwanted signals and leave the desired one [Ward, 1996].

Because of their noiselike characteristics, the spread spectrum codes are sometimes referred to as pseudorandom noise (PRN) codes. Each PRN code is derived from two

code generators, namely G1/G2 for C/A-code, and X1/X2 for P-code. In order to generate a *unique* PRN code for each GPS satellite, the output of one of the code generators (e.g. G2 and X2) is delayed with respect to the other one (i.e. G1 and X1), by a certain amount which is different for each satellite, before their outputs are added to each other [Ward, 1996]. The block diagram of the PRN code generator used in GPS satellites, and the amount of code delay for each satellite, is given in Appendix II.

3.1.1 Coarse/Acquisition (C/A) Code

The C/A-code is a sequence of 1023 chips which is repeated every 1 ms, giving a chipping rate of 1.023 MHz. The C/A-code is generated by means of tapped linear feedback shift registers (LFSR), where each LFSR generates a maximal-length sequence of $N = 2^n - 1$ elements, with n being the number of shift register stages. The GPS C/A-code is the sum of *two* maximal-length sequences of length $2^{10} - 1 = 1023$ [Borre et al., 2007]. The C/A-code generator containing two shift-registers G1 and G2 is shown in Figure 3.1.

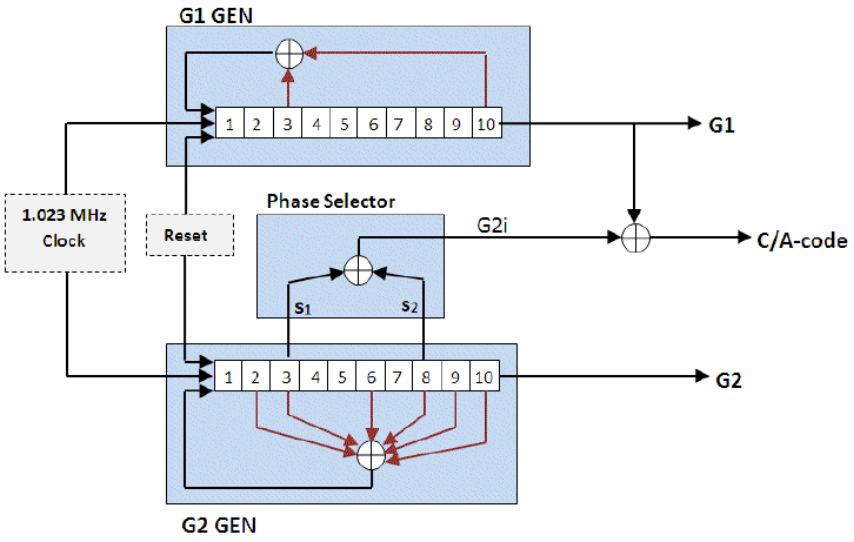

Figure 3.1: GPS C/A-code generator [modified after Borre et al., 2007].

Each unique C/A-code is the result of G1 sequence modulo-2 added to a delayed version of G2. The G2i sequence, in Figure 3.1, represents the delayed version of G2. The amount of delay (shift) is obtained through the exclusive-or of the particular positions of the (s_1, s_2) taps [Ward, 1996]. Each C/A-code PRN number is associated with a unique set of (s_1, s_2). In Figure 3.1, for example, the two taps are selected to be the 3rd and the 8th cell of the G2 shift register which corresponds to PRN31 (details provided in Appendix II).

3.1.2 Precision (P) Code

The GPS P-code is a sequence of approximately 2.35×10^{14} chips, with a chipping rate of 10.23 MHz. The code is derived from two code generators X1 and X2; each consists of two 12-bit shift registers. To generate the P-code, a delayed version of X2 sequence (having 15,345,037 chips) is combined with the X1 sequence (having 15,345,000 chips) via an exclusive-or circuit. The length of the resulting code is slightly longer than 38 weeks. Since the actual length of P-code is one week, the 38-week-long code is divided into 37 different P-codes and each GPS satellite (from total of 32 satellites), uses a different portion of the code [Ward, 1996].

As the P-code is designed primarily for military purposes, it is not directly transmitted by the GPS satellites. Instead, the encrypted P(Y)-code (where $Y = P \oplus W$, with W being an unknown encrypting code), is transmitted to the users. The encrypted P(Y)-code is not available to non-authorized users [Tsui, 2000].

3.1.3 Navigation Data

The navigation data are transmitted by GPS satellites at a rate of 50 bps. Each frame of the message is 1500-bit long containing 5 subframes. Subframes 1, 2 and 3 are repeated in each frame. Subframes 4 and 5, however, have 25 versions, referred to as page 1 to 25 [Borre et al., 2007], as shown in Figure 3.2.

Each subframe begins with the telemetry (TLM) and the handover word (HOW). TLM contains an 8-bit preamble and is used for frame synchronization. HOW contains the time of week and the subframe ID. In addition to the TLM and HOW, the first subframe contains clock information, and health data specifying if the transmitted data are reliable. The second and third subframes contain satellite ephemeris data. The fourth and fifth subframes contain almanac data for all GPS satellites in orbit. Satellite health indicators and ionospheric parameters are also transmitted in the last two subframes [Borre et al., 2007].

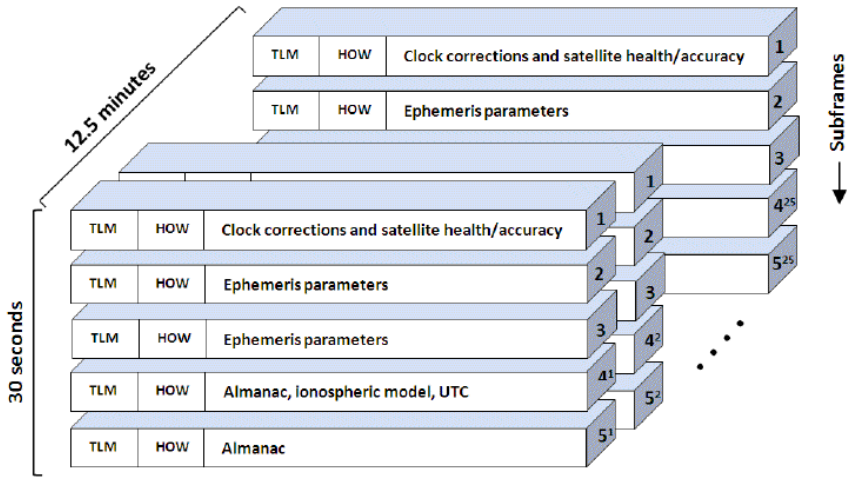

Figure 3.2: GPS navigation data structure [modified after Borre et al., 2007].

3.2 Correlation Properties of Gold Codes

The GPS C/A-, and P-code are chosen from a particular family of codes, known as *Gold codes*, because of their special correlation properties. The Gold codes are *nearly orthogonal* and, therefore, have high auto-correlation value and nearly zero cross-correlation values. This property provides a great advantage in weak signal acquisition

process. For example, to acquire a weak signal in the presence of several strong interferers, it is essential that the auto-correlation peak of the weak signal be higher than the cross-correlation peaks of interferers, otherwise a wrong signal will be picked up [Tsui, 2000].

The normalized cross-correlation level of the Gold codes is given by [Tsui, 2000]:

$$\left\{ -\frac{t(n)}{N},\ -\frac{1}{N},\ \frac{t(n)-2}{N} \right\} \tag{3.3}$$

where n denotes the number of shift register stages, $N = 2^n - 1$ is the code period, and $t(n)$ is expressed by [**after modification from** Tsui, 2000]

$$t(n) = \begin{cases} 2^{(n+1)/2} + 1, & n \ \ is \ \ odd \\ 2^{(n+2)/2} + 1, & n \ \ is \ \ even \end{cases} \tag{3.4}$$

For the GPS C/A-code, with $n = 10$, the normalized auto-correlation value is *1*, while the cross-correlation values are [*-65/1023, -1/1023, 63/1023*].

3.3 GPS Signals Power Level

The minimum received power levels for the two GPS signals are summarized in Table 3.1. The L_1 C/A-code is 3 dB stronger than L_1 P(Y)-code, and 6 dB stronger than L_2 P(Y)-code. This level of minimum power is expected when the satellite is either at the user's zenith, or at 5 degrees elevation angle. As a GPS satellite rises above the horizon, the minimum received power increases, reaches its highest level around 40 degrees elevation angle, and decreases afterwards as shown in Figure 3.3 [Ward, 1996].

Table 3.1: GPS signals minimum received power level [from Ward, 1996]

Parameter	L_1 C/A-Code	L_1 P(Y)-Code	L_2 P(Y)-Code
User minimum received power (dBw)	-160	-163	-166

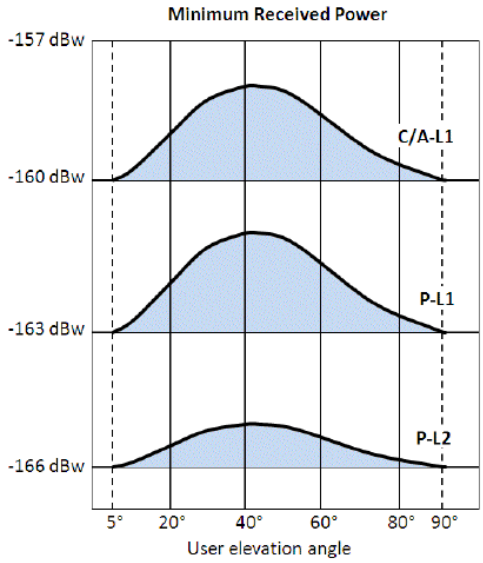

Figure 3.3: GPS user minimum received signal power vs. elevation angle [modified after Ward, 1996].

3.4 GPS Signal Simulator

A GPS signal simulator is implemented in MATLAB by the author following the block diagram shown in Figure 3.4. The simulated signal includes radio frequency carrier wave, C/A-code, P-code, navigation message, thermal noise, the effect of satellite-platform dynamics, and ionospheric scintillation. The actual C/A-code sequences are implemented in the simulator using the C/A-code generator shown in Figure 3.1. Since P-code and the

navigation message are not relevant to the tracking algorithm, they are considered as random sequences of ±1. The GPS signal is *scintillated* via complex modulation algorithm, and is included in the simulation results by adding phase scintillation to the phase of the carrier wave and multiplying the carrier wave amplitude by the square root of intensity scintillation.

As shown in Figure 3.4 (block **I**), a 1.023 MHz square pulse generator is employed in the simulation of the GPS C/A-code. The resulting square pulses are fed into a settable counter (the C/A-code counter) to make it count up at every falling edge of the input pulse until it reaches 1023, corresponding to the 1023 chips in one complete PRN sequence. Following this is a two-dimensional C/A-code look-up table. The first dimension of the table designates the list of current PRN numbers (ranges from 1 to 32) and, for each PRN number, the second dimension determines the corresponding pseudo noise sequence (containing 1023 chips as controlled by the C/A-code counter). The resulting C/A-code is then combined with the navigation message, and modulated onto a cosine carrier wave.

Each navigation data bit is 20 ms long (corresponding to 50 Hz bit rate), and contains 20 copies of the C/A-code PRN sequence. As illustrated in block **II** in Figure 3.4, the output of the C/A-code counter is used to simulate the navigation data sequence. Accordingly, the navigation period counter (the first counter in block **II**) is reset by the C/A-code counter after running through 20 PRN sequence replicas. The next block is the navigation message counter. This counter is reset by the navigation period counter every 30 seconds, corresponding to 1500 navigation bits in one complete navigation frame. The next block is the navigation data look-up table which determines if there should be any bit transition in the navigation data.

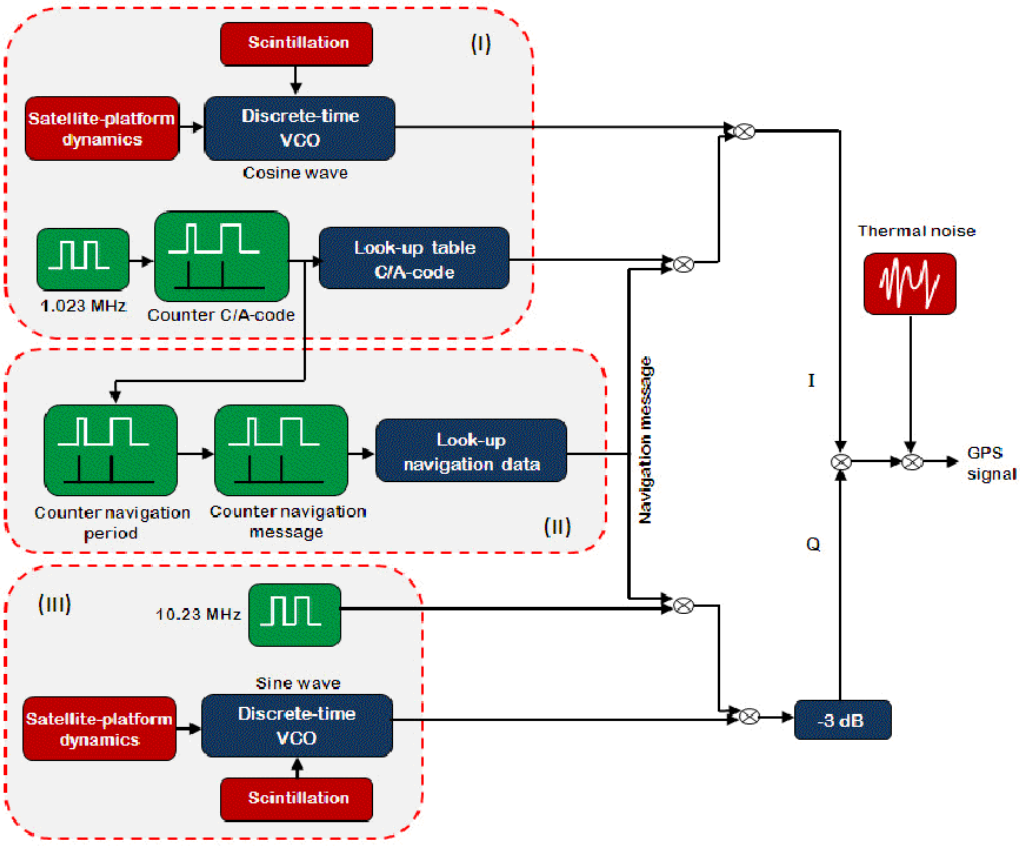

Figure 3.4: GPS signal simulator. Blocks I, II and III simulate the C/A-code, the navigation data message, and the P-code, respectively [modified after Borre et al., 2007].

Shown in block **III** is the generation of the P-code. Since it is not relevant to the tracking algorithm, the P-code is simulated as a random sequence of ±1 using a 10.23 MHz square pulse generator. The resulting code is then combined with the navigation message, generated in block **II**, and modulated onto a sine carrier wave. Following Section 3.3, the L_1 P-code is attenuated by 3 dB relative to L_1 C/A-code before the two components are combined. In the last step of the simulation, the resulting noise from noise generator is added to the GPS signal.

The signal simulator is capable of generating up to 32 (for 32 PRN) signals. The required parameters to run the simulation are summarized in Figure 3.5.

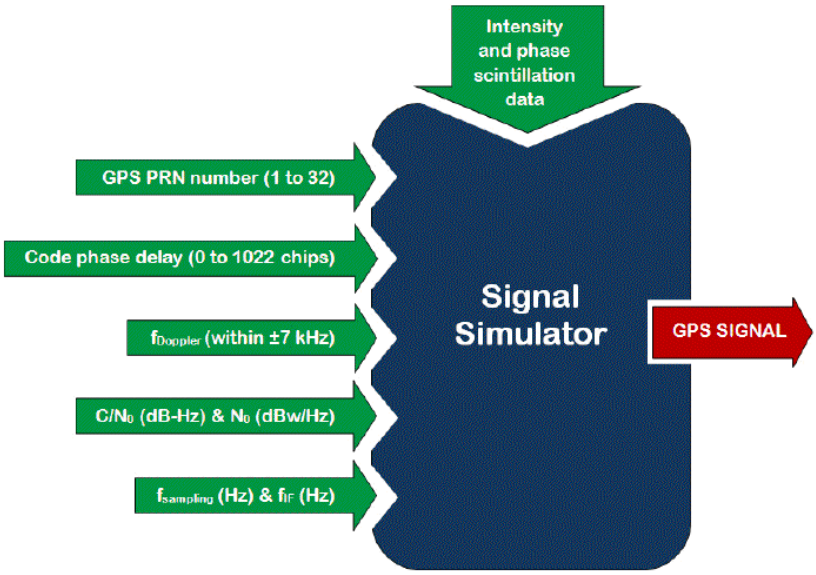

Figure 3.5: GPS signal simulator input parameters.

To show an example, a simulated *unperturbed* GPS signal is illustrated in Figure 3.6. The output is a combination of four signals corresponding to PRN1, PRN3, PRN7 and PRN11. To generate this signal, the following settings are applied:

- PRN number: PRN1, PRN3, PRN7 and PRN11.
- Code phase shift (chips): 200, 60, 312 and 120, respectively, for PRNs 1, 3, 7 and 11.
- Doppler frequency shift (Hz): 900, 550, 720 and 160.
- C/N_0 (dB-Hz): 39, 39, 42 and 46.
- N_0 (dBw/Hz): -201.
- Intermediate and sampling frequencies (Hz): 9.548E+6 and 38.192E+6.

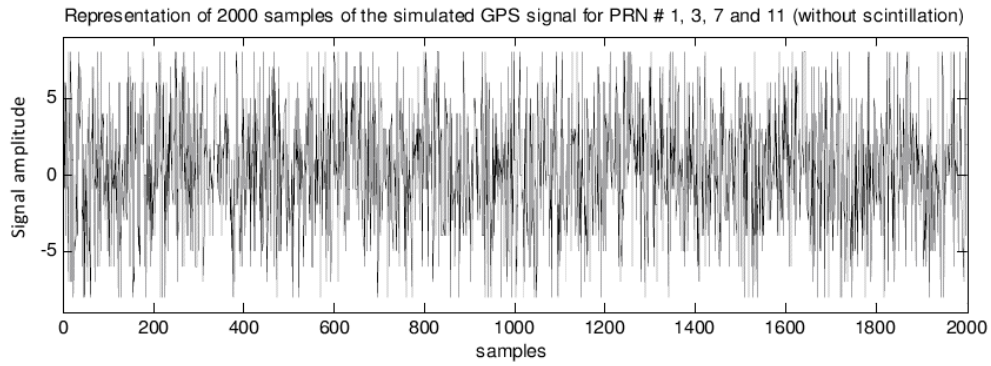

Figure 3.6: Simulated GPS signal in time domain. The sampling interval is equal to $t_s = 1/f_s$ = 2.61E-8 sec. Using a 4-bit quantizer, the signal output is shown within ±8 discrete levels.

In the second example, a *scintillated* GPS signal (here, PRN3) is generated through the complex modulation with the intensity and phase scintillation data, shown below in Figure 3.7. To generate the scintillation data, the scintillation simulator in Chapter two is used assuming $\nu = 1.33$ and $C_s = 5 \times 10^{19}$, which corresponds to a strong scintillation level in the equatorial region. Before modulation, the scintillation data needs to be sampled with the same sampling frequency as the simulated GPS signals. The resulting scintillated signal combined with the other three unperturbed signals (PRN1, PRN7 and PRN11) is given in Figure 3.8.

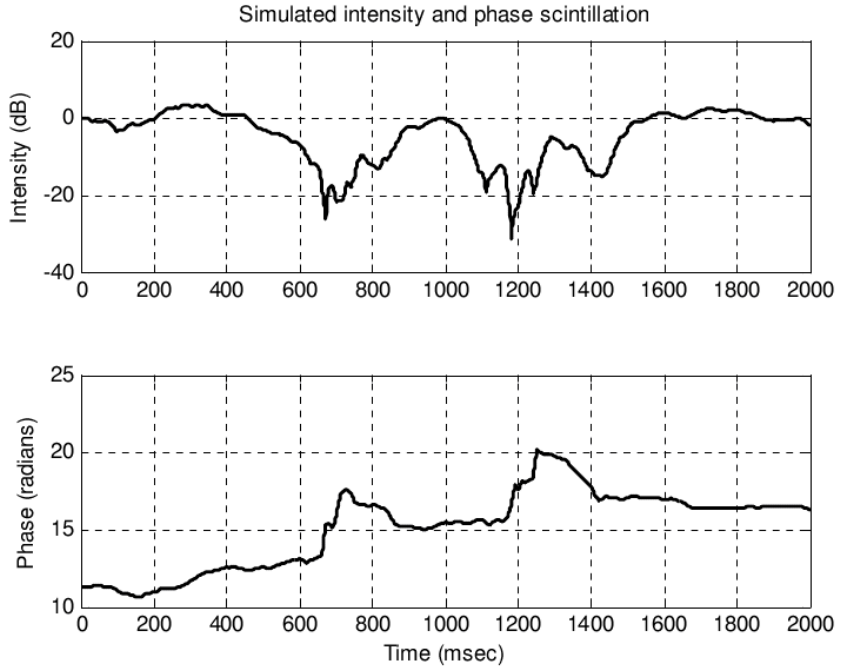

Figure 3.7: Intensity and phase scintillation realization using the scintillation simulator in Chapter two with $C_s = 5\times10^{19}$, $\nu = 1.33$, and the GPS L_1 as the propagating signal.

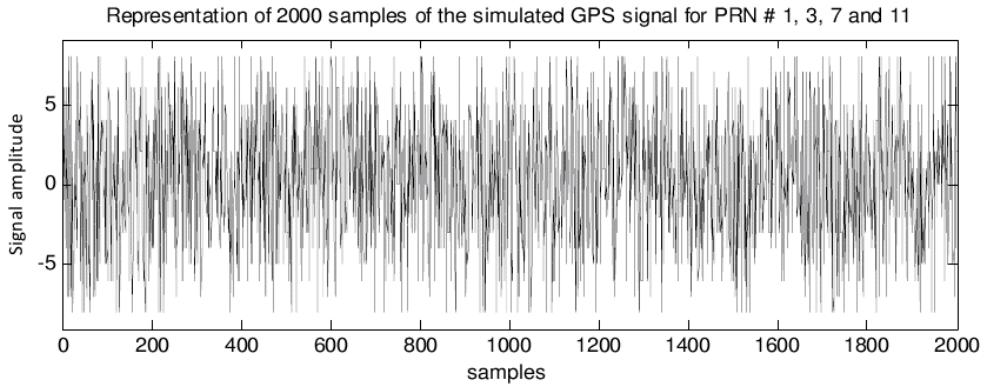

Figure 3.8: Simulated GPS signal in time domain with scintillation being added to PRN3. As in Figure 3.6, the sampling interval is equal to t_s = 2.61E-8 sec.

Using only data samples, such as the ones shown in Figure 3.6 and Figure 3.8, it is not easy to realize the difference between the unperturbed and the scintillated GPS signal. The difference, however, will be clear when processing these signals in the receiver tracking loops. This is the subject of the next chapter.

Chapter Four: GPS Software Receiver Implementation

A GPS receiver, in general, consists of an antenna, a reference oscillator, signal amplifiers, signal processors, and (often) a display screen. In order to determine the user's three-dimensional position, and the time offset in the receiver's internal clock with respect to the satellite clock, a GPS receiver needs to generate observations for at least four GPS satellites simultaneously. GPS receivers typically have around 12 to 24 channels or more. The block diagram of a generic GPS receiver is illustrated in Figure 4.1. The receiver antenna is the first element in the signal path, and is adjusted to the frequencies transmitted by the GPS satellites. Due to the huge path loss, the received signal is extremely weak at the antenna (approximately -160 dBW or 10^{-16} watts) and has been affected by natural noise and electromagnetic interference from external sources. The signal, therefore, is not directly suitable for computer processing, and *signal conditioning* is required [Misra and Enge, 2006].

During conditioning, the receiver front-end amplifies the signal power by roughly ten orders of magnitude (~100 dB). It also removes interfering signals in neighboring frequency bands via filtering the incoming signal. To further ease the signal processing phase, the incoming carrier frequency is reduced by a factor between 100 and 1000. The resulting frequency is referred to as intermediate frequency (IF). After conditioning, the analog signal is converted to a digital form using an analog-to-digital converter (ADC) [Misra and Enge, 2006]. The conditioned signal can be expressed by

$$S(t) = \sqrt{C}\;\; X(t-\tau(t))\, D(t-\tau(t))\cos\left(2\pi(f_{IF}+f_D)t+\theta(t)\right)+n(t) \qquad (4.1)$$

where C is the amplified received power, X and D are the satellite C/A-code and navigation message, respectively, τ is the code delay, f_{IF} is the intermediate frequency corresponding to the L_1 carrier frequency, f_D is the carrier Doppler shift frequency, θ is

the carrier phase perturbation due to accumulated delta range, and n is the stationary zero-mean Gaussian thermal noise with a power spectral density of N_0 W/Hz within the IF band.

Now that the signal is well suited for processing, accurate estimates of code delay (τ), Doppler shift (f_D), and carrier phase (θ) are required to determine user position, velocity and time. The estimation process includes two parts [Misra and Enge, 2006]:

- *Signal acquisition* to determine approximate values of (τ, f_D).
- *Signal tracking* to obtain accurate estimates of (τ, f_D and θ).

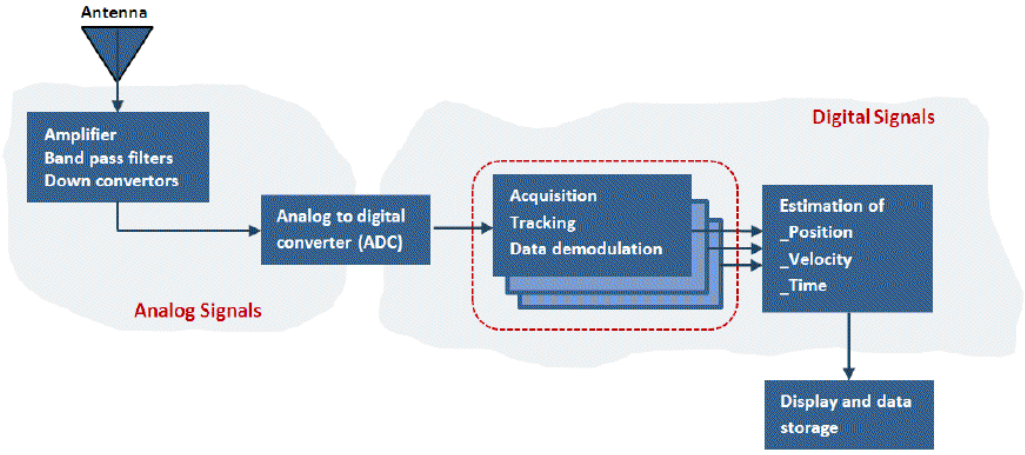

Figure 4.1: GPS receiver block diagram [modified after Misra and Enge, 2006].

4.1 Signal Acquisition

As shown in Equation (4.1), the received GPS signal is a combination of carrier wave, PRN (C/A) code, and navigation message. In order to extract the navigation message from the GPS signal, it is necessary to demodulate the carrier wave and de-spread the C/A-code. Signal acquisition is performed in a GPS receiver for two reasons: to determine visible satellites and, for each visible satellite, to estimate approximate values of C/A-code phase (τ) and carrier wave Doppler shift (f_D) [Borre et al., 2007].

Acquisition process can be time consuming, particularly when the receiver is mobile [Misra and Enge, 2006]. To determine which satellites are in view, a GPS receiver requires valid almanac data, and reasonable estimates of its position and time. When this information is either unavailable or unreliable, the receiver performs a *cold start*, in which it searches for all 32 possible satellite PRNs. This process is lengthy and may take up to several minutes to complete. The receiver performs a *warm start* when it knows its last calculated position (within a few hundred kilometers), current time (within ten minutes or so), and has valid almanac data. Based on this, the receiver has general information to determine which satellites to search for [Misra and Enge, 2006].

For each satellite in view, the receiver estimates approximate values of Doppler shift (f_D) and code phase (τ). The estimations are made by correlating the incoming signal and its replica generated by the receiver. The code phase (τ) is the time alignment between the received C/A-code and its replica in the current block of data. An accurate estimate of (τ) is required by the receiver to perfectly de-spread the C/A-code from the received signal [Borre et al., 2007]. Due to the relative motion between the receiver and a satellite, the incoming carrier frequency usually deviates from its nominal value by an amount which is referred to as Doppler frequency or Doppler shift (f_D). For a stationary receiver the amount of frequency deviation is up to ±5 kHz, and for a high dynamic receiver this value increases to about ±10 kHz. The exact frequency is required to generate a proper local carrier to perfectly remove the incoming carrier wave [Borre et al., 2007].

4.1.1 Acquisition Search Algorithm

To wipe off the carrier wave, the receiver generates an in-phase ($S_{Ir}(t)$) and a quadrature ($S_{Qr}(t)$) reference signal with respect to the incoming signal as follows [Misra and Enge, 2006].

$$S_{Ir}(t) = \cos\left(2\pi(f_{IF} + \hat{f}_D)t + \hat{\theta}\right) \tag{4.2}$$

$$S_{Qr}(t) = \sin\left(2\pi(f_{IF} + \hat{f}_D)t + \hat{\theta}\right) \tag{4.3}$$

where $\hat{f}_D$ and $\hat{\theta}$ are the receiver's best estimates of f_D and θ, respectively.

As illustrated in Figure 4.2, the reference signals are first multiplied by the incoming signal to wipe off the incoming carrier wave. In the next step, a code replica generated by the receiver is correlated with the resulting signals to de-spread the C/A-code as follows [Misra and Enge, 2006].

$$S_I(\Delta\tau, \Delta f_D, \Delta\theta) = \frac{\sqrt{C}D}{T}\int_0^T X(t-\tau)X(t-\hat{\tau})\cos(2\pi\,\Delta f_D\, t + \Delta\theta)\,dt \tag{4.4}$$

$$S_Q(\Delta\tau, \Delta f_D, \Delta\theta) = \frac{\sqrt{C}D}{T}\int_0^T X(t-\tau)X(t-\hat{\tau})\sin(2\pi\,\Delta f_D\, t + \Delta\theta)\,dt \tag{4.5}$$

where $\hat{\tau}$ is the receiver's best estimates of τ, and $\Delta f_D = f_D - \hat{f}_D$, $\Delta\theta = \theta - \hat{\theta}$ and $\Delta\tau = \tau - \hat{\tau}$ represent the estimation errors.

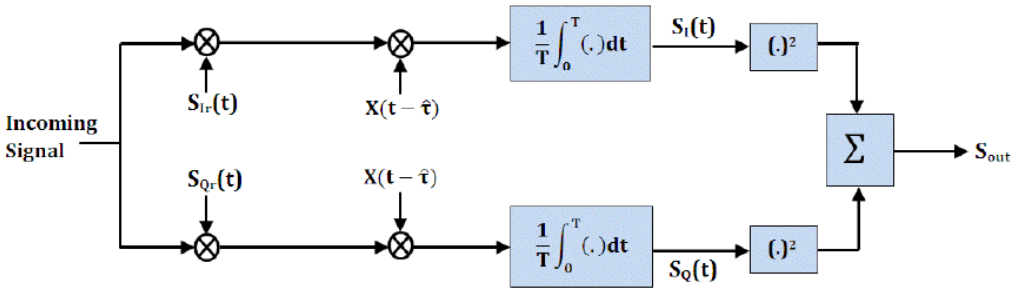

Figure 4.2: Block diagram of the serial search algorithm [modified after Misra and Enge, 2006].

To estimate $\Delta\tau$ and Δf_D, the receiver takes the magnitude of S_{out} (see Figure 4.2) and searches over the entire ($\Delta\tau$, Δf_D) space, shown in Figure 4.3, to find the maximum correlation peak. If a peak is detected, the corresponding value of $\Delta\tau$ and Δf_D is saved and the receiver moves to the tracking mode.

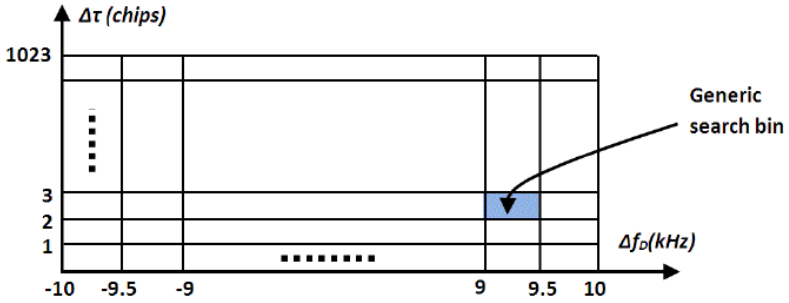

Figure 4.3: Signal search area covers code phase ($\Delta\tau$) and Doppler frequency error (Δf_D) [modified after Misra and Enge, 2006].

The search over the code error axis is broken into one-chip steps (1023 steps overall to cover one block of the C/A-code), and the search over the Doppler error axis is broken into 500 Hz wide search bins (40 bins overall to cover the maximum Doppler range ±10 kHz). According to this, the GPS receiver may need to perform the total number of 1023×40 = 40920 tests to find the true correlation peak. The algorithm described above is known as *serial search* in time domain. Serial search is a common method for signal acquisition used in CDMA systems such as GPS [Borre et al., 2007].

4.1.2 Data Length for Acquisition

The selection of data size for acquisition depends on three factors: the probability of successful signal acquisition, the processing time, and the length of the navigation data bit [Borre et al., 2007].

Even though longer data usually improves the signal-to-noise ratio (SNR) and increases the probability of successful signal acquisition, it will also slow the computations down and increase the processing time quite considerably. The third factor, the length of the navigation data, also limits the selection of long data period. Since each navigation data bit is 20 ms long, the possible longest acquisition data length is 10 ms. This is based on the fact that if the first 10 ms of the data has a phase transition due to the navigation data bit, there will be no phase transition in the next 10 ms of data. The shortest possible acquisition data length is 1 ms as one complete C/A-code is 1 ms long. If fast acquisition is of interest, it is adequate to perform acquisition on 1 ms of data and to make sure that satellites will be acquired the process can be repeated for the second time [Zheng, 2005].

After determining approximate estimates of code phase and Doppler shift, the incoming signal is forwarded to the code and carrier tracking loops along with the corresponding PRN number and estimated values of $\Delta\tau$ and Δf_D for each visible satellite.

4.2 Signal Tracking

After the acquisition process has considerably reduced the code phase error ($\Delta\tau$) and the Doppler error (Δf_D), the receiver will switch from acquisition mode to tracking mode. The tracking loops further refine the estimates of $\Delta\tau$ and Δf_D, track their changes, and extract the navigation data from the incoming signal. A typical GPS receiver contains two types of tracking loops: the code and the carrier tracking loop.

4.2.1 Code Tracking Loop

The code tracking loop or delay locked loop (DLL) refines the initial estimate of code phase error and tracks its variation. To accomplish this, the DLL generates a replica C/A-code and keeps it aligned with the received code by using a feedback control system as shown in Figure 4.4. In this figure, $T(s)$ and $\hat{T}(s)$ denote the Laplace transform of the input and replica code delay, respectively, and $N(s)$ represents the effect of thermal noise.

To perform code alignment, the DLL measures the difference between the incoming code delay and the replica code. The result would be the error signal $\Delta(s)$. Based on this error signal, the loop filter $F(s)$ issues speed-up/slow-down commands $C(s)$ to the code generator $G(s)$ that cause the replica code to shift earlier or later in time. Eventually, these commands align the replica code with the received code.

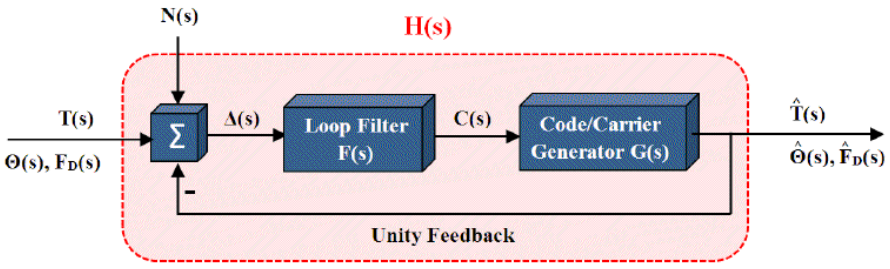

Figure 4.4: Block diagram of the feedback control system employed by the GPS receiver tracking loops.

What does the error signal Δ(s) look like? In other words, how does the tracking loop determine whether the replica code should be shifted earlier or later in time? To make this decision, the tracking loop first wipes off the carrier wave by multiplying the incoming signal with the locally generated carrier wave. This is illustrated in Figure 4.5(a). Subsequently, the signal is multiplied with the code replica, referred to as the *prompt* code, and two shifted versions of it, namely the *early* and *late* codes. The early and late codes are usually shifted by ±0.5 chip with respect to the prompt code. In the next step, the three outputs are summed up over the accumulation time η (e.g. η =1 ms), and the correlation results I_E, I_P, and I_L, which are numerical values, are compared to determine which one provides the highest correlation value [Borre et al., 2007].

Figure 4.5(b) shows an example of code tracking, in which the late code has the highest correlation value indicating that the code sequence must be delayed.

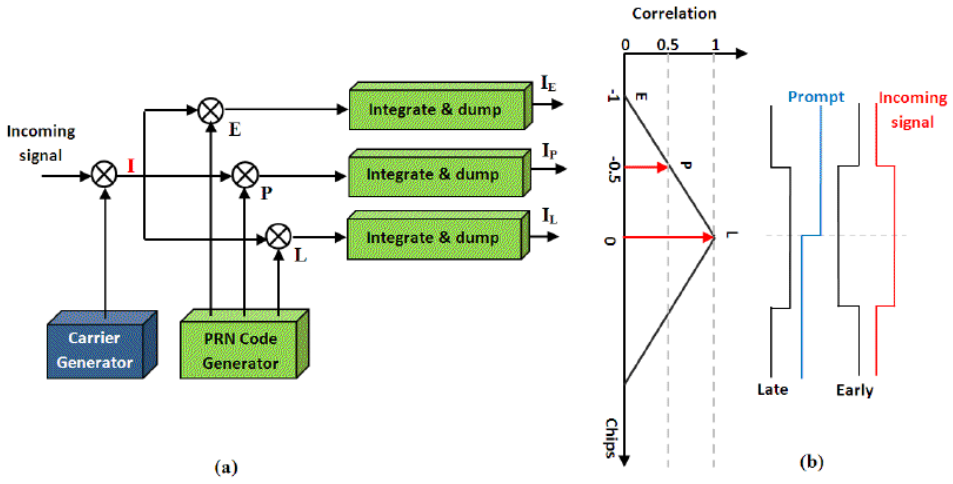

Figure 4.5: The block diagram of the basic code tracking loop [modified after Borre et al., 2007].

4.2.1.1 Coherent and Noncoherent Delay Lock Loop

The DLL introduced in Figure 4.5 is known as the *coherent* DLL. A coherent DLL has optimal functionality only when the locally generated carrier wave is perfectly aligned, in phase and frequency, with the incoming carrier wave. Otherwise, the DLL cannot easily maintain code lock. To overcome this problem, many receivers use a *non-coherent* DLL as shown in Figure 4.6. Accordingly, if the local carrier wave is in phase with the incoming signal, all the energy will be in the in-phase signal, but if not, the energy is distributed between the in-phase and the quadrature signals. In either case, the DLL would be able to perform the code phase lock [Borre et al., 2007].

In both coherent and non-coherent DLLs, the feedback from the correlators to the code generator is provided via using a code discriminator and a loop filter, as depicted in Figure 4.6. Based on this arrangement, the six correlator outputs enter the code discriminator to determine the code phase difference (i.e. the error signal) between the incoming and the replica code. The loop filter reduces the effect of noise on the error signal before passing it to the code generator. Using the error signal, the code generator will shift the replica code earlier or later in time to align it with the incoming code. Typical code tracking loop discriminators used for feedback, along with their characteristics, are listed in Table 4.1 [Ward et al., 2006].

The prompt code will be used in the carrier tracking loop in order to de-spread the PRN code from the incoming signal. This is given in more detail in the following section.

Table 4.1: Common delay lock loop discriminators [from Ward et al., 2006].

Type	Discriminator	Characteristics
Coherent	$(I_E - I_L) \cdot I_P$	**Dot-product.** • Can be used only when carrier loop is in phase lock. • Low computational load. • Most accurate code measurement.
Noncoherent	$(I_E - I_L) \cdot I_P + (Q_E - Q_L) \cdot Q_P$	**Dot-product power.** • Uses all three correlators. • Low computational load. • For 0.5 chip correlator spacing, it produces nearly true tracking error output within ±0.5 chip of input error.
	$(I_E^2 + Q_E^2) - (I_L^2 + Q_L^2)$	**Early-minus-late power.** • Moderate computational load. • Essentially the same error performance as early-minus-late envelope within ±0.5 chip of input error.
	$\sqrt{(I_E^2 + Q_E^2)} - \sqrt{(I_L^2 + Q_L^2)}$	**Early-minus-late envelope.** • Higher computational load. • For 0.5 chip correlator spacing, it produces good tracking error within ±0.5 chip of input error.
	$\frac{\sqrt{(I_E^2 + Q_E^2)} - \sqrt{(I_L^2 + Q_L^2)}}{\sqrt{(I_E^2 + Q_E^2)} + \sqrt{(I_L^2 + Q_L^2)}}$	**Normalized early-minus-late envelope.** • Highest computational load. • For 0.5 chip correlator spacing, it produces good tracking error within less than ±1.5 chip of input error. • Becomes unstable (divide by zero) at ±1.5 chip input error.

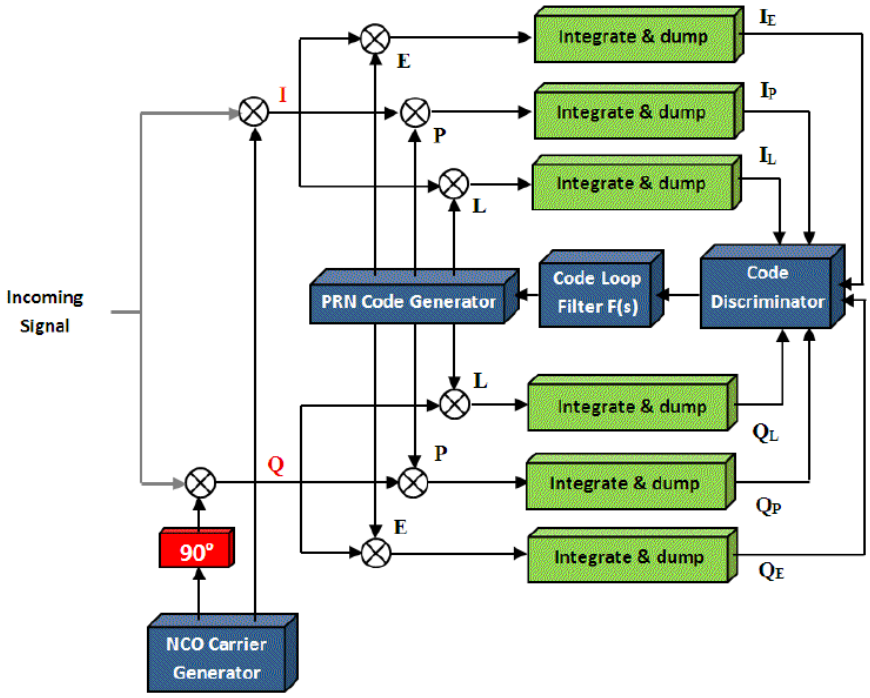

Figure 4.6: Block diagram of a DLL with six correlators [modified after Borre et al., 2007].

4.2.2 Carrier Tracking Loop

The carrier tracking loop or phase locked loop (PLL) refines the coarse estimate of Doppler error (Δf_D) and carrier phase error ($\Delta\theta$), and tracks their changes. To accomplish this, the PLL generates a sinusoidal carrier and adjusts the frequency and phase of the replica sinusoid to match the incoming carrier wave. Similar to the DLL, the PLL is modeled as a control system that uses feedback to control the behavior of the carrier wave generator, better known as the numerically controlled oscillator (NCO). The control model previously shown in Figure 4.4 is applicable to the carrier tracking loop as well. In this figure, $\Theta(s)$ and $F_D(s)$ denote the Laplace transform of the input carrier phase $\theta(t)$ and Doppler frequency $f_D(t)$, respectively, while $\hat{\Theta}(s)$ and $\hat{F}_D(s)$ denote the

Laplace transform of the replica carrier phase $\hat{\theta}(t)$ and replica Doppler frequency $\hat{f}_D(t)$. As before, *N(s)* represents the effect of thermal noise.

According to this model, the PLL attempts to control the carrier generator *G(s)* so that the Doppler and phase estimates for the signal are accurate. To do this, the PLL measures the difference between the received carrier phase and its replica. Based on the error signal $\Delta(s)$, the loop filter *F(s)* issues speed-up/slow-down commands *C(s)* to the carrier generator to shift the frequency and phase of the carrier wave replica by amounts that reduce the error signal.

4.2.2.1 Coherent and Noncoherent Phase Lock Loop

The block diagram of a *coherent* PLL is illustrated in Figure 4.7. This simple algorithm is applicable when the navigation data bits are known in advance. Following the diagram, multiplication with the carrier replica demodulates the incoming carrier wave, and multiplication with the in-phase prompt code de-spreads the PRN code. The carrier loop discriminator is employed in the next step to determine the error signal as a function of phase difference between the input carrier wave and its replica. The error signal is then filtered and used as a feedback control signal to the carrier wave generator. This type of PLL is sensitive to 180 degree phase reversals [Borre et al., 2007].

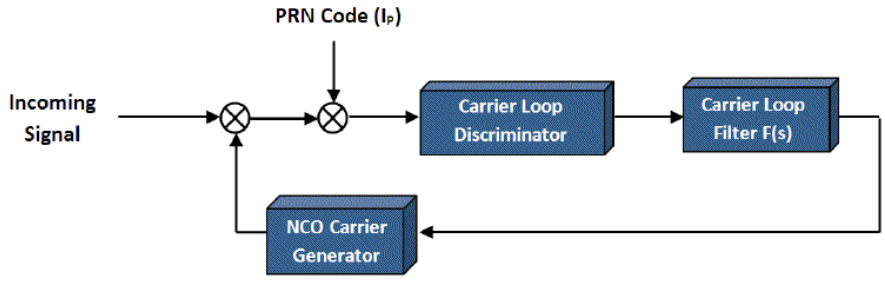

Figure 4.7: GPS receiver coherent carrier tracking loop block diagram.

Since the navigation data bits (thus, the bit transition times) are not usually known in advance, the PLL used in a GPS receiver must be insensitive to bit transition. The well-known Costas phase locked loop is a qualified candidate for this case. The main property of this *non-coherent* loop is that it is insensitive to 180 degrees phase reversals from navigation data. The block diagram of a generic Costas loop is shown in Figure 4.8.

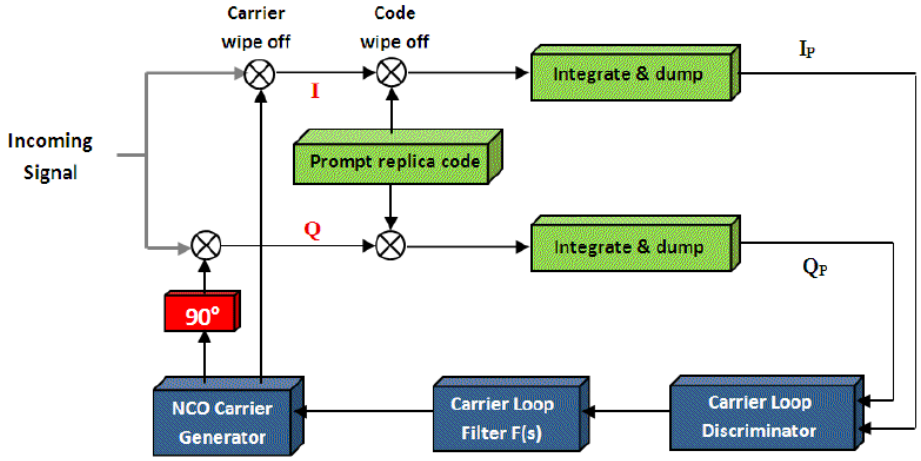

Figure 4.8: Model of a generic Costas phase locked loop.

According to this diagram, the in-phase (I) and quadrature (Q) signals are generated from the incoming signal through multiplication with the in-phase and quadrature reference signals produced by the NCO. Next, the PRN code is wiped off from the in-phase and quadrature signals through multiplication with a prompt replica code generated within the delay locked loop. The resulting signals are then low-pass filtered by a pair of pre-detection integrate-and-dump filters, which results in numerical values I_p and Q_p. Using I_p and Q_p values, the phase discriminator generates an error signal which

represents the phase difference between the incoming carrier wave and the NCO signal. The filtered error signal is then used in the tracking loop as a feedback control signal to change the frequency of the NCO in order to decrease the phase error in following phase measurements. Some common Costas phase discriminator functions used in carrier tracking loops are given in Table 4.2 [Ward, 1996].

Table 4.2: Common Costas phase discriminator functions [from Ward, 1996].

Discriminator	Output	Characteristics
sign(I).Q	$\sin(\theta_e)$	Near optimal at high SNR. Slope proportional to signal amplitude A. Least computational burden.
I.Q	$\sin(2\theta_e)$	Near optimal at low SNR. Slope proportional to signal amplitude A^2. Moderate computational burden.
Q/I	$\tan(\theta_e)$	Suboptimal, but good at low and high SNR. Slope is not signal amplitude dependent. Higher computational burden and must check for divide by zero error near $\pm 90°$
atan(Q/I)	θ_e	Two-quadrant arctangent. Optimal (maximum likelihood estimator) at high and low SNR. Slope is not signal amplitude dependent. Highest computational burden.

4.2.3 Tracking Loop Filters

The loop filter is responsible for attenuating the effect of noise appearing at the phase detector output, thereby generating an accurate and smooth estimate of the incoming signal at its output [Ward, 1996]. Figure 4.9 shows the block diagrams of first-, second-, and third-order analog filters, where ω_n denotes the loop natural frequency, and $1/s$ represents the signal integrator in Laplace form.

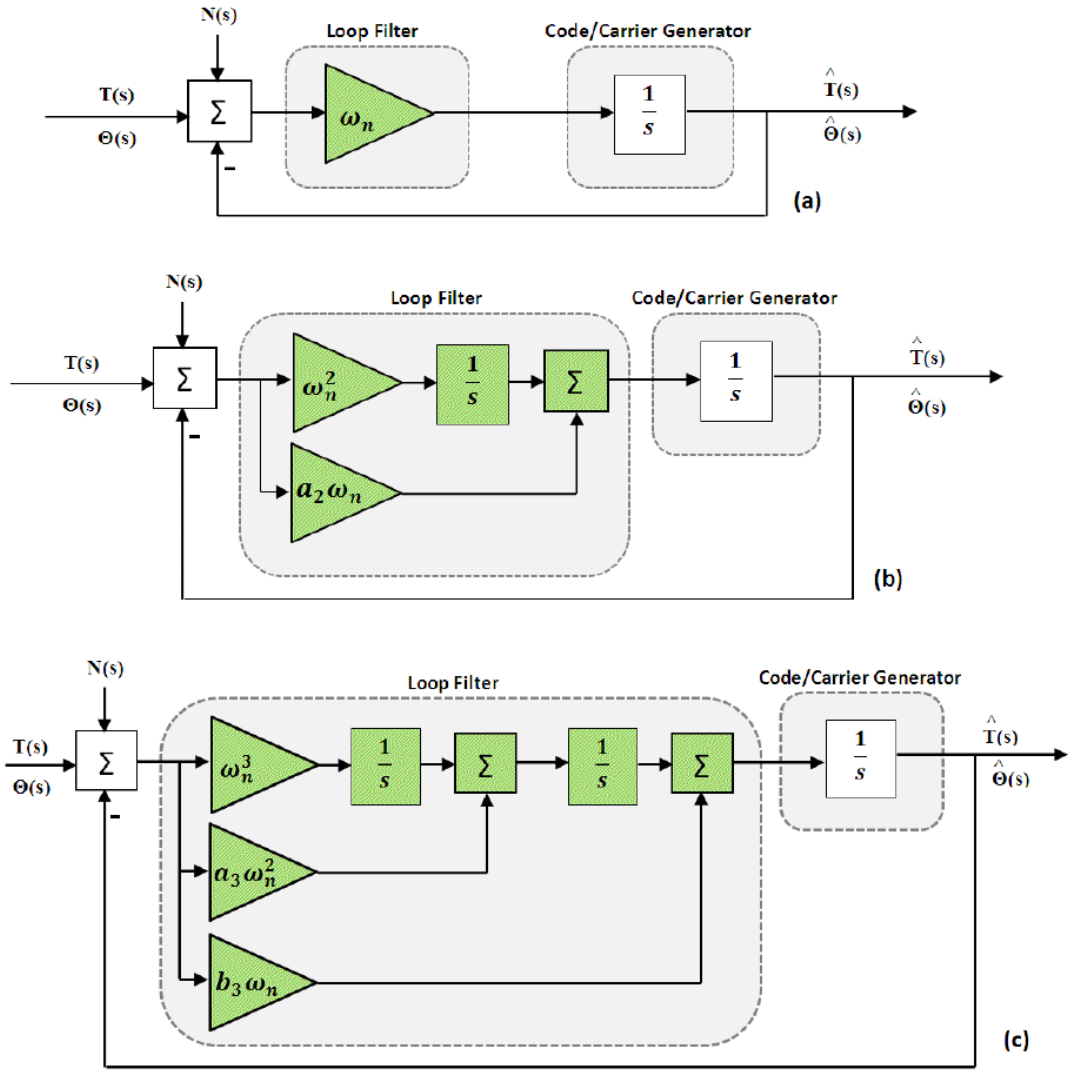

Figure 4.9: The block diagrams of (a) first-, (b) second-, and (c) third-order analog loop filters [modified after Ward, 1996].

The single-side equivalent noise bandwidth (B_n) and the loop filter order (β) are two main parameters of the PLL/DLL loop filter which determine the filter's response to signal dynamics and measurement noise [Ward, 1996]. These two parameters, together with the number of integrators completely determine the loop filter's design. Following the diagrams in Figure 4.9, the loop filter function *F(s)* is calculated for each loop order and summarized in Table 4.3. The filter coefficients are considered as $a_2 = 2\zeta$ where $\zeta = 0.707$, and $a_3 = b_3 = 2$ [Knight et al., 1998]. Other typical filter coefficients include $a_2 = 1.414$, $a_3 = 1.1$, and $b_3 = 2.4$ [Ward, 1996].

Table 4.3: Loop filter function, closed loop transfer functions and single-sided equivalent noise bandwidth for a GPS receiver tracking loop.

Loop Order (β)	*Loop Filter F(s)*	*Noise Bandwidth B_n*	*Closed Loop Transfer Function H(s)*	*Loop Characteristics*
First	ω_n	$\frac{\omega_n}{4}$	$\frac{\omega_n}{s+\omega_n}$	Sensitive to velocity stress. Best operation under static condition.
Second	$a_2\omega_n + \omega_n^2/s$ $= 2\zeta\omega_n + \omega_n^2/s$	$\left(\frac{a_2^2+1}{4a_2}\right)\omega_n$ $= \left(\frac{4\zeta^2+1}{8\zeta}\right)\omega_n$	$\frac{2\zeta\omega_n s + \omega_n^2}{s^2 + 2\zeta\omega_n s + \omega_n^2}$	Sensitive to acceleration stress. Best operation under constant velocity.
Third	$b_3\omega_n + a_3\omega_n^2/s + \omega_n^3/s^2$ $= 2\omega_n + 2\omega_n^2/s + \omega_n^3/s^2$	$\frac{\omega_n(a_3b_3^2 + a_3^2 - b_3)}{4(a_3b_3 - 1)}$ $= \frac{\omega_n}{1.2}$	$\frac{2\omega_n s^2 + 2\omega_n^2 s + \omega_n^3}{s^3 + 2\omega_n s^2 + 2\omega_n^2 s + \omega_n^3}$	Sensitive to jerk stress. Best operation under constant acceleration.

4.2.3.1 Equivalent Noise Bandwidth

The equivalent noise bandwidth (B_n) of a particular filter F(s) is defined as the bandwidth of an ideal filter that permits the same amount of noise as F(s) [Misra and Enge, 2006]. For a tracking loop with transfer function $H(j\omega)$, the noise bandwidth is expressed as [Misra and Enge, 2006]

$$B_n = \frac{1}{\left|H(0)\right|^2}\int_0^\infty \left|H(j\omega)\right|^2 df, \qquad (Hz) \tag{4.6}$$

where $\omega = 2\pi f$, and the magnitude of the frequency response is

$$\left|H(j\omega)\right|^2 = H(j\omega)\cdot H(-j\omega) \tag{4.7}$$

Using the feedback control model in Figure 4.4, the closed loop transfer function that gives the estimate $\hat{\Theta}(s)$ as a function of the input $\Theta(s)$ can be obtained via

$$H(s) = \frac{\hat{\Theta}(s)}{\Theta(s)} = \frac{F(s)G(s)}{1+F(s)G(s)} \tag{4.8}$$

As an example, for the first-order filter, the closed loop transfer function $H(s)$ is calculated by substituting $G(s)=1/s$, and $F(s) = \omega_n = 2\pi f_n$ in Equation (4.8)

$$H(s) = \frac{2\pi f_n}{s+2\pi f_n}. \tag{4.9}$$

With $s = j2\pi f$, the frequency response and the corresponding noise bandwidth is calculated as

$$H(s = j2\pi f) = \frac{f_n}{jf + f_n} \tag{4.10}$$

$$\begin{aligned} B_n &= \frac{1}{\left|H(j0)\right|^2} \int_0^\infty \left|H(j2\pi f)\right|^2 df \\ &= \frac{1}{\left|H(j0)\right|^2} \int_0^\infty \left(\frac{f_n^2}{f^2 + f_n^2}\right) df \\ &= \frac{\pi f_n}{2} \end{aligned} \tag{4.11}$$

The same procedure is repeated for the second-, and third-order loop and the resulting $H(s)$ and B_n are listed in Table 4.3.

The loop noise bandwidth is one of the key parameters to be considered when analyzing the tracking error performance. Under normal ionospheric conditions, thermal noise and satellite-platform dynamics are the main factors causing tracking errors in the GPS receivers. Under irregular ionospheric conditions, ionospheric scintillation appears as an additional source of error whose impact on tracking loop may even result in a complete loss of signal lock. Thermal noise and system dynamics error are briefly studied in this chapter. The effect of scintillation on tracking loop error is investigated in Chapter five.

Closed-form expressions for the tracking error caused by thermal noise are given below for the *early-minus-late power* and *dot-product* type of code tracking loops, respectively, in Equations (4.12) and (4.13) as [Jwo, 2001]

$$\sigma_{tDLL} = \left[\frac{B_n d}{2(c/n_0)} \left(1 + \frac{2}{\eta(2-d)(c/n_0)} \right) \right]^{1/2} \quad (chips) \tag{4.12}$$

$$\sigma_{tDLL} = \left[\frac{B_n d}{2(c/n_0)} \left(1 + \frac{1}{\eta(c/n_0)} \right) \right]^{1/2} \quad (chips) \tag{4.13}$$

where σ_{tDLL} is the standard deviation of tracking error in units of PRN chips, B_n is the DLL noise bandwidth in Hz, η is the pre-detection integration time in seconds, d is the early-to-late correlator spacing in chips (usually *d=1*), and c/n_0 is the carrier-to-noise ratio value where $(C/N_0)_{dB-Hz} = 10 \cdot \log_{10}(c/n_0)$.

Thermal noise for the Costas-type PLL is defined according to the following expression [Jwo, 2001].

$$\begin{aligned} \sigma_{tPLL} &= \left[\frac{B_n}{(c/n_0)} \left(1 + \frac{1}{2\eta(c/n_0)} \right) \right]^{1/2} \quad (rad) \\ &= \left[\frac{B_n}{(c/n_0)} \left(1 + \frac{1}{2\eta(c/n_0)} \right) \right]^{1/2} \cdot \frac{360}{2\pi} \quad (\text{deg}) \end{aligned} \tag{4.14}$$

where σ_{tPLL} is the standard deviation of tracking error in units of radians (or degrees), and B_n is the PLL noise bandwidth in Hz.

The bandwidth of a GPS receiver code tracking loop is typically in the range of 1-4 Hz, while for carrier tracking loop, it is in the range of 5-15 Hz [Jwo, 2001]. Figure 4.10 shows one-sigma thermal error of the early-minus-late power (upper panel) and dot-product (lower panel) non-coherent DLL, and Figure 4.11 shows one-sigma thermal error of the Costas-type PLL. Parameters considered for these plots include $\eta = 1$ ms, $d = 1$

chip, C/N_0 =25-40 dB-Hz, B_{nDLL} = 1, 2.5, 4 and 10 Hz, and B_{nPLL} = 5, 15, 25 and 35 Hz.

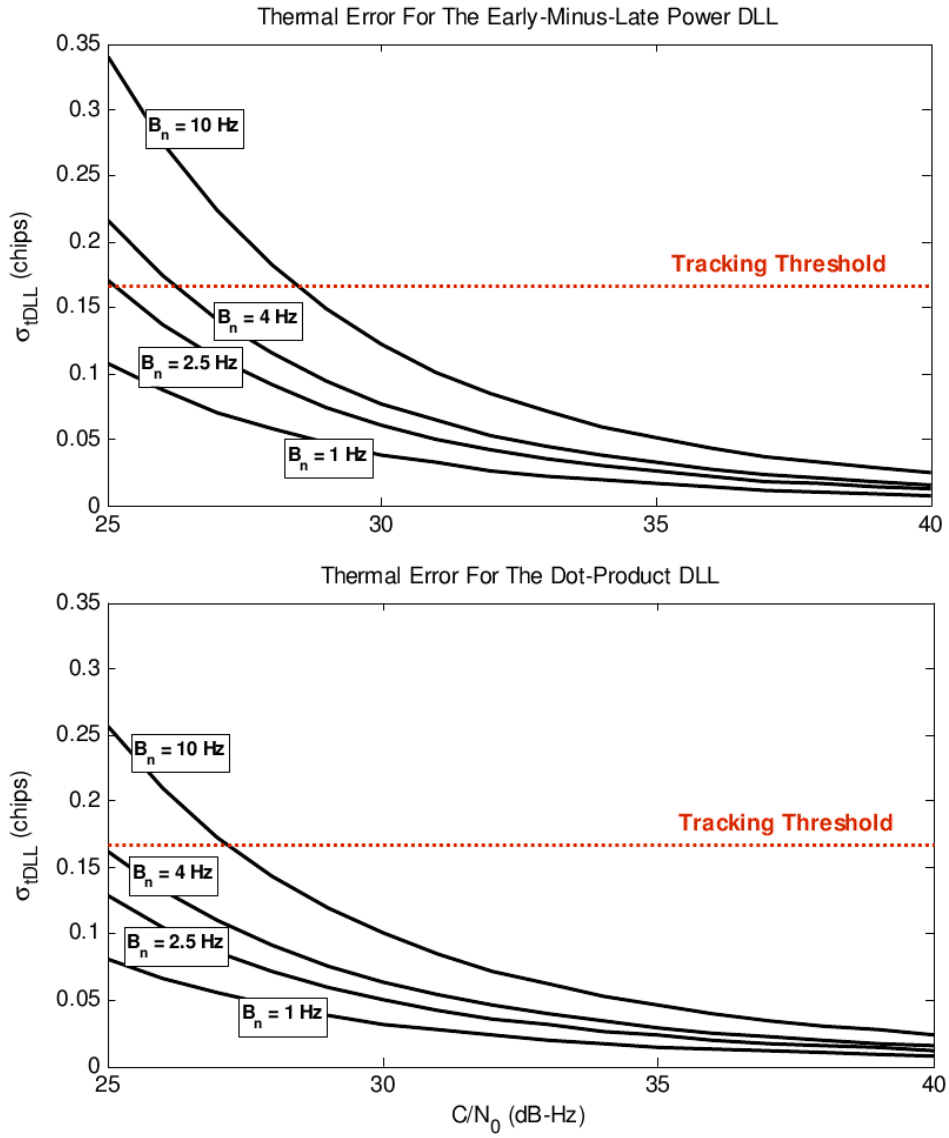

Figure 4.10: One-sigma thermal error for (a) early-minus-late power DLL, and (b) dot-product DLL.

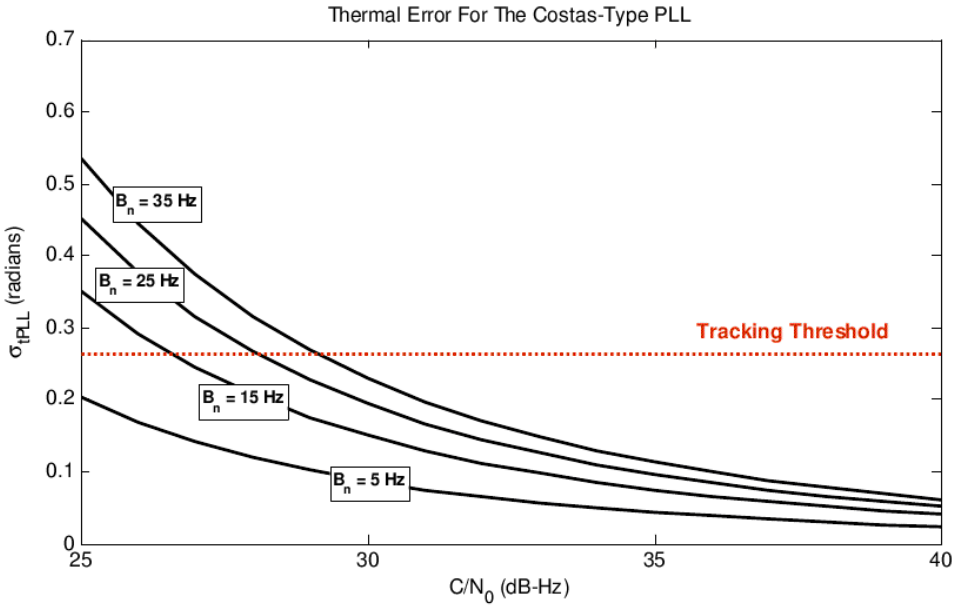

Figure 4.11: One-sigma thermal error for Costas-type PLL.

As a rule of thumb, the one-sigma code tracking error should not exceed 1/6 of the chip length, and the one-sigma carrier tracking error should not exceed $\pi/12$ radians or 15 degrees[10] [Jwo, 2001; Misra and Enge, 2006]. In Figure 4.10 and Figure 4.11, the threshold level is shown with a horizontal dashed line. For the typical range of GPS signal C/N_0 (i.e. 35-55 dB-Hz), tracking error remains below the threshold line for the considered bandwidths. For very low C/N_0 (< 30 dB-Hz), however, both code and carrier tracking loops show much better performance (i.e. lower tracking error) under narrower bandwidths. As also indicated in Equations (4.12) to (4.14), the tracking loop thermal error is directly related to the loop noise bandwidth; thus narrower bandwidths are able to reject thermal noise more effectively.

---

[10] *The one-sigma carrier tracking error threshold is about 10 degrees for aviation applications [Hegarty et al., 2001].*

What is the limiting factor when it comes to implement a very narrow loop bandwidth in the tracking loop design? To answer this question, the response of the first-order carrier tracking loop to a step change in pseudorange is studied here. Using Equations (4.9) and (4.11), the loop response to a step change in pseudorange follows

$$\begin{aligned} y(t) &= L^{-1}\{U(s)H(S)\} \\ &= L^{-1}\left\{\frac{2\pi f_n}{s(s+2\pi f_n)}\right\} \\ &= 1-\exp(-2\pi f_n t) \\ &= 1-\exp(-4B_n t) \end{aligned} \tag{4.15}$$

where $U(s)=1/s$ is the Laplace transform of the input step function $u(t)$.

The step response is plotted for B_n = 5, 15 and 25 Hz in Figure 4.12. As can be seen, while loop response is slow under narrow bandwidths (e.g. B_n = 5 Hz), wider noise bandwidths (e.g. B_n = 25 Hz) provide a more accommodating loop with rapid rise times that closely follow the input step. Since under high system dynamics relatively fast tracking loop responses are required, too narrow bandwidths should be avoided in the design of tracking loops.

In summary, there is always a tradeoff between the noise performance and the dynamic performance of a tracking loop when selecting the best loop bandwidth [Misra and Enge, 2006]. For a good dynamic performance the carrier tracking loop requires a relatively wide bandwidth to precisely track changes in the carrier phase due to satellite-platform dynamics (see Figure 4.12). For good noise performance, on the other hand, the loop requires a narrow bandwidth in order to reject the measurement noise as much as possible (see Figure 4.10 and Figure 4.11).

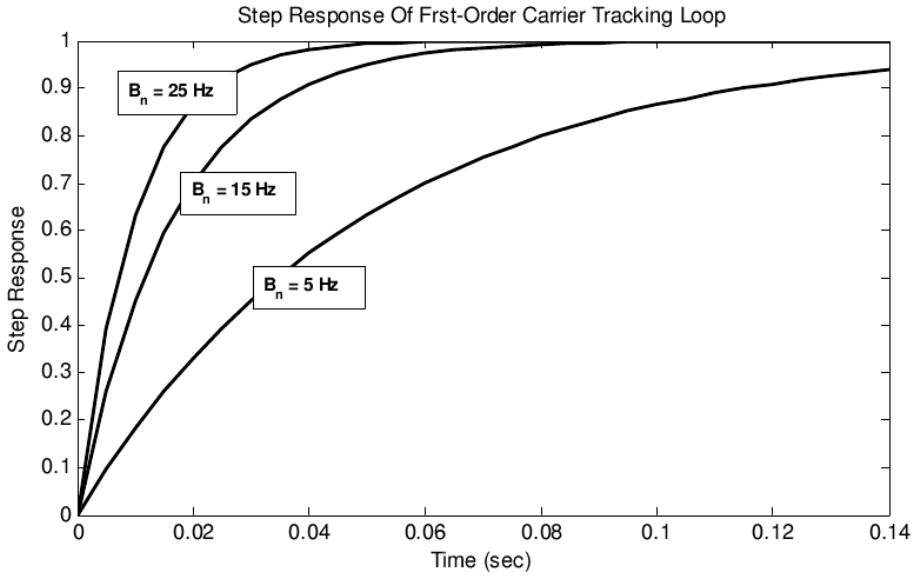

Figure 4.12: Step response of first-order tracking loop.

4.2.3.2 Loop Filter Order

Loop order defines the filter sensitivity to the system dynamics. To further explain this, the steady state response of the first-, second-, and third-order tracking loop to *step*, *ramp* and *parabolic* input is investigated. A small steady-state error (SSE) is usually taken as a sign of good tracking performance [Jwo, 2001]. The SSE is evaluated using the final value theorem of the Laplace transforms as [Misra and Enge, 2006]

$$\lim_{t\to\infty} \Delta(t) = \lim_{s\to 0} \left(s\,\Delta(s)\right) \tag{4.16}$$

where, according to the feedback control system shown in Figure 4.4,

$$\begin{aligned}\Delta(s) &= \Theta(s) - \hat{\Theta}(s) \\ &= \Theta(s)\big(1 - H(s)\big).\end{aligned} \tag{4.17}$$

The result of SSE is calculated for three loop orders, and summarized in Table 4.4. Accordingly, the first order loop is sensitive to velocity stress, the second order loop is sensitive to acceleration stress, and the third order loop is sensitive to jerk stress.

In a position control system, the step input function represents an abrupt change in reference position, while the ramp and parabolic input functions represent the change in velocity and acceleration, respectively. In such system, for the unit step input, in the fullness of time, the first-order PLL will converge to the right answer, thus result in zero steady state error. The loop, however, is not able to keep up with the ramp function. To overcome this, the PLL loop order has to be either two or three. For the parabolic input function, only the third-order PLL meets the requirements [Misra and Enge, 2006].

Both the loop filter order (β) and the equivalent noise bandwidth (B_n) play key roles in the design and the performance of a tracking loop. By carefully determining these parameters, the performance of the code and carrier tracking loops of a GPS receiver can increase considerably.

Table 4.4: Steady state error for first-, second-, and third-order tracking loop filter.

Input function, $\theta(t)$		**Laplace Transform,** $\Theta(s)$
Step:	$u(t)=\begin{cases}1 & t\ge 0\\ 0 & t<0\end{cases}$	$1/s$
Ramp:	$r(t)=t\,u(t)$	$1/s^2$
Parabolic:	$p(t)=\frac{1}{2}t^2u(t)$	$1/s^3$
First-order loop (β=1)		
$\Theta(s) = 1/s,$	$\lim_{s\to 0} s\Theta(s)\left(1-H(s)\right)=\lim_{s\to 0}\left(\frac{s}{s+2\pi f_n}\right)=0$	
$\Theta(s) = 1/s^2,$	$\lim_{s\to 0}\frac{1}{s}\left(\frac{s}{s+2\pi f_n}\right)=\frac{1}{2\pi f_n}\ (meters)\ =\ \frac{2\pi}{\lambda}\frac{1}{2\pi f_n}\ \ (radians)$	
Second-order loop (β=2)		
$\Theta(s) = 1/s,$	$\lim_{s\to 0}\ \left(\frac{s^2}{s^2+2\zeta(2\pi f_n)s+(2\pi f_n)^2}\right)=0$	
$\Theta(s) = 1/s^2,$	$\lim_{s\to 0}\ \frac{1}{s}\left(\frac{s^2}{s^2+2\zeta(2\pi f_n)s+(2\pi f_n)^2}\right)=0$	
$\Theta(s) = 1/s^3,$	$\lim_{s\to 0}\frac{1}{s^2}\left(\frac{s^2}{s^2+2\zeta(2\pi f_n)s+(2\pi f_n)^2}\right)=\frac{1}{(2\pi f_n)^2}\ \ (meters)$	
Third-order loop (β=3)		
$\Theta(s) = 1/s,$	$\lim_{s\to 0}\ \left(\frac{s^3}{s^3+2\omega_n s^2+2\omega_n^2 s+\omega_n^3}\right)=0$	
$\Theta(s) = 1/s^2,$	$\lim_{s\to 0}\ \frac{1}{s}\left(\frac{s^3}{s^3+2\omega_n s^2+2\omega_n^2 s+\omega_n^3}\right)=0$	
$\Theta(s) = 1/s^3,$	$\lim_{s\to 0}\frac{1}{s^2}\left(\frac{s^3}{s^3+2\omega_n s^2+2\omega_n^2 s+\omega_n^3}\right)=0$	

4.3 GPS Tracking Loop Implementation

Software implementations of GPS receiver tracking loops are employed in this work to validate theoretical models. Accordingly, a conventional second-order code tracking loop with normalized early-minus-late envelope discriminator (commonly used as its output error is linear over a 1-chip range [Ward et al., 2006]), and both second-, and third-order carrier tracking loop with arctangent discriminator (optimal at high and low SNR) are implemented in MATLAB using the combined tracking channel diagram shown in Figure 4.13. The optimum damping ratio of $\zeta = 0.7$ is considered for both code and carrier tracking loop filters. The tracking loop updates are obtained typically every 1 ms, 10 ms, or 20 ms. In this work, the loop update interval is set to $\eta = 1$ ms. The settings are summarized below:

Costas loop simulator settings:

Intermediate frequency	f_{IF} = 9.548 MHz
Sampling frequency	$f_{sampling}$ = 38.192 MHz
Damping ratio:	ζ_{PLL} = 0.7
Noise bandwidth :	$B_{n,PLL}$ = 5-35 Hz (adjustable)
Pre-detection integration time:	η = 1 ms
Discriminator type (Table 4.2):	$a\tan(Q_P / I_P)$

Code tracking loop simulator settings:

Correlator spacing:	d = 0.5 chips
Damping ratio:	ζ_{DLL} = 0.7
Noise bandwidth :	$B_{n,DLL}$ = 2.5 Hz
Pre-detection integration time:	η = 1 ms
Discriminator type (Table 4.1):	$\dfrac{\sqrt{(I_E^2 + Q_E^2)} - \sqrt{(I_L^2 + Q_L^2)}}{\sqrt{(I_E^2 + Q_E^2)} + \sqrt{(I_L^2 + Q_L^2)}}$

In the combined tracking loop channel shown in Figure 4.13, the carrier wave replica required in the DLL to remove the carrier wave is provided by the PLL, and the prompt code replica used in the PLL to de-spread the PRN code is provided by the DLL.

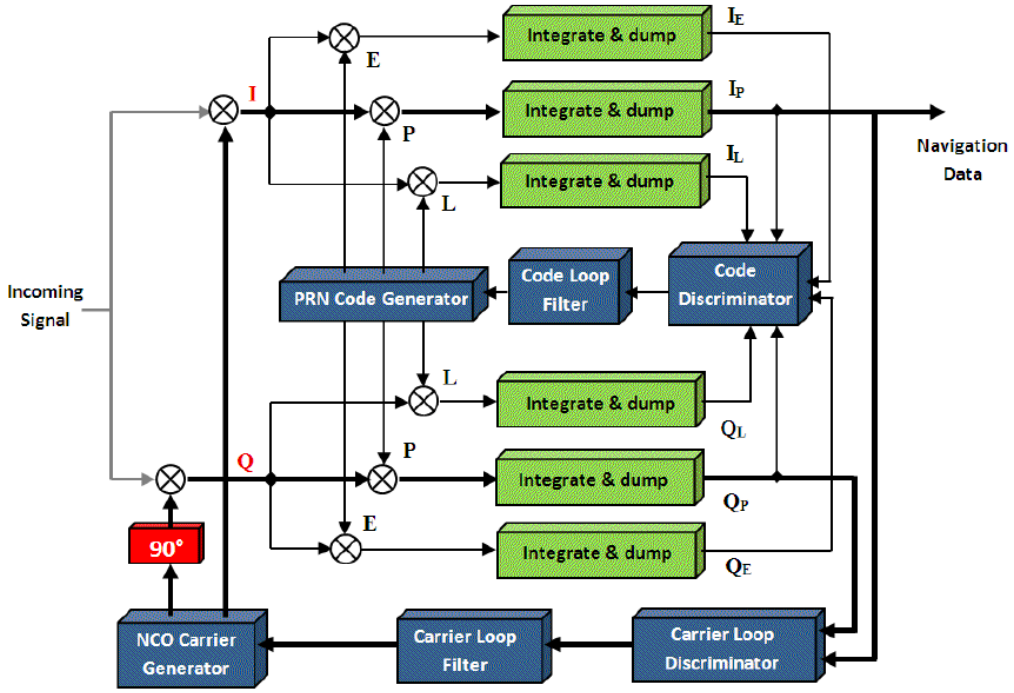

Figure 4.13: The block diagram of a complete tracking channel.

According to this diagram, for every 1 ms of input signal, the in-phase (I) and quadrature (Q) signals are generated from the incoming signal through multiplication with the in-phase and quadrature reference signals produced by the NCO. Subsequently, the signals are multiplied with the prompt, early and late code replicas, with the early and late codes being ±0.5 chips shifted with respect to the prompt code. Following this, the

outputs are integrated (summed up) over $\eta = 1$ ms integration (accumulation) time. The six correlation output numerical values (I_E, I_P, I_L, Q_E, Q_P and Q_L) are then used in the code and carrier loop discriminators to generate error signals. The carrier loop discriminator uses I_P and Q_P to generate carrier tracking error signal

$$\theta_{e,PLL} = \frac{\tan^{-1}(Q_p / I_p)}{2\pi}, \qquad (cycle) \tag{4.18}$$

and the code loop discriminator uses (I_E, I_L, Q_E and Q_L) to generate code tracking error

$$\theta_{e,DLL} = \frac{\sqrt{(I_E^2 + Q_E^2)} - \sqrt{(I_L^2 + Q_L^2)}}{\sqrt{(I_E^2 + Q_E^2)} + \sqrt{(I_L^2 + Q_L^2)}}, \qquad (cycle) \tag{4.19}$$

Based on the error signals, the carrier and code loop filters issue speed-up/slow-down commands, respectively, to the carrier and code generator to change their frequencies in a way that decreases the error in the following measurement epochs. The amount of frequency change is adjusted through the loop filter coefficients.

4.3.1 Loop Filter Coefficients and Frequency Update

Using the bilinear z-transform model, the loop filter transfer function can be described via [Skone et al., 2005]

$$F(z) = \frac{\sum_{m=0}^{M-1} b_m z^{-m}}{(1 - z^{-1})^{M-1}} = \frac{b_0 + b_1 z^{-1} + b_2 z^{-2} + \ldots + b_{M-1} z^{-(M-1)}}{(1 - z^{-1})^{M-1}} \tag{4.20}$$

where M is the order of the tracking loop, and b_m ($m = 0, 1, \ldots, M-1$) are the loop filter coefficients.

In the case of a *second-order* tracking loop ($M = 2$), the block diagram of the digital loop filter is given in Figure 4.14. This diagram is analogous to the one shown in Figure 4.9b, and has been obtained by substituting $s = 2(z-1)/(\eta(z+1))$ to transform from s domain to bilinear z domain. Figure 4.14 along with Equation (4.20) can be used to determine the corresponding loop coefficients (b_0 and b_1) as follows.

$$F(z) = \frac{y(z)}{x(z)} = \frac{b_0 + b_1 z^{-1}}{1 - z^{-1}} = \frac{(\eta\omega_n^2/2 + a_2\omega_n) + (\eta\omega_n^2/2 - a_2\omega_n)\, z^{-1}}{1 - z^{-1}} \tag{4.21}$$

where $b_0 = (\eta\omega_n^2/2 + a_2\omega_n)$, $b_1 = (\eta\omega_n^2/2 - a_2\omega_n)$, η is the pre-detection integration time, and for given ζ and B_n (see Table 4.3), $a_2 = 2\zeta = 1.414$, and

$$\omega_n = \frac{4a_2}{a_2^2 + 1} B_n = \frac{8\zeta}{4\zeta^2 + 1} B_n \tag{4.22}$$

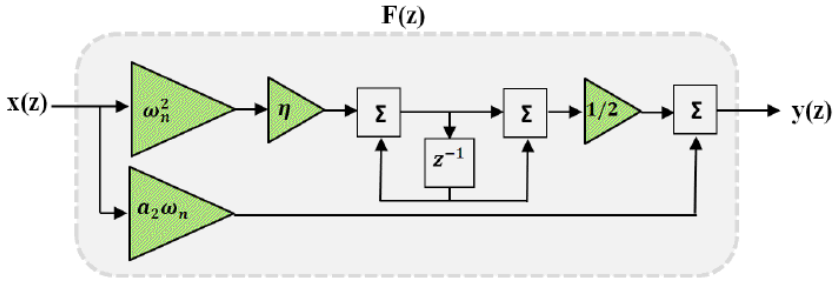

Figure 4.14: Block diagram of the 2nd-order digital loop filter [modified after Ward, 1996].

Having the coefficients, the loop filter given in Equation (4.21) can be implemented in software using the following equation.

$$f[n] = f[n-1] + b_0 \cdot \theta_e[n] + b_1 \cdot \theta_e[n-1], \qquad n = 1, 2, 3, ... \tag{4.23}$$

assuming $f[0] = 0$ and $\theta_e[0] = 0$. In this equation, $f[n]$ represents the current code/carrier filter output, in units of Hz, $f[n-1]$ denotes the filter output in the previous measurement epoch, $\theta_e[n]$ represents the current code/carrier phase discriminator output, in units of cycle, and $\theta_e[n-1]$ denotes the discriminator output in the previous epoch. The phase and frequency measurements are obtained every $\eta = 1$ ms.

For a *third-order* tracking loop ($M = 3$), the block diagram of the digital loop filter is displayed in Figure 4.15, and has been obtained by substituting $s = 2(z-1)/(\eta(z+1))$ in Figure 4.9c. According to this block diagram and Equation (4.20),

$$\begin{aligned} F(z) &= \frac{y(z)}{x(z)} = \frac{b_0 + b_1 z^{-1} + b_2 z^{-2}}{(1-z^{-1})^2} \\ &= \frac{\left(\frac{\eta^2\omega_n^3}{4} + \frac{a_3\eta\omega_n^2}{2} + b_3\omega_n\right) + \left(\frac{\eta^2\omega_n^3}{2} - 2b_3\omega_n\right) z^{-1} + \left(\frac{\eta^2\omega_n^3}{4} - \frac{a_3\eta\omega_n^2}{2} + b_3\omega_n\right) z^{-2}}{(1-z^{-1})^2} \end{aligned} \tag{4.24}$$

where η is the pre-detection integration time, $a_3 = 1.1$, $b_3 = 2.4$ [Ward, 1996], and

$$\omega_n = \frac{4(a_3 b_3 - 1)}{(a_3 b_3^2 + a_3^2 - b_3)} B_n = 1.27\, B_n \tag{4.25}$$

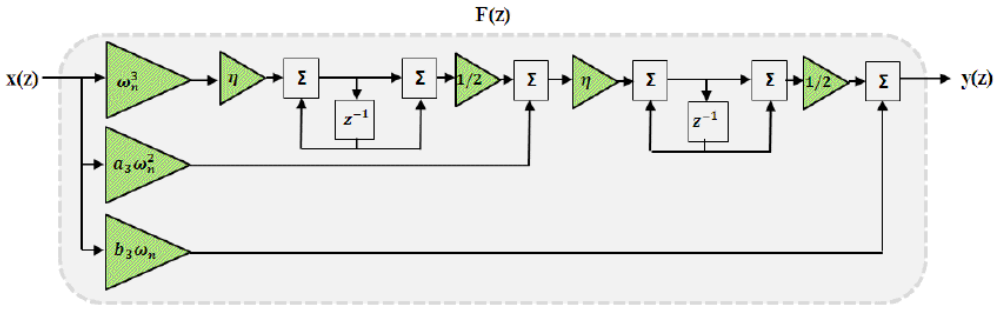

Figure 4.15: Block diagram of the 3rd-order digital loop filter [modified after Ward, 1996].

Using (b_0, b_1 and b_2), the loop filter given in Equation (4.24) can be implemented in software through

$$\begin{aligned} f[n] &= 2f[n-1] - f[n-2] \\ &+ b_0 \cdot \theta_e[n] + b_1 \cdot \theta_e[n-1] + b_2 \cdot \theta_e[n-2], \qquad n = 2, 3, ... \end{aligned} \tag{4.26}$$

assuming $f[0] = f[1] = 0$ and $\theta_e[0] = \theta_e[1] = 0$. As before, $f[n]$ represents the current code/carrier filter output, while $f[n-1]$ and $f[n-2]$ represent the filter output in two previous measurement epochs.

The amount of frequency determined by Equations (4.23) and (4.26), respectively for the second-, and third-order tracking loops, is then applied to the carrier and code generators to reduce the error signals.

To give an example, the simulated *unperturbed* GPS signal shown in Figure 3.6 is processed in the receiver tracking loop simulators (using the 2nd-order code and carrier tracking loops), and the corresponding results for PRN3 are displayed in Figure 4.16. The upper frame shows the carrier tracking loop phase discriminator output in units of cycle.

To highlight the general trend of phase variation, the discriminator output is smoothed using a 25 ms moving average window. The resulting smoothed phase is given in the upper frame of Figure 4.16 along with the raw phase data. In addition, the phase error standard deviation is calculated continuously using a 200 ms moving window as shown in the lower frame of Figure 4.16. It can be seen from the figure that, in the absence of scintillation, the phase error standard deviation varies between 0.01 to 0.02 cycles (3.6 to 7.2 degrees), which is well below the typical tracking threshold of 15 degrees.

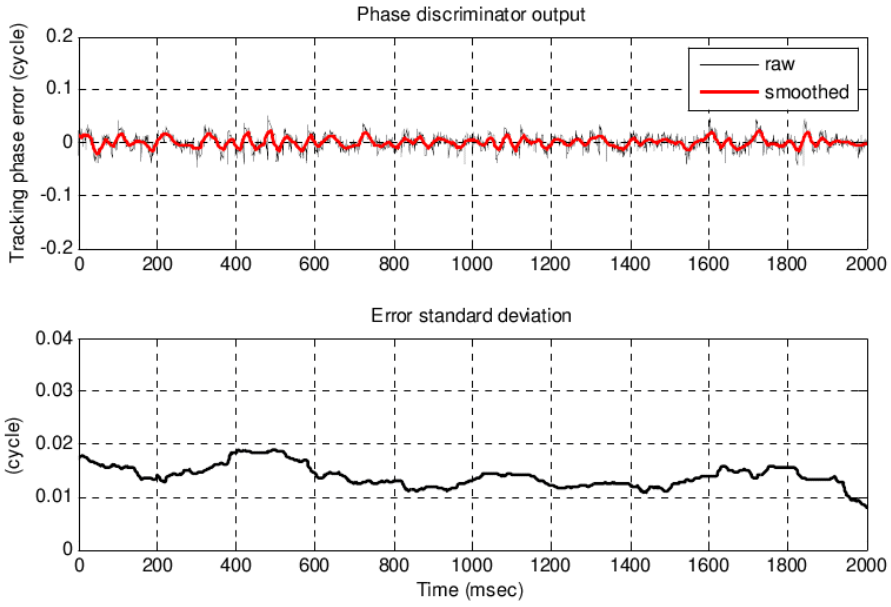

Figure 4.16: Carrier tracking loop phase discriminator output and phase error standard deviation (in units of cycles) with no scintillation effects.

As stated earlier in the simulation methodology flowchart in Figure 1.7, the tracking loop simulators are driven mostly by *scintillated* GPS L_1 signals. To generate a scintillated signal, the simulated unperturbed GPS L_1 signal is modulated by phase and intensity scintillation data using the complex modulation algorithm. The complex modulation is

performed by adding the phase scintillation to the phase of the GPS carrier signal, and multiplying the carrier signal by the square root of intensity scintillation records. Eventually, the scintillated GPS signal is processed in the tracking loop simulators to give the simulation results. As an example, the carrier tracking loop output after adding scintillation is shown in Figure 4.17. To generate this plot, the *scintillated* GPS signal shown in Figure 3.8 is processed in the second-order tracking loops and the results for PRN3 are illustrated here.

Comparing this figure with Figure 3.7, it is observed that during the times of severe phase and intensity scintillations (about 600-800 ms, and 1100-1500 ms from the start of the time axis), carrier tracking loop experiences high tracking errors, for which the error standard deviation reaches up to 0.1 cycles (~ 36 degrees). This value is well above the tracking threshold, and most likely results in cycle slips and/or loss of phase lock.

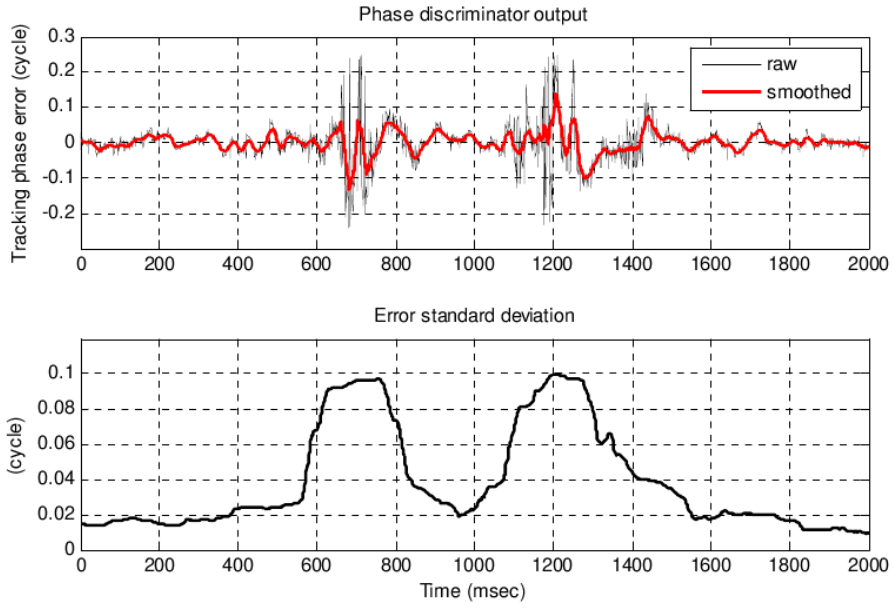

Figure 4.17: Carrier tracking loop phase discriminator output and phase error standard deviation (in units of cycles) after adding scintillation effects. The standard deviation is obtained by moving a 200 ms window along the phase data.

Comparing the results of Figure 4.16 and Figure 4.17, the tracking error standard deviation shows a significant increase in the presence of severe phase and intensity scintillation activities. The carrier tracking error is *quantified* in terms of intensity and phase scintillation parameters (T_{scin}, ν, S_4) in the next chapter.

4.4 Simulation Model Verification

In order for a simulation algorithm to be validated, its results should be compared against experimental results. The scintillation simulation algorithm used in this research is evaluated through comparison with real scintillation data. The real data - provided by Dr. Theodore Beach of Air Force Research Laboratory (AFRL) - were collected at Ascension Island (7.9°S, 14.3°W) during a solar maximum period using a NAVSYS DSR-100 receiver [cf. May et al., 1999]. To decrease the signal processing time, from 45 minutes of available scintillated data (corresponding to 8:45 PM - 9:30 PM of March 18, 2001), about 15 minutes (from 9:05 PM to 9:20 PM) is used for scintillation analysis in this work. In the selected time period, both quiet and active scintillation conditions are observable. During this 15-minute period, six healthy satellites, namely PRN1, PRN7, PRN8, PRN13, PRN19 and PRN27 were acquired. Except for the PRN8 signal, the other five signals were found to be significantly corrupted by the ionospheric scintillation effects. Among these, PRN1 and PRN7 signals are used in this section to highlight the effect of scintillation on the GPS receiver performance.

Using the GPS receiver tracking loop simulators, Figure 4.18 shows the 15 minutes tracking results of PRN1 and PRN7 signals, assuming the loop bandwidth of $B_n = 15$ Hz, and the accumulation time of $\eta = 1$ ms. The result of PLL generated C/N_0 for PRN1 is shown in the left panel. This signal is weakly scintillated during the first 4 minutes where C/N_0 changes between 30 and 40 dB-Hz. From 4 to 11 minutes, a stronger scintillation begins with a maximum of ~15 dB fading in a number of epochs. After 11 minutes, the signal faces a very strong scintillation with more than 25 dB fading. PRN7 (right panel), on the other hand, experiences no scintillation or a very low level during the first 8

minutes of signal tracking. From 8 to 12 minutes, a weak scintillation with ~5 dB fading commences. After about 12 minutes of tracking, the signal experiences a very strong scintillation with nearly 30 dB fading in several epochs.

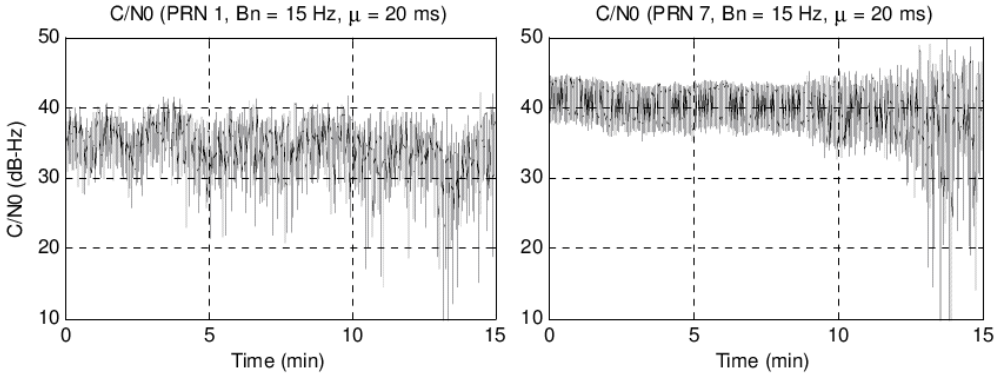

Figure 4.18: Carrier tracking loop generated C/N_0 for PRN1 and PRN7 signals. Data corresponds to 9:05 PM to 9:20 PM of March 18, 2001.

To determine the strength of scintillation activity, the intensity scintillation index (S_4) is used. The S_4 index represents the normalized standard deviation of signal intensity (SI), and is typically computed over 60-second intervals, via

$$S_{4T} = \sqrt{\frac{\langle SI^2 \rangle - \langle SI \rangle^2}{\langle SI \rangle^2}} \tag{4.27}$$

where S_{4T} denotes the *total* S_4 including the effects of ambient noise, as well as signal intensity variations due to changing range and multipath. In Equation (4.27), the received signal intensity SI is defined as the difference between the signal's narrow-band power (NBP) and wide-band power (WBP), measured over the same interval every 20 ms as follows [Van Dierendonck et al., 1993]:

$$NBP = \left(\sum_{i=1}^{20} I_i \right)^2 + \left(\sum_{i=1}^{20} Q_i \right)^2 \tag{4.28}$$

$$WBP = \sum_{i=1}^{20} \left(I_i^2 + Q_i^2 \right) \tag{4.29}$$

$$SI = NBP - WBP \tag{4.30}$$

where I and Q represent the 1 kHz in-phase and quadraphase accumulation results of the channel correlators. To obtain the actual S_4 values, the received signal intensity needs to be detrended and the ambient noise needs to be removed.

4.4.1 Detrending Signal Intensity

Detrending the raw signal intensity measurements is accomplished in two steps: first, low-pass filtering the raw intensity measurements to remove the trend and, second, normalizing the received signal intensity to the filter output obtained in the first step.

Following Fremouw et al., [1978] and Van Dierendonck et al. [1993], a 6th-order *low-pass* Butterworth filter with a 0.1 Hz cutoff frequency is implemented in this work to filter the 50 Hz raw signal intensity measurements obtained from Equation (4.30). The *detrended normalized* signal intensity (SI_{det}) is then calculated from

$$SI_{\text{det}} = \frac{SI}{(SI)_{LPF}} = \frac{NBP - WBP}{(NBP - WBP)_{LPF}} \tag{4.31}$$

The SI_{det} values (if detrended properly) fluctuate around a value of 1. Figure 4.19 shows the results of processing raw (SI_{raw}), low-pass filtered (SI_{LPF}), and detrended normalized (SI_{det}) intensity measurements for the PRN1 (top panels) and the PRN7 (bottom panels).

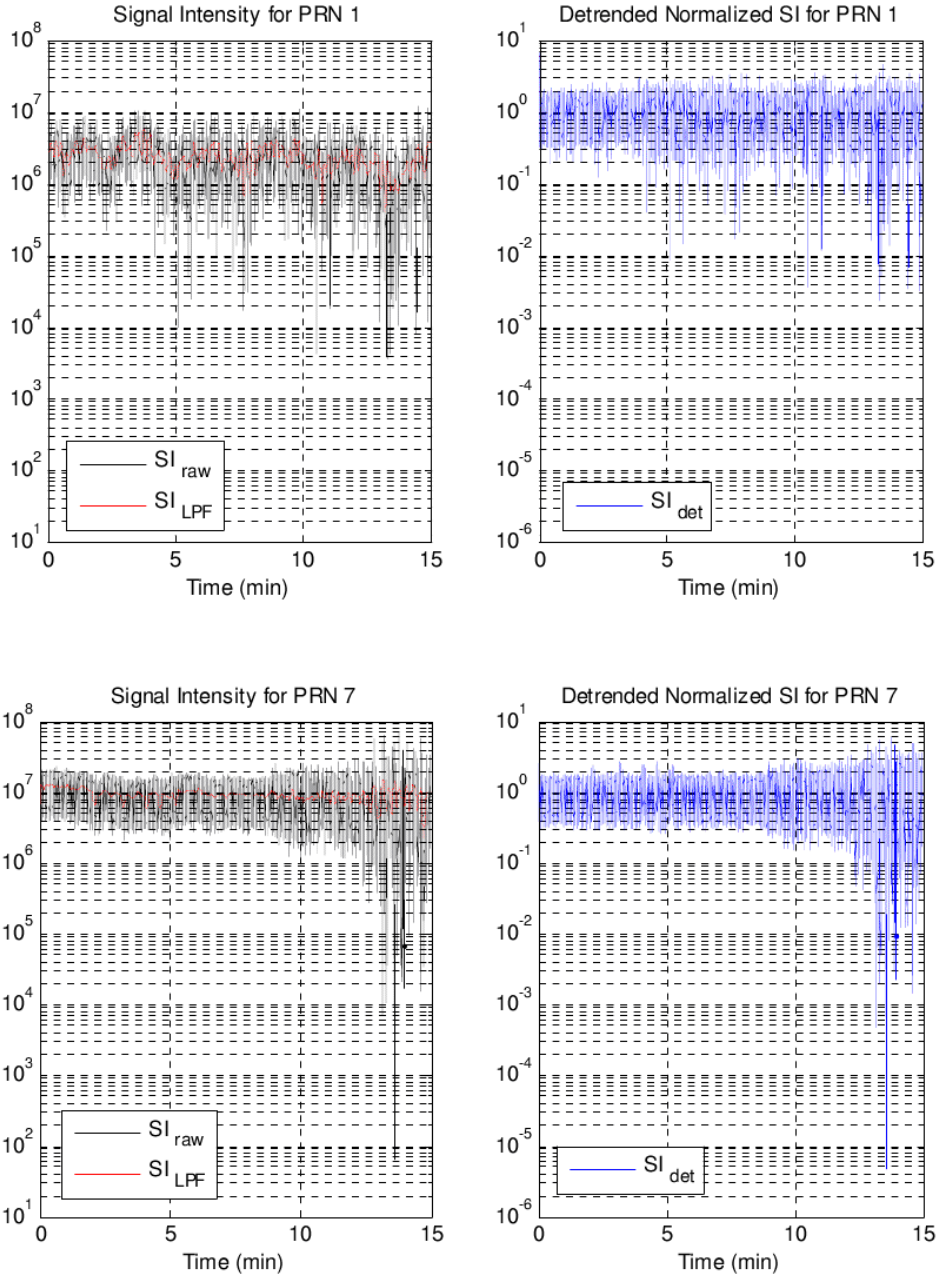

Figure 4.19: Raw and detrended signal intensity for PRN1 (top) and PRN7 (bottom) using a 6th-order low-pass Butterworth filter.

4.4.2 Eliminating the Effects of Ambient Noise

For given C/N_0 level, the intensity scintillation index due to ambient noise (S_{4N_0}) is given by [Van Dierendonck et al., 1993]

$$S_{4N_0} = \sqrt{\frac{100}{C/N_0}\left(1+\frac{500}{19\,C/N_0}\right)} \tag{4.32}$$

The clean (as opposed to noisy) S_4 values can be obtained by subtracting the square of S_{4N_0} from the square of detrended S_{4T} via [Van Dierendonck et al., 1993]

$$S_4 = \sqrt{\frac{\left\langle SI_{\text{det}}{}^2\right\rangle - \left\langle SI_{\text{det}}\right\rangle^2}{\left\langle SI_{\text{det}}\right\rangle^2} - \frac{100}{C/N_0}\left(1+\frac{500}{19\,C/N_0}\right)} \tag{4.33}$$

Using Equations (4.27) to (4.33), the intensity scintillation index S_4 before and after eliminating ambient noise is calculated and depicted in Figure 4.20 for the PRN1 (left panel), and PRN7 (right panel). The plots of detrended normalized signal intensity are repeated in Figure 4.20 as reference. As can be seen from the figure, the difference between the clean and the noisy S_4 is negligible for the PRN7 signal. This is due to its high level of C/N_0, which decreases the effect of ambient noise. For the PRN1 signal, the intensity scintillation index varies between 0.4 and 0.6 during the entire 15 minutes of tracking. This range of S_4 corresponds (mostly) to a moderate equatorial scintillation level. This is the same for the PRN7 signal during the first 12 minutes of tracking. Since then, the PRN7 S_4 value exceeds 0.6 and reaches the value of 1 nearly at the end of tracking. The S_4 values above 0.6 represent strong scintillation scenarios.

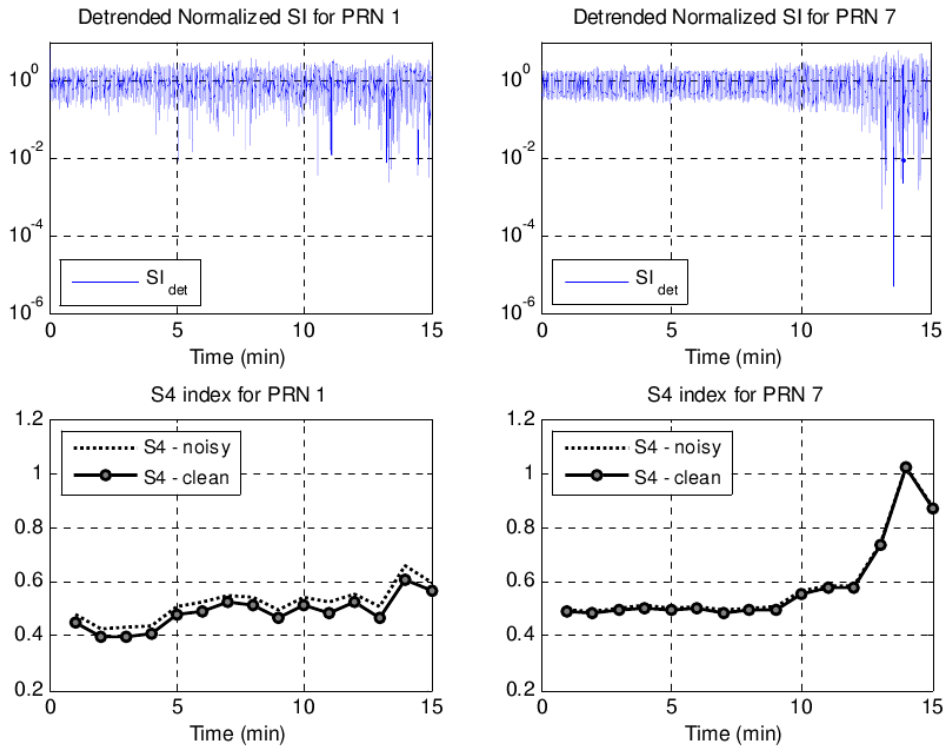

Figure 4.20: Intensity scintillation index before and after eliminating ambient noise for PRN1 (left) and PRN7 (right).

4.4.3 Detrending Carrier Phase

As with the signal intensity measurements, the GPS signal carrier phase measurements need to be detrended to remove the effects of integrated Doppler due to satellite-receiver motion, satellite/user clocks, and multipath. Typically, a 6th-order *high-pass* Butterworth filter with a 0.1 Hz cutoff frequency is used for filtering the 50 Hz phase measurements [cf. Van Dierendonck et al., 1993]. Applying this filter, the results of detrended carrier phase standard deviation (σ_ϕ), calculated in units of radians over 60-second intervals, are illustrated in Figure 4.21 for the PRN1 (left panel), and PRN7 (right panel).

For a weak phase scintillation activity, the carrier phase standard deviation normally ranges between 0.1 and 0.4 radians, while for a moderate to strong scintillation level, it ranges between 0.5 and 1. For the results shown below, the carrier phase standard deviation values are very low (i.e. $\sigma_\phi < 0.4$ rad) for both signals, indicating weak phase scintillation activities during the entire tracking process.

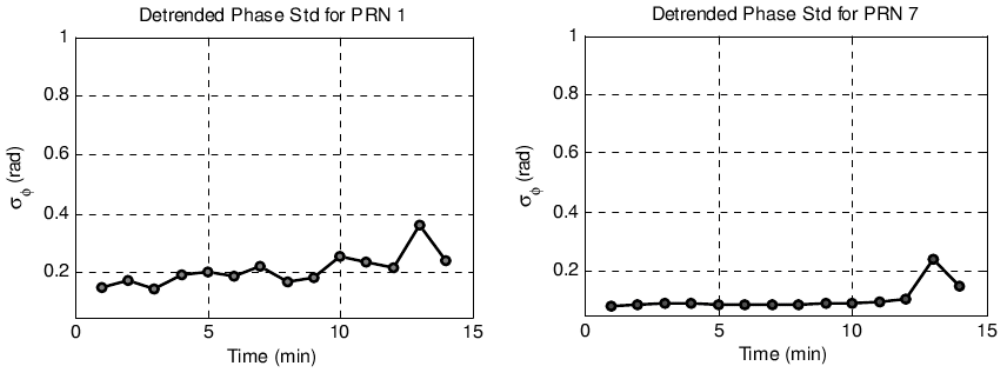

Figure 4.21: Carrier phase standard deviation for PRN1 (left), and PRN7 (right).

Due to uncertainties about the suitability of using σ_ϕ for characterizing phase scintillation [cf. Beach, 2006], the phase scintillation can be characterized instead using the phase spectrum strength (T_{scin}) at 1 Hz frequency, and the spectrum index (ν) above 0.1 Hz cutoff frequency. The plots shown in Figure 4.21 are used in the next section as references in phase scintillation power spectrum analysis only, but *not for characterizing the phase scintillation level.*

4.4.4 Power Spectrum Analysis

The spectral density function (SDF) of both phase and intensity scintillation follows an inverse power-law distribution of the form [see Chapter 2, Section 2.4.3]

$$\Phi(f) = \frac{T_{scin}}{(f_o^2 + f^2)^{\nu}} \tag{4.34}$$

Assuming $f >> f_0$ [Rino, 1979], the SDF can be approximated reasonably well by

$$\Phi(f) \approx \frac{T_{scin}}{f^{2\nu}} = \frac{T_{scin}}{f^{p}} \tag{4.35}$$

where f denotes the frequency of phase and intensity fluctuations in Hz, ν is the power spectral index, and $p = 2\nu$ denotes the power spectrum slope.

Considering the results of intensity scintillation index S_4 in Figure 4.20, and carrier phase standard deviation σ_ϕ in Figure 4.21, the last two minutes of data (i.e. 9:18 PM to 9:20 PM) represent the highest level of intensity and phase fluctuations in each plot. For this data segment, the intensity scintillation spectrum is calculated using the detrended normalized signal intensity, and the phase scintillation spectrum is computed using the detrended carrier phase measurements. For each signal, the resulting intensity scintillation power spectrum is plotted in Figure 4.22, and the phase scintillation power spectrum is depicted in Figure 4.23.

To obtain the spectrum parameters T_{scin} and ν, the power-law relationship given in Equation (4.35) needs to be linearized as follows [Zhang et al., 2010]:

$$10 \cdot \log_{10}\left(\Phi(f)\right) = 10 \cdot \log_{10}\left(T_{scin}\right) - 20\nu \cdot \log_{10}\left(f\right) \tag{4.36}$$

Selecting m data points from the linear section of power spectrum (the linear section is selected visually), the linearized power-law equation can be rearranged into the matrix format of

$$Z = XY \tag{4.37}$$

where

$$X = \begin{bmatrix} 1 & -20 \cdot \log_{10}(f_1) \\ 1 & -20 \cdot \log_{10}(f_2) \\ \dots & \dots \\ 1 & -20 \cdot \log_{10}(f_m) \end{bmatrix}$$

$$Y = \begin{bmatrix} 10 \cdot \log_{10}(T_{scin}) \\ \nu \end{bmatrix} \tag{4.38}$$

$$Z = \begin{bmatrix} 10 \cdot \log_{10}\left(\Phi(f_1)\right) \\ 10 \cdot \log_{10}\left(\Phi(f_2)\right) \\ \dots \\ 10 \cdot \log_{10}\left(\Phi(f_m)\right) \end{bmatrix}$$

The two unknowns T_{scin} and ν can therefore be obtained from the linear least square algorithm given below.

$$Y = \left(X^T X\right)^{-1} X^T Z. \tag{4.39}$$

Following this method, the linearly fitted power-law spectrum is calculated for the linear segment of power spectrum of each signal, and is depicted with a solid red line, along with the power spectrums, in Figure 4.22 and Figure 4.23.

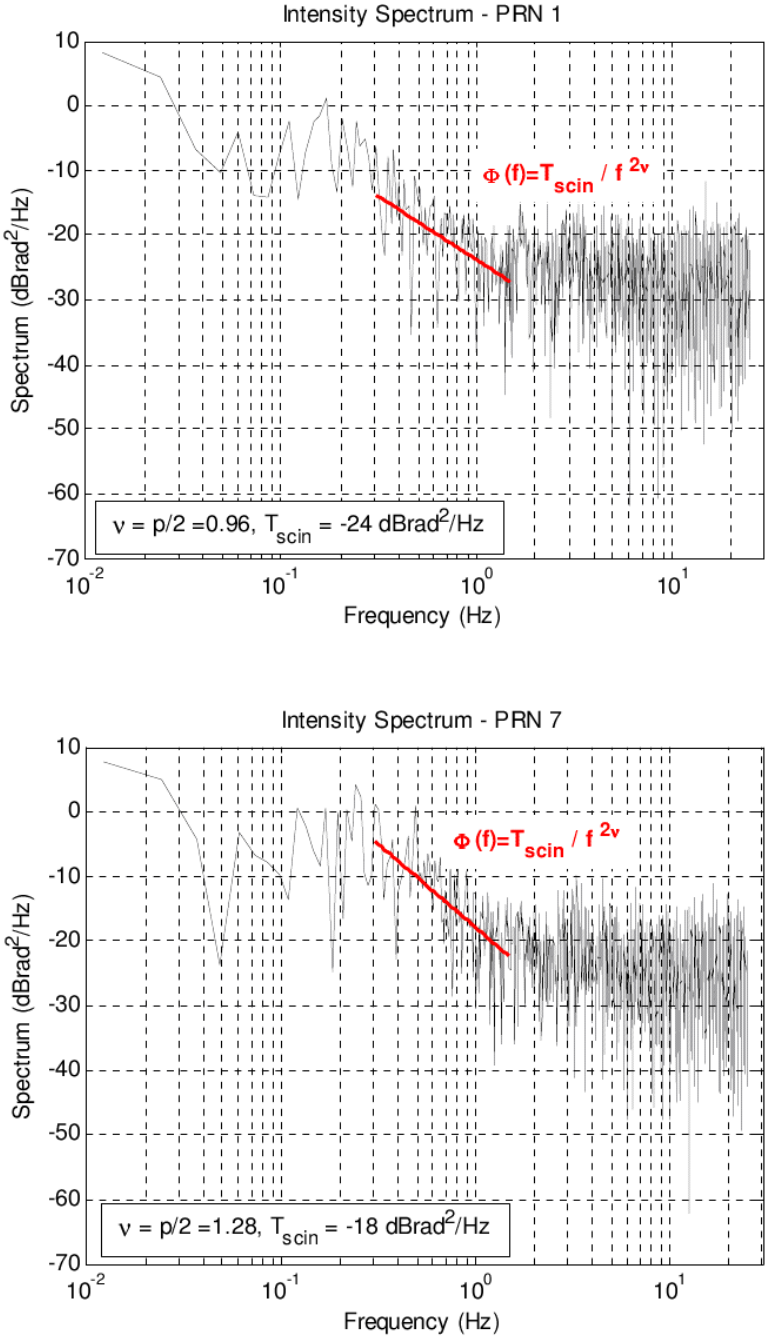

Figure 4.22: Intensity scintillation spectrum and power-law fitting (red line) for PRN1 (top), and PRN7 (bottom).

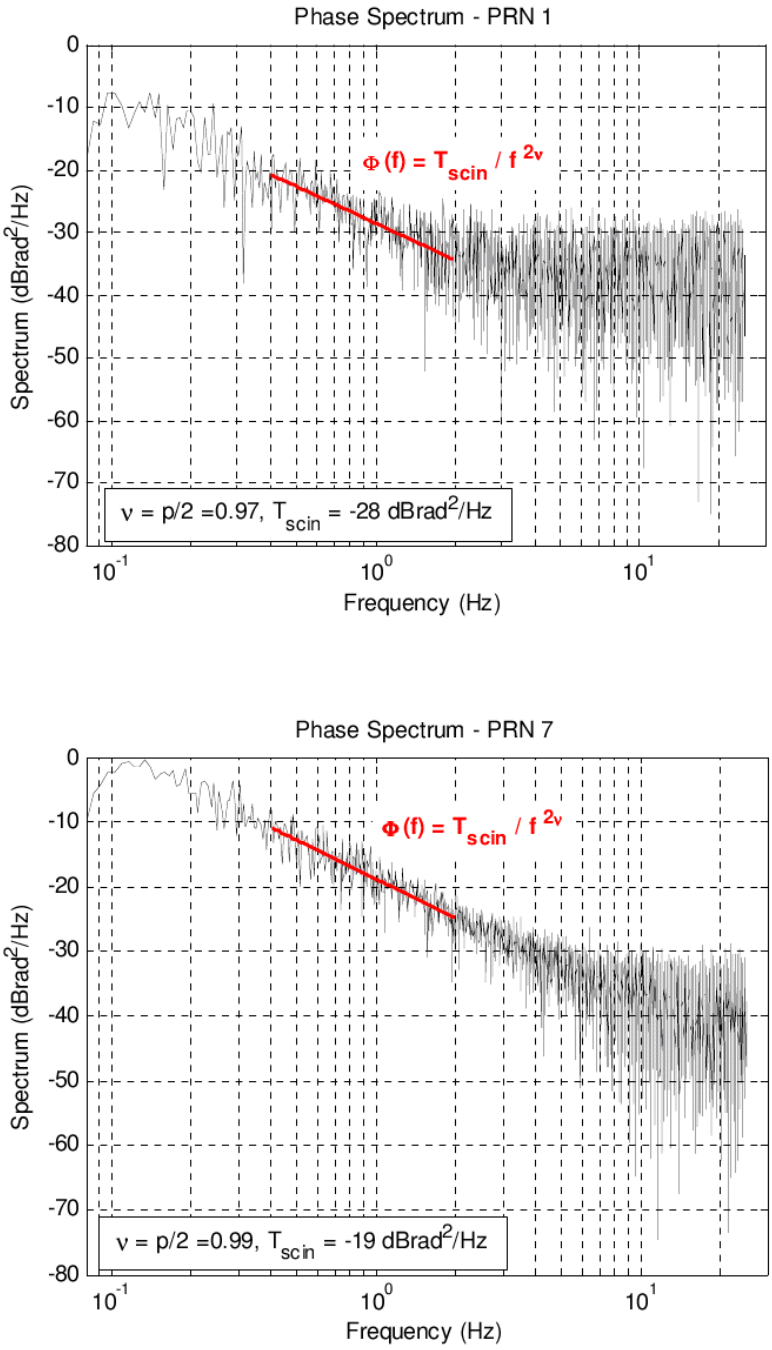

Figure 4.23: Phase scintillation spectrum and power-law fitting (red line) for PRN1 (top), and PRN7 (bottom).

Considering Figure 4.22, the strength of the *intensity spectrum* at 1 Hz frequency is found to be $T_{scin} = -24$ dBrad^2/Hz for the PRN1 signal, and $T_{scin} = -18$ dBrad^2/Hz for the PRN7 signal. In this context, a larger T_{scin} value is an indicator of a stronger scintillation activity. Consequently, the PRN7 signal experiences much stronger intensity scintillation (signal fading) during the last two minutes of tracking, compared with the PRN1 signal. The same conclusion can be drawn from the results of intensity scintillation index S_4 shown in Figure 4.20 where it specifies a higher intensity scintillation level for the PRN7, compared to the PRN1, during the last two minutes of tracking. The S_4 will be used hereafter for characterizing the intensity scintillation.

From the results illustrated in Figure 4.23, the strength of the *phase spectrum* at 1 Hz frequency is about $T_{scin} = -28$ dBrad^2/Hz for the PRN1 signal, and $T_{scin} = -19$ dBrad^2/Hz for the PRN7 signal. As with the intensity power spectrum, larger phase spectrum strength T_{scin} represents a stronger phase scintillation activity. Therefore, unlike the results of carrier phase standard deviation shown in Figure 4.21 (in which PRN1 is scintillated more than the PRN7), the results of phase scintillation power spectrum strength indicates that the PRN7 signal experiences a much stronger phase scintillation than the PRN1 signal. In this thesis, the *phase* spectrum strength T_{scin} is considered as an indicator for characterizing the phase scintillation level.

4.4.5 Simulation Model Evaluation

In this section, the results of processing *real scintillation data* for the PRN7 signal (i.e. the phase spectrum strength T_{scin} , and the spectrum index ν) shown in Figure 4.23 are used to evaluate the scintillation simulation algorithm. Accordingly, 3.5 seconds phase and intensity scintillation time histories are generated (see Figure 4.24) following the simulation algorithm introduced in Chapter two, assuming $\nu = 0.99$ and $C_s = 22 \times 10^{20}$. The subsequent simulated scintillation record has the phase spectrum strength of

$T_{scin} = -19$ dBrad^2/Hz, the spectrum index of $\nu = 0.99$, and the intensity scintillation index of $S_4 \geq 0.8$; all consistent with the results of processing real data shown in Figure 4.20 and Figure 4.23.

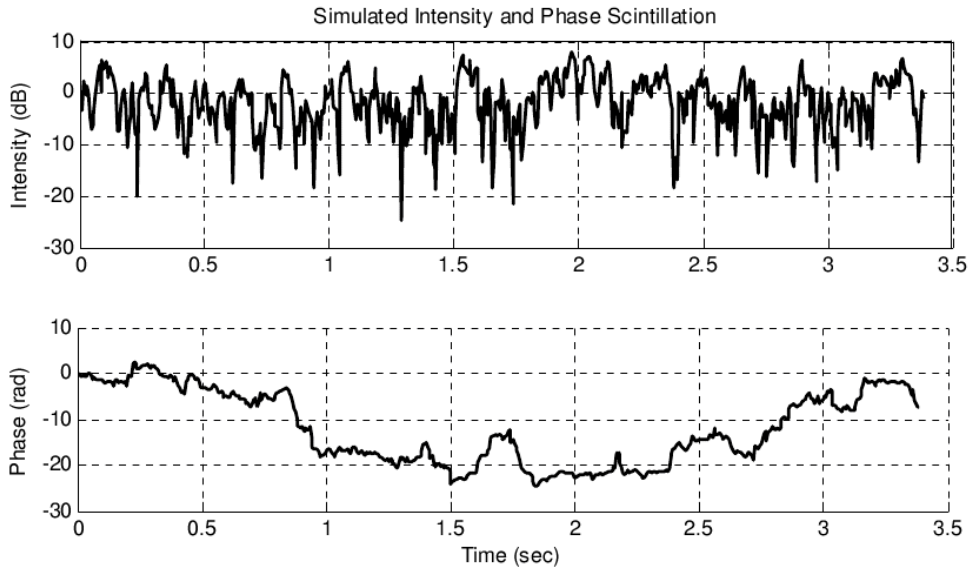

Figure 4.24: Intensity and phase scintillation realization using the scintillation simulator with $C_s = 22\times10^{20}$, $\nu = 0.99$, and the GPS L_1 as the propagating signal.

Next, an unperturbed GPS PRN7 signal (with $C/N_0 = 46$ dB-Hz) is generated using the signal simulator in Chapter three, and is scintillated through the complex modulation with the simulated intensity and phase scintillation data record shown in Figure 4.24. The simulated GPS signal - before and after adding scintillation effects - is processed in the receiver tracking loop simulators (with $B_n = 15$ Hz, and $\eta = 1$ ms), and the corresponding results (here, the carrier tracking error) are displayed in Figure 4.25. The upper frame shows the carrier tracking loop phase discriminator output in units of cycle, and the lower frame displays the phase error standard deviation, which is calculated continuously using

a 100 ms moving window. In each frame, the first 2.5 seconds corresponds to the results of processing the unperturbed GPS signal, and the last 2.5 seconds is for the scintillated signal. As can be seen from the figure, in the absence of scintillation (labeled as *quiet region* in Figure 4.25), the average phase error standard deviation is about 0.03 cycles (~ 11 degrees), which is below the typical tracking threshold of 15 degrees. This value increases to about 0.08 cycles (~ 30 degrees) in the presence of scintillation (labeled as *active region* in Figure 4.25), which is above the tracking threshold. For the results shown in Figure 4.25, considering the tracking threshold of 15 degrees (0.0417 cycles), the tracking error is measured to exceed the threshold level for nearly 53 percent of the time in the active region. This number is negligible for the quiet region.

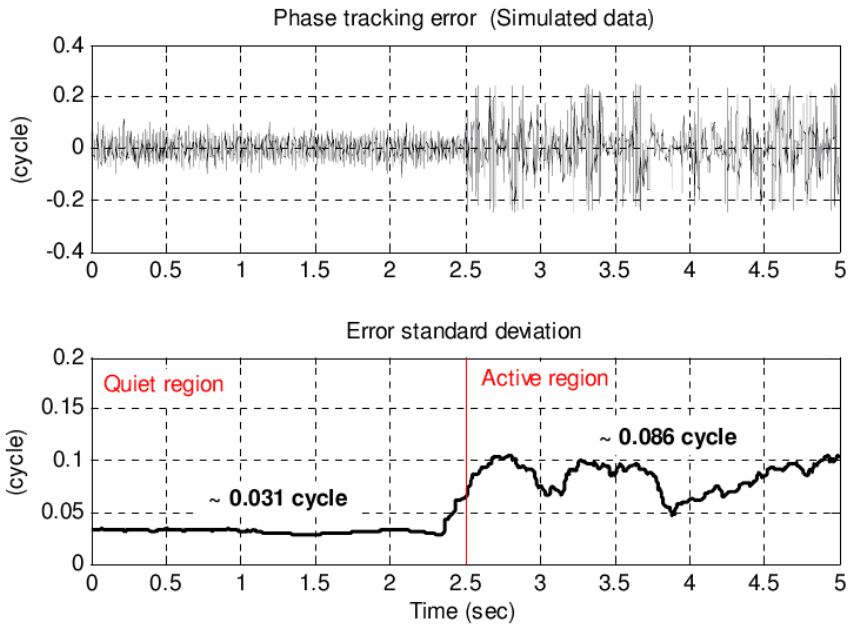

Figure 4.25: Carrier phase tracking error, and phase error standard deviation for simulated data in the absence (quiet region) and presence of scintillation (active region).

Considering the results of PLL-generated C/N_0 in Figure 4.18, the PRN7 signal experiences no scintillation or a very low level during the first 8 minutes of signal tracking, while experiences a very strong scintillation with nearly 30 dB fading after about 12 minutes. For 2.5 seconds of *real data*, selected arbitrarily from the quiet scintillation region, and another 2.5 seconds of real data selected from the scintillated region (for which the results of phase spectrum is illustrated in Figure 4.23), the results of carrier phase tracking error and carrier error standard deviation is shown in Figure 4.26. For the data segment taken from the quiet region, the average phase error standard deviation is about 0.024 cycles (~ 8.6 degrees), while for the active region, this number increase to about 0.079 cycles (~ 28.5 degrees) and exceeds the threshold. For the results shown below, the tracking error is measured to exceed the threshold level nearly 53 percent of the time in the active region, which is very similar to the result obtained from the simulated data in Figure 4.25.

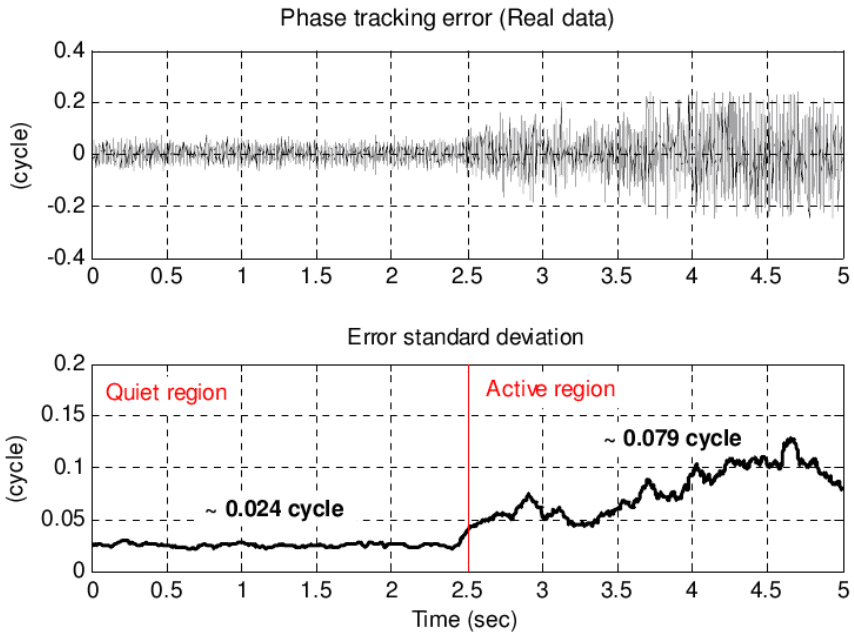

Figure 4.26: Carrier phase tracking error, and phase error standard deviation for real data in the absence (quiet region) and presence of scintillation (active region).

The comparison between the results of processing synthetic scintillation data (Figure 4.25) and those obtained from processing real data (Figure 4.26) confirms the effectiveness of the scintillation simulation algorithm in generating real-world-like scintillation time histories. In other words, the simulation model is capable of capturing the characteristics of the real-world processes in generating scintillation parameters, as their subsequent scintillated data exhibits similar stochastic behaviors, including similar power-law features, variance/standard deviation, and probabilities (here, probability of loss of lock).

The simulation model is used extensively in the next two chapters to generate different levels of phase and intensity scintillation.

Chapter Five: Modeling the Impact of Scintillation on Carrier Phase and Carrier Velocity Errors

Among various environmental factors, the disturbed ionosphere and associated ionospheric scintillations are known to significantly affect the performance of the Global Positioning System (GPS). The small scale time-varying irregularities within the ionosphere cause rapid random variations (scintillation) in the phase and amplitude of the received GPS signals. Ionospheric phase and intensity scintillations can affect GPS receivers at the tracking loop stage. Phase scintillation induces a frequency shift in the received signal carrier wave. When frequency shift exceeds the phase locked loop bandwidth, the signal may be lost and need to be reacquired. Intensity scintillation can cause signals to fade. During severe fading conditions, the signal strength may drop almost entirely below the receiver lock threshold, and signal loss and cycle slips are encountered [Klobuchar, 1996].

Studying the impact of scintillation on the tracking loop performance is required due to an increasing dependence on satellite-based navigation and communication systems in today's society, which are susceptible to ionospheric disturbances and scintillation. Besides, determining the accuracy and reliability of GPS receivers and predicting their behavior under extreme ionospheric conditions are becoming more important in the years preceding the solar maximum of 2013, as it is expected that both the frequency and severity of scintillation activity will significantly increase.

To accomplish this, in the current chapter, ionospheric scintillation effects on the GPS receiver carrier tracking loop performance are investigated, and quantified by defining two receiver performance measures (here, the carrier phase error and carrier velocity error), as a function of scintillation parameters T_{scin}, ν and S_4. Moreover, the amplitude and phase scintillation thresholds, beyond which the carrier tracking loop is expected to lose lock, or the carrier velocity error is expected to exceed a preset level are determined.

To reach these objectives, two methodologies are implemented as shown in Figure 5.1. Referring to the simulation sections in Chapters two to four, a physics-based simulation of low-latitude scintillation has been employed as a means of providing a variety of test cases for the simulated carrier tracking loop. In parallel, a widely used stochastic model of scintillation activity [Knight and Finn, 1998; Conker et al., 2003; Rino, 2011] is combined with a Costas-type carrier tracking loop model in order to produce a collection of receiver performance measures. Simulation results are used to validate theoretical predictions. Results presented in this chapter demonstrate the capabilities and potential of employing such tools to investigate GPS receiver performance under scintillation conditions.

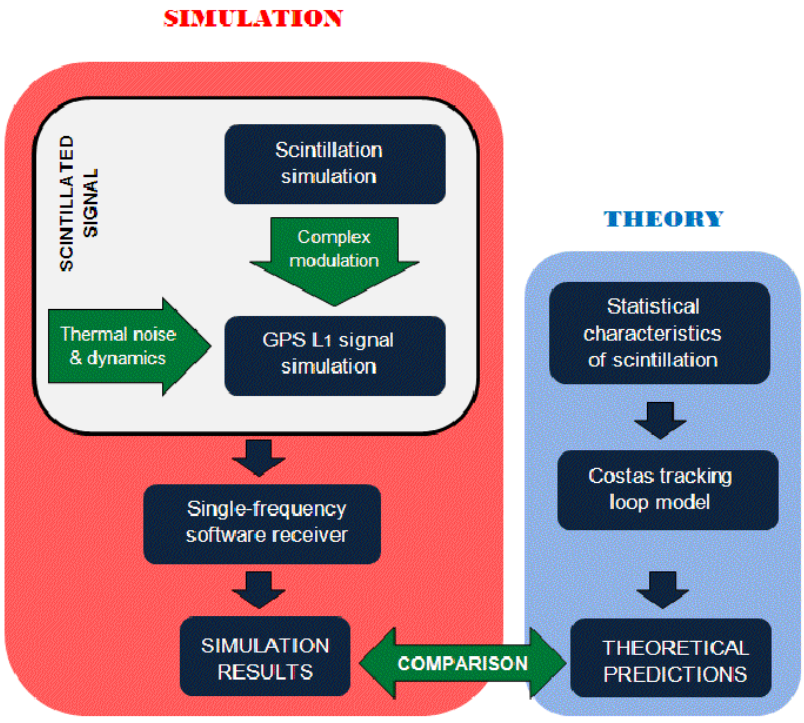

Figure 5.1: Simulation methodology.

5.1 Simulated Scintillation Time Histories

To study the performance of a generic GPS receiver carrier tracking loop in the presence of ionospheric irregularities, a number of ionospheric scintillation realizations are simulated in this work using the scintillation simulator described in Chapter two.

Following the simulation procedure given in Section 2.5, the signal transmitter is chosen to be the GPS satellite PRN3, for which the TLE corresponding to July 28, 2009 is provided as input to the simulator. A virtual ground station is considered in the equatorial region at 15°N, -51°E and 48 m, and a single phase screen is assumed at 350 km altitude. For the spectral index $\nu = 4/3 \approx 1.33$ (a common value for the equatorial region [Rino, 2011]), and the turbulent strength $C_s = 10^n$ with $n = 17, ..., 21$, different sets of phase and intensity scintillation time histories are generated. For each set of data, the magnitude of phase scintillation power spectral density T_{scin} (in rad^2/Hz), and intensity scintillation index (S_4) are determined using Equations (2.60) and (2.35), respectively. The geometric and anisotropy corrections are applied in the calculation of S_4 index, as described in Appendix V.

The ionospheric scintillation parameters T_{scin} and S_4 are used in this work as indicators of phase and intensity scintillation strength, respectively. In order to provide general information about different levels of scintillation activity, the results of seven simulated scintillation time histories corresponding to weak, moderate and severe scintillation levels are given in Table 5.1. As shown in the table, the scintillation levels are classified in three categories:

- Weak scintillation, where $T_{scin} \le -30$ dBrad^2/Hz and $S_4 \le 0.5$,
- Moderate to strong scintillation, where $-30 < T_{scin} \le -20$ dBrad^2/Hz and $0.5 < S_4 \le 0.85$,
- Severe scintillation, where $T_{scin} > -20$ dBrad^2/Hz and $S_4 > 0.85$.

Table 5.1: Different examples of simulated scintillation levels assuming v = 4/3. For each level of turbulent strength, the corresponding T_{scin} and S_4 are provided.

Scintillation Parameters	Scintillation Level						
	Weak			Moderate to Strong		Severe	
Turbulent strength (C_s)	5×10^{17}	25×10^{17}	5×10^{18}	25×10^{18}	5×10^{19}	25×10^{19}	5×10^{20}
Magnitude of phase scintillation spectrum (T_{scin}) in dBrad^2/Hz	-45	-38	-35	-28	-25	-18	-15
Intensity scintillation index (S_4)	0.08	0.17	0.24	0.52	0.75	> 0.85	

Among the examples listed in Table 5.1, three sets of simulated phase and intensity scintillation time histories, corresponding to T_{scin} = -38, -28 and -18 dBrad^2/Hz, are shown in Figure 5.2, from top to bottom. Each phase/intensity scintillation data set is then modulated on the simulated GPS signal, through the complex modulation technique, and processed in the software receiver.

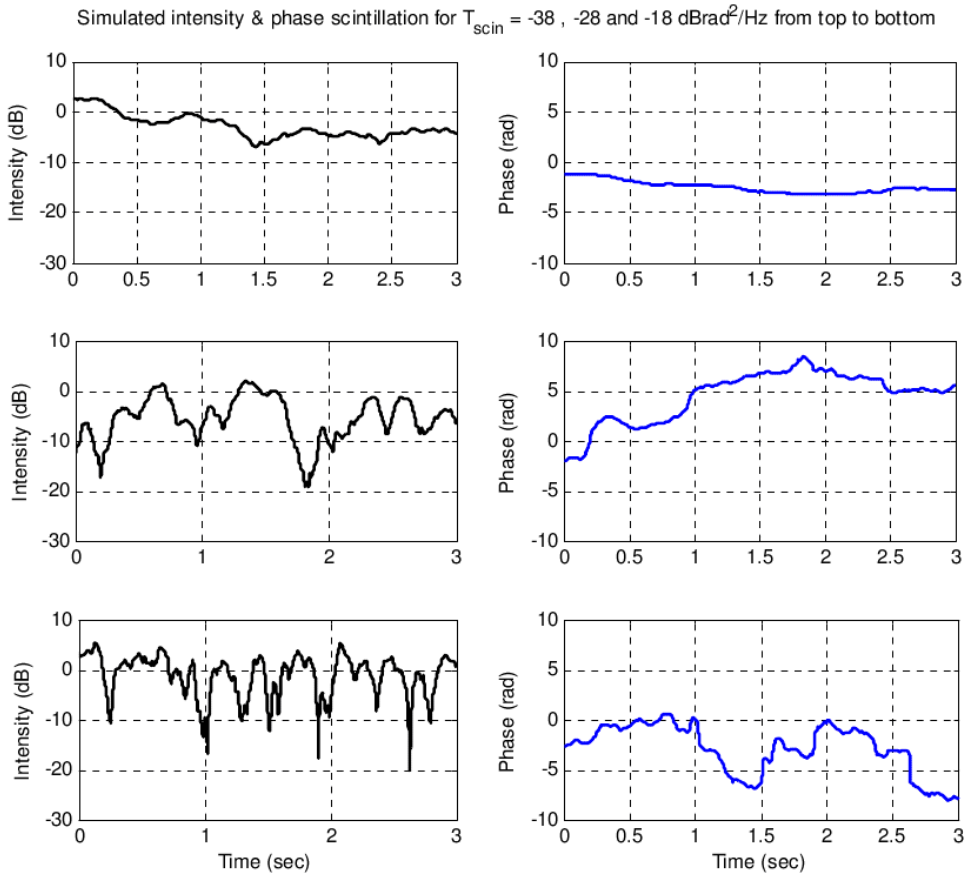

Figure 5.2: Three examples of the simulated intensity and phase scintillation data set corresponding to weak, moderate and severe scintillation from top to bottom.

5.2 Tracking Loop Model

The carrier phase tracking error variance is often considered as an indicator of receiver performance. To calculate the error variance in the presence of thermal noise, ionospheric scintillation, receiver oscillator noise, and system dynamics, the feedback control system previously shown in Figure 4.4 is employed. According to this diagram, the closed loop transfer function that gives the estimate $\hat{\Theta}(s)$ as a function of the input $\Theta(s)$ is expressed by

$$H(s) = \frac{\hat{\Theta}(s)}{\Theta(s)} = \frac{F(s)G(s)}{1 + F(s)G(s)} \tag{5.1}$$

By defining the tracking loop error as $\Theta_e(s) = \Theta(s) - \hat{\Theta}(s)$, and using Equation (5.1), the closed loop transfer function that relates the loop error $\Theta_e(s)$ to the input $\Theta(s)$ can be obtained via

$$\frac{\Theta_e(s)}{\Theta(s)} = 1 - H(s) \tag{5.2}$$

Based on Equation (5.2), the feedback control system is rearranged in Figure 5.3 so that the phase error $\theta_e(t)$ would be the tracking loop output. In this model, $\theta(t)$ denotes the total phase entering the loop, and $\hat{\theta}(t)$ denotes the loop's best estimate of $\theta(t)$. The closed loop transfer function model in Figure 5.3 is used throughout this chapter to derive different tracking loop expressions as a function of scintillation parameters.

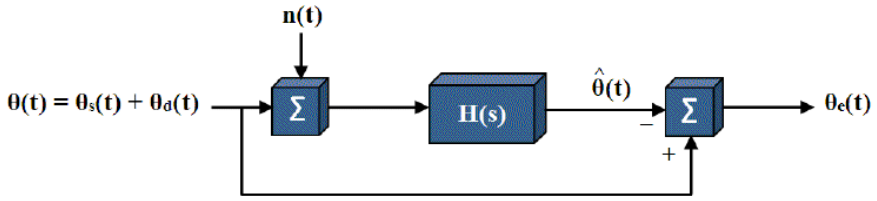

Figure 5.3: Closed loop transfer function model of a phase locked loop (PLL).

5.3 Phase Tracking Error Variance

The normalized intermediate frequency (IF) signal entering the carrier tracking loop can be represented by

$$S(t) = X(t-\tau(t))\,D(t-\tau(t))\cos\left(\omega_{IF}t+\theta(t)\right)+n(t) \tag{5.3}$$

where X and D are the satellite PRN code and navigation message, respectively, $\tau(t)$ is the code delay, ω_{IF} is the carrier intermediate frequency, $\theta(t)=\theta_d(t)+\theta_o(t)$ is the carrier phase perturbation due to the effects of satellite-platform dynamics $\theta_d(t)$ and the oscillator phase noise $\theta_o(t)$, and $n(t)$ is stationary zero-mean Gaussian thermal noise.

The effect of scintillation is modeled as a *complex modulation* of the GPS signal where scintillation is shown as $\sqrt{I_s(t)}\,\exp\{j\theta_s(t)\}$ with $I_s(t)$ and $\theta_s(t)$ being the intensity and phase scintillation processes, respectively (see Section 2.5.7 for details). Based on this model, the IF signal in Equation (5.3), including scintillation, can be expressed as

$$S(t) \;= \sqrt{I_s(t)}\;X(t-\tau(t))\,D(t-\tau(t))\;\cos(\omega_{IF}t+\theta(t))\;+n(t) \tag{5.4}$$

whose carrier phase perturbation

$$\theta(t)=\theta_d(t)+\theta_o(t)+\theta_s(t) \tag{5.5}$$

now represents the effect of system dynamics, oscillator noise, and phase scintillations.

Considering the PLL closed loop transfer function model of Figure 5.3, and assuming the principal sources of *phase error* as thermal noise, ionospheric scintillations, system dynamics and oscillator noise, the phase tracking mean square error would be

$$\left\langle \theta_e^2 \right\rangle = \left\langle \theta_n^2 \right\rangle + \left\langle \theta_s^2 \right\rangle + \left\langle \theta_d^2 \right\rangle + \left\langle \theta_o^2 \right\rangle, \qquad (rad^2) \tag{5.6}$$

where $\left\langle \theta_n^2 \right\rangle$, $\left\langle \theta_s^2 \right\rangle$, $\left\langle \theta_d^2 \right\rangle$ and $\left\langle \theta_o^2 \right\rangle$ denote the mean square error components due to thermal noise, phase scintillation, system dynamics, and oscillator noise, respectively. To determine $\left\langle \theta_e^2 \right\rangle$, the effect of each source of error is studied first.

5.3.1 Thermal Noise Error

In this context, thermal noise is referred to the receiver internal noise generated by the random movement of free electrons in the electronic conductors [Langley, 1997]. In the tracking loop model of Figure 5.3, the effect of thermal noise is denoted as $n(t)$, and is assumed to have zero-mean Gaussian distribution. In the absence of signal fading resulting from intensity scintillation, the thermal noise mean square error (which is equal to its variance) is calculated from Equation (4.14):

$$\left\langle \theta_n^2 \right\rangle = \frac{B_n}{(c/n_0)}\left(1 + \frac{1}{2\eta(c/n_0)}\right), \qquad (rad^2) \tag{5.7}$$

where B_n is the carrier tracking loop noise bandwidth in Hz, η is the pre-detection integration time in seconds, and c/n_0 is the carrier-to-noise ratio value.

This equation is plotted in Figure 5.4 as a function of $C/N_0 = 10 \cdot \log_{10}(c/n_0)$, in dB-Hz, and loop noise bandwidth B_n. As can be seen from the figure, the effect of thermal noise is very high at low carrier-to-noise ratio levels and high bandwidths.

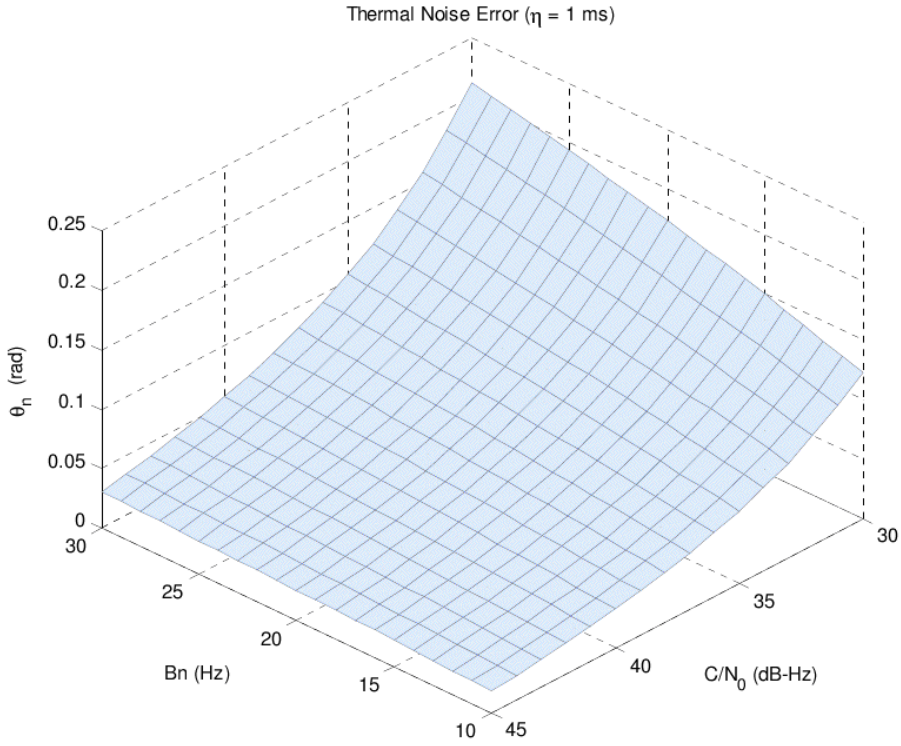

Figure 5.4: Thermal noise error in a Costas-type tracking loop.

Except for very low C/N_0, the choice of pre-detection integration time η does not significantly affect the thermal noise error. This is shown in Figure 5.5, where the error is plotted against the loop bandwidth for η = 1 ms and η = 20 ms at C/N_0= 30, 35 and 40 dB-Hz. At a very low C/N_0 level (e.g. 30 dB-Hz), a larger integration time (e.g. η = 20 ms) shows a slightly better error results. This is due to the fact that averaging the noisy I and Q samples over a longer time interval generally results in a smaller value, and the influence of noise is suppressed more effectively. On the other hand, a short pre-detection integration time is usually preferred over a long one, as it allows faster signal processing, which is also an important factor in the receiver design. For all the simulation results presented in this thesis, the pre-detection integration time is set to 1 ms.

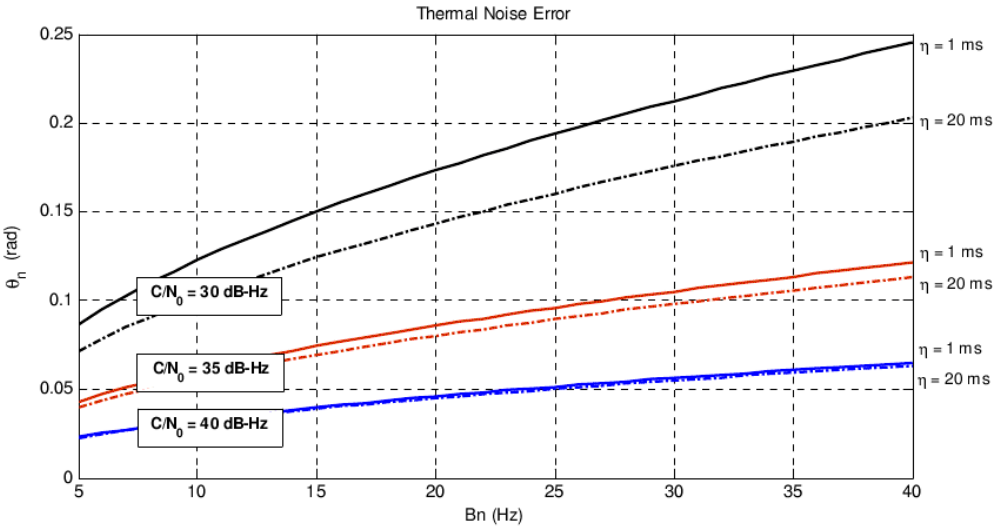

Figure 5.5: Thermal noise error at different pre-detection integration times.

5.3.2 Phase Scintillation Error

Phase scintillation, produced by ionospheric irregularities, induces a frequency shift in the received signal carrier wave. This will be troublesome if the shift goes beyond the phase locked loop bandwidth. Using the tracking loop model of Figure 5.3, the phase scintillation mean square error $\left\langle \theta_s^2 \right\rangle$ can be expressed via [Conker et al., 2003]

$$\left\langle \theta_s^2 \right\rangle = \int_{-\infty}^{\infty} \Phi_{\theta_S}(f)\,|1-H(f)|^2\,df\,, \qquad (rad^2) \tag{5.8}$$

where $\Phi_{\theta_S}(f)$ is the SDF of the phase scintillation, and $H(f)$ is the loop transfer function. From Table 4.3, the general form of the loop transfer function is calculated as (see Appendix III for details)

$$|H(f)|^2 = \frac{{f_n}^{2\beta}}{({f^{2\beta} + {f_n}^{2\beta}})}\left[1+(2\beta-2)\left(\frac{f}{f_n}\right)^{(2\beta-2)}\right] \tag{5.9}$$

$$\left|1-H(f)\right|^2 = \frac{f^{2\beta}}{f^{2\beta}+f_n^{2\beta}} \tag{5.10}$$

where $f_n = \omega_n / 2\pi$ is the loop natural frequency in Hz, and β is the loop order.

By substituting $\left|1-H(f)\right|^2$ from Equation (5.10), and $\Phi_{\theta_s}(f)$ from Equation (2.58) in Equation (5.8), the phase scintillation component of the tracking mean square error can be expressed as

$$\left\langle \theta_s^2 \right\rangle = \int_{-\infty}^{\infty} \left(\frac{T_{scin}}{(f_o^2 + f^2)^{\nu}} \cdot \frac{f^{2\beta}}{f^{2\beta}+f_n^{2\beta}} \right) df. \tag{5.11}$$

The phase scintillation transfer function $1-H(f) = \sqrt{f^{2\beta}/(f^{2\beta}+f_n^{2\beta})}$ is plotted in Figure 5.6 for three loop orders ($\beta = 1$, 2 and 3). It is evident from the figure that the transfer function is a high pass filter to the frequency components of the phase scintillation SDF. Therefore, a low frequency component such as f_0, which is much smaller than the loop natural frequency f_n, can be neglected in the above equation[11].

---

[11] *For a typical loop bandwidth B_n=15 Hz, and damping factor ζ=0.707, the loop natural frequency (f_n) is equal to 9.54, 4.5 and 2.86 Hz, respectively, for the first-, second-, and third-order loop, while f_0 typically changes in the range of 0.01 to 0.1 Hz.*

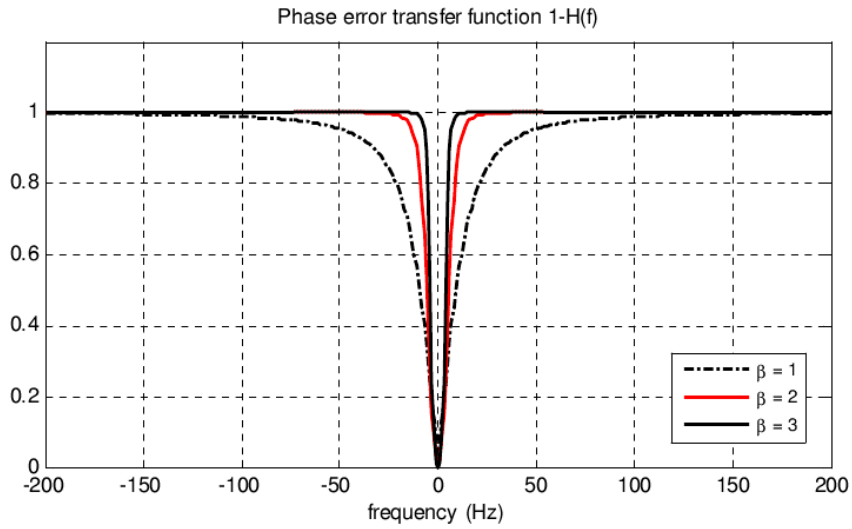

Figure 5.6: PLL transfer function for the phase scintillation power spectrum.

As a result, Equation (5.11) can be approximated reasonably well by

$$\left\langle \theta_s^2 \right\rangle \approx \int_{-\infty}^{\infty} \left(\frac{T_{scin}}{f^{2\nu}} \cdot \frac{f^{2\beta}}{f^{2\beta} + f_n^{2\beta}} \right) df . \tag{5.12}$$

From table of integrals:

$$\int_0^{\infty} \frac{x^m}{(x^n + a^n)}\, dx = \frac{\pi}{n} a^{m+1-n} \csc\left(\frac{\pi(m+1)}{n}\right), \qquad 0 < m+1 < n \tag{5.13}$$

Following Equation (5.13), the phase scintillation mean square error in Equation (5.12) is calculated as

$$\begin{aligned}\left\langle \theta_s^2 \right\rangle &\approx T_{scin} \int_{-\infty}^{\infty} \left(\frac{f^{2(\beta-\nu)}}{f^{2\beta} + f_n^{2\beta}} \right) df \\ &\approx T_{scin} \frac{\pi}{\beta} f_n^{1-2\nu} \csc\left(\frac{\pi(\nu - 0.5)}{\beta} \right), \qquad (rad^2)\end{aligned} \tag{5.14}$$

where ν is the phase scintillation power spectral index, and T_{scin} is the magnitude of the phase scintillation power spectrum in rad^2/Hz.

Phase scintillation carrier tracking error in Equation (5.14) is plotted in Figure 5.7 as a function of loop bandwidth assuming ν=1.33, β=2 and T_{scin}= -35, -25 and -15 dBrad^2/Hz. As expected, larger phase scintillation errors correspond to higher levels of scintillation strength. For example, at $B_n = 10$ Hz the tracking error is about 0.01, 0.03, and 0.09 radians for T_{scin} = -35, -25, and -15 dB, respectively. Moreover, the error rate is much higher at lower carrier tracking loop bandwidths (e.g. $B_n <$ 15 Hz). This indicates that although both phase scintillation and thermal noise are random-like processes, they behave opposite of one another at low noise bandwidths: for better phase scintillation performance, unlike thermal noise performance, higher bandwidth is of more interest.

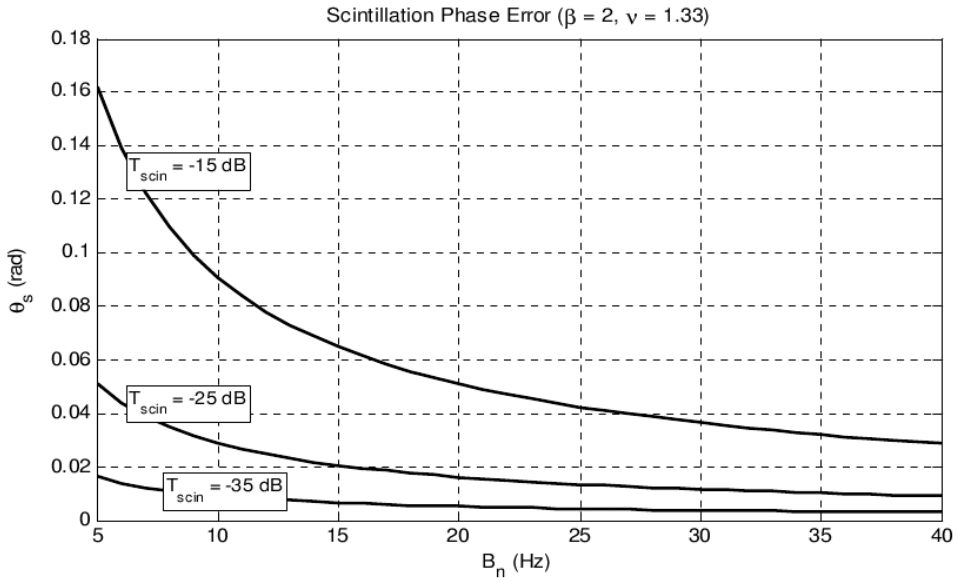

Figure 5.7: Phase scintillation carrier tracking error vs. loop noise bandwidth.

By adding Equations (5.7) and (5.14), the carrier phase tracking mean square error in the presence of *thermal noise* and *phase scintillations* is obtained as

$$\left\langle \theta_e^2 \right\rangle \approx \frac{B_n}{(c/n_0)}\left(1+\frac{1}{2\eta(c/n_0)}\right)+T_{scin}\,\frac{\pi}{\beta}\,f_n^{\,1-2\nu}\csc\left(\frac{\pi(\nu-0.5)}{\beta}\right), \qquad (rad^2) \qquad (5.15)$$

This equation provides useful information regarding the relation between scintillation spectral strength (T_{scin}), spectral index (ν), and loop noise bandwidth (B_n).

Theoretical predictions and simulation results are compared in Figure 5.8, where the phase tracking error is plotted with respect to the phase scintillation strength at different loop bandwidths.

To display the theoretical results, the following parameters are considered in Equation (5.15): $\beta = 2$, $C/N_0 = 50$ dB-Hz, $\eta = 1$ ms, $\nu = 1.33$ and $B_n = 5$, 10, 15 and 25 Hz.

To generate the simulation results, the scintillation simulator, the GPS signal simulator, and the tracking loop simulators (respectively given in Chapters two to four) are employed. In the signal simulator, the carrier-to-noise ratio is set to 50 dB-Hz, and in the 2nd-order tracking loop simulators, the pre-detection integration time is set to 1 ms, and the noise bandwidth is set to 5, 10, 15 and 25 Hz. As described in Section 5.1, by choosing $\nu = 4/3 \approx 1.33$ and different turbulent strength values (C_s) as input to the scintillation simulator, different realizations, corresponding to weak, moderate and severe scintillation levels are generated. For each realization, the power spectral strength (T_{scin}) is calculated using Equation (2.60). At the same time, the simulated phase and intensity scintillation time histories are modulated on a simulated GPS signal and the resulting scintillated signal is processed in the tracking loop simulators. At the end, the simulation results (here, the standard deviation of the carrier phase error) is measured and compared with the theory, for the same level of T_{scin}.

It can be seen from Figure 5.8 that for relatively high bandwidths (≥ 15 Hz), the simulation results closely follow the theory, while for $B_n = 5$ Hz (the highest solid curve in Figure 5.8), the result of simulation fails to follow the theory when scintillation level is relatively high. This can be explained as follows: during times of strong phase scintillation, the phase of the incoming radio frequency signal experiences large random fluctuations which can spread out the spectrum of the received signal over a large bandwidth. Accordingly, a narrow-bandwidth loop (e.g. $B_n = 5$ Hz) may lose phase lock due to lack of sufficient signal power within the specified bandwidth. Such a bandwidth, therefore, while beneficial for reducing noise, cannot accommodate the scintillation phase dynamics.

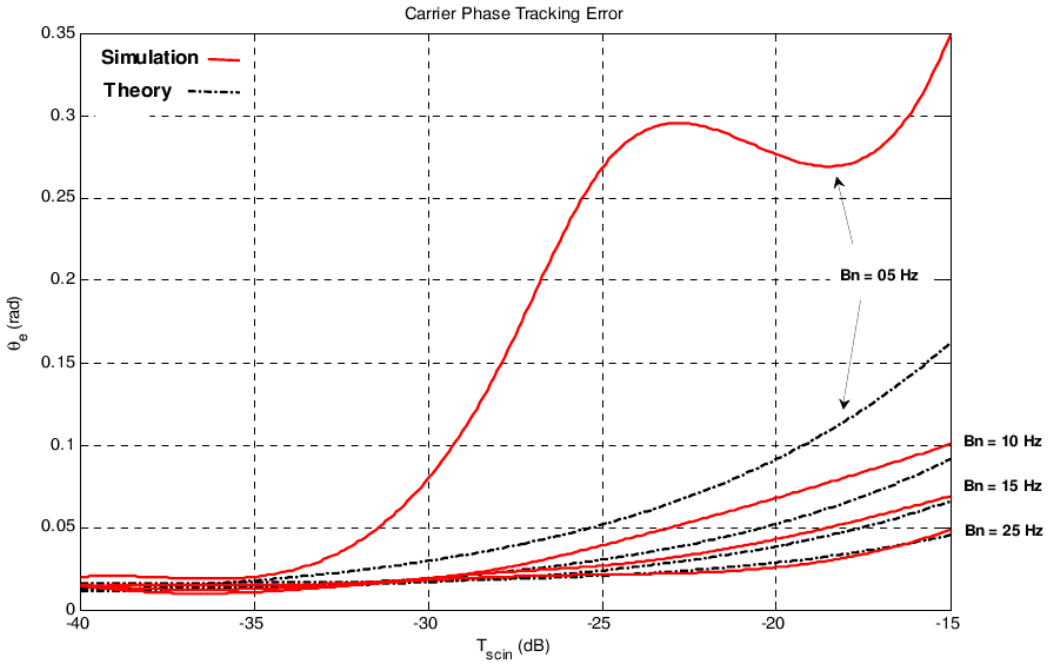

Figure 5.8: Carrier tracking error in the presence of phase scintillations and thermal noise.

From the rule of thumb, the one-sigma carrier phase error should not exceed $\pi/12 = 0.2618$ radians; otherwise, the loop is considered to lose lock [Jwo, 2001]. According to this, Equation (5.15) can be rearranged to obtain a *threshold level* for the phase scintillation spectral strength, beyond which the tracking loop is expected to lose phase lock. For the carrier tracking mean square error threshold $\left\langle \theta_e^2 \right\rangle_{threshold} = (\pi/12)^2$, the phase scintillation strength threshold is obtained via

$$T_{scin,TH} = \frac{\beta}{\pi} f_n^{\,2\nu-1} \sin\left(\frac{\pi(\nu-0.5)}{\beta}\right)\left[\left\langle \theta_e^2 \right\rangle_{threshold} - \frac{B_n}{(c/n_0)}\left(1+\frac{1}{2\eta(c/n_0)}\right)\right] \qquad (5.16)$$

The scintillation strength threshold is plotted in Figure 5.9 as a function of loop noise bandwidth for $\beta = 1$, 2 and 3, assuming $C/N_0 = 50$ dB-Hz and $\nu = 1.33$. As illustrated in the figure, the performance of the 2nd-, and 3rd-order loop are very similar, in the sense that for a specific loop bandwidth almost the same level of scintillation strength may result in loss of phase lock. The 1st-order loop, however, seems to be more susceptible as it can lose phase lock at much lower level of scintillation strength (e.g. about 6 to 7 dBrad^2/Hz lower) compared to the other two loop orders.

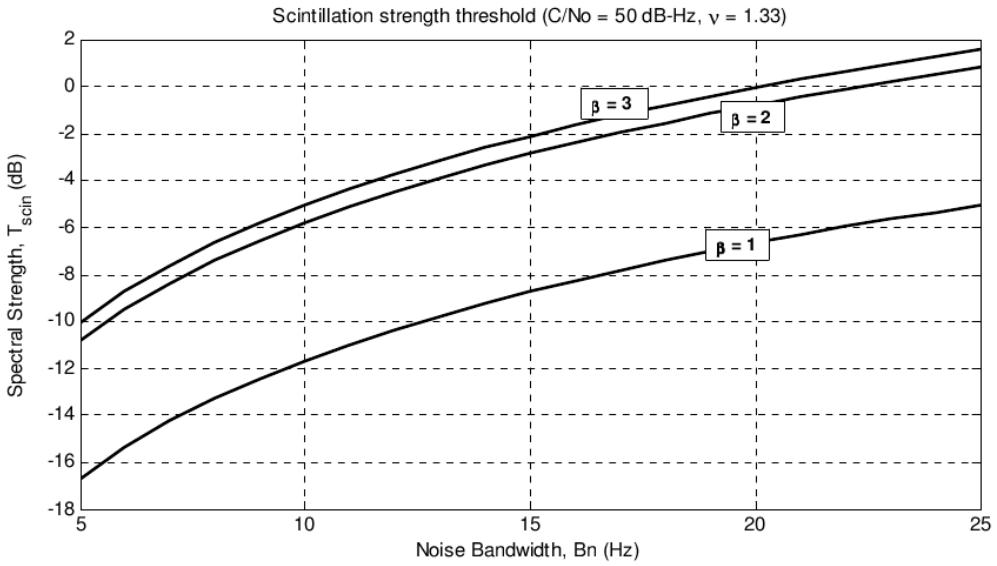

Figure 5.9: Scintillation strength threshold ($T_{scin,TH}$) as a function of loop noise bandwidth.

For B_n = 15 Hz, C/N_0 = 50 dB-Hz, η = 1 ms, and ζ = 0.707, scintillation strength threshold is plotted against spectral index ν in Figure 5.10. The scale-free spectral index usually varies in the range of 0.5 to 1.5 under normal to severe ionospheric conditions. For extremely severe conditions, it may even reach the value 2.5 [Rino, 2011]. It can be seen from Figure 5.10 that the 1st-order loop, unlike the 2nd-, and 3rd-order loops, fails to

maintain phase lock when $\nu \to 1.2$. In other words, the scintillation strength threshold, beyond which the tracking loop loses lock, decreases rapidly as ν exceeds the 1.2 value. Thus, for a receiver to be robust against severe scintillation impacts, especially in the equatorial regions with $\nu \approx 1.33$, a 1st-order loop would not be an appropriate choice.

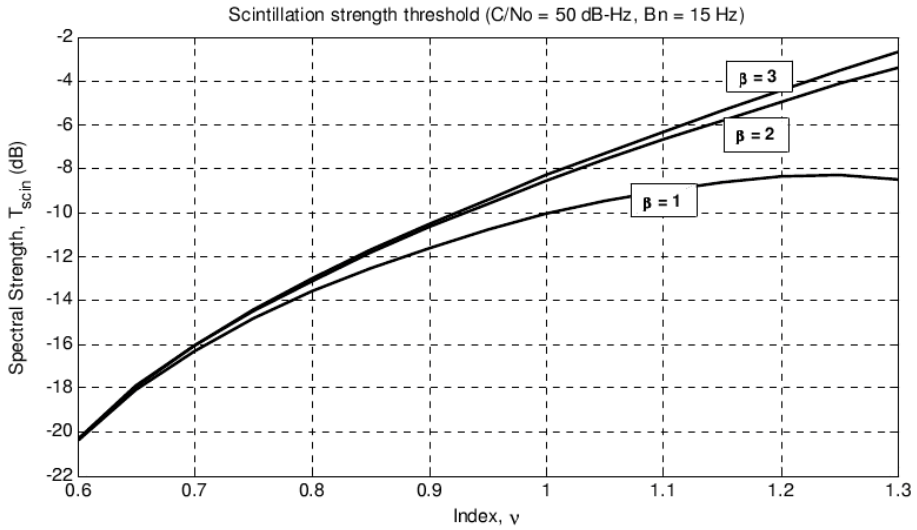

Figure 5.10: Scintillation strength threshold ($T_{scin,TH}$) as a function of spectral index (ν).

The previous two plots are combined in Figure 5.11 for the 2nd-order loop. It can be seen that better tracking loop performance is obtained under wider loop bandwidths; much higher scintillation strength is required to result in loss of phase lock. Comparing the results of this section with that of Section 4.2.3.1, one can observe that the ionospheric phase scintillation effect on the carrier tracking loop is more like the effect of system dynamics than the effect of measurement noise: for better phase scintillation and dynamic performance, the tracking loop requires a wide bandwidth, whereas for better noise performance, a narrow bandwidth performs better.

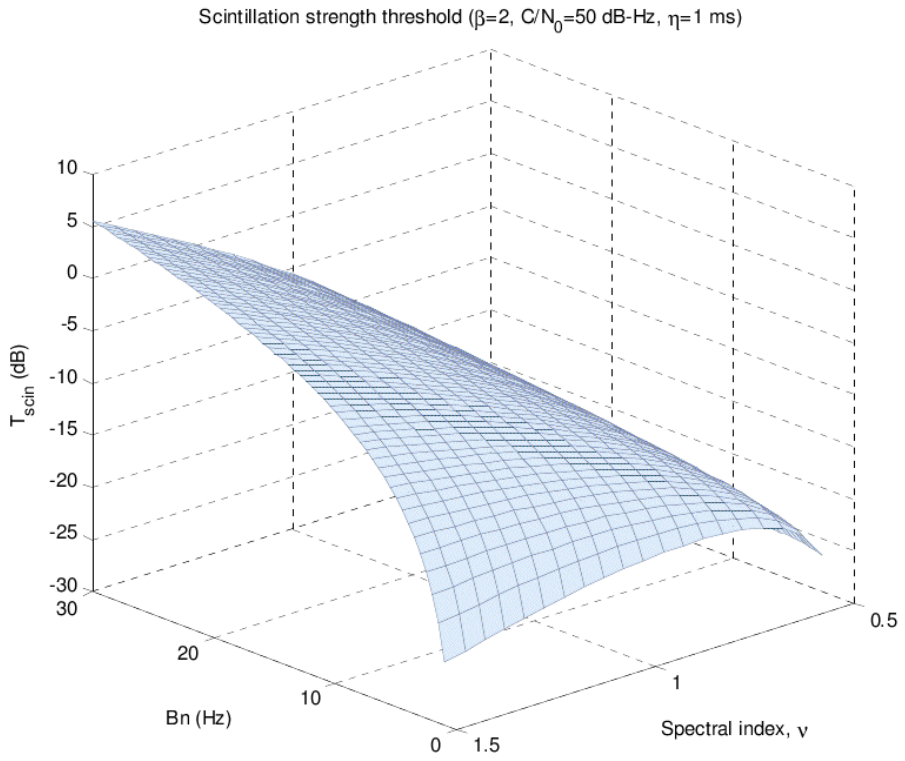

Figure 5.11: Phase scintillation strength threshold for the 2nd-order phase locked loop.

5.3.3 Intensity Scintillation Error

In the absence of signal fading resulting from ionospheric intensity scintillation, the standard thermal noise mean square error is defined according to Equation (5.7). Intensity scintillation I_s can significantly alter the C/N_0 level, thus increasing the thermal noise error. The C/N_0 degradation at receiver level can be expressed as

$$c/n = I_s \cdot c/n_0 \tag{5.17}$$

or in decibel form

$$C/N = (I_s)_{dB} + C/N_0 \tag{5.18}$$

Consequently, $(I_s)_{dB} = 0\,\text{dB}$ is equal to $I_s = 1$ in Equation (5.17), denoting no intensity scintillation effects. Considering the effect of signal fading, Equation (5.7) is changed to

$$\begin{aligned} \left\langle \theta_n^2 \right\rangle &= \frac{B_n}{I_s \cdot (c/n_0)} \left(1 + \frac{1}{2\eta I_s \cdot (c/n_0)} \right) \\ &= \frac{B_n}{(c/n_0)} \left(\frac{1}{I_s} + \frac{1}{2\eta I_s^2 \cdot (c/n_0)} \right), \qquad (rad^2) \end{aligned} \tag{5.19}$$

According to this expression, the thermal noise mean square error is inversely proportional to the scintillation intensity. Thus, for I_s below a certain value, the noise variance can exceed the tracking lock threshold. The strength of scintillation activity is generally measured through the intensity scintillation index $S_4 = \sqrt{\left\langle I_s^2 \right\rangle - \left\langle I_s \right\rangle^2} \Big/ \left\langle I_s \right\rangle$ with $\left\langle I_s \right\rangle$ being the *average* intensity of signal. The S_4 index is used in this section to derive an expression for the carrier phase error variance, when the loop is subject to thermal noise and intensity scintillation.

Using Equation (5.19), the *average* phase tracking mean square error can be shown as

$$\begin{aligned} \left\langle \theta_n^2 \right\rangle_{ave} &= \int_0^\infty \left\langle \theta_n^2 \right\rangle \cdot p(I_s)\ dI_s \\ &= \int_0^\infty \left(\frac{B_n}{(c/n_0) \cdot I_s} + \frac{B_n}{2\eta I_s^2 \cdot (c/n_0)^2} \right) \cdot p(I_s)\ dI_s \\ &= \underbrace{\frac{B_n}{(c/n_0)} \int_0^\infty \frac{p(I_s)}{I_s}\, dI_s}_{Integration\ I} + \underbrace{\frac{B_n}{2\eta \cdot (c/n_0)^2} \int_0^\infty \frac{p(I_s)}{I_s^2}\, dI_s}_{Integration\ II} \end{aligned} \tag{5.20}$$

where $p(I_s)$ represents the intensity scintillation pdf, and is given in Equation (2.32).

Ionospheric intensity scintillation is assumed to follow the Nakagami-m distribution with $\langle I_s \rangle = 1$ [Hegarty et al., 2001]. Substituting $p(I_s)$ from Equation (2.32) in (5.20) results in

Integration I :

$$\begin{aligned} \frac{B_n}{(c/n_0)} \int_0^\infty \frac{p(I_s)}{I_s}\, dI_s &= \frac{B_n\ u^u}{(c/n_0)\ \ \Gamma(u)} \int_0^\infty I_s^{u-2}\, e^{-uI_s}\, dI_s \\ &= \frac{B_n\ u^u}{(c/n_0)\ \ \Gamma(u)} \cdot \frac{\Gamma(u-1)}{u^{u-1}} \\ &= \frac{B_n}{(c/n_0)} \cdot \frac{u}{u-1} \end{aligned} \tag{5.21}$$

Integration II :

$$\begin{aligned} \frac{B_n}{2\eta \cdot (c/n_0)^2} \int_0^\infty \frac{p(I_s)}{I_s^2}\, dI_s &= \frac{B_n\, u^u}{2\eta \cdot (c/n_0)^2\ \ \Gamma(u)} \int_0^\infty I_s^{u-3}\, e^{-uI_s}\, dI_s \\ &= \frac{B_n\, u^u}{2\eta \cdot (c/n_0)^2\ \ \Gamma(u)} \cdot \left(\frac{\Gamma(u-2)}{u^{u-2}} \right) \\ &= \frac{B_n}{2\eta \cdot (c/n_0)^2} \cdot \frac{u^2}{(u-1)(u-2)} \end{aligned} \tag{5.22}$$

By substituting Equations (5.21) and (5.22) in Equation (5.20) and using $u = 1/S_4^2$ from Equation (2.34), the carrier tracking mean square error can be obtained via

$$\left\langle \theta_e^2 \right\rangle = \left\langle \theta_n^2 \right\rangle = \frac{B_n}{(c/n_0)} \left(\frac{2\eta (c/n_0)(1-2S_4^2)+1}{2\eta (c/n_0)(1-3S_4^2+2S_4^4)} \right), \qquad S_4 < 1/\sqrt{2} \tag{5.23}$$

This equation defines the carrier phase mean square error as a function of intensity scintillation index S_4. The error is plotted in Figure 5.12 with respect to S_4, assuming $B_n = 5$, 15, 25 and 35 Hz, $\eta = 1$ ms, and $C/N_0 = 42$ dB-Hz.

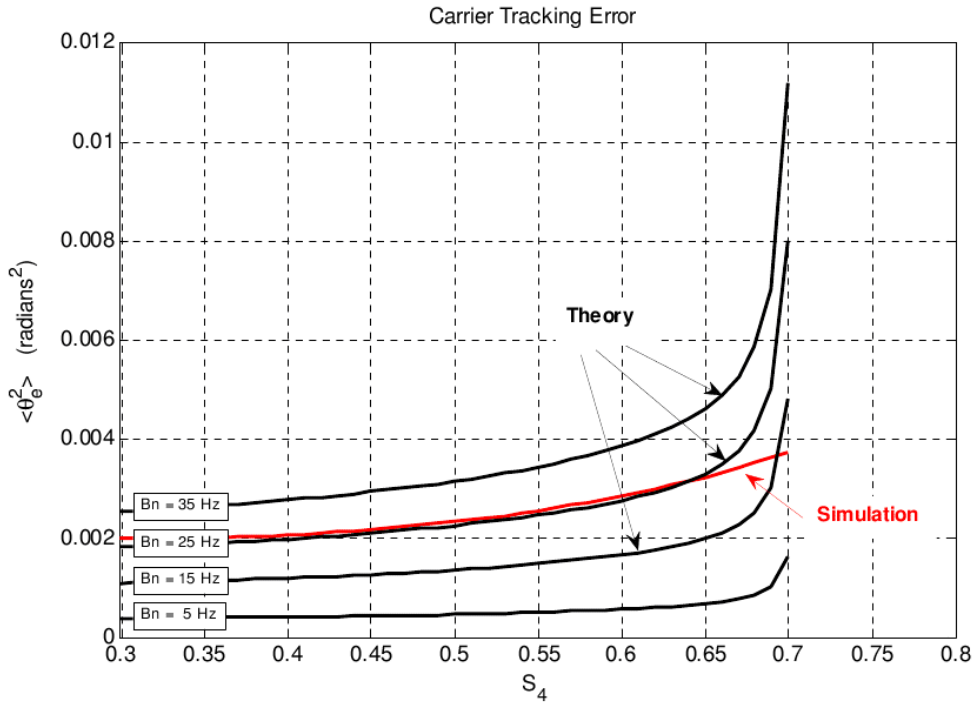

Figure 5.12: Tracking error in the presence of thermal noise and intensity scintillation. Theoretical results, using Equation (5.23), are compared with simulation for B_n = 25 Hz.

Considering the tracking error threshold $\left\langle \theta_e^2 \right\rangle_{threshold} = (\pi/12)^2 = 0.0685$ rad^2, one can clearly see from Figure 5.12 that intensity scintillation alone is not as large a concern for the carrier phase tracking, except for severe scintillation conditions and wide loop bandwidths.

The simulation results for $B_n = 25$ Hz are also shown in the figure. To attain these results, different intensity scintillation realizations, corresponding to $S_4 =$ 0.3 to 0.7, are generated and modulated on the GPS signal. For the tracking loop bandwidth $B_n = 25$ Hz, the output of tracking loop simulator (here, the carrier tracking mean square error) is measured and plotted in Figure 5.12. As shown in the figure, the simulation results closely follow the theory, except when $S_4 \to 1/\sqrt{2} \approx 0.7$.

Equation (5.23) fails to predict the tracking error behavior when S_4 approaches the 0.7 value (the error function becomes infinite due to the *pole* at $S_4 = 1/\sqrt{2}$). The function discontinuity however, can be corrected using the error function's slope at a S_4 value close enough the point of discontinuity (e.g. $S_4 = 0.6$). This is done through:

$$\left\langle \theta_e^2 \right\rangle = \left\langle \theta_n^2 \right\rangle = \begin{cases} \dfrac{B_n}{(c/n_0)} \left(\dfrac{2\eta\,(c/n_0)(1-2S_4^2)+1}{2\eta\,(c/n_0)(1-3S_4^2+2S_4^4)} \right), & 0 \le S_4 \le 0.6 \\ (S_4 - 0.6) \cdot \Omega\big|_{S_4=0.6} + \left\langle \theta_n^2 \right\rangle \Big|_{S_4=0.6}, & 0.6 < S_4 \le 1 \end{cases} \tag{5.24}$$

where the function's slope (Ω) is defined via

$$\Omega = \frac{\left(2\eta\,(c/n_0) B_n S_4 (1-2S_4^2)^2 + B_n (3S_4 - 4S_4^3)\right)}{\eta\,(c/n_0)^2 (1-3S_4^2+2S_4^4)^2} \tag{5.25}$$

Equations (5.23) and (5.24), along with the simulation results for $B_n = 25$ Hz, are plotted in Figure 5.13, in which simulation almost closely follows the theoretical predictions given in Equation (5.24).

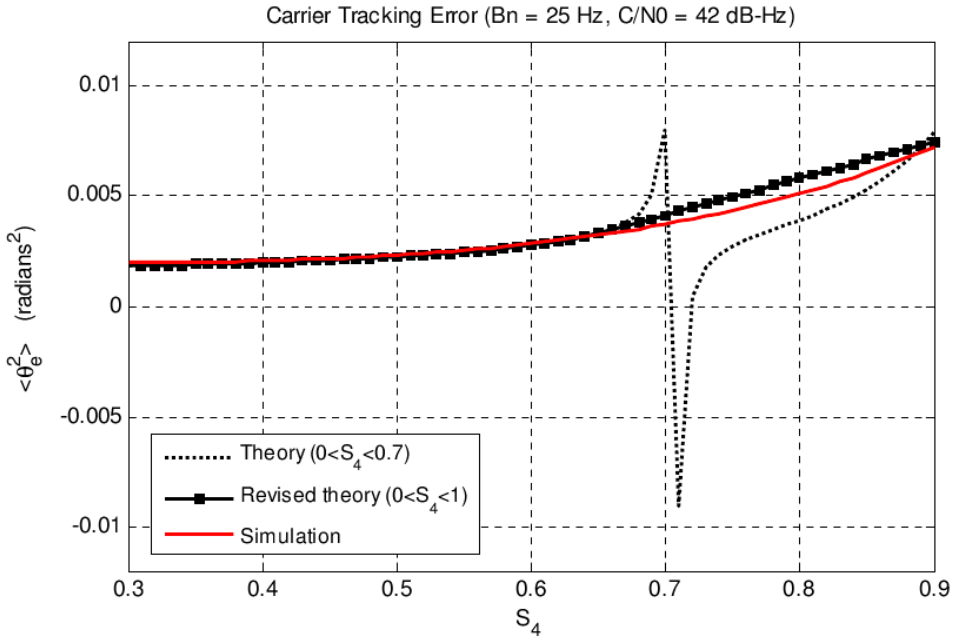

Figure 5.13: Tracking error in the presence of thermal noise and intensity scintillation. Theoretical discontinuity at $S_4 = 0.7$ is solved through Equation (5.24).

Using Equations (5.15) and (5.23), the total phase tracking mean square error in the presence of *thermal noise* and *scintillation components* is obtained via

$$\left\langle \theta_e^2 \right\rangle \approx \frac{B_n}{(c/n_0)} \left(\frac{2\eta (c/n_0)(1-2S_4^2)+1}{2\eta (c/n_0)(1-3S_4^2+2S_4^4)} \right) + T_{scin} \frac{\pi}{\beta} f_n^{1-2\nu} \csc\left(\pi(\nu-0.5)/\beta\right). \tag{5.26}$$

This equation is plotted in Figure 5.14 for two scintillation conditions (weak and moderate), assuming $C/N_0 = 45$ dB-Hz $B_n = 3$ to 30 Hz, $\nu = 4/3$ and $\eta = 1$ ms.

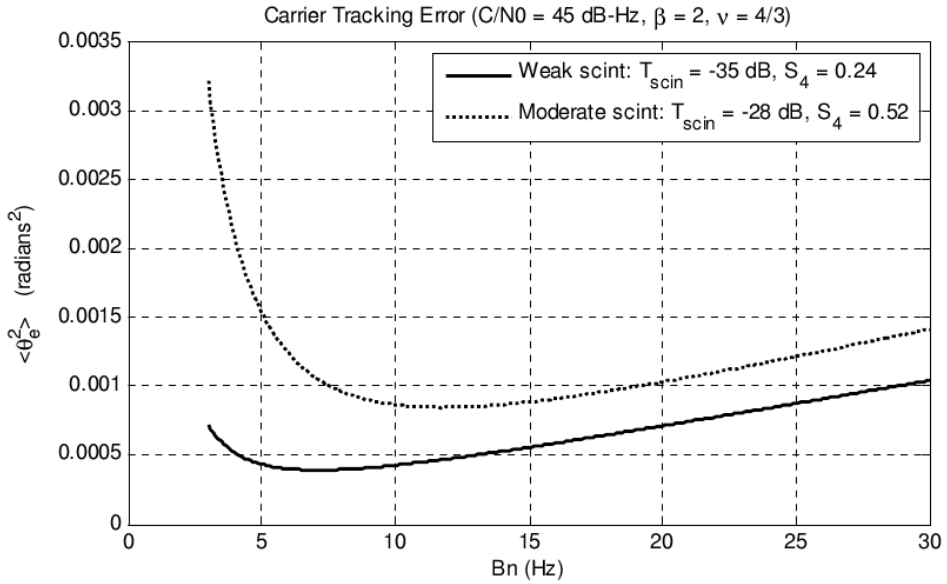

Figure 5.14: Phase tracking error in the presence of thermal noise and scintillation.

5.3.4 System Dynamics Error

Due to the relative motion between a GPS satellite and the receiver, an additional error term should be included in the carrier tracking error variance in Equation (5.26). This term is referred to as system dynamics error, and is obtained from the general Doppler expression [Misra and Enge, 2006]

$$\theta_d(t) = \underbrace{k_P\,u(t)}_{\substack{change\ in\\ reference\ position}} + \underbrace{k_V\ t\ u(t)}_{\substack{change\ in\\ velocity}} + \underbrace{0.5\,k_A\,t^2\,u(t)}_{\substack{change\ in\\ acceleration}} + \underbrace{\quad ... \quad}_{\substack{change\ in\ higher\\ order\ dynamics}} \qquad (m)$$

$$= \frac{2\pi}{\lambda}\left(k_P + k_V\,t + \frac{1}{2}k_A\,t^2 + ...\right)u(t), \qquad (rad) \tag{5.27}$$

where $u(t)$ denotes the unit step function, and the constants k_P, k_V, and k_A represent the amount of change in the position, velocity, and acceleration components of the satellite-platform relative motion, respectively.

Tracking error due to system dynamics consists of two parts: *transient* and *steady state* errors. Transient error results from imperfectly tracking the sudden changes in user dynamics. The remaining error, in the fullness of time, is referred to as the steady state error.

5.3.4.1 Steady State Error

According to the tracking loop model in Figure 5.3 and Equation (4.8), for the input dynamic phase $\theta_d(t)$, the *equivalent phase error* $\theta_{dE}(t)$ is expressed by

$$\begin{aligned}\Theta_{dE}(s) &= \left(1-H(s)\right)\Theta_d(s)\\ &= \left(1-\frac{F(s)G(s)}{1+F(s)G(s)}\right)\Theta_d(s)\\ &= \left(\frac{s}{s+F(s)}\right)\Theta_d(s)\end{aligned} \tag{5.28}$$

where $F(s)$ is the loop filter, $\Theta_{dE}(s)$ is the Laplace transform of $\theta_{dE}(t)$, and

$$\Theta_d(s) = \frac{2\pi}{\lambda}\left(\frac{k_P}{s}+\frac{k_V}{s^2}+\frac{k_A}{s^3}+\ldots\right) \tag{5.29}$$

is the Laplace transform of $\theta_d(t)$. The steady state response measures the error when the loop has reached steady state (i.e. $t \to \infty$). The steady state error (SSE) is evaluated by means of the final value theorem as [Misra and Enge, 2006]

$$\theta_{SSE} = \lim_{s \to 0} \left(s \, \Theta_{dE}(s) \right) \tag{5.30}$$

Therefore, by substituting Equation (5.29) in (5.28), and then substituting the result in Equation (5.30), the SSE can expressed by

$$\theta_{SSE} = \lim_{s \to 0} \left(\frac{2\pi}{\lambda} \cdot \left(\frac{k_P \; s}{s + F(s)} + \frac{k_V}{s + F(s)} + \frac{k_A}{s(s + F(s))} + \ldots \right) \right) \tag{5.31}$$

The result of the SSE is calculated in Table 5.2 for three loop order and dynamic process, using $F(s)$ from Table 4.3.

Following Equation (5.31), for the 1st-order tracking loop, if the input phase is a step function of magnitude k_P, the SSE would always be zero, independent of loop filter. For the input frequency step of magnitude k_V, the SSE reaches k_V / ω_n with ω_n being the loop natural frequency. In this case, a large loop natural frequency ($\omega_n >> k_V$) can result in a small SSE. This approach, however, will increase the loop equivalent noise bandwidth $B_n = \omega_n / 4$, and so the thermal noise. For the 2nd-order tracking loop, the SSE would be zero for a step change in the input phase and frequency. Nevertheless, for a step change of magnitude k_A in the rate of frequency change, the error reaches k_A / ω_n^2. In this case, the SSE can be made small by choosing a large loop natural frequency ($\omega_n >> k_A$). This, however, will increase the loop equivalent noise bandwidth $B_n = \omega_n \zeta / 2 + \omega_n / 8\zeta$, and the thermal noise error given in Equation (5.7). Finally, in a 3rd-order tracking loop, the SSE would be zero for phase and frequency steps, as well as step in rate of frequency change [Chien, 2001].

Table 5.2: Steady state tracking errors for the specified dynamic process.

First-order loop	
$\theta_d(t) = k_P.u(t)$	$\theta_{SSE} = \frac{2\pi}{\lambda}\left(\lim_{s\to 0}\left(\frac{k_P\, s}{s+\omega_n}\right)\right) = 0$
$\theta_d(t) = k_V.t.u(t)$	$\theta_{SSE} = \frac{2\pi}{\lambda}\left(\lim_{s\to 0}\left(\frac{k_V}{s+\omega_n}\right)\right) = \frac{2\pi k_V}{\lambda\omega_n}, \quad (rad)$
$\theta_d(t) = 0.5k_A.t^2.u(t)$	$\theta_{SSE} = \frac{2\pi}{\lambda}\left(\lim_{s\to 0}\left(\frac{k_A}{s(s+\omega_n)}\right)\right) = \infty$
Second-order loop	
$\theta_d(t) = k_P.u(t)$	$\theta_{SSE} = \frac{2\pi}{\lambda}\left(\lim_{s\to 0}\left(\frac{k_P\, s}{s+(2\zeta\omega_n+\omega_n^2/s)}\right)\right) = 0$
$\theta_d(t) = k_V.t.u(t)$	$\theta_{SSE} = \frac{2\pi}{\lambda}\left(\lim_{s\to 0}\left(\frac{k_V}{s+(2\zeta\omega_n+\omega_n^2/s)}\right)\right) = 0$
$\theta_d(t) = 0.5k_A.t^2.u(t)$	$\theta_{SSE} = \frac{2\pi}{\lambda}\left(\lim_{s\to 0}\left(\frac{k_A}{s(s+(2\zeta\omega_n+\omega_n^2/s))}\right)\right) = \frac{2\pi k_A}{\lambda\omega_n^2}$
Third-order loop	
$\theta_d(t) = k_P.u(t)$	$\theta_{SSE} = \frac{2\pi}{\lambda}\left(\lim_{s\to 0}\left(\frac{k_P\, s}{s+(2\omega_n+2\omega_n^2/s+\omega_n^3/s^2)}\right)\right) = 0$
$\theta_d(t) = k_V.t.u(t)$	$\theta_{SSE} = \frac{2\pi}{\lambda}\left(\lim_{s\to 0}\left(\frac{k_V}{s+(2\omega_n+2\omega_n^2/s+\omega_n^3/s^2)}\right)\right) = 0$
$\theta_d(t) = 0.5k_A.t^2.u(t)$	$\theta_{SSE} = \frac{2\pi}{\lambda}\left(\lim_{s\to 0}\left(\frac{k_A}{s(s+(2\omega_n+2\omega_n^2/s+\omega_n^3/s^2))}\right)\right) = 0$

5.3.4.2 Transient Error

The transient response characterizes the performance of the tracking loop's NCO as it tracks the input signal phase [Chien, 2001]. Similar to Equation (5.8), the effects of transient dynamics on the carrier phase tracking mean square error can be expressed as

$$\left\langle \theta_d^2 \right\rangle = \int_{-\infty}^{\infty} \Phi_{\theta_d}(f)\ \left|1 - H(f)\right|^2 df \tag{5.32}$$

where $\Phi_{\theta_d}(f)$ represents the SDF of the dynamic process. For a step change in position, $\Phi_{\theta_d}(f)$ can be determined from[12] [Cusumano, 2005]

$$\begin{aligned} \Phi_{\theta_d}(f)\Big|_{position} &= E\left\{\Theta_d(s)\Theta_d^*(s)\right\}\Big|_{s=j2\pi f} \\ &= \frac{2\pi k_P}{\lambda(j2\pi f)} \cdot \frac{2\pi k_P}{\lambda(-j2\pi f)} = \left(\frac{2\pi k_P}{\lambda}\right)^2 \frac{1}{(2\pi f)^2} \end{aligned} \tag{5.33}$$

Similarly, for a step change in velocity and acceleration,

$$\Phi_{\theta_d}(f)\Big|_{velocity} = \left(\frac{2\pi k_V}{\lambda}\right)^2 \frac{1}{(2\pi f)^4} \tag{5.34}$$

$$\Phi_{\theta_d}(f)\Big|_{acceleration} = \left(\frac{2\pi k_A}{\lambda}\right)^2 \frac{1}{(2\pi f)^6} \tag{5.35}$$

with $\Theta_d(s)$ being the Laplace transform of input dynamic phase $\theta_d(t)$. Equations (5.33) to (5.35) can be expressed in the general form

---

[12] *For $s = j\omega = j2\pi f$, the Laplace transform becomes the Fourier transform.*

$$\Phi_{\theta_d}(f)=\frac{D^2}{(2\pi f)^{2n}};\qquad \begin{cases} D=2\pi k_P/\lambda & (rad) \quad , \ n=1 \\ D=2\pi k_V/\lambda & (rad/s) \quad , \ n=2 \\ D=2\pi k_A/\lambda & (rad/s^2) \quad , \ n=3 \end{cases} \tag{5.36}$$

where n represents the order of dynamics. By substituting $\Phi_{\theta_d}(f)$ and $\left|1-H(f)\right|^2$ from Equations (5.36) and (5.10) in (5.32), and using the results of Equation (5.13), the transient mean square error can be derived as

$$\begin{aligned} \left\langle \theta_d^2 \right\rangle &= \int_{-\infty}^{\infty} \frac{D^2}{(2\pi f)^{2n}} \frac{f^{2\beta}}{f^{2\beta}+f_n^{2\beta}} df \\ &= \int_{-\infty}^{\infty} \frac{D^2}{(2\pi)^{2n}} \frac{f^{2\beta-2n}}{f^{2\beta}+f_n^{2\beta}} df \\ &= \frac{D^2}{(2\pi)^{2n}} \frac{\pi}{\beta} f_n^{1-2n} \csc\left(\frac{\pi(n-0.5)}{\beta}\right). \end{aligned} \tag{5.37}$$

Transient mean square error is plotted as a function of D for the 1st-order tracking loop that is subject to a position step, in Figure 5.15, and for the 1st-, and 2nd-order tracking loop that is subject to a velocity step, in Figure 5.16.

A position step of magnitude k_P (m) is equivalent to an input phase step of magnitude $((2\pi k_P/\lambda) \bmod 2\pi)$ (rad), and a velocity step of magnitude k_V (m/s), corresponds to an input frequency step of magnitude $2\pi k_V/\lambda$ (rad/s). Similar to the steady state error, in order for $\left\langle \theta_d^2 \right\rangle$ to be finite, the loop order must be greater than or equal to the order of the dynamics $(\beta \geq n)$. The 1st-order loop fails this condition in Figure 5.16 and the tracking loop loses phase lock.

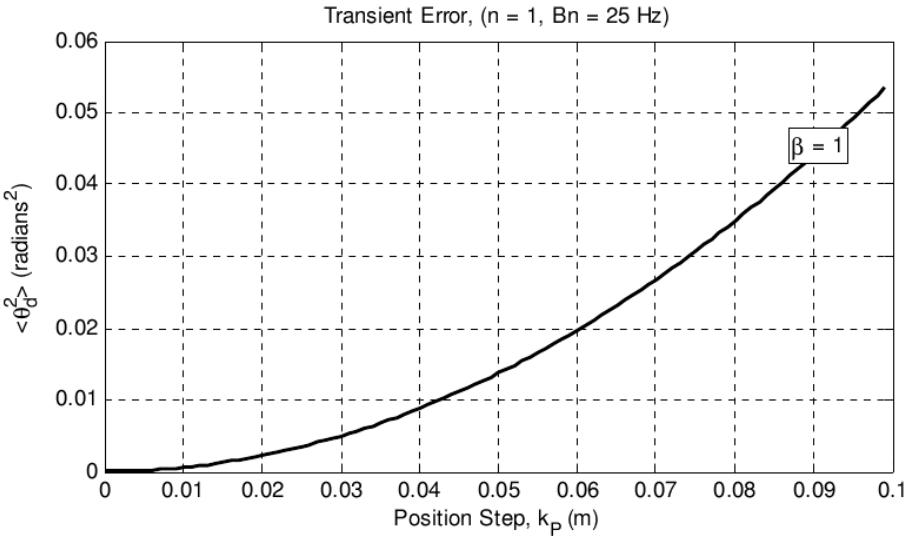

Figure 5.15: Transient error for a 1st-order loop that is subject to a position step.

Figure 5.16: Transient error for a 1st and 2nd-order loop, subject to a velocity step.

By substituting Equations (5.14), (5.23) and (5.37) in Equation (5.6), and assuming $\left\langle \theta_o^2 \right\rangle = 0.01$ rad^2 [Conker et al., 2003], the carrier phase tracking mean square error in the presence of thermal noise, phase and intensity scintillations, oscillator noise and system dynamics is derived as

$$\begin{aligned}\left\langle \theta_e^2 \right\rangle &= \left\langle \theta_n^2 \right\rangle + \left\langle \theta_s^2 \right\rangle + \left\langle \theta_d^2 \right\rangle + \left\langle \theta_o^2 \right\rangle \\ &= \frac{B_n}{(c/n_0)} \left(\frac{2\eta (c/n_0)(1-2S_4^2)+1}{2\eta (c/n_0)(1-3S_4^2+2S_4^4)} \right) \\ &+ T_{scin} \frac{\pi}{\beta} f_n^{1-2\nu} \csc\left(\frac{\pi(\nu-0.5)}{\beta} \right) \\ &+ \frac{D^2}{(2\pi)^{2n}} \frac{\pi}{\beta} f_n^{1-2n} \csc\left(\frac{\pi(n-0.5)}{\beta} \right) + \left\langle \theta_o^2 \right\rangle \Big|_{=0.01}\end{aligned} \tag{5.38}$$

This equation provides useful information regarding the relation between dynamic parameters (D,n), scintillation parameters (T_{scin}, S_4, ν), and the loop bandwidth (B_n). For example, for the tracking error threshold $\left\langle \theta_e^2 \right\rangle_{threshold} = (\pi/12)^2$, Equation (5.38) can be used to determine an upper boundary for the dynamic component D at different loop bandwidths, beyond which the tracking loop is expected to lose phase lock. To this aim, Equation (5.38) is rearranged to give

$$\begin{aligned}D^2 &= (2\pi)^{2n} \frac{\beta}{\pi} f_n^{2n-1} \sin\left(\frac{\pi(n-0.5)}{\beta} \right) \times \\ &\left[\left\langle \theta_e^2 \right\rangle_{threshold} - \frac{B_n}{(c/n_0)} \left(\frac{2\eta (c/n_0)(1-2S_4^2)+1}{2\eta (c/n_0)(1-3S_4^2+2S_4^4)} \right) \right. \\ &\left. - T_{scin} \frac{\pi}{\beta} f_n^{1-2\nu} \csc\left(\frac{\pi(\nu-0.5)}{\beta} \right) - 0.01 \right].\end{aligned} \tag{5.39}$$

By substituting $T_{scin} = -35$ and -25 dBrad^2/Hz, $\nu = 1.33$, $C/N_0 = 38$ dB-Hz, $\zeta = 0.707$, $\eta = 1$ ms, and $\beta = 2$ in Equation (5.39), the upper boundary for the position step is calculated in Figure 5.17 as a function of loop bandwidth, for the first-order dynamics. For these settings, the upper boundary is in the range of few centimeters (~ 3 - 9 cm), beyond which the loop is expected to lose phase lock, as the tracking error will go above the threshold. As can be seen from the figures, the boundaries increase by increasing the loop bandwidth; this shows that stronger dynamics can be handled by the tracking loop at wider noise bandwidths. On the other hand, the scintillation activities, whether weak or strong, only slightly affect the level of dynamic boundaries. This indicates that *in the presence of all sources of error*, the total tracking error is mostly due to the satellite-platform dynamics and thermal noise. Therefore, even a moderate level of scintillation (as an extra error term) can cause the tracking error to exceed the threshold and result in loss of phase lock.

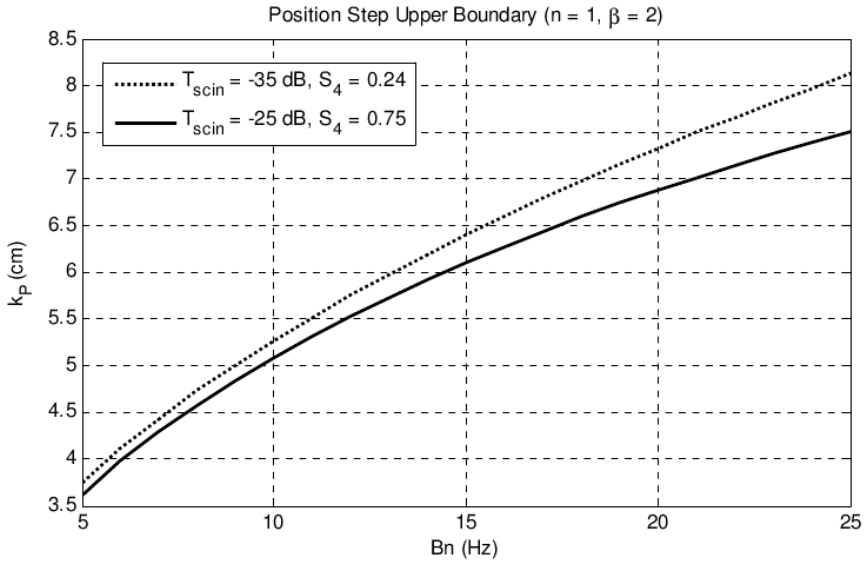

Figure 5.17: Position step upper boundary at two scintillation levels (weak and strong) for the 2nd order loop.

It is important to note that the results obtained in Figure 5.17 are based on the assumption that the carrier tracking loop phase discriminator function is linear over the entire input phase error range (i.e. $\pm\infty$ rad). In reality, however, the linear region is determined by the tracking loop discriminator function. For the case of arctangent discriminator, as shown in Figure 5.18, the function is linear only over $\pm\pi/2$ rad, and the upper boundary for the position step is practically limited to this region. Considering that one complete signal wavelength (19 cm for GPS L_1 signal) corresponds to 2π radians carrier phase change, the position step upper boundary is limited to one-quarter of this length, which is approximately 5 cm. Therefore, in Figure 5.17, increasing the loop bandwidth above 10 Hz will not practically increase the loop's capability to track larger phase step, but only increase the thermal noise.

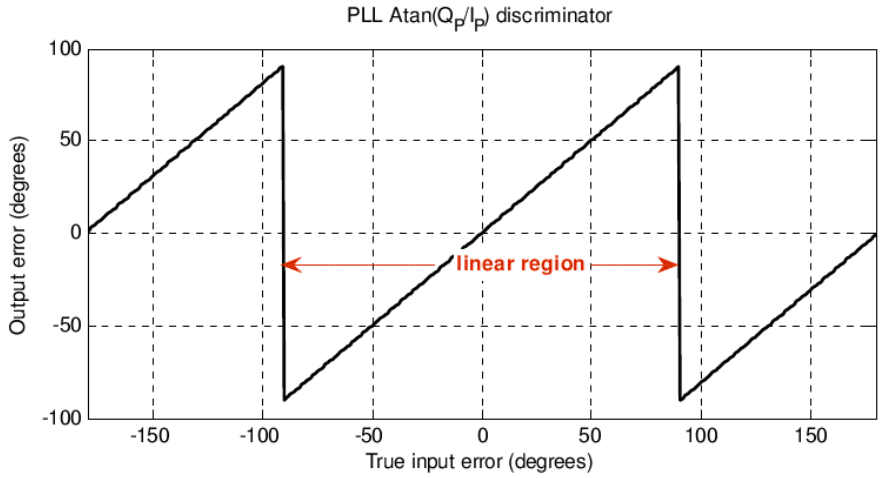

Figure 5.18: Costas phase tracking loop atan (Q/I) discriminator.

5.3.5 Carrier Phase Multipath Error

The carrier phase tracking mean square error given in Equation (5.38) is obtained based on an early assumption that the GPS input signal consists of only the direct (line-of-sight) signal. In reality, however, the incoming signal contains the line-of-sight signal transmitted by the GPS satellite and usually more than one reflected signal. These reflected signals are collectively referred to as multipath signals. As multipath signals are uncorrelated, their effects on the tracking loop error cannot be eliminated through differential correction methods [Fantino et al., 2008]. In order to investigate the effects of multipath on the carrier tracking loop performance, the behavior of the carrier phase discriminator function in the presence and absence of multipath needs to be analyzed first.

5.3.5.1 Carrier Tracking Error in the Absence of Multipath

In the absence of multipath, the GPS receiver receives only the line-of-sight signal from the satellite. Neglecting the navigation data bit, the *direct* input signal at the receiver can be expressed by

$$S_{IF}(t) = X(t-\tau_0)\cos(\omega_{IF}t + \theta_0) \tag{5.40}$$

where X is the satellite PRN code, τ_0 is the code delay, ω_{IF} is the carrier wave intermediate frequency, and θ_0 is the carrier phase offset.

According to the GPS receiver code and carrier tracking loops diagram shown in Figure 4.13, the input signal is mixed with the in-phase and quadrature reference signals produced by the NCO. Subsequently, the signals are correlated with the prompt, early and late code replicas (with the early and late codes being ±0.5 chips shifted with respect to the prompt code), and the correlation outputs are integrated over $\eta = 1$ ms pre-detection integration time. The six correlation output numerical values (I_E, I_P, I_L, Q_E, Q_P and Q_L)

are then used in the code and carrier loop discriminators to generate error signals. The frequency and phase of the local carrier replica produced by the NCO is equal to the receiver's estimate of the incoming signal frequency and phase (i.e. $\hat{\omega}_{IF}, \hat{\theta}_0$). Likewise, the amount of code delay in the prompt code replica is equal to the receiver's estimate of the incoming signal code delay (i.e. $\hat{\tau}_0$). Following this, for the prompt correlator, the locally generated signals are defined as [Ray, 2000]

$$S_{IP}(t) = X(t-\hat{\tau}_0)\cos(\hat{\omega}_{IF}t + \hat{\theta}_0) \tag{5.41}$$

$$S_{QP}(t) = X(t-\hat{\tau}_0)\sin(\hat{\omega}_{IF}t + \hat{\theta}_0) \tag{5.42}$$

From these two equations, the in-phase and quadrature prompt correlation values, assuming perfect alignment between the incoming carrier frequency and its replica, is given by [Ray, 2000]

$$\begin{aligned} I_P &= \int_0^{\eta} X(t-\tau_0)X(t-\hat{\tau}_0)\cos(\omega_{IF}t+\theta_0)\cos(\hat{\omega}_{IF}t+\hat{\theta}_0)\,dt \\ &\approx \frac{1}{2}R(\hat{\tau}_0-\tau_0)\cos(\theta_0-\hat{\theta}_0) \end{aligned} \tag{5.43}$$

$$\begin{aligned} Q_P &= \int_0^{\eta} X(t-\tau_0)X(t-\hat{\tau}_0)\cos(\omega_{IF}t+\theta_0)\sin(\hat{\omega}_{IF}t+\hat{\theta}_0)\,dt \\ &\approx \frac{1}{2}R(\hat{\tau}_0-\tau_0)\sin(\theta_0-\hat{\theta}_0) \end{aligned} \tag{5.44}$$

where η denotes the pre-detection integration period, and $R(\cdot)$ denotes the PRN code correlation function.

A sufficient approximation of $R(\cdot)$ is given by Braasch, [1996]

$$R(\tau)=\begin{cases}1-\dfrac{|\tau|}{T_c}, & |\tau|\le T_c \\ 0, & |\tau|> T_c\end{cases} \tag{5.45}$$

and is plotted in Figure 5.19 for $-T_c \le \tau \le T_c$, with T_c being the PRN code chip period.

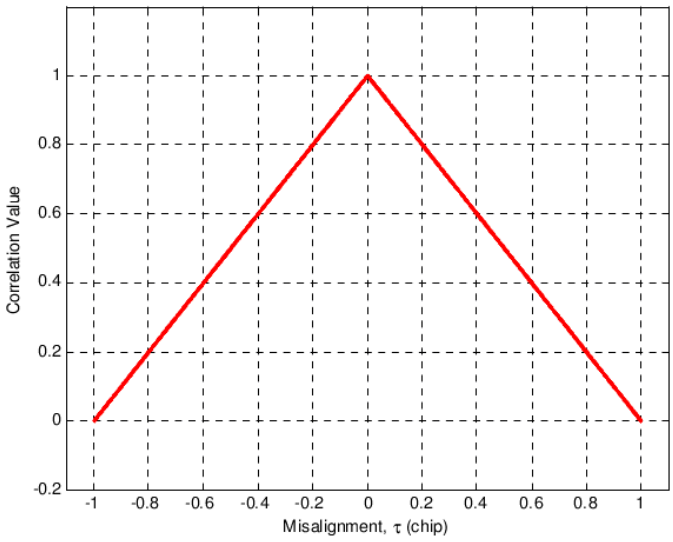

Figure 5.19: Normalized correlation triangle R(τ).

Substituting the in-phase and quadrature prompt correlation values from Equations (5.43) and (5.44) in an arctangent type of discriminator, the tracking loop error, corresponding to the output of the discriminator function (see Table 4.2), can be expressed as

$$\begin{aligned}\theta_e &= \tan^{-1}\left(\frac{Q_p}{I_P}\right) \\ &= \tan^{-1}\left(\frac{R(\hat{\tau}_0-\tau_0)\sin(\theta_0-\hat{\theta}_0)}{R(\hat{\tau}_0-\tau_0)\cos(\theta_0-\hat{\theta}_0)}\right) \\ &= \theta_0-\hat{\theta}_0.\end{aligned} \tag{5.46}$$

5.3.5.2 Carrier Tracking Error in the Presence of Multipath

In the presence of multipath, the composite signal (line-of-sight plus multipath) is defined by [Ray, 2000]

$$S_{IF}(t)=\sum_{i=0}^{n}\alpha_i\,X(t-\tau_i)\,\cos(\omega_{IF}t+\theta_i) \tag{5.47}$$

where n is the number of reflected signals with $n=0$ for the direct signal, and α_i are the direct and reflected signal coefficients with $\alpha_0=1$ for the direct signal. The coefficient α is related to the signal-to-multipath ratio (SMR) via SMR = 20 log10(1/α) [Ray, 2000].

The in-phase and quadrature prompt correlation values can be obtained from Equations (5.43), (5.44) and (5.47) as

$$I_P=\sum_{i=0}^{n}\frac{1}{2}\alpha_i\,R(\hat{\tau}_c-\tau_i)\cos(\theta_i-\hat{\theta}_c) \tag{5.48}$$

$$Q_P=\sum_{i=0}^{n}\frac{1}{2}\alpha_i\,R(\hat{\tau}_c-\tau_i)\sin(\theta_i-\hat{\theta}_c) \tag{5.49}$$

where $\hat{\tau}_c$ is the receiver's best estimate of the incoming composite signal code delay, and $\hat{\theta}_c$ is the best estimate of the signal's carrier phase.

In the presence of multipath, the phase of the incoming composite signal deviates from the phase of the line-of-sight signal, thus results in phase measurement errors. The effect of multipath on the carrier tracking loop error can be understood better using a phasor diagram as given in Figure 5.20. Assuming one dominant reflector around the receiver antenna, and zero code delay and phase offset ($\tau_0 = 0,\ \theta_0 = 0$) for the line-of-sight signal, the phase of the multipath is given by the angle θ_1. The angle θ_c, therefore, denotes the error in the carrier tracking loop results from multipath [Ray, 2000; Fantino et al., 2008].

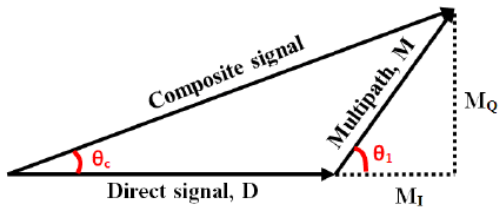

Figure 5.20: A phasor diagram showing the effect of multipath on the composite signal [modified after Fantino et al., 2008].

The magnitude of the direct (D), and multipath (M) signal shown in Figure 5.20 is given by [Fantino et al., 2008]

$$D = \alpha_0\, R(\hat{\tau}_c - \tau_0) = R(\hat{\tau}_c) \tag{5.50}$$

$$M = \alpha_1\, R(\hat{\tau}_c - \tau_1) \tag{5.51}$$

Using Equation (5.51), the in-phase and quadrature components of the multipath signal can be obtained via the following equations [Fantino et al., 2008].

$$M_I = M\cos(\theta_1) = \alpha_1 R(\hat{\tau}_c - \tau_1)\cos(\theta_1) \tag{5.52}$$

$$M_Q = M\sin(\theta_1) = \alpha_1 R(\hat{\tau}_c - \tau_1)\sin(\theta_1) \tag{5.53}$$

Following the phasor diagram in Figure 5.20 and Equations (5.50) to (5.53), the carrier phase multipath error θ_c is then calculated as

$$\begin{aligned}
\theta_c &= \tan^{-1}\left(\frac{M_Q}{D + M_I}\right) \\
&= \tan^{-1}\left(\frac{M\sin(\theta_1)}{D + M\cos(\theta_1)}\right) \\
&= \tan^{-1}\left(\frac{\alpha_1 R(\hat{\tau}_c - \tau_1)\sin(\theta_1)}{R(\hat{\tau}_c) + \alpha_1 R(\hat{\tau}_c - \tau_1)\cos(\theta_1)}\right), \qquad (rad) \\
&= \frac{\lambda}{2\pi}\cdot\tan^{-1}\left(\frac{\alpha_1 R(\hat{\tau}_c - \tau_1)\sin(\theta_1)}{R(\hat{\tau}_c) + \alpha_1 R(\hat{\tau}_c - \tau_1)\cos(\theta_1)}\right), \qquad (m)
\end{aligned} \tag{5.54}$$

The multipath components (α_1, τ_1 and θ_1) are defined with respect to the line-of-sight signal [Ray, 2000]. As can be seen from Equation (5.54), the error's amplitude is a function of the multipath delay. For large delays, both the correlation value (see Figure 5.19) and the multipath error decrease [Ray, 2000].

Equation (5.54) can be used to determine the multipath phase θ_1 corresponding to the maximum and minimum multipath error. Letting $(\partial\theta_c/\partial\theta_1) = 0$ and solving for θ_1 will result in [Ray, 2000]

$$\theta_{1,boundary} = 2\pi \pm \cos^{-1}\left(-\frac{\alpha_1 R(\hat{\tau}_c - \tau_1)}{R(\hat{\tau}_c)}\right), \qquad (rad) \tag{5.55}$$

Using Equations (5.54) and (5.55), and assuming SMR = 20 and 10 dB, the multipath error envelopes of the L_1 carrier phase multipath is plotted with respect to multipath delay (in chips) in Figure 5.21.

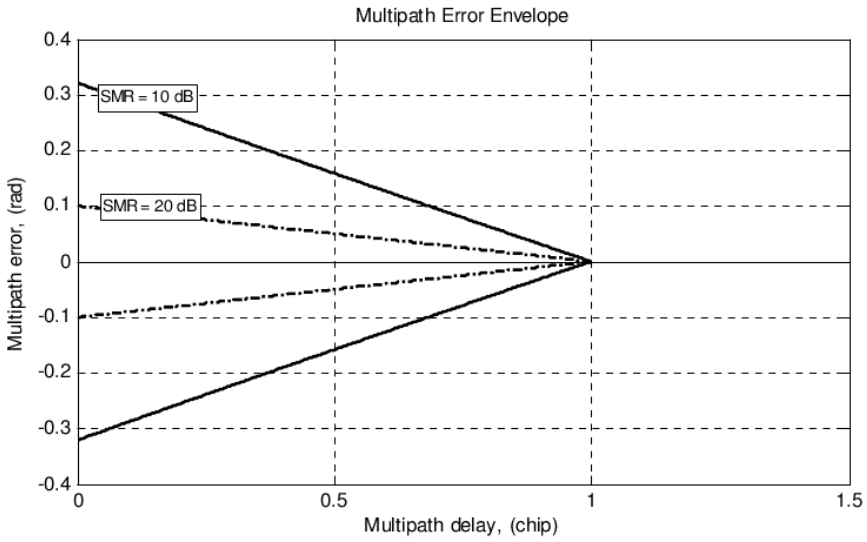

Figure 5.21: Multipath error envelope.

For the multipath code delay τ_1 = 0 to 1 chip, with 0.1-chip steps, and $\alpha_1 = 10^{-SMR/20}$, assuming SMR = 20 dB, the maximum multipath phase values θ_1 are determined from Equation (5.55). For each pair of (θ_1, τ_1) and SMR = 20 dB, a multipath signal, corresponding to the GPS signal PRN3 is simulated using the signal simulator in Chapter three (assuming no scintillation effects). The composite signal (i.e. PRN3 plus the delayed version of it based on θ_1, τ_1 and α_1) is processed in the tracking loop simulator described in Chapter four, and the simulation results (here, the standard deviation of the phase tracking error) are generated and compared with theory in Figure 5.22. As depicted

in the figure, carrier phase multipath error decreases as the multipath delay approaches the code chip.

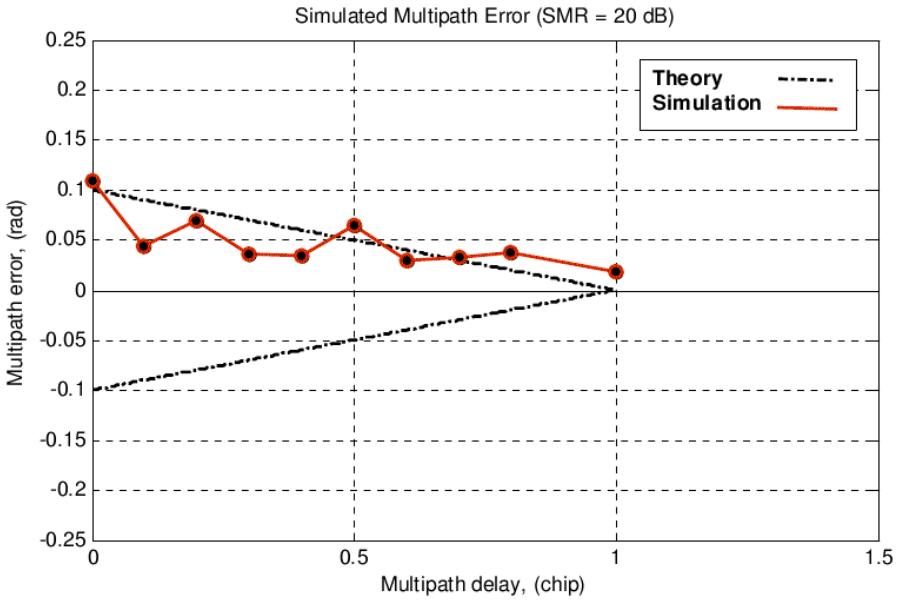

Figure 5.22: Multipath error, comparison between theoretical predictions and simulation results.

5.4 Velocity Error Variance

In the block diagram shown in Figure 5.3, the tracking loop provides the best estimate $\hat{\theta}(t)$ of the incoming phase $\theta(t)$ in order to minimize the tracking error $\theta_e(t)$. For the cases when the incoming phase is scintillated, the carrier loop's estimated phase will also be corrupted by the scintillation effect. The impact of phase scintillations on the carrier velocity measurements can be shown as

$$\omega_{es} = \frac{c}{\omega_L} \frac{d\hat{\theta}_s(t)}{dt}, \qquad (m/s) \tag{5.56}$$

where $\hat{\theta}_s(t)$ is the phase scintillation estimate obtained by the PLL, c is the speed of light, in m/s, and $\omega_L = 2\pi f_L$ is the propagating signal angular frequency in rad/s. Using the tracking loop model of Figure 5.3 and Equation (5.56), the carrier velocity mean square error would be

$$\left\langle \omega_{es}^2 \right\rangle = \left(\frac{c}{\omega_L} \right)^2 \int_{-\infty}^{\infty} (2\pi f)^2 |H(f)|^2 \, \Phi_{\theta_S}(f) \, df, \qquad (m/s)^2 \tag{5.57}$$

Using $\left|H(f)\right|^2$ from Equation (5.9), and $\Phi_{\theta_S}(f)$ from Equation (2.58), the carrier velocity mean square error (caused by scintillation) can be obtained as

$$\left\langle \omega_{es}^2 \right\rangle = \left(\frac{c}{\omega_L} \right)^2 \int_{-\infty}^{\infty} (2\pi f)^2 \frac{{f_n}^{2\beta}}{({f}^{2\beta} + {f_n}^{2\beta})} \left(1 + (2\beta - 2) \left(\frac{f}{f_n} \right)^{(2\beta-2)} \right) \cdot \frac{T_{scin}}{(f_o^2 + f^2)^{\nu}} df \tag{5.58}$$

The absolute value of the transfer function

$$(2\pi f) H(f) = (2\pi f) \cdot \sqrt{\frac{{f_n}^{2\beta}}{({f}^{2\beta} + {f_n}^{2\beta})} \left(1 + (2\beta - 2)(f/f_n)^{(2\beta-2)} \right)} \tag{5.59}$$

is plotted in Figure 5.23 for three loop orders. Since $\left|(2\pi f) H(f)\right|$ is a high pass filter to frequency components of the phase scintillation SDF, ignoring a low frequency component such as f_0 will not significantly affect the velocity error variance. To support

this assumption, velocity error in Equation (5.58) is numerically calculated, and plotted in Figure 5.24 as a function of loop bandwidth for three values of the outer scale size frequency f_0. As can be seen from the figure, for the typical range of f_0 (0.01 to 0.1 Hz), the velocity mean square error only changes about $1\,(cm/s)^2$ which is negligible in most applications. Therefore, f_0 is ignored in the following calculations.

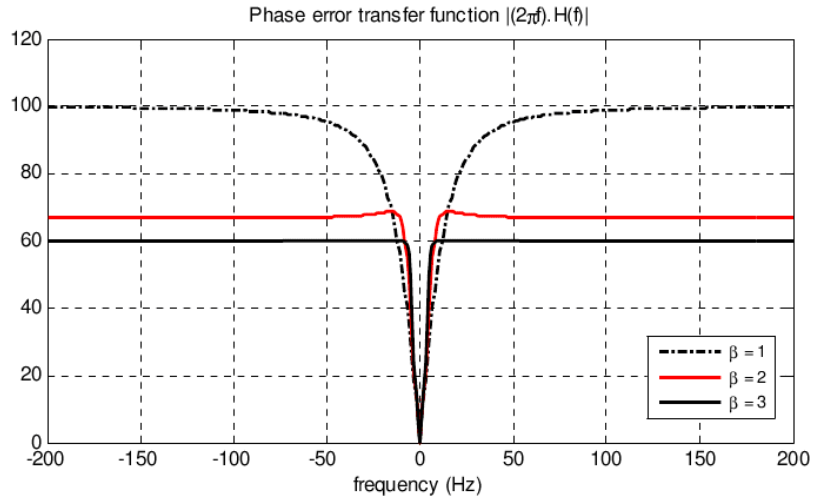

Figure 5.23: Loop transfer function.

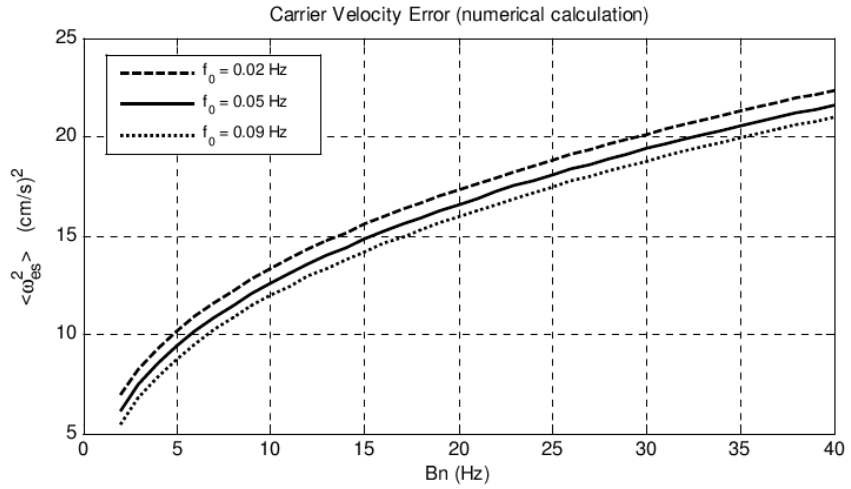

Figure 5.24: Numerical calculation of carrier velocity error for three f_0 values.

Thus, Equation (5.58) is simplified to

$$\begin{aligned}\left\langle \omega_{es}^2 \right\rangle \approx & \int_{-\infty}^{\infty} (2\pi f c/\omega_L)^2 \, \frac{T_{scin}}{f^{2\nu}} \cdot \frac{f_n^{2\beta}}{(f^{2\beta}+f_n^{2\beta})} \, [1+(2\beta-2)(f/f_n)^{(2\beta-2)}]\,df \\ = & \underbrace{\int_{-\infty}^{\infty} (2\pi f_n^{\beta} c/\omega_L)^2 \, \frac{T_{scin}\, f^{2-2\nu}}{(f^{2\beta}+f_n^{2\beta})}\, df}_{Integration\ I} \\ + & \underbrace{\int_{-\infty}^{\infty} (2\pi f_n c/\omega_L)^2 \, \frac{(2\beta-2)\, T_{scin}\, f^{2\beta-2\nu}}{(f^{2\beta}+f_n^{2\beta})}\, df}_{Integration\ II}\end{aligned} \tag{5.60}$$

Using the results of Equation (5.13), the two integration parts (*I* and *II*) are calculated as

$$\begin{aligned} \textit{Integlation I}: \quad & \int_{-\infty}^{\infty} \left(2\pi f_n^{\beta} c/\omega_L\right)^2 \frac{T_{scin} f^{2-2\nu}}{(f^{2\beta} + f_n^{2\beta})} \, df \\ & = \left(\frac{f_n^{1.5-\nu} c}{f_L}\right)^2 T_{scin} \frac{\pi}{\beta} \csc\left(\frac{\pi(1.5-\nu)}{\beta}\right), \end{aligned} \tag{5.61}$$

$$\begin{aligned} \textit{Integlation II}: \quad & \int_{-\infty}^{\infty} \left(2\pi f_n c/\omega_L\right)^2 \frac{(2\beta-2)\, T_{scin} f^{2\beta-2\nu}}{(f^{2\beta} + f_n^{2\beta})} \, df \\ & = \left(\frac{f_n^{1.5-\nu} c}{f_L}\right)^2 (2\beta-2) T_{scin} \frac{\pi}{\beta} \csc\left(\frac{\pi(\nu-0.5)}{\beta}\right) \end{aligned} \tag{5.62}$$

Substituting Equations (5.61) and (5.62) in Equation (5.60), the carrier velocity mean square error due to scintillation is derived as

$$\left\langle \omega_{es}^2 \right\rangle \approx \left(\frac{f_n^{1.5-\nu} c}{f_L}\right)^2 T_{scin} \frac{\pi}{\beta} \left[\csc\left(\frac{\pi(1.5-\nu)}{\beta}\right) + (2\beta-2)\csc\left(\frac{\pi(\nu-0.5)}{\beta}\right) \right] \tag{5.63}$$

This equation provides a means to study the effect of scintillation strength (T_{scin}) and the noise bandwidth (B_n) on the velocity error. The error is plotted as a function of noise bandwidth for T_{scin} = -28 dB in Figure 5.25. The simulation results, corresponding to the same level of scintillation activity, are also depicted in the figure. The difference between the simulation results and the theoretical predictions were found to be less than 1 $(cm/s)^2$. As can be seen from the figure, under moderate scintillation activities, the average velocity error is about 10 $(cm/s)^2$. For stronger scintillation levels, however, the error would be of the order of a couple of tens of $(cm/s)^2$ which is significant for high precision applications.

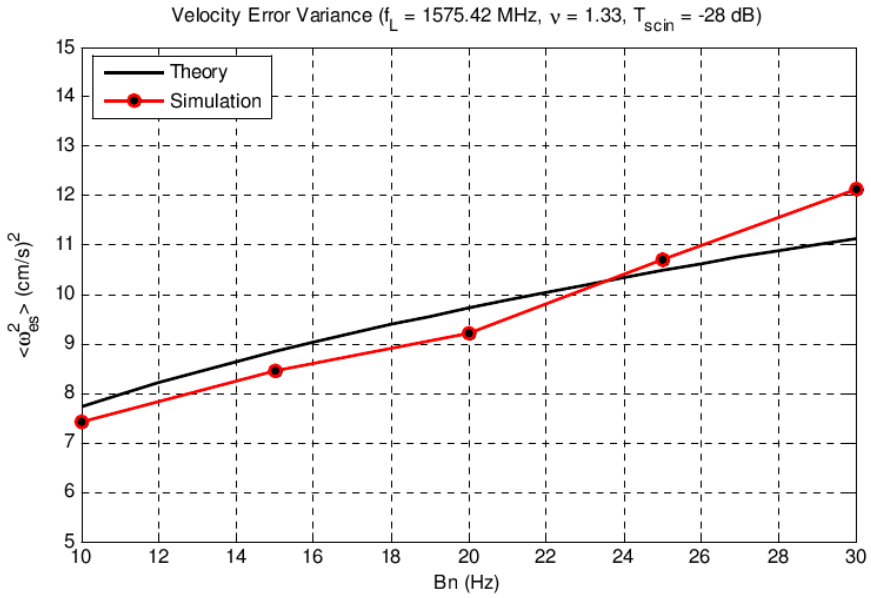

Figure 5.25: Carrier velocity error caused by moderate ionospheric scintillation.

Equation (5.63) is rearranged in Equation (5.64) to obtain a threshold level for the scintillation spectral strength $T_{scin,TH2}$, beyond which a predefined velocity mean square error $\left\langle \omega_{es}^2 \right\rangle_{threshold}$ will be exceeded, for a given loop order and loop bandwidth:

$$T_{scin,TH2} = \frac{\left\langle \omega_{es}^2 \right\rangle_{threshold} \frac{\beta}{\pi} \left(\frac{f_L}{f_n^{1.5-\nu} c} \right)^2}{\left[\csc\left(\frac{\pi(1.5-\nu)}{\beta} \right) + (2\beta - 2)\csc\left(\frac{\pi(\nu - 0.5)}{\beta} \right) \right]} \tag{5.64}$$

This is plotted in Figure 5.26 as a function of noise bandwidth B_n, assuming $\left\langle \omega_{es}^2 \right\rangle_{threshold} = 10$ and $30\ (cm/s)^2$, $\nu = 1.33$, $\beta = 2$ and $f_L = 1575.42$MHz.

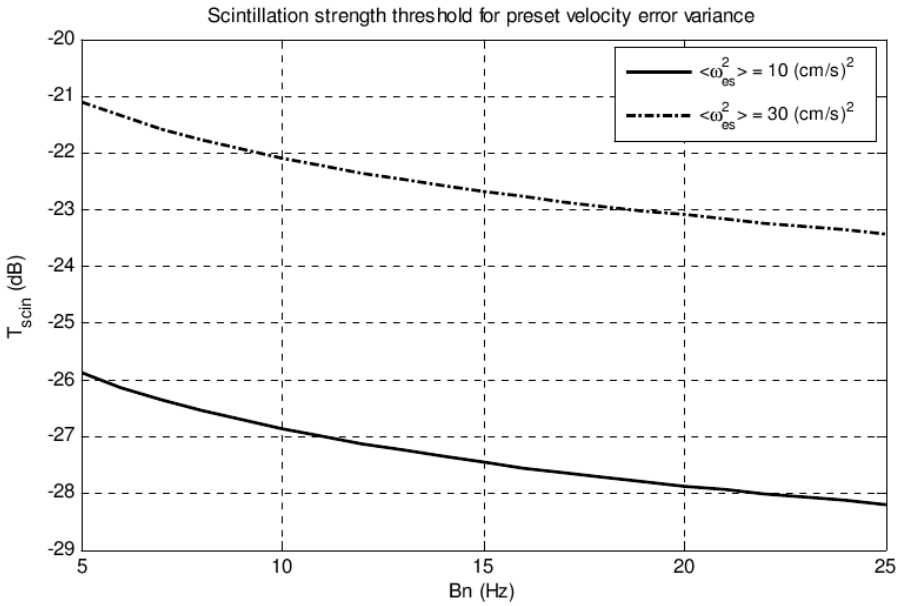

Figure 5.26: Scintillation spectral strength threshold for a predefined velocity error.

5.5 Summary

The behavior of a generic GPS receiver carrier tracking loop, subject to ionospheric scintillation, satellite-platform dynamics, and thermal noise, was studied in this chapter. Accordingly, two receiver performance measures (i.e. the carrier phase error and carrier velocity error) were defined in terms of tracking loop parameters (β, η, f_n and B_n), scintillation parameters (T_{scin}, v and S_4), and system dynamics parameters (n and D). Such tools can be used to determine expected receiver performance under various levels of scintillation.

For example, the effect of thermal noise on the carrier phase error is considerably high at low carrier-to-noise ratio levels and higher bandwidths. These effects become worse in the presence of phase and intensity scintillation; as intensity scintillation (signal fading) alters the level of carrier-to-noise ratio at the receiver, and phase scintillation (appears as

a high frequency modulation) spreads out the spectrum of the received signal over a large bandwidth, to accommodate which the loop requires a wider bandwidth.

By assuming a tracking threshold for the carrier phase and carrier velocity errors, a threshold level for the scintillation strength (T_{scin}) and the dynamics parameter (D) were obtained, beyond which the carrier tracking loop is expected to lose lock, or the carrier velocity error is expected to exceed a preset level.

In regard to scintillation effects, the performance of the second-, and third-order loop were found to be very similar, in the sense that for a specific loop bandwidth almost the same level of scintillation strength may result in loss of phase lock. The first-order loop was found to be more susceptible as it can lose phase lock at much lower level of scintillation strength compared to the other two loop orders.

Chapter Six: Carrier Tracking Loop Performance in the Presence of Scintillation

Equations for ionospheric scintillation effects on GPS receiver carrier tracking phase error and carrier velocity error were determined in Chapter five. In this chapter, the tools developed (closed form equations and software simulations) are used to investigate the impact of scintillation on the probability of loss of lock and the probability of cycle slips. In addition, the optimum loop noise bandwidth for a minimum tracking loop error is calculated as function of scintillation parameters (T_{scin}, S_4, ν). Finally, the effects of scintillation on the correlation of different L-band signals transmitted by the GPS are explored, and further used in the determination of carrier tracking error of a semi-codeless receiver. These investigations demonstrate capabilities of such tools to assess expected receiver performance and develop new receiver design.

6.1 Probability of Loss of Phase Lock

The thermal noise is given as a function of the scintillation intensity I_s in Equation (5.19). Accordingly, there exists an *intensity threshold level* ($I_{s,TH}$) below which the noise error would exceed the tracking lock threshold. The probability that the signal intensity will drop below the $I_{s,TH}$, therefore resulting in loss of phase lock can be obtained from [Knight and Finn, 1998]

$$\begin{aligned} P_{LOSS} &= \int_0^{I_{s,TH}} p(I_S)\, dI_S \\ &= \frac{u^u}{\Gamma(u).\langle I_S \rangle^u} \int_0^{I_{s,TH}} I_S^{u-1} e^{-u.I_S/\langle I_S \rangle}\, dI_S \end{aligned} \tag{6.1}$$

where $p(I_s)$ represents the intensity scintillation probability density function defined in Equation (2.32), and $u = 1/S_4^2$. The intensity scintillation threshold $I_{s,TH}$ can be obtained from Equation (5.19) as

$$I_{s,TH} = \frac{1 + \sqrt{1 + 2\left\langle \theta_n^2 \right\rangle / (\eta B_n)}}{2\left\langle \theta_n^2 \right\rangle (c/n_0)/B_n} \tag{6.2}$$

This equation is plotted in Figure 6.1, as a function of B_n and C/N_0 assuming $\left\langle \theta_n^2 \right\rangle_{threshold} = (\pi/12)^2$ and $\eta = 1$ ms. As shown in the figure, for C/N_0= 40 dB-Hz, the intensity threshold is calculated as -16.5, -13.5 and -12 dB, respectively, at B_n= 5, 15 and 25 Hz. This means that, in order for the tracking loop to maintain phase lock, the signal fading should not be less than -16.5 dB when B_n = 5 Hz, and should not be less than -12 dB when B_n = 25 Hz. Thus, similar to thermal noise and unlike phase scintillation, better intensity scintillation performance is obtained at lower loop bandwidth.

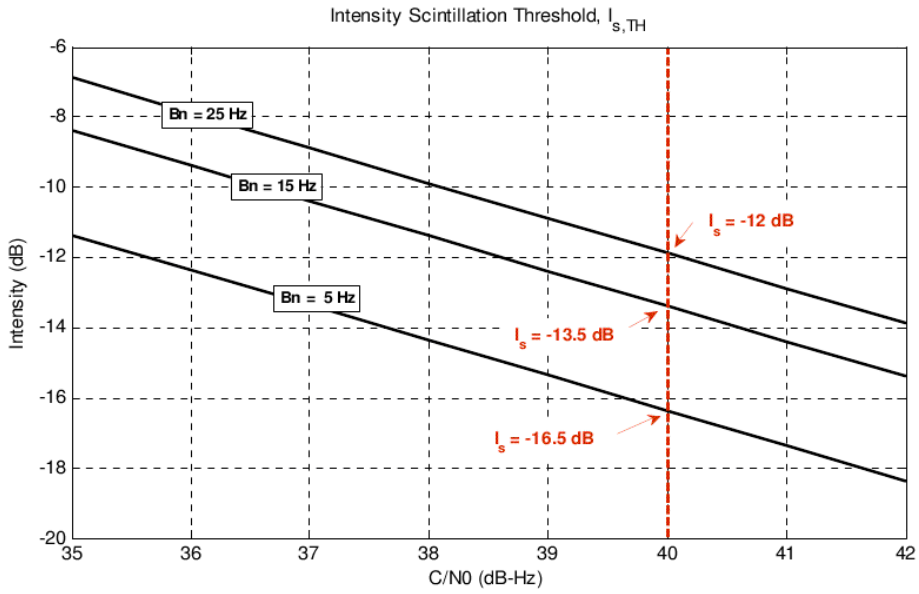

Figure 6.1: Intensity scintillation threshold for minimum probability of losing lock.

Using Equations (5.23) and (6.2), the probability of loss of lock at different intensity scintillation levels is calculated and illustrated in Figure 6.2. As expected, probability of loss of lock is considerably lower at relatively high carrier-to-noise ratios.

For the simulation part, intensity scintillation records corresponding to S_4 = 0.3 to 1 are generated and modulated on the GPS L_1 signal. The scintillated signal is then processed in the carrier tracking loop simulators, and the tracking error is measured. For ten seconds of data (including 10000 samples), the percentage of time that the tracking error has exceeded the tracking error threshold (i.e. $\pm\pi/12$ radians) is determined. The simulation results for C/N_0= 41 dB-Hz, B_n = 25 Hz, η=1ms, and S_4 = 0.3 to 1 are shown in Figure 6.2 (solid red line). Simulation closely follows the theory at the same C/N_0 level.

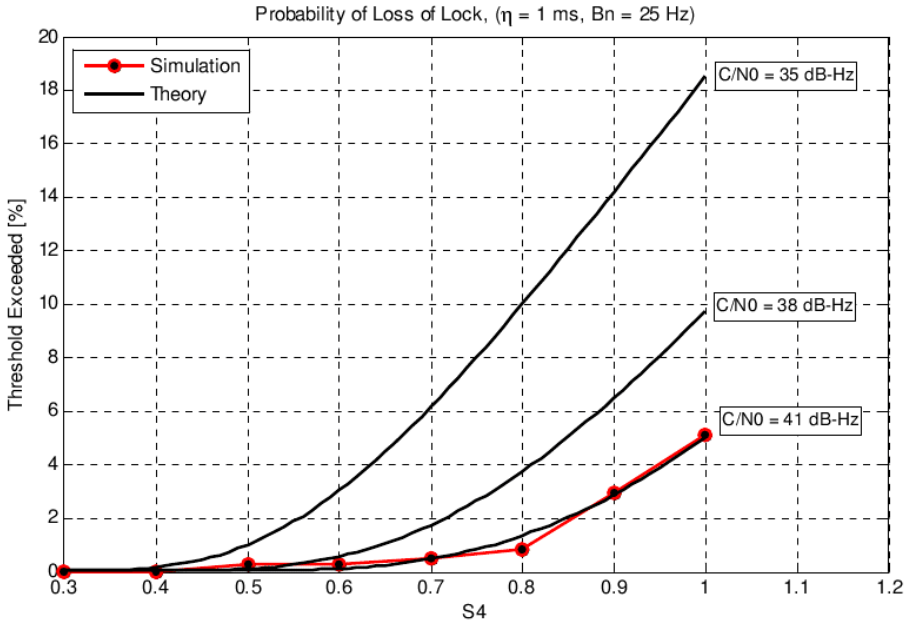

Figure 6.2: Probability of loss of lock.

6.2 Impact of Intensity Scintillation on Mean Cycle Slip Time

In the GPS context, a cycle slip refers to a sudden discontinuity in the GPS carrier phase observable caused by temporary signal loss. Cycle slips may occur in a GPS receiver when tracking is interrupted due to [Kim and Langley, 2002; El-Rabbany, 2002]

- Satellite signal blockage by trees, buildings, bridges, etc.
- Weak received signals results from high satellite-platform dynamics, severe ionospheric disturbances, radio interference, etc.
- Failure in the receiver's software signal processing algorithms.

Cycle slips may occur momentarily or may persist over a longer time. Since they can cause data loss, cycle slips need to be monitored carefully if accurate positioning is to be achieved. The impact of severe ionospheric disturbances (in terms of intensity scintillation or signal fading) on the mean cycle slip time is investigated in this section.

The mean cycle slip time $\overline{T}_{slip}$ is defined as the *average time* where the carrier tracking error exceeds $\pm\pi$ radians for a squaring-type phase-locked loop (e.g. Costas), and $\pm 2\pi$ for a non-squaring loop [Humphreys et al., 2010]. For a first-order Costas-type tracking loop, the $\overline{T}_{slip}$, in units of seconds, is given as [Holmes and Raghavan, 2009]

$$\overline{T}_{slip} = \frac{\pi^2 \rho}{2B_n} I_0^2(\rho), \tag{6.3}$$

where $\rho = 1/4\langle\theta_n^2\rangle$ is the loop signal-to-noise ratio (SNR) with $\langle\theta_n^2\rangle$ being the phase error variance due to thermal noise, and $I_0(\cdot)$ is the modified Bessel function of the first kind of order zero.

For higher-loop SNRs, mean cycle slip time can be approximated by [Holmes and Raghavan, 2009]

$$\overline{T}_{slip} = \frac{\pi}{4B_n} e^{2\rho}. \tag{6.4}$$

To evaluate the discrepancy between the exact and the approximate expression for a first-order carrier tracking loop mean cycle time, Equations (6.3) and (6.4) are plotted in Figure 6.3 assuming $B_n = 25$ Hz.

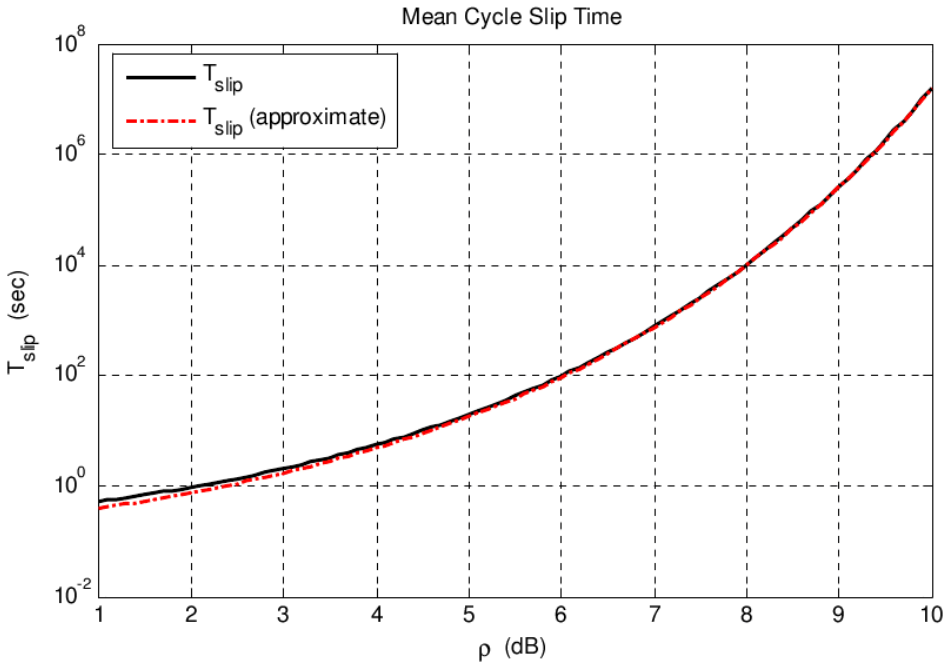

Figure 6.3: Exact and approximate mean cycle slip time for the 1st order tracking loop.

As can be seen from the figure, both expressions are effectively the same after about 4 dB loop SNR. In order to determine the mean slip time for higher order tracking loops, Holmes and Raghavan [2009] have applied a modification to Equation (6.4) as

$$\overline{T}_{slip} \approx \frac{\pi}{4B_n} e^{2\alpha\rho} \tag{6.5}$$

where α is an effective SNR loss and its value depends on the carrier tracking loop order. Holmes and Raghavan [2009] have shown that for sufficiently large loop signal-to-noise ratios ($\rho \geq 4$ dB), Equation (6.5) fits the simulation data very well with $\alpha = 1$, $\alpha = 0.891$, and $\alpha = 0.794$ for a first-, second-, and third-order carrier tracking loop, respectively.

Using Equation (6.5) along with Equations (5.18), (5.19) and (5.23), a new expression is derived in this section which defines the mean cycle slip time $\overline{T}_{slip}$ as a function of intensity scintillation index S_4. In the absence of intensity scintillation or signal fading, the thermal noise tracking error variance follows Equation (5.7) and, as a result, the mean cycle slip time can be expressed as

$$\begin{aligned}\overline{T}_{slip} &\approx \frac{\pi}{4B_n}\exp(2\alpha\rho) \\ &\approx \frac{\pi}{4B_n}\exp\left(\frac{\eta\alpha(c/n_0)^2}{B_n(1+2\eta(c/n_0))}\right).\end{aligned} \tag{6.6}$$

According to this equation, for a fixed loop bandwidth and pre-detection integration time, a longer mean cycle slip time corresponds to a higher C/N_0 level. Shorter mean cycle slip times are therefore expected in the presence of intensity scintillation, as it decreases the level of C/N_0 given in Equation (5.18), and increases the thermal noise error given in Equations (5.19). By substituting the average thermal noise mean square error in the presence of intensity scintillation from Equation (5.23) in Equation (6.6), $\overline{T}_{slip}$ can be expressed, as a function of S_4, via

$$\overline{T}_{slip} \approx \frac{\pi}{4B_n}\exp\left(\frac{\alpha\eta(c/n_0)^2(1-3S_4^2+2S_4^4)}{B_n[1+2\eta(c/n_0)(1-2S_4^2)]}\right), \qquad S_4 < 1/\sqrt{2} \tag{6.7}$$

The effect of signal fading on $\overline{T}_{slip}$ is plotted in Figure 6.4 for the second-order tracking loop, where α=0.891. In this figure, the black line represents the mean slip time in the absence of signal fading (i.e. S_4= 0), and the red line denotes the mean slip time when moderate scintillation is applied (S_4= 0.6). As can be seen from the figure, in the

presence of signal fading, the loop signal-to-noise ratio (ρ) decreases along with the corresponding mean slip time. In other words, cycle slips occur more frequently compared to the time when there is weak or no intensity scintillation activity. The parameters considered in this plot include B_n = 25 Hz, η=1 ms, C/N_0= 25 - 32 dB-Hz, and S_4 = 0.6.

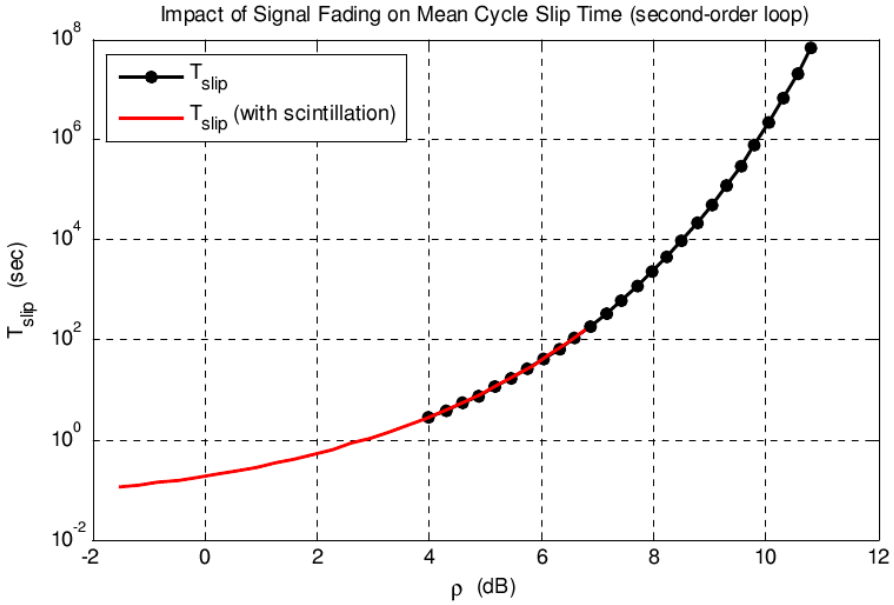

Figure 6.4: Mean slip time in the presence of intensity scintillation for the 2nd order loop.

6.3 Probability of Cycle Slips

The impact of intensity scintillation on the mean time to cycle slip is determined in the previous section in Equation (6.7). In this section, the relationship between the probability of a cycle slip and signal's fade depth and duration is studied. In addition, the effect of ionospheric intensity scintillation on the probability of cycle slips is explored.

Theoretically, for the fade depth (F) and fade duration (τ), the probability of cycle slip is defined via [Hegarty, 1999]

$$P_{slip} = 1 - \exp\left(- \frac{\tau}{\overline{T}_{slip}} \right). \tag{6.8}$$

Substituting $\overline{T}_{slip}$ from Equation (6.6) provides an approximate expression for the probability of cycle slip through

$$P_{slip} \approx 1 - \exp\left(- \frac{4 \tau B_n}{\pi \exp(2\alpha\rho)} \right), \tag{6.9}$$

where

$$\rho = \frac{1}{4\left\langle \theta_n^2 \right\rangle} = \frac{\eta \left((c/n)_{faded} \right)^2}{2B_n \left(1 + 2\eta (c/n)_{faded} \right)}. \tag{6.10}$$

and $(c/n)_{faded} = F \cdot (c/n_0)_{unfaded}$ or, in decibel form, $C/N = F_{dB} + C/N_0$.

The probability of cycle slip is plotted in Figure 6.5 for a 2nd-order loop ($\alpha = 0.891$), assuming the fade duration τ = 0.0001 to 1 s, the fade depth F = -25 to -5 dB, the unfaded carrier-to-noise ratio C/N_0 = 35 dB-Hz, the noise bandwidth B_n = 25 Hz, and the pre-detection integration time η = 1 ms. As one may expect, higher probability of cycle slip corresponds to deeper fade and longer fade durations.

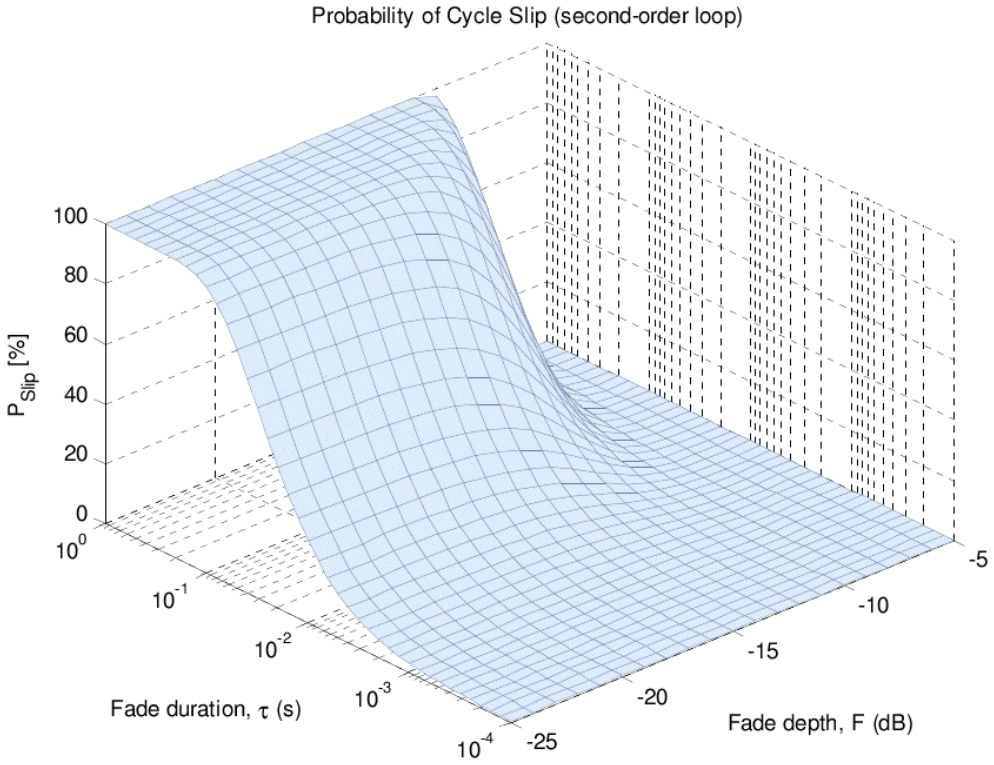

Figure 6.5: Probability of cycle slips as a function of fade depth and fade duration.

As discussed by Humphreys et al. [2010], ionospheric scintillation can cause cycle slipping through, (i) deep power fades accompanied by sudden approximately half-cycle phase transitions, and (ii) prolonged signal intensity fadings. Equations (6.3) and (6.8) apply to the latter case.

In order to study the impact of intensity scintillation on P_{slip}, three seconds of intensity scintillation data is simulated using the scintillation simulator in Chapter two. To generate the data $\nu = 1.33$ and $C_s = 5 \times 10^{20}$ (corresponding to severe scintillation with $T_{scin} \approx -15$ dBrad^2/Hz) are considered. To simplify the calculation of fade depth and fade duration, the intensity scintillation magnitude is quantized, in 5 dB steps, as shown in the

second panel of Figure 6.6. Using Equation (5.9), the probability of cycle slip is calculated for the quantized fade depth and duration, assuming the unfaded $C/N_0 = 42$ dB-Hz, $\eta = 1$ ms, and $B_n = 25$ Hz.

As can be seen from the figure, even under the severe scintillation activities, the probability of cycle slip, *caused by prolonged amplitude fading*, barely exceeds 1.5 percent. The very short fade durations, in comparison with much longer mean time to cycle slip, keep the probability of cycle slip at a low level, even though signal fades are deep.

By substituting Equation (5.23) in the loop signal-to-noise ratio term, a new expression for the probability of cycle slips, in the presence of intensity scintillation, is derived via

$$\begin{aligned} P_{slip} &\approx 1 - \exp\left(-\frac{4\tau B_n}{\pi \exp(2\alpha\rho)} \right) \\ &\approx 1 - \exp\left(-\frac{4\tau B_n}{\pi} \exp\left(\frac{\alpha\eta (c/n_0)^2 (1 - 3S_4^2 + 2S_4^4)}{B_n \ [2\eta (c/n_0)(2S_4^2 - 1) - 1]} \right) \right), \qquad S_4 < 1/\sqrt{2} \end{aligned} \tag{6.11}$$

Equation (6.11) is plotted in Figure 6.7 as a function of fade duration τ, considering the unfaded carrier-to-noise ratio $C/N_0 = 32$ dB-Hz, $B_n = 25$ Hz, $S_4 = 0.6$ and $\eta = 1$ ms.

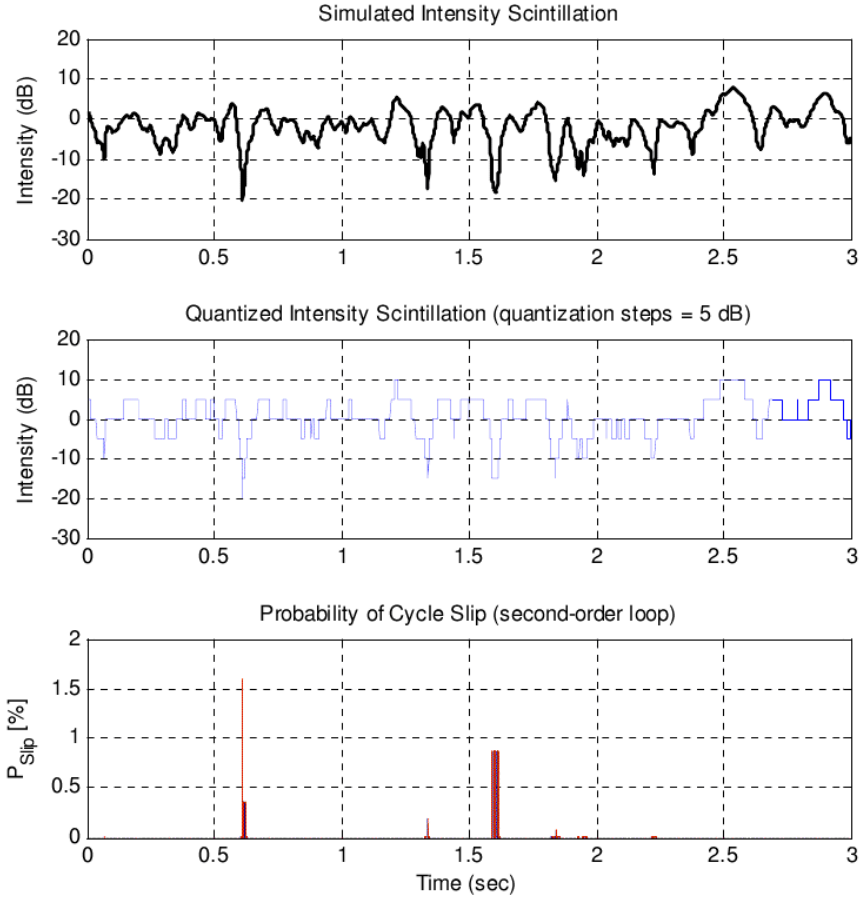

Figure 6.6: Probability of cycle slips for a simulated scintillation data set.

Once again, the results of Figure 6.7 confirms that the impact of *prolonged amplitude fading* on probability of cycle slip is marginal; even at a relatively strong scintillation level $S_4 = 0.6$. For example, for the fade duration $\tau = 3$ s, the probability of one cycle slip is only about 2 percent.

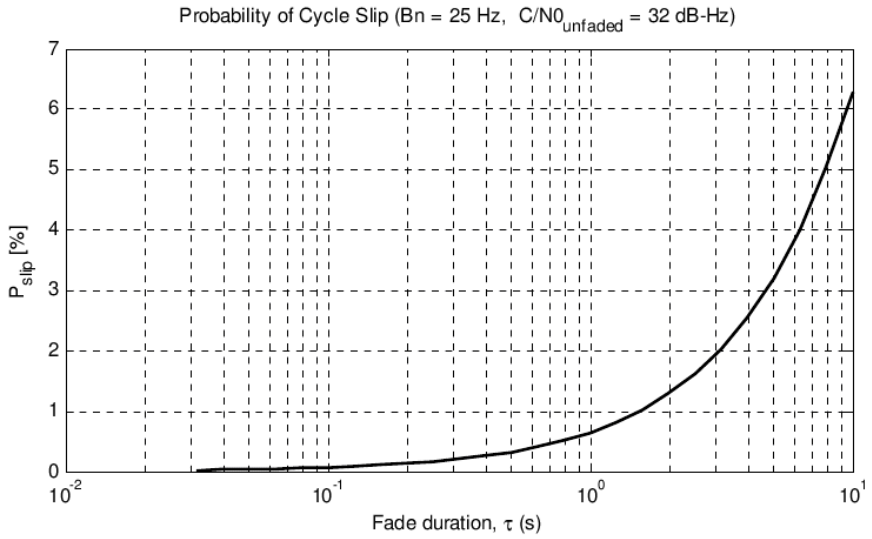

Figure 6.7: Probability of cycle slip in the presence of intensity scintillation.

6.4 Optimum Loop Bandwidth for Minimum Mean Square Error

The equivalent noise bandwidth B_n is a key parameter in the tracking loop design for its direct impact on the loop performance when the loop is subject to system dynamics, ionospheric disturbances and thermal noise. An incorrect choice of loop noise bandwidth can significantly increase the tracking loop error. As mentioned earlier, for a reasonable dynamic and phase scintillation performance, the carrier tracking loop requires a wide bandwidth, whilst for a better thermal noise and intensity scintillation performance a narrow bandwidth is required. An *optimum* loop noise bandwidth, in this context, refers to a *minimum* possible bandwidth (cf. Figure 5.14) that minimizes the total carrier tracking loop mean square error when all sources of errors are present.

The phase tracking mean square errors, given in Equations (5.26) and (5.38), are used in this section to derive an expression for the optimum equivalent noise bandwidth which

leads to the minimum mean square tracking error. The optimum bandwidth ($B_{n,OP}$) is determined for two cases: that is when the tracking loop is subject to

- Thermal noise and ionospheric scintillation,
- Thermal noise, ionospheric scintillation, and system dynamics.

6.4.1 $B_{n,OP}$ in the Presence of Thermal Noise and Scintillation Components

The phase tracking mean square error $\left\langle \theta_e^2 \right\rangle$ in the presence of thermal noise and ionospheric scintillation is given in Equation (5.26). In this equation, the loop natural frequency $f_n = \omega_n / 2\pi$ is related to the loop bandwidth B_n via $f_n = \gamma B_n$ where, from Table 4.3,

$$\gamma = \begin{cases} \dfrac{4}{2\pi}, & \beta = 1 \\ \dfrac{8\zeta}{2\pi(4\zeta^2+1)}, & \beta = 2 \\ \dfrac{1.2}{2\pi}, & \beta = 3 \end{cases} \tag{6.12}$$

Using Equations (5.26) and (6.12), the derivative of $\left\langle \theta_e^2 \right\rangle$ with respect to the loop noise bandwidth is calculated as

$$\begin{aligned} \frac{\partial \left\langle \theta_e^2 \right\rangle}{\partial B_n} = & \left(\frac{2\eta (c/n_0)(1-2S_4^2)+1}{2\eta (c/n_0)^2 (1-3S_4^2+2S_4^4)} \right) \\ & + (1-2\nu) T_{scin} \frac{\pi}{\beta} \gamma^{1-2\nu} B_n^{-2\nu} \csc\left(\frac{\pi(\nu-0.5)}{\beta} \right). \end{aligned} \tag{6.13}$$

Consequently, letting $\partial \left\langle \theta_e^2 \right\rangle / \partial B_n = 0$, and solving for B_n will result in

$$B_{n,OP} = \left(\frac{T_{scin}\ \pi\ (2\nu - 1)\csc\left(\frac{\pi(\nu - 0.5)}{\beta}\right)}{\beta\,\gamma^{2\nu-1}\,\frac{2\eta(c/n_0)(1-2S_4^2)+1}{2\eta(c/n_0)^2(1-3S_4^2+2S_4^4)}} \right)^{\frac{1}{2\nu}}, \qquad S_4 < 1/\sqrt{2} \qquad (6.14)$$

Equation (6.14) is plotted in Figure 6.8 as a function of phase scintillation strength T_{scin} and intensity scintillation index S_4, assuming $\beta = 2$, $\eta = 1$ ms, $\nu = 1.33$ and $C/N_0 = 45$ dB-Hz. For this optimum loop bandwidth, the minimum mean square error, given in Equation (5.26), is plotted in Figure 6.9.

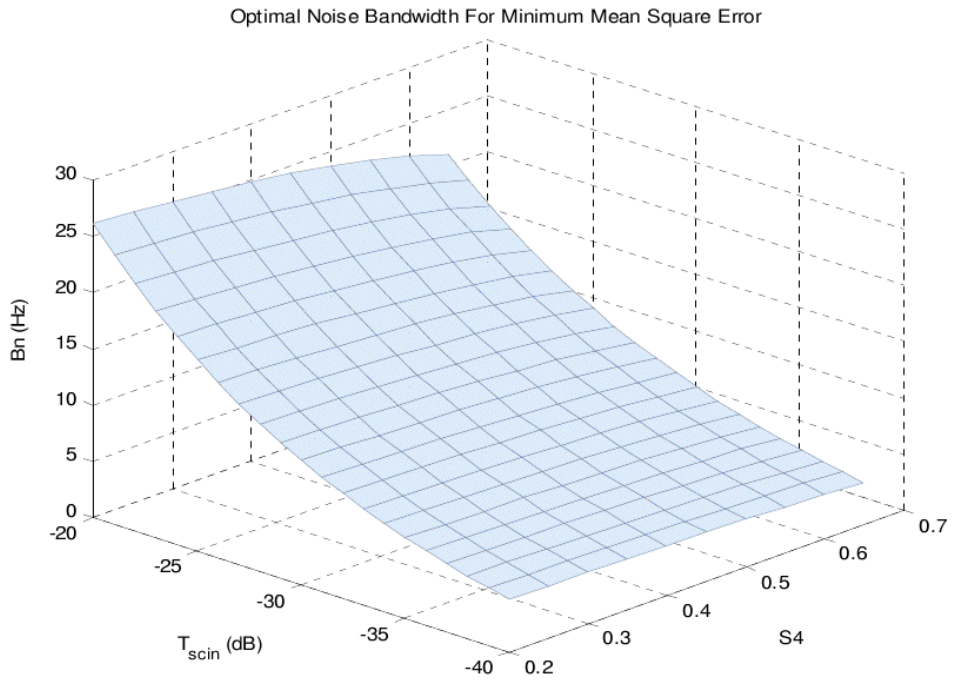

Figure 6.8: $B_{n,OP}$ in the presence of thermal noise and ionospheric scintillation components.

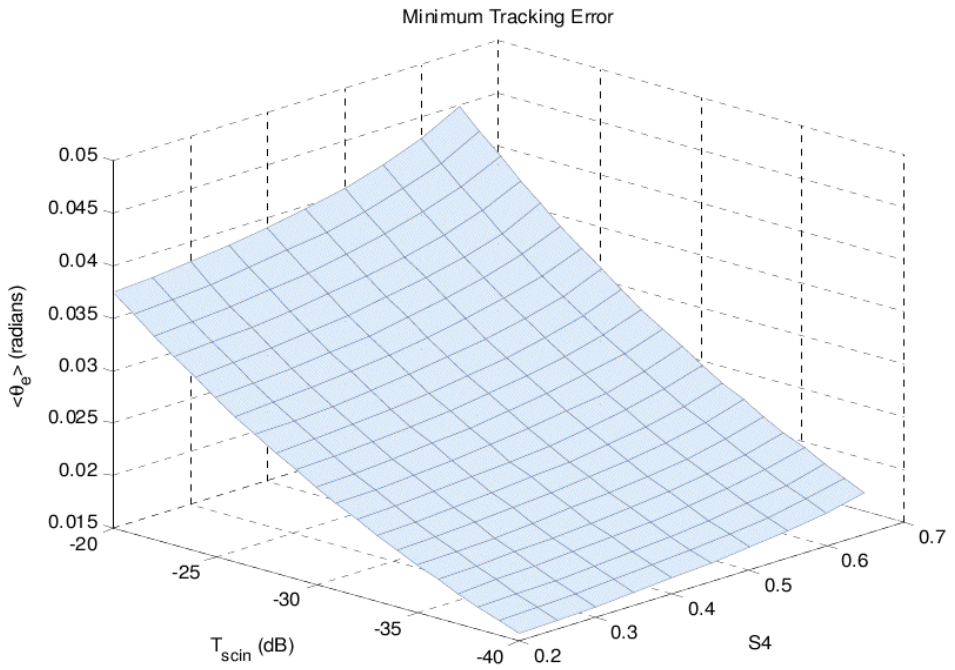

Figure 6.9: Minimum mean square error for $B_{n,OP}$ shown in Figure 6.8.

The plot of the minimum mean square error is repeated in Figure 6.10 to compare the theoretical predictions with the simulation results. To generate the simulation results, two scintillation realizations, corresponding to

(i) Weak scintillation with T_{scin} = -35 dBrad^2/Hz and S_4 = 0.24,

(ii) Moderate scintillation with T_{scin} = -28 dBrad^2/Hz and S_4 = 0.52

are simulated using the scintillation simulator in Chapter two. For each realization, the resulting scintillated GPS signal is processed in the tracking loop simulators. Substituting the weak scintillation parameters in Equation (6.14) results in $B_{n,OP}$ = 7 Hz, and for the moderate scintillation, results in $B_{n,OP}$ = 11.7 Hz. Accordingly, the bandwidth of the carrier tracking loop simulator was set to 7 Hz and 11.7 Hz when processing the weak

and moderate scintillation scenarios, respectively. For each scenario, the carrier tracking error, in radians, is measured and displayed in Figure 6.10 with a solid red circle.

In the second test, for each simulation scenario, the bandwidth of the tracking loop simulator was set to a value smaller than the theoretically-predicted optimum bandwidth, for which the simulation results are shown in Figure 6.10 with solid blue circles. The two simulation results with $B_n = B_{n,OP}$ perfectly match the theoretical predictions, while for $B_n < B_{n,OP}$, the tracking error is significantly larger than the predictions for optimal settings.

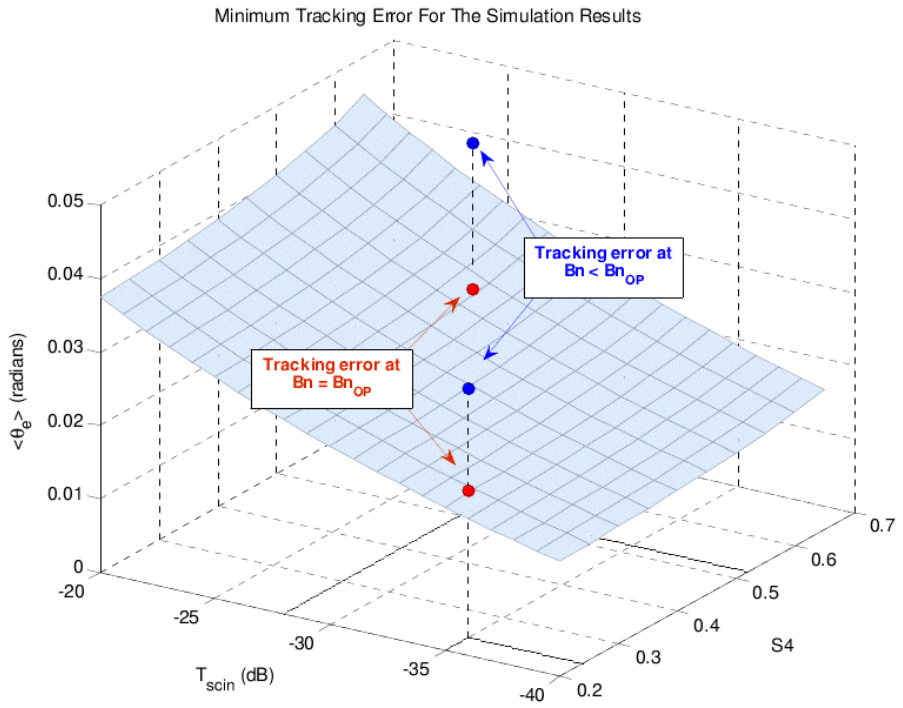

Figure 6.10: Minimum mean square error. Comparison between theory and simulation.

6.4.2 $B_{n,OP}$ in the Presence of Thermal Noise, Ionospheric Scintillation, System Dynamics

In the presence of thermal noise, phase and intensity scintillations, system dynamics and receiver oscillator noise, the phase tracking mean square error is defined according to Equation (5.38). As before, by replacing f_n with γB_n from Equation (6.12), and letting $\partial\left\langle\theta_e^2\right\rangle/\partial B_n = 0$, the optimum (minimum) bandwidth can be obtained via

$$\begin{aligned}\frac{\partial\left\langle\theta_e^2\right\rangle}{\partial B_n} = & \frac{2\eta(c/n_0)(1-2S_4^2)+1}{2\eta(c/n_0)^2(1-3S_4^2+2S_4^4)} \\ & + (1-2\nu)\,T_{scin}\,\frac{\pi}{\beta\,\gamma^{2\nu-1}}B_n^{-2\nu}\csc\left(\frac{\pi(\nu-0.5)}{\beta}\right) \\ & + (1-2n)\,\frac{D^2}{(2\pi)^{2n}}\frac{\pi}{\beta\,\gamma^{2n-1}}\,B_n^{-2n}\csc\left(\frac{\pi(n-0.5)}{\beta}\right) \\ & = 0\end{aligned} \tag{6.15}$$

Therefore,

$$\begin{aligned}\frac{2\eta(c/n_0)(1-2S_4^2)+1}{2\eta(c/n_0)^2(1-3S_4^2+2S_4^4)} = & \underbrace{\left(\frac{\pi(2\nu-1)\,T_{scin}}{\beta\,\gamma^{2\nu-1}}\csc\left(\frac{\pi(\nu-0.5)}{\beta}\right)\right)}_{A_1}B_n^{-2\nu} \\ & + \underbrace{\left(\frac{\pi(2n-1)D^2}{(2\pi)^{2n}\beta\,\gamma^{2n-1}}\csc\left(\pi\beta^{-1}(n-0.5)\right)\right)}_{A_2}B_n^{-2n} \\ & = A_1\,B_n^{-2\nu} + A_2\,B_n^{-2n}\end{aligned} \tag{6.16}$$

Since $0.5 < \nu < 1.5$, Equation (6.16) would generally be a polynomial with a non-integer order and, therefore, it would be hard to obtain a closed form expression for $B_{n,OP}$. The

equation has to be solved either numerically or analytically for integer values of ν. As an example, for $\nu = n = 1$, the optimum bandwidth is obtained via

$$B_{n,OP} = \sqrt{\frac{2\eta(c/n_0)^2(1-3S_4^2+2S_4^4)(A_1+A_2)}{2\eta(c/n_0)(1-2S_4^2)+1}}. \tag{6.17}$$

where A_1 and A_2 are given in Equation (6.16).

6.5 Impact of Ionospheric Scintillation on L-band Signals Correlation

The concept of correlation or linear dependence defined in probability and statistics can be extended to time-varying scintillated GPS signals. The purpose of this section is to determine the relationship between the scintillation-induced phase fluctuations of two GPS signals (e.g. L_1/L_2 and L_1/L_5) as they pass through the ionospheric irregularities.

To quantitatively describe the correlation of different GPS L-band signals, the phase correlation coefficient [Gherm et al., 2006]

$$\rho_{\delta\phi_i,\delta\phi_j} = \frac{\langle \delta\varphi_i \, \delta\varphi_j \rangle}{\sqrt{\langle \delta\varphi_i^2 \rangle \langle \delta\varphi_j^2 \rangle}} \qquad -1 < \rho_{\delta\phi_i,\delta\phi_j} < 1 \tag{6.18}$$

is calculated for two sets of simulated phase scintillation records, where the terms $\delta\varphi_i$ and $\delta\varphi_j$ represent phase fluctuations, and $\langle \delta\varphi^2 \rangle$ denotes phase mean square value (which is equal to its variance, as phase scintillation follows a *zero-mean* Gaussian distribution). From Equation (2.36), the phase mean square value is related to the turbulent strength C_s via

$$\left\langle \delta\phi^2 \right\rangle = k^2 l_p C_s \frac{\Gamma(\nu - 1/2)}{4\pi\,\Gamma(\nu + 1/2) q_o^{2\nu-1}}. \tag{6.19}$$

Following Rino and Owen [1984], the relationship between the scale-free turbulent strength C_s and the variance of electron density $\left\langle \delta N_e^2 \right\rangle$ is given as

$$\left\langle \delta N_e^2 \right\rangle = \frac{C_s \;\; q_o^{2-2\nu} \;\; \Gamma(\nu - 1)}{8 \;\; \pi^{3/2} \;\; \Gamma\left(\nu + 1/2\right)}. \tag{6.20}$$

By substituting C_s from Equation (6.20) in Equation (6.19), the scintillated signal phase variance can be related to the variance of electron density via

$$\left\langle \delta\phi^2 \right\rangle = \frac{2\sqrt{\pi}\, k^2 l_p \;\; \Gamma(\nu - 1/2)}{q_o \;\; \Gamma(\nu - 1)} \;\; \left\langle \delta N_e^2 \right\rangle. \tag{6.21}$$

The range of the electron density for the ionosphere is about 10^9 to $10^{12}\, el/m^3$ with approximately 1 percent fluctuation level for the moderate to severe ionospheric conditions [Rino, 2011]. From Equation (6.21), one can expect that the correlation coefficient in Equation (6.18) will decrease as electron density variance increases. To support this, the turbulent strength C_s is determined for the typical range of electron density variance and plotted in Figure 6.11, assuming $\nu = 1.33$, and $q_0 = 0.001$.

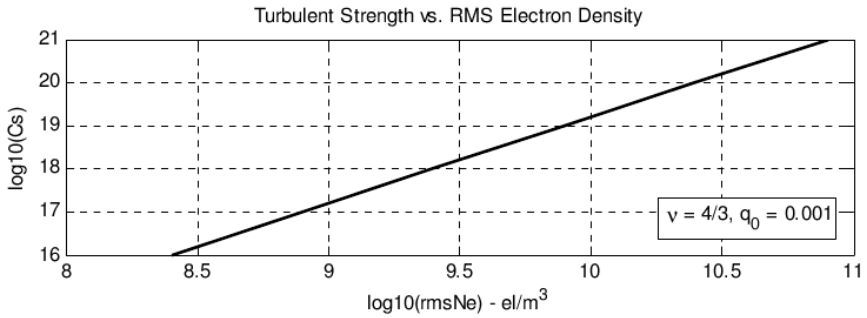

Figure 6.11: Turbulent strength as a function of electron density variance.

For this range of C_s, two sets of phase scintillation records (corresponding to L_1 / L_2 and L_1 / L_5 frequencies) are obtained using the scintillation simulator in Chapter two. The simulation results, along with the corresponding correlation coefficients, and the turbulent strength C_s are illustrated in Figure 6.12 through Figure 6.15. The results indicate that the correlation of phase at spaced frequencies depends on the variance of the electron density fluctuations, and the value of the correlation coefficient for different pairs of frequencies generally decreases as the variance of the electron density fluctuations increases.

Two sets of data with the correlation coefficient $\rho_{\delta\phi_i,\delta\phi_j} \geq 0.8$ are usually considered to be (highly) correlated. As a result, the two sets of phase scintillation records, shown in Figure 6.12 and Figure 6.14, are considered highly correlated only under weak scintillation conditions; otherwise, the correlation is violated (see Figure 6.13 and Figure 6.15). The results of this section are used in the following section when determining the carrier phase mean square error of a semi-codeless receiver.

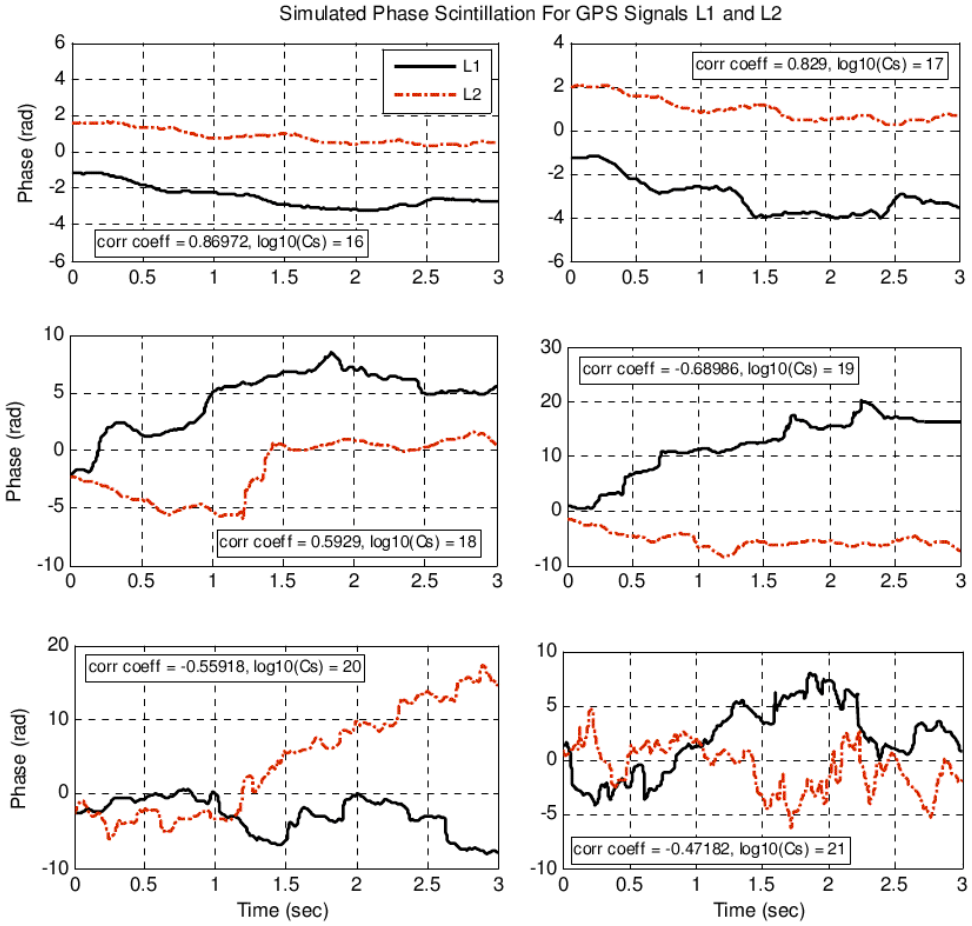

Figure 6.12: Phase scintillation records for GPS L_1 (solid), and L_2 (dashed) signals for Cs values of 10^{16} (weak scintillation) to 10^{21} (severe scintillation).

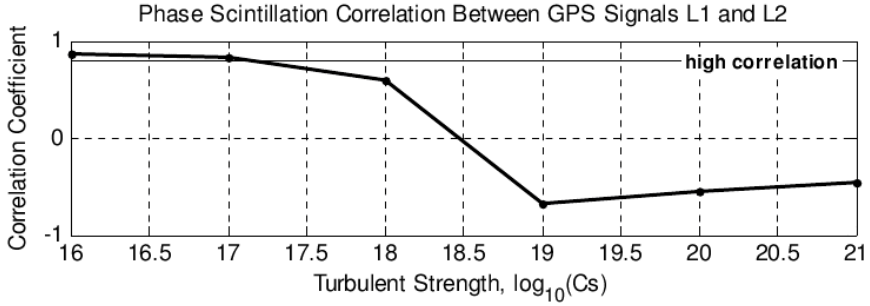

Figure 6.13: The impact of scintillation on the correlation of L_1/L_2 signals.

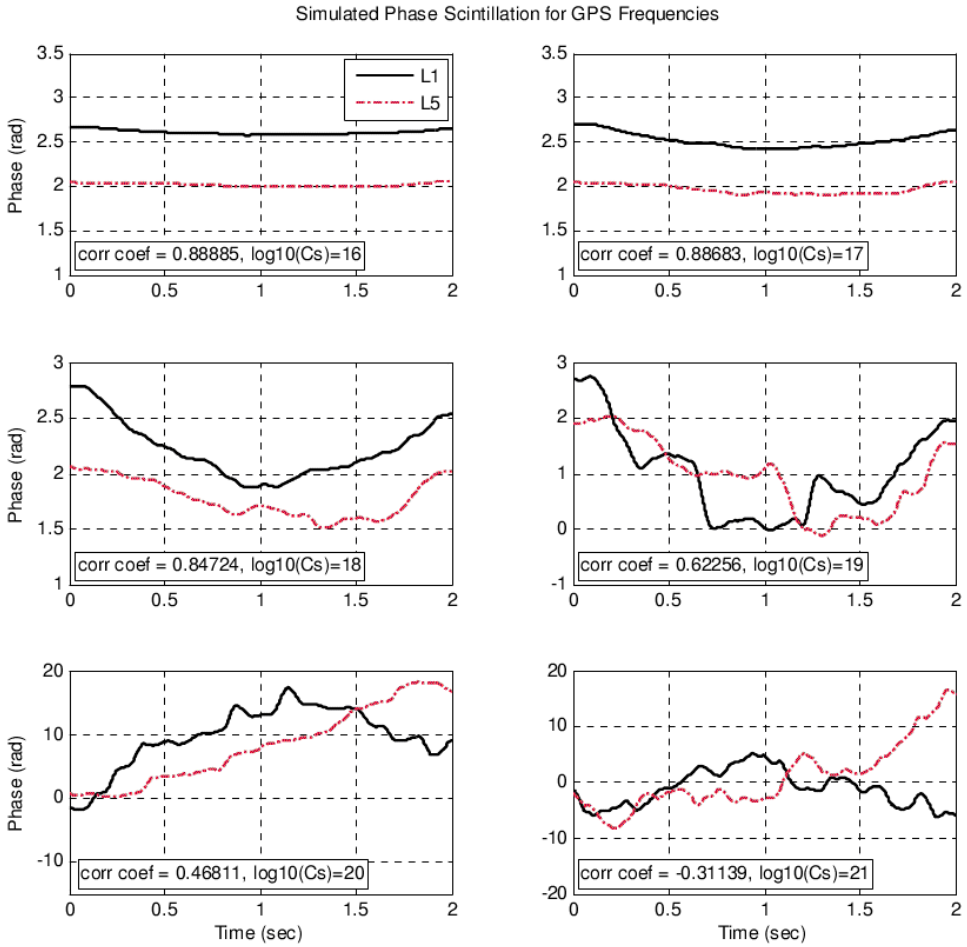

Figure 6.14: Phase scintillation records for GPS L_1 (solid), and L_5 (dashed) signals for Cs values of 10^{16} (weak scintillation) to 10^{21} (severe scintillation).

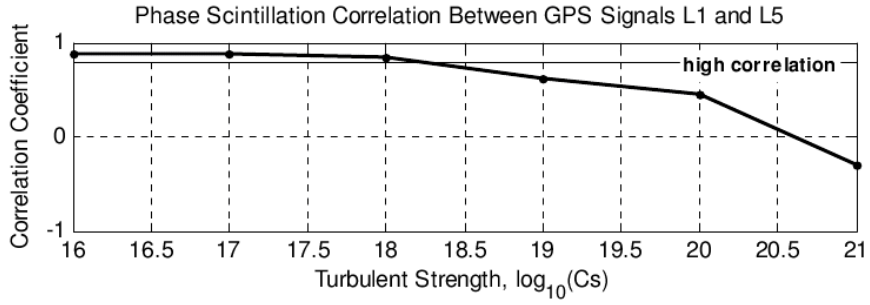

Figure 6.15: The impact of scintillation on the correlation of L_1/L_5 signals.

6.6 Carrier Tracking Error for Semi-codeless Receivers

The GPS L_1 signal is modulated by both C/A-code and P-code, while the L_2 signal is modulated by P-code[13]. As the P-code is designed primarily for military purposes, it is not directly transmitted by the GPS satellites. Instead, the encrypted P(Y)-code (where $Y = P \oplus W$, with W being an unknown encrypting code), is transmitted to the users. The encrypted P(Y)-code is not available to non-authorized users [Tsui, 2000]. Non-authorized users, therefore, require codeless or semi-codeless techniques to extract the encrypted L_2 signal. In applying the semi-codeless technique, the GPS receiver employs the known P-code, along with the bandwidth of the W-code (~500 KHz). The receiver applies the codeless technique without having any information about the encrypted Y-code [Woo, 1999]. Many receivers currently rely on codeless or semi-codeless techniques to extract L_2 observations, particularly those deployed in reference networks for ionospheric or atmospheric studies. Such receivers are highly susceptible to loss of L_2 observations during scintillation events.

The semi-codeless techniques incur a smaller SNR penalty compared with the codeless methods. To increase the probability of signal acquisition and maintain phase lock, both codeless and semi-codeless methods depend on cross-correlation of the signals received at L_1 and L_2 carriers, which is susceptible to ionospheric scintillation effects [Gherm et al., 2006]. Thus, it is important to determine how well the L_1 and L_2 signals are correlated at the carrier phase level when scintillation is present, the seeding source of which is now known to be the time-varying ionospheric electron density fluctuations.

The carrier tracking loop mean square error of a semi-codeless L_2 receiver aided by L_1 signal has previously been determined by Conker et al. [2003] for the case when the loop is subject to scintillation and thermal noise. Their work is modified in this section, by including the user dynamics in the equations and, therefore, achieving more realistic

---

[13] *Few GPS satellites currently transmit the new civilian L2C signal (using L_2 frequency) which is modulated by CM/CL codes.*

results. In addition, an optimum loop noise bandwidth is derived for the semi-codeless L_2 receivers that will result in minimum carrier tracking error. The mean square error is derived for two cases: (a) weak to relatively moderate scintillation level, for which L-band signals are assumed to be fully correlated and, (b) strong scintillation level where L-band signals are considered to be non-correlated.

6.6.1 Tracking Loop Model

Among different available semi-codeless techniques for carrier phase tracking of L_2 signal [e.g. Woo, 1999], the tracking loop model of the semi-codeless L_2 receiver aided by L_1 signal, also known as cross-correlation technique, is considered in this work (see Figure 6.16). The P-code of the L_1 and L_2 signals are synchronized when transmitted from a GPS satellite. Due to the effect of ionospheric refraction, the received signals encounter propagation delay. The amount of delay, in radians, is proportional to the signal wavelength; thus, the L_2 signal is delayed more than the L_1 signal. According to this, at the receiver phase tracking level, the L_1 signal must be delayed with respect to L_2 so that the P-code modulation of the two signals would be aligned. The delayed L_1-P(Y) signal is multiplied with the L_2-P(Y) signal to remove the Y-code modulation (carrier phases are subtracted from one another). The resulting output signal enters the PLL. Using the reconstructed L_1 carrier from C/A-code correlation (with its carrier phase equal to $\theta_1(t)$), the L_2 carrier phase can be recovered [Woo, 1999]. In the model shown below, $\hat{\theta}_2(t)$ denotes the total phase entering the loop, including the effect of both L_1 and L_2 signal incoming phase, and $\theta_e(t)$ denotes the carrier tracking phase error.

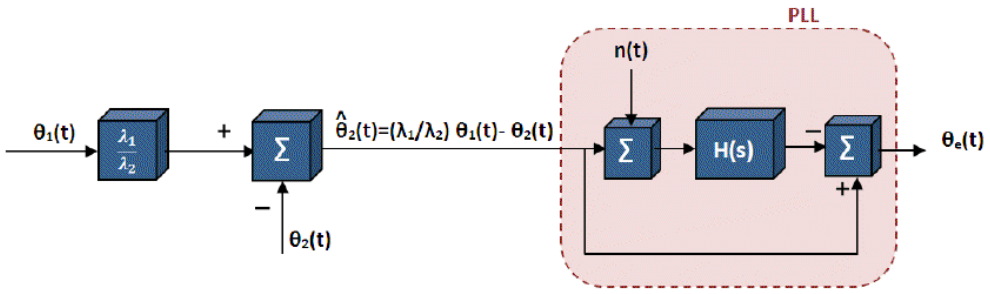

Figure 6.16: Semi-codeless tracking loop model [modified Conker et al., 2003].

6.6.2 Tracking Error under Weak Scintillation Activities

Following Equation (5.6), for a semi-codeless L_2 receiver, the phase tracking mean square error is the sum of the phase scintillation and system dynamic error terms with respect to L_2, plus the thermal noise and receiver oscillator noise:

$$\begin{aligned}\left\langle \theta_e^2 \right\rangle_{P_2} &= \left\langle \theta_n^2 \right\rangle_{P_2} + \left\langle \hat{\theta}_2^2 \right\rangle + \left\langle \theta_o^2 \right\rangle \\ &= \left\langle \theta_n^2 \right\rangle_{P_2} + \left(\left\langle \theta_s^2 \right\rangle + \left\langle \theta_d^2 \right\rangle \right)_{P_2} + \left\langle \theta_o^2 \right\rangle, \qquad (rad^2)\end{aligned} \tag{6.22}$$

The thermal noise component $\left\langle \theta_n^2 \right\rangle_{P_2}$ is dependent on L_1 and L_2 frequencies, and is given by [Conker et al., 2003]

$$\left\langle \theta_n^2 \right\rangle_{P_2} = \frac{B_n}{(c/n_0)_{P_2}(1-S_{4,L2}^2)}\left(1+\frac{1}{2\eta_Y (c/n_0)_{P_1}(1-S_{4,L1}^2)}\right). \tag{6.23}$$

where η_Y is the GPS pre-detection integration time for P(Y)-code on L_2. From Section 2.3.4 of this thesis, $S_{4,L2} \approx 1.4 S_{4,L1}$, and from Table 3.1,

$$\begin{aligned}(C/N_0)_{P_1} &= (C/N_0)_{C/A} - 3 \ dB \\ &= 10 \cdot \log_{10}(c/n_0)_{P_1}\end{aligned} \tag{6.24}$$

and

$$\begin{aligned}(C/N_0)_{P_2} &= (C/N_0)_{C/A} - 6 \ dB \\ &= 10 \cdot \log_{10}(c/n_0)_{P_2}\end{aligned} \tag{6.25}$$

Following Equation (5.8)

$$\left\langle \hat{\theta}_2^2 \right\rangle = \left(\left\langle \theta_s^2 \right\rangle + \left\langle \theta_d^2 \right\rangle \right)_{P_2} = \int_{-\infty}^{\infty} \Phi_{\hat{\theta}_2}(f) \, |1 - H(f)|^2 \ df \tag{6.26}$$

where $\Phi_{\hat{\theta}_2}(f)$ represents the SDF of $\hat{\theta}_2(t)$. For weak scintillation activities, corresponding to a low electron density variance as mentioned in Section 6.5, the L-band signals are assumed to be fully correlated. Therefore, $\Phi_{\hat{\theta}_2}(f)$ is related to the SDF of phase scintillation and system dynamics, with respect to L_1, via [Conker et al., 2003]

$$\Phi_{\hat{\theta}_2}(f) = \Phi_{\theta_1}(f) \cdot \left(\alpha^2 + 1/\alpha^2 - 2 \right), \tag{6.27}$$

where $\alpha = f_{L_2}/f_{L_1} = \lambda_1/\lambda_2$. Equation (6.26) can therefore be calculated using Equations (5.14), (5.37) and (6.27) through

$$\left\langle \hat{\theta}_2^2 \right\rangle = \left[T_{scin} \frac{\pi}{\beta} f_n^{\,1-2\nu} \csc\left(\frac{\pi(\nu - 0.5)}{\beta} \right) + \frac{D^2}{(2\pi)^{2n}} \frac{\pi}{\beta} f_n^{1-2n} \csc\left(\frac{\pi(n-0.5)}{\beta} \right) \right] \times \left(\alpha^2 + 1/\alpha^2 - 2 \right) \tag{6.28}$$

By substituting Equations (6.28) and (6.23) back in Equation (6.22), and assuming $\left\langle \theta_o^2 \right\rangle = 0.01\ (rad^2)$, a new expression for the carrier tracking mean square error of a semi-codeless L_2 receiver aided by L_1 signal is derived as

$$\begin{aligned} \left\langle \theta_e^2 \right\rangle_{P_2} &= \left\langle \theta_n^2 \right\rangle_{P_2} + \left\langle \hat{\theta}_2^2 \right\rangle + \left\langle \theta_o^2 \right\rangle \\ &= \frac{B_{n,P_2}}{(c/n_0)_{P_2}(1 - S_{4,L2}^2)} \left(1 + \frac{1}{2\eta_\gamma (c/n_0)_{P_1}(1 - S_{4,L1}^2)} \right) \\ &+ \left[\frac{T_{scin}\,\pi}{\beta f_{n,P_2}^{\,2\nu-1}} \csc\left(\frac{\pi(\nu - 0.5)}{\beta} \right) + \frac{D^2}{(2\pi)^{2n}} \frac{\pi}{\beta} f_{n,P_2}^{1-2n} \csc\left(\frac{\pi(n-0.5)}{\beta} \right) \right] \\ &\times \left(\alpha^2 + \frac{1}{\alpha^2} - 2 \right) + 0.01 \end{aligned} \tag{6.29}$$

which represents the error in the presence of thermal noise, ionospheric scintillation components, system dynamics, and oscillator noise.

6.6.3 Tracking Error under Strong Scintillation Activities

For a strong scintillation level, L-band signals are considered to be non-correlated. Under this assumption, $\Phi_{\hat{\theta}_2}(f)$ is related to $\Phi_{\theta_1}(f)$ through [Conker et al., 2003]

$$\Phi_{\hat{\theta}_2}(f) = \Phi_{\theta_1}(f) \cdot \left(\alpha^2 + 1/\alpha^2\right) \tag{6.30}$$

thus, the total carrier tracking mean square error in Equations (6.29) changes to

$$\begin{aligned}
\left\langle \theta_e^2 \right\rangle_{P_2} &= \left\langle \theta_n^2 \right\rangle_{P_2} + \left\langle \hat{\theta}_2^2 \right\rangle + \left\langle \theta_o^2 \right\rangle \\
&= \frac{B_{n,P_2}}{(c/n_0)_{P_2}(1-S_{4,L2}^2)}\left(1+\frac{1}{2\eta_Y (c/n_0)_{P_1}(1-S_{4,L1}^2)}\right) \\
&+\left[\frac{T_{scin}\,\pi}{\beta f_{n,P_2}^{\,2\nu-1}}\csc\left(\frac{\pi(\nu-0.5)}{\beta}\right)+\frac{D^2}{(2\pi)^{2n}}\frac{\pi}{\beta}f_{n,P_2}^{1-2n}\csc\left(\frac{\pi(n-0.5)}{\beta}\right)\right] \\
&\times\left(\alpha^2+\frac{1}{\alpha^2}\right)+0.01
\end{aligned} \tag{6.31}$$

Total tracking error, in radians, is plotted in Figure 6.17 in the presence of thermal noise, system dynamics, and oscillator noise for two scintillation realizations corresponding to

(i) Weak scintillation level with T_{scin} = -35 dBrad^2/Hz and $S_{4,L1}$ = 0.24,

(ii) Moderate scintillation with T_{scin} = -28 dBrad^2/Hz and $S_{4,L2}$ = 0.52

and assuming the following parameters: $\nu = 1.33$, $B_{n,P_2} = 0.25$ Hz, $\eta_Y = 1.96\times10^{-6}$ s, $(C/N_0)_{C/A} = 30$ to 50 dB-Hz, $\beta = 2$, $n = 1$ and $r_0 = 0.01$.

The tracking threshold $\left\langle \theta_e^2 \right\rangle_{P_2} = (\pi/12)^2$ is also shown in the figure with a horizontal red line. As can be seen from the figure, a semi-codeless receiver with L_2 aided by L_1 is far more susceptible to scintillation effects than full code correlation receivers, that even a moderate scintillation level ($S_{4,L1} = 0.52$) can result in loss of phase lock at relatively high levels of C/N_0.

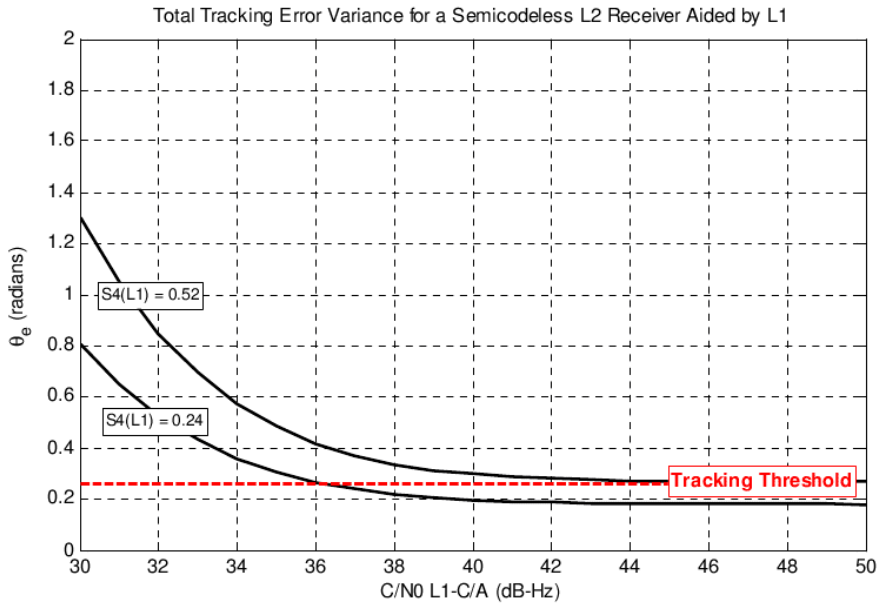

Figure 6.17: Carrier Phase Tracking Error for L_2 semi-codeless method aided by L_1 carrier.

6.6.4 Optimum Loop Bandwidth for a Semi-codeless L_2 Receiver

The general expression for the carrier phase tracking mean square error of a semi-codeless loop, which is subject to thermal noise, ionospheric scintillation and system dynamics, is derived, respectively, in Equation (6.29), for weak scintillation, and in Equation (6.31), for strong scintillation activities. In both cases, $\left\langle \theta_e^2 \right\rangle_{P_2}$ is related to the loop noise bandwidth B_{n,P_2}, either directly (in the thermal noise error term), or through the loop natural frequency $f_{n,P_2} = \gamma B_{n,P_2}$ (in the scintillation and user dynamics error terms), where γ is given in Equation (6.12). Hence, by differentiating $\left\langle \theta_e^2 \right\rangle_{P_2}$ with respect to B_{n,P_2}, equating it to zero, and solving for B_{n,P_2}, the loop bandwidth corresponding to the minimum tracking error can be obtained.

In this section, the general expression for the optimum loop bandwidth $B_{n,OP2}$ that results in minimum mean square error is determined for two cases: that is when the tracking loop is subject to (i) thermal noise and ionospheric scintillation, and (ii) thermal noise, ionospheric scintillation, and system dynamics.

6.6.4.1 Optimum Bandwidth in the Presence of Thermal Noise and Scintillation

Using Equation (6.29), neglecting the effects of system dynamics, the tracking mean square error in the presence of thermal noise and weak scintillation activities can be expressed by

$$\begin{aligned}\left\langle \theta_e^2 \right\rangle_{P_2} &= \frac{B_{n,P_2}}{(c/n_0)_{P_2}(1-S_{4,L2}^2)}\left(1+\frac{1}{2\eta_Y (c/n_0)_{P_1}(1-S_{4,L1}^2)}\right) \\ &+\left(\frac{\pi}{\beta}T_{scin}\,\gamma^{1-2\nu}B_{n,P_2}{}^{1-2\nu}\csc\left(\frac{\pi(\nu-0.5)}{\beta}\right)\right)\times\left(\alpha^2+\frac{1}{\alpha^2}-2\right)+0.01\end{aligned} \tag{6.32}$$

In which f_{n,P_2} is replaced by $(\gamma B_{n,P_2})$. Letting $\partial\left\langle \theta_e^2 \right\rangle_{P_2} \Big/ \partial B_{n,P_2} = 0$, and solving for B_{n,P_2}, the optimum noise bandwidth can therefore be derived as

$$B_{n,OP2} = \left(\frac{T_{scin}\ \pi\ (2\nu-1)\csc\left(\frac{\pi(\nu-0.5)}{\beta}\right)\left(\alpha^2+\frac{1}{\alpha^2}-2\right)}{\beta\,\gamma^{2\nu-1}\,\frac{1+2\eta_Y (c/n_0)_{P_1}(1-S_{4,L1}^2)}{2\eta_Y (c/n_0)_{P_1}(c/n_0)_{P_2}(1-S_{4,L1}^2)(1-S_{4,L2}^2)}} \right)^{\frac{1}{2\nu}} \tag{6.33}$$

Under strong scintillation activities, the term (α^2+1/α^2-2) in the numerator of Equation (6.33) should be replaced by (α^2+1/α^2).

Equation (6.33) is plotted in Figure 6.18 as a function of phase scintillation strength T_{scin} and L_1 signal intensity scintillation index $S_{4,L1}$, assuming $\nu = 1.33$, $\eta_\gamma = 1.96\times10^{-6}$ s, $(C/N_0)_{C/A} = 50$ dB-Hz and $\beta = 2$. Similar to the results of full-code correlation receiver shown in Figure 6.8, wider loop bandwidths are generally required under strong phase scintillation activities (manifested through larger T_{scin} values), while narrower bandwidths are preferred under high intensity scintillation activities (manifested through larger $S_{4,L1}$ values). Equation (6.33) applies the tradeoff between these two opposite conditions to obtain the best loop bandwidth.

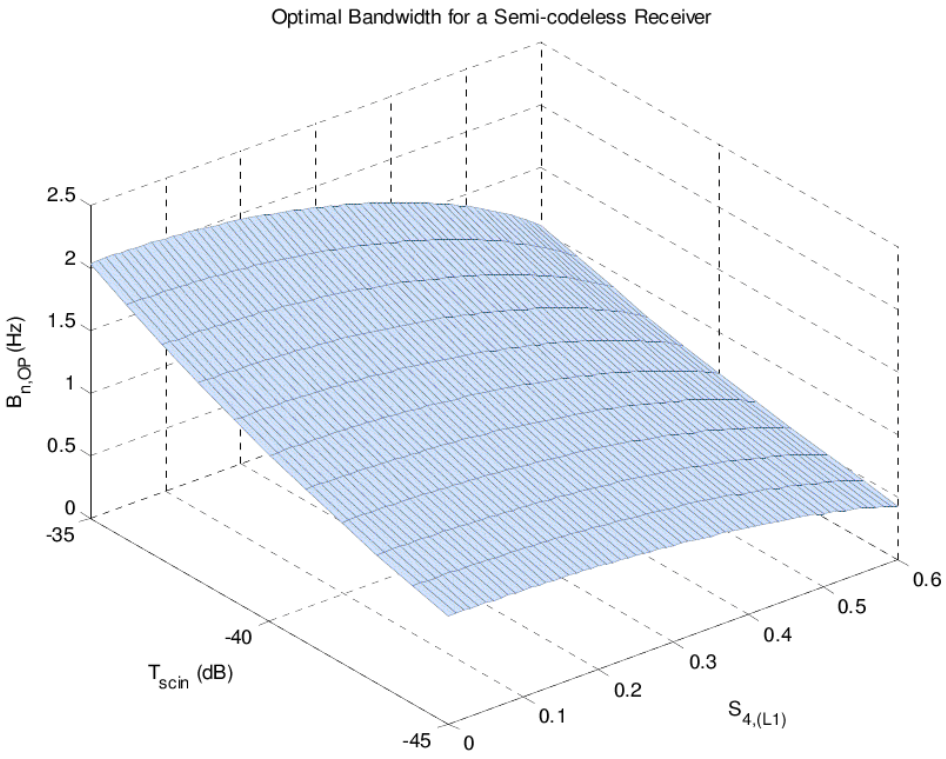

Figure 6.18: Optimum loop bandwidth for minimum mean square error for L_2 semi-codeless aided by L_1 carrier.

6.6.4.2 *Optimum Bandwidth in the Presence of Thermal Noise, Scintillation and System Dynamics*

When the tracking loop is subject to thermal noise, weak scintillation and user dynamics, the optimum bandwidth can be determined through differentiating Equation (6.29) with respect to B_{n,P_2}, which results in

$$\begin{aligned}\frac{\partial\left\langle\theta_e^2\right\rangle_{P_2}}{\partial B_{n,P_2}} &= \frac{\left(1+\dfrac{1}{2\eta_Y (c/n_0)_{P_1}(1-S_{4,L1}^2)}\right)}{(c/n_0)_{P_2}(1-S_{4,L2}^2)} \\ &+ \underbrace{\left[(1-2\nu)\frac{\pi T_{scin}}{\beta\gamma^{2\nu-1}}\csc\left(\frac{\pi(\nu-0.5)}{\beta}\right)\left(\alpha^2+\frac{1}{\alpha^2}-2\right)\right]}_{M_1} B_{n,P_2}{}^{-2\nu} \\ &+ \underbrace{\left[(1-2n)\frac{\pi D^2}{\beta\gamma^{2n-1}(2\pi)^{2n}}\csc\left(\frac{\pi(n-0.5)}{\beta}\right)\left(\alpha^2+\frac{1}{\alpha^2}-2\right)\right]}_{M_2} B_{n,P_2}{}^{-2n} = 0\end{aligned} \tag{6.34}$$

In this case, a closed form expression for $B_{n,OP2}$ is difficult to obtain as Equation (6.34) is generally a polynomial with a non-integer order. However, for $\nu = 1$ and $n = 1$, the equation can be solved analytically via

$$B_{n,OP2} = \sqrt{\frac{2\eta_Y (c/n_0)_{P_1}(c/n_0)_{P_2}(1-S_{4,L1}^2)(1-S_{4,L2}^2)(M_1+M_2)}{1+2\eta_Y (c/n_0)_{P_1}(1-S_{4,L1}^2)}}. \tag{6.35}$$

6.7 Summary

Using the thermal noise mean square error expression for given loop bandwidth and carrier-to-noise ratio in the presence of intensity scintillation, an intensity threshold level $(I_{s,TH})$ was obtained in this chapter, below which the carrier tracking loop may lose lock.

This expression was further used to determine the impact of signal fading on the probability of loss of phase lock (P_{LOSS}). Based on the results achieved in this work, the probability of loss of lock was found to be highly dependent on the effective carrier-to-noise ratio and can be considerably high in the presence of strong signal fadings.

The probability of cycle slip (P_{slip}) is a function of mean cycle slip time ($\overline{T}_{slip}$) and signal fade duration (τ). By defining $\overline{T}_{slip}$ in terms of intensity scintillation index (S_4), a new expression was derived in this chapter which can be used to determine the probability of cycle slips in the presence of intensity scintillation. As shown by the simulation results, the very short fade durations, in comparison with much longer mean cycle slip time, keep the probability of cycle slip, caused by prolonged amplitude fading, at a marginal level.

The phase tracking mean square error expression obtained in Chapter five was used to derive an expression for the optimum (minimum possible) equivalent noise bandwidth in terms of scintillation, tracking loop and system dynamics parameters. This optimum bandwidth is believed to result in a minimum mean square tracking error when the loop is subject to thermal noise, ionospheric scintillation, and system dynamics.

To study the effects of scintillation on the correlation of different L-band signals transmitted by the GPS, two sets of phase scintillation records (corresponding to L_1 / L_2 and L_1 / L_5 frequencies) were simulated, and for each data set, the phase correlation coefficient was determined. The phase correlation at different spaced frequencies was found to be dependent on the variance of the electron density fluctuations and, in general, the value of the correlation coefficient for different pairs of frequencies decreased as the variance of the electron density fluctuations increased. The simulated phase scintillation records were considered highly correlated only under weak scintillation conditions.

An expression was obtained for the carrier phase mean square error of a semi-codeless L_2 receiver aided by L_1 for the case when the loop was subject to scintillation, thermal noise, and user dynamics. In addition, an expression for the optimum loop noise bandwidth was

derived for the semi-codeless L_2 receivers that would result in minimum carrier tracking error. As shown in the results, a semi-codeless receiver with L_2 aided by L_1 is far more susceptible to scintillation effects than full code correlation receivers and even a moderate scintillation level can result in loss of phase lock at relatively high levels of C/N_0.

Chapter Seven: Summary, Conclusions, Recommendations, and Future Studies

7.1 Overview

The performance of a generic GPS receiver carrier tracking loop, subject to ionospheric scintillations, is studied in this thesis via theoretical analyses and simulation results. A physics-based simulation of equatorial scintillations has been employed to provide a full variety of test cases for the simulated carrier tracking loop to assess GPS receiver performance. This simulation tool is novel in allowing oblique signal propagation for multiple frequencies. The scintillation simulation algorithms have been verified through comparison with real scintillation data collected in the equatorial region (Ascension Island) during the solar maximum of 2001. The simulation is determined to accurately represent realistic scintillation effects. The utilization of the scintillation simulation tool is demonstrated through applying it to a GNSS signal (GPS L_1 signal is chosen as an example), and evaluating the subsequent effects on a generic GPS tracking loop model. Accordingly, a widely used stochastic model of scintillation is combined with a Costas-type carrier tracking loop model to define a set of receiver performance parameters. Theoretical predictions – from the derived equations – are verified through comparison with simulation results.

In the presence of thermal noise and user dynamics, scintillation effects on the carrier tracking loop performance are quantified in Chapter five through the definition of two receiver performance measures, namely the carrier tracking phase error and carrier velocity error, as a function of scintillation parameters (T_{scin}, ν and S_4), and tracking loop parameters (f_n, B_n, η and β). Furthermore, the system dynamics upper boundaries and the scintillation thresholds, beyond which the carrier tracking loop may lose lock or the carrier velocity error may exceed a preset level, are calculated.

Using the results of Chapter five, the relationship between the tracking loop mean square error and the loop noise bandwidth is determined in Chapter six, from which an expression for the optimum loop bandwidth resulting in minimum tracking loop error is derived as a function of scintillation parameters (T_{scin}, ν and S_4), and tracking loop parameters (f_n, η and β). In addition, the impacts of scintillations on the probability of loss of lock and the probability of cycle slips are investigated. An equation is obtained that defines the probability of cycle slips as a function of intensity scintillation index S_4.

The effects of scintillation on the correlation of different GPS L-band signals are explored, and further used in the determination of carrier tracking error of semi-codeless L_2 receivers. The general expression for the carrier tracking loop mean square error of a semi-codeless L_2 receiver aided by L_1 signal is amended via including the user dynamics in the equations in order to achieve more realistic results. An optimum loop noise bandwidth for a minimum carrier tracking error is derived for the semi-codeless L_2 receivers.

7.2 Conclusions and Recommendations

Based on the analysis conducted in this thesis, the following conclusions and recommendations are identified:

- There is always a tradeoff between the noise performance and the dynamic performance of a tracking loop when selecting the best loop bandwidth. The carrier tracking loop requires a relatively wide bandwidth to precisely track changes in the carrier phase due to satellite-platform dynamics and ionospheric phase scintillation. On the other hand, the loop requires a narrow bandwidth in order to reject the measurement noise and suppress the effect of intensity scintillation. Results suggest that $B_n \approx 15\,\text{Hz}$ can be considered as a reasonable bandwidth for a conventional Costas carrier tracking loop when the loop is subject to scintillation effects as well as thermal noise and system dynamics.

- Intensity scintillation alone is not as large a concern for the carrier phase tracking, except for severe scintillation conditions and wide loop bandwidths. The effects of phase scintillations on carrier tracking loop error, on the other hand, are found to be considerably higher compared with intensity scintillation. The impact of phase scintillations on the carrier velocity error is also found to be significant even under moderate scintillation levels.

- The probability of loss of lock is highly dependent on the tracking loop's effective carrier-to-noise ratio and can be considerably higher in the presence of strong signal fadings.

- Strong intensity scintillations or signal fading can reduce the mean cycle slip time through decreasing the effective loop signal-to-noise ratio. As a result, cycle slips occur more frequently compared to the time when there is weak or no intensity scintillation activity.

- The overall probability of cycle slip caused by prolonged amplitude fading is relatively low, even under severe scintillation activities. The very short fade durations in comparison with much longer mean time to cycle slip keep the probability of cycle slip at quite low levels.

- In regard to scintillation effects, the performance of the 2^{nd}-, and 3^{rd}-order carrier tracking loop are very similar, in the sense that for a specific loop bandwidth almost the same level of scintillation strength may result in loss of phase lock. The 1^{st}-order loop, however, is more susceptible as it can lose phase lock at much lower level of scintillation strength (approximately 6 dBrad^2/Hz lower at $\nu = 1.33$, and all bandwidths) compared to the other two loop orders.

- The choice of the pre-detection integration time does not significantly affect the carrier tracking error, provided that the signal's carrier-to-noise ratio level is not very low.

- Semi-codeless receivers are far more vulnerable to the phase and intensity scintillation effects than full code correlation receivers. This is mainly due to the narrow bandwidth of semi-codeless carrier tracking loops which increases their sensitivity to phase scintillations, and their low SNR that increases the sensitivity to intensity scintillations. Using the GPS new civil signals will decrease the need for semi-codeless tracking algorithms.

- Finally, the scintillation simulation model introduced in Chapter two is capable of capturing the characteristics of the real-world processes in generating intensity and phase scintillation time histories with parameters (e.g. T_{scin}, ν and S_4) analogous to those for real scintillation data.

7.3 Future Studies

For further studying the effects of ionospheric phase and intensity scintillations on a generic GPS receiver performance one may consider

- Employing hardware simulations to evaluate theoretical analyses. This can be accomplished through processing simulated scintillation data (similar to the results shown in Chapter three of this thesis) in real GPS receivers that are subject to system dynamics, scintillations, multipath and/or electromagnetic interference.

- Employing new developments in GPS technology, namely the new achievements in the signal tracking architectures, and the new civil signals (L_5 and L2C), together with signals from other satellite-based navigation systems such as GLONASS or Galileo. The new tracking loop algorithms might be effective in designing loops that are more robust to scintillation effects. In addition, using one of the new civil signals along with the existing L_1 C/A code, it might be possible to reduce the effect of scintillation on the incoming signal, especially at weak to moderate scintillation levels where the signals are believed to be highly correlated. The scintillation simulation model and the tracking

loop error quantification algorithm developed in this work have potential for many more evaluation of GNSS signals and systems. They can be employed as effective tools in determining expected scintillation impacts on a new system and/or designing better tracking loop models.

- Modeling the impact of the oscillator induced phase jitter in calculating the carrier tracking loop error variance. Unlike thermal noise, the oscillator induced phase jitter increases with decreasing tracking loop equivalent noise bandwidth, thereby limits the lower bound of loop noise bandwidth. Furthermore, it changes the threshold levels of phase scintillation and system dynamics derived in Chapter five.

References

Aarons, J. (1982) "Global Morphology of Ionospheric Scintillations", *Proceedings of IEEE*, vol. 70, no. 4.

Afraimovich, E. L., V. V. Demyanov, P.V. Tatarinov, E. I. Astafieva and I. V. Zhivetiev (2006) "GPS Users Positioning Errors during Disturbed Near-Earth Space Conditions", *Characterizing the Ionosphere*, Meeting Proceedings RTO-MP-IST-056, pp.1-14.

Alban, S., D. M. Akos, S. M. Rock and D. Gebre-Egziabher (2003) "Performance Analysis and Architectures for INS-Aided GPS Tracking Loops", Presented at the ION National Technical Meeting, Anaheim, CA.

Alfonsi, L., L. Spogli, J.R. Tong, G. De Franceschi, V. Romano, A. Bourdillon, M. Le Huy and C.N. Mitchell (2010) "GPS scintillation and TEC gradients at equatorial latitudes in April 2006", *Advances in Space Research*, vol. 47, no. 10, pp. 1750-1757.

Beach, T. L. (2006) "Perils of the GPS phase scintillation index", *Radio Science*, vol. 41, RS5S31.

Beniguel, Y., B. Forte, S. M. Radicella, H. J. Strangeways, V. E. Gherm and N. N. Zernov (2004) "Scintillations effects on satellite to Earth links for telecommunication and navigation purposes", *Annals of Geophysics*, vol. 47, no. 2/3.

Borre, K., D. M. Akos, N. Bertelsen, P. Rinder and S. H. Jensen (2007) "A Software-Defined GPS and Galileo Receiver", Birkhäuser, Boston.

Braasch, M.S. (1996), "Multipath Effects", Global Positioning Systems: Theory and Applications, vol. I, ed. B.W. Parkinson and J.J. Spilker Jr., American Institute of Aeronautics and Astronautics, Washington DC, pp. 547-568.

Brunner, F. K., and M. Gu (1991) "An improved model for the dual frequency ionospheric correction of GPS observations", *Manuscripta Geodaetica*, vol. 16, pp. 205-214.

Chien, C. (2001) "Digital Radio Systems on a Chip: A Systems Approach", Kluwer Academic Publishers, Norwell, MA, USA.

Conker, R. S., M. B. El-Arini, C. J. Hegarty and T. Hsiao (2003) "Modeling the effects of ionospheric scintillation on GPS/Satellite-Based Augmentation System availability", *Radio Science*, vol. 38, no. 1.

Cusumano, J. P. (2005) "The Power Spectral Density and the Autocorrelation (Supplemental Handout)", Experimental Nonlinear Dynamics course, Department of Mechanical Engineering & Applied Mechanics, University of Rhode Island.

de Rezende, L. F. C., E. R. de Paula, I. S. Batista, I. J. Kantor and M. T. de Assis Honorato Muella (2007) "Study of Ionospheric Irregularities During Intense Magnetic Storms", *Revista Brasileira de Geofisica*, vol. 25, supl. 2, pp. 151-158.

El-Gizawy, M. L. (2003) "Development of an Ionosphere Monitoring Technique Using GPS Measurements for High Latitude GPS Users", MSc Thesis, Department of Geomatics Engineering, University of Calgary, Calgary, Alberta, Canada.

El-Rabbany, A. (2002) "Introduction to GPS: The Global Positioning System", Artech House.

Fantino, M., G. Marucco, P. Mulassano and M. Pini (2008) "Performance analysis of MBOC, AltBOC and BOC modulations in terms of multipath effects on the carrier tracking loop within GNSS receivers" *IEEE/ION PLANS 2008*, Monterey, CA, USA.

Fejer, B. G., L. Scherliess and E. R. de Paula (1999) "Effects of the vertical plasma drift velocity on the generation and evolution of equatorial spread F", *Journal of Geophysical Research*, vol. 104, no. A9, pp. 19859-19869.

Finlay, C. C., et al. (2010) "International geomagnetic reference field: The eleventh generation", *Geophysical Journal International*, vol. 183, no. 3, pp. 1216-1230.

Fontana, R. D., W. Cheung, P. M. Novak and T. A. Stansell (2001) "The New L2 Civil Signal", *Proceedings of the 14th International Technical Meeting of the Satellite Division of The Institute of Navigation (ION GPS 2001)*, pp. 617-631, Salt Lake City, UT.

Fremouw, E. J., R. L. Leadabrand, R. C. Livingston, M. D. Cousins, C. L. Rino, B. C. Fair and R A. Long (1978) "Early Results from the DNA Wideband Satellite Experiment - Complex-Signal Scintillation", *Radio Science*, vol. 13, no. 1, pp. 167-187.

Frernouw, E. J. and J. A. Secan (1984) "Modeling and scientific application of scintillation results", *Radio Science*, vol. 19, no. 3, pp. 687-694.

Fremouw, E. J., and A. Ishimaru (1992) "Intensity scintillation index and mean apparent radar cross section on monostatic and bistatic paths", *Radio Science*, vol. 27, no. 4, pp. 539-543.

Gherm, V. E., N. N. Zernov and H. J. Strangeways (2006) "Effect of scintillations on the correlation of different frequency L-band satellite navigation signals on the same transionospheric link", Department of Radio Physics, University of St. Petersburg, St. Petersburg, Russia.

Gopalswamy, N. (2009) "Coronal mass ejections and space weather", Climate and Weather of the Sun-Earth System (CAWSES): Selected Papers from the 2007 Kyoto Symposium, pp. 77–120.

Hegarty, C. J. (1999) “Evaluation of the Proposed Signal Structure for the New Civil GPS Signal at 1176.45 MHz”, The MITRE Corporation, McLean, Virginia.

Hegarty, C., M. B. El-Arini, T. Kim and S. Ericson (2001) “Scintillation modeling for GPS Wide Area Augmentation System receivers”, *Radio Science*, vol. 36, no. 5, pp. 1221-1231.

Hinks, J. C., T. E. Humphreys, B. O’Hanlon, M. L. Psiaki and P. M. Kintner (2008) “Evaluating GPS Receiver Robustness to Ionospheric Scintillation”, *Proceedings ION GNSS 2008*, Savannah, GA.

Holmes, J. K. and S. Raghavan (2009) “The Mean Cycle Slip Time for First-, Second-, and Third-Order PLLs”, Aerospace conference, 2009 IEEE, Big Sky, MT.

Humphreys, T. E., M. L. Psiaki, J. C. Hinks, B. O’Hanlon and P. M. Kintner (2009) “Simulating Ionosphere-Induced Scintillation for Testing GPS Receiver Phase Tracking Loops”, *IEEE Journal of Selected Topics in Signal Processing*, vol. 3, no. 4.

Humphreys, T. E., M. L. Psiaki, J. C. Hinks and P. M. Kintner (2010) “Modeling the Effects of Ionospheric Scintillation on GPS Carrier Phase Tracking”, *IEEE Transactions on Aerospace and Electronic Systems*, vol. 46, no. 4.

Jwo, D. J. (2001) “Optimisation and sensitivity analysis of GPS receiver tracking loops in dynamic environments”, *IEE Proceeding*, Radar-Sonar Navigation, vol. 148, No. 4.

Kamel, A. M. (2010) “Design and Testing of an Intelligent GPS Tracking Loop for Noise Reduction and High Dynamics Applications”, *Proceeding of ION GNSS 2010* - Portland, OR.

Kaplan, E. D. (1996) "Understanding GPS: Principles and Applications", Mobile Communications Series, Artech House.

Kelecy, T., D. Hall, K. Hamada and D. Stocker (2007) "Satellite Maneuver Detection Using Two-line Elements Data", *Proceedings of the Advanced Maui Optical and Space Surveillance Technologies Conference*, Maui, HI.

Kim, D. and R. B. Langley (2002) "Instantaneous real-time cycle-slip correction for quality control of GPS carrier-phase measurements", *Journal of the Institute of Navigation*, vol. 49, pp. 205-222.

Kintner, P. M., H. Kil, T. L. Beach and E. R. de Paula (2001) "Fading timescales associated with GPS signals and potential consequences", *Radio Science*, vol. 36, no. 4, pp. 731-743.

Kintner, P. M., B. M. Ledvina and E. R. de Paula (2007) "GPS and ionospheric scintillations", *Space Weather*, vol. 5, no. S09003.

Klobuchar, J. A. (1991) "Ionospheric effects on GPS", *GPS World*, vol. 2, no. 4, pp. 48-51.

Klobuchar, J. A. (1996) "Global Positioning System: Theory and Applications", vol. I, Progress in Astronautics and Aeronautics, vol. 163, Chapter 12, pp. 485-515.

Knight, M., and A. Finn (1996) "The impact of ionospheric scintillation on GPS performance", *Proceedings of ION GPS-96,* Institute of Navigation, pp. 555-564, Kansas City, MO.

Knight, M., and A. Finn (1998) "The effects of ionospheric scintillations on GPS", Presented at ION-GPS-1998, Institute of Navigation, Nashville, Tenn.

Knight, M., A. Finn and M. Cervera (1998) "Ionospheric effects on Global Positioning System Receivers – Research Report", DSTO Electronics and Surveillance Research Laboratory, 1998.

Langley, R. B., (1997) "GPS Receiver System Noise", GPS World, pp. 40-45.

Lühr, H., and C. Xiong (2010) "IRI-2007 model overestimates electron density during the 23/24 solar minimum", *Geophysical Research Letters*, vol. 37, no. L23101.

Macmillan, S., and M. J. Rycroft (2010) "The Earth's Magnetic Field", Encyclopedia of Aerospace Engineering.

May, M., A. Brown, and B. Tanju (1999) "Applications of Digital Storage Receivers for Enhanced Signal Processing", *Proceedings of the Institute of Navigation GPS 1999*, 14-17 September, Nashville, TN.

Misra, P., and P. Enge (2006) "Global Positioning System - Signals, Measurements, and Performance", Second Edition, Ganga-Jamuna Press.

Mitchell, S. (2008) "Electromagnetic Wave Propagation - Theory and Application to Bathymetric Lidar Simulation", University of Colorado at Boulder, ASEN 6849.

Nichols, J., A. Hansen, T. Walter and P. Enge (1999) "High Latitude Measurements of Ionospheric Scintillation Using the NSTB", *Proceeding of 1999 Technical Meeting and 19th Biennial Guidance Test Symposium*, San Diego, CA.

Olsen, N., G. Hulot and T. J. Sabaka (2007) "The present field", *Treatise on Geophysics*, vol. 5, pp. 33-75.

Prikryl, P., P. T. Jayachandran, S. C. Mushini, D. Pokhotelov, J.W. MacDougall, E. Donovan, E. Spanswick and J.P. St.-Maurice (2010) "GPS TEC, scintillation and cycle slips observed at high latitudes during solar minimum", *Annales Geophysicae*, vol. 28, pp. 1307-1316.

Psiaki, M. L., T. E. Humphreys, A. P. Cerruti, S. P. Powell and P. M. Kintner (2007) "Tracking L1 C/A and L2C Signals through Ionospheric Scintillations", ION GNSS 20th International Technical Meeting of the Satellite Division, Fort Worth, TX.

Ray, J. K. (2000) "Mitigation of GPS Code and Carrier Phase Multipath Effects Using a Multi-Antenna System", PhD Thesis, Department of Geomatics Engineering, University of Calgary, Calgary, Alberta, Canada.

Rino, C. L. (1979) "A power law phase screen model for ionospheric scintillation, 1-Weak scatter", *Radio Science*, vol. 14, no. 6, pp. 1135-1145.

Rino, C. L. (1982) "On the application of phase screen models to the interpretation of ionospheric scintillation data", *Radio Science*, vol. 17, no. 4, pp. 855-867.

Rino, C. L. and J. Owen (1984) "Numerical simulations of intensity scintillation using the power law phase screen model", *Radio Science*, vol.19, no. 3, pp. 891-908.

Rino, C. L. (2011) "The Theory of Scintillation with Applications in Remote Sensing", Wiley-IEEE Press, Hoboken, N.J., ISBN 978-0-470-64477-5.

Secan, J. A., R. M. Bussey, E. J. Fremouw and S. Basu (1995) "An improved model of equatorial scintillation", *Radio Science*, vol. 30, no. 3, pp. 607-617.

Seo, J., T. Walter, E. Marks, T. Y. Chiou and P. Enge (2007) "Ionospheric Scintillation Effects on GPS Receivers during Solar Minimum and Maximum", International Beacon Satellite Symposium, Boston, MA.

Seo, J., T. Walter, T. Y. Chiou, J. Blanch and P. Enge (2008) "Evaluation of Deep Signal Fading Effects Due to Ionospheric Scintillation on GPS Aviation Receivers", Institute of Navigation GNSS 2008, Savannah, GA.

Skone, S. (1998) "Wide Area Ionosphere Grid Modeling in the Auroral Region", PhD Thesis, published as report No. 21023, Department of Geomatics Engineering, University of Calgary, Canada.

Skone, S., G. Lachapelle, D. Yao, W. Yu and R. Watson (2005) "Investigating the Impact of Ionospheric Scintillation using a GPS Software Receiver", Presented at the ION GNSS 2005 Conference, Long Beach, CA.

Skone, S. (2009) "Atmospheric Effects on Satellite Navigation Systems, ENGO 633 Course Notes", Department of Geomatics Engineering, University of Calgary, Canada.

Sojka, J. J., M. V. Subramanium, L. Zhu and R. W. Schunk (1998) "Gradient drift instability growth rates from global-scale modeling of the polar ionosphere", *Radio Science*, vol. 33, no. 6, pp. 1915-1928.

Trochim, W. and S. Davis, (1996) "Computer Simulations for Research Design", Retrieved October 5, 2011 from http://www.socialresearchmethods.net/simul/simul.htm.

Tsui, J. B., (2000) "Fundamentals of Global Positioning System Receivers: A Software Approach" John Wiley & Sons, Inc., New York.

Vallado, D. A., P. Crawford, R. Hujsak and T. S. Kelso (2006) "Revisiting Spacetrack Report #3", Technical Report AIAA 2006-6753-Rev1, America Institute of Aeronautics and Astronautics.

Van Dierendonck, A.J., J. Klobuchar and Q. Hua (1993) "Ionospheric Scintillation Monitoring Using Commercial Single Frequency C/A Code Receivers", *Proceedings of the 6th International Technical Meeting of the Satellite Division of The Institute of Navigation (ION GPS 1993)*, Salt Lake City, UT, pp. 1333-1342.

Van Dierendonck, A.J. (1996) "Global Positioning System: Theory and Applications", vol. I, Progress in Astronautics and Aeronautics, vol. 163, Chapter 8, pp. 329-407.

Vermeille, H. (2002) "Direct transformation from geocentric coordinates to geodetic coordinates", *Journal of Geodesy*, vol.76, pp. 451–454.

Vollath, D. (2007) "Plasma Synthesis of Nanoparticles", KONA, no.25, Primelweg 3, D-76297 Stutensee, Germany.

Walter, T., J. Blanch, P. Enge, B. Pervan, and L. Gratton (2008) "Future Architectures to Provide Aviation Integrity", *Proceedings of the 2008 National Technical Meeting of The Institute of Navigation*, pp. 394-401, San Diego, CA.

Ward, P. (1996) "GPS Satellite Signal Characteristics", Understanding GPS Principles and Applications, E. D. Kaplan, Norwood, MA, Artech House, Chapter 4.

Ward, P.W., J.W. Betz and C.J. Hegarty (2006) "Satellite Signal Acquisition, Tracking, and Data Demodulation", Understanding GPS Principles and Applications, E. D. Kaplan and C.J. Hegarty, Norwood, MA, Artech House, Chapter 5.

Wernik, A. W., J. A. Secan and E. J. Fremouw (2003) "Ionospheric Irregularities and Scintillation", *Advances in Space Research*, vol. 31, no. 4, pp. 971-981.

Woo, K. T. (1999) "Optimum Semi-codeless Carrier Phase Tracking of L2", Presented at the 12th International Technical Meeting of the Satellite Division of the Institute of Navigation, Nashville, Tennessee, September 14-17.

Zhang, L., Y. Morton, F. van Graas and T. Beach (2010) "Characterization of GNSS Signal Parameters under Ionosphere Scintillation Conditions using Software-based Tracking Algorithms", *Proceedings of IEEE/ION PLANS 2010*, pp. 264-275, Indian Wells, CA.

Zheng, S. Y., (2005) "Signal Acquisition and Tracking for a Software GPS Receiver", MSc Thesis, Submitted to the Faculty of the Virginia Polytechnic Institute and State University.

Appendix

Appendix I: Two-line element set (TLE)

The two-line element set (TLE) is generally used for obtaining the orbital information of a satellite. It consists of a title line and two lines of formatted data. The following is an example of a TLE (the satellite is selected to be the GPS satellite PRN3 used in this thesis).

NAVSTAR 37 (USA 117)
1 23833U 96019A 09209.25904431 .00000016 00000-0 10000-3 0 444
2 23833 53.0842 149.8698 0119344 52.1144 308.9346 2.00566908 97732

Title

Field	Columns	Content	Example
1	01–24	Satellite name	NAVSTAR 37 (USA 117)

Line1

Field	Columns	Content	Example
1	01–01	Line number	1
2	03–07	Satellite number	23833
3	08–08	Classification (U=Unclassified)	U
4	10–11	International Designator (Last two digits of launch year)	96
5	12–14	International Designator (Launch number of the year)	019
6	15–17	International Designator (Piece of the launch)	A
7	19–20	Epoch Year (Last two digits of year)	09
8	21–32	Epoch (Day of the year and fractional portion of the day)	209.25904431
9	34–43	First Time Derivative of the Mean Motion divided by two	.00000016
10	45–52	Second Time Derivative of Mean Motion divided by six (decimal point assumed)	00000-0
11	54–61	BSTAR drag term (decimal point assumed)	10000-3
12	63–63	The number 0 (Originally this should have been "Ephemeris type")	0
13	65–68	Element number	44
14	69–69	Checksum (Modulo 10)	4

Line2

Field	Columns	Content	Example
1	01–01	Line number	2
2	03–07	Satellite number	23833
3	09–16	Inclination [Degrees]	53.0842
4	18–25	Right Ascension of the Ascending Node [Degrees]	149.8698
5	27–33	Eccentricity (decimal point assumed)	0119344
6	35–42	Argument of Perigee [Degrees]	52.1144
7	44–51	Mean Anomaly [Degrees]	308.9346
8	53–63	Mean Motion [Revs per day]	2.00566908
9	64–68	Revolution number at epoch [Revs]	9773
10	69–69	Checksum (Modulo 10)	2

Appendix II: GPS PRN code generator

The GPS L_1 signal is modulated by two PRN codes: the C/A- and P-code. L_2 signal is modulated by P-code only. As mentioned in Chapter 3, each PRN code is derived from two code generators that is G1/G2 for C/A-code, and X1/X2 for P-code. In order to generate a *unique* PRN code for each GPS satellite, the output of one of the code generators (e.g. G2 and X2) is delayed with respect to the other one (i.e. G1 and X1), by a certain amount which is different for each satellite, before their outputs are added to each other [Ward, 1996]. The block diagram of the PRN code generator used in each GPS satellite is shown in Figure AII.1, and the amount of code delay is summarized in columns 3 and 4 of Table AII.1 for the C/A-code and P-code, respectively.

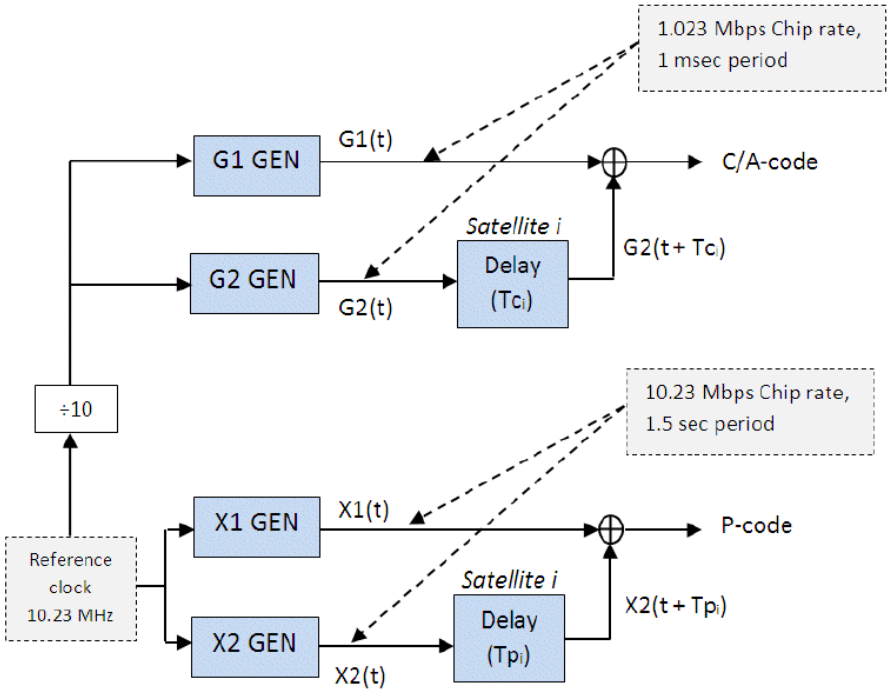

Figure AII.1 GPS code generators [modified after Ward, 1996].

Table AII.1. GPS code-phase assignments [Ward, 1996].

Satellite PRN number	C/A-code tap selection (s_1,s_2)	C/A-code delay (chips)	P-code delay (chips)
1	(2,6)	5	1
2	(3,7)	6	2
3	(4,8)	7	3
4	(5,9)	8	4
5	(1,9)	17	5
6	(2,10)	18	6
7	(1,8)	139	7
8	(2,9)	140	8
9	(3,10)	141	9
10	(2,3)	251	10
11	(3,4)	252	11
12	(5,6)	254	12
13	(6,7)	255	13
14	(7,8)	256	14
15	(8,9)	257	15
16	(9,10)	258	16
17	(1,4)	469	17
18	(2,5)	470	18
19	(3,6)	471	19
20	(4,7)	472	20
21	(5,8)	473	21
22	(6,9)	474	22
23	(1,3)	509	23
24	(4,6)	512	24
25	(5,7)	513	25
26	(6,8)	514	26
27	(7,9)	515	27
28	(8,10)	516	28
29	(1,6)	859	29
30	(2,7)	860	30
31	(3,8)	861	31
32	(4,9)	862	32

Appendix III: Loop transfer function for the 1st-, 2nd-, and 3rd-order PLL

According to Table 4.3, for the first-order loop ($\beta=1$)

$$\begin{aligned} H(s) = \frac{F(s)G(s)}{1+F(s)G(s)} &= \frac{F(s)}{s+F(s)} \\ &= \frac{\omega_n}{s+\omega_n} \end{aligned} \tag{AIII.1}$$

Substituting $s = j2\pi f$ results in

$$\begin{aligned} \left|H(f)\right|^2 &= \frac{2\pi f_n}{j2\pi f + 2\pi f_n} \cdot \frac{2\pi f_n}{-j2\pi f + 2\pi f_n} \\ &= \frac{f_n}{jf + f_n} \cdot \frac{f_n}{-jf + f_n} \\ &= \frac{f_n^2}{f^2 + f_n^2} \\ &= \frac{f_n^{2\beta}}{f^{2\beta} + f_n^{2\beta}}, \qquad (\beta = 1) \\ &= \frac{f_n^{2\beta}}{f_n^{2\beta} + f^{2\beta}} \left[1 + (2\beta - 2)\left(\frac{f}{f_n} \right)^{(2\beta-2)} \right], \qquad (\beta = 1) \end{aligned} \tag{AIII.2}$$

Similarly, for the second-order loop ($\beta=2$)

$$\begin{aligned} H(s) = \frac{F(s)}{s+F(s)} &= \frac{2\zeta\omega_n + \omega_n^2 / s}{s + 2\zeta\omega_n + \omega_n^2 / s} \\ &= \frac{2\zeta\omega_n s + \omega_n^2}{s^2 + 2\zeta\omega_n s + \omega_n^2}. \end{aligned} \tag{AIII.3}$$

Thus, for $s = j2\pi f$

$$|H(f)|^2 = \frac{2\zeta\omega_n(j2\pi f)+\omega_n^2}{(j2\pi f)^2+2\zeta\omega_n(j2\pi f)+\omega_n^2}\cdot\frac{2\zeta\omega_n(-j2\pi f)+\omega_n^2}{(-j2\pi f)^2+2\zeta\omega_n(-j2\pi f)+\omega_n^2}$$

$$= \frac{64\pi^4\zeta^2 f^2 f_n^2+16\pi^4 f_n^4}{16\pi^4(f_n^2-f^2)^2+64\pi^4\zeta^2 f^2 f_n^2}, \qquad (\zeta = 1/\sqrt{2})$$

$$= \frac{2f^2 f_n^2+f_n^4}{f_n^4+f^4} = \frac{f_n^4}{f_n^4+f^4}+\frac{2f^2 f_n^2}{f_n^4+f^4} \qquad \text{(AIII.4)}$$

$$= \frac{f_n^4}{f_n^4+f^4}\left[1+2\left(\frac{f}{f_n}\right)^2\right]$$

$$= \frac{f_n^{2\beta}}{f_n^{2\beta}+f^{2\beta}}\left[1+(2\beta-2)\left(\frac{f}{f_n}\right)^{(2\beta-2)}\right], \qquad (\beta = 2)$$

Finally, for the third-order loop ($\beta = 3$)

$$H(s) = \frac{F(s)}{s+F(s)} = \frac{2\omega_n s^2+2\omega_n^2 s+\omega_n^3}{s^3+2\omega_n s^2+2\omega_n^2 s+\omega_n^3} \qquad \text{(AIII.5)}$$

Substituting $s = j2\pi f$ results in

$$|H(f)|^2 = \frac{2\omega_n(j2\pi f)^2 + 2\omega_n^2(j2\pi f) + \omega_n^3}{(j2\pi f)^3 + 2\omega_n(j2\pi f)^2 + 2\omega_n^2(j2\pi f) + \omega_n^3} \times$$

$$\frac{2\omega_n(-j2\pi f)^2 + 2\omega_n^2(-j2\pi f) + \omega_n^3}{(-j2\pi f)^3 + 2\omega_n(-j2\pi f)^2 + 2\omega_n^2(-j2\pi f) + \omega_n^3}$$

$$= \frac{\omega_n^6 + 4\omega_n^2(2\pi f)^4}{\omega_n^6 + (2\pi f)^6} = \frac{f_n^6 + 4f_n^2 f^4}{f_n^6 + f^6} \qquad \text{(AIII.6)}$$

$$= \frac{f_n^6}{f_n^6 + f^6}\left[1 + 4\left(\frac{f}{f_n}\right)^4\right]$$

$$= \frac{f_n^{2\beta}}{f_n^{2\beta} + f^{2\beta}}\left[1 + (2\beta - 2)\left(\frac{f}{f_n}\right)^{(2\beta-2)}\right], \qquad (\beta = 3)$$

Appendix IV: Calculating propagation parameters

- ***Satellite range and range-rate***

If $\overline{x}_{sat,tcs}(t) = [x_1(t), x_2(t), x_3(t)]$ and $\overline{v}_{sat,tcs}(t) = [v_1(t), v_2(t), v_3(t)]$ represent the satellite position and velocity vectors in the receiver TCS system (with the system's origin being at the receiver location), then the satellite range and range-rate can be calculated via

$$sat_{range}(t) = \sqrt{x_1^2(t) + x_2^2(t) + x_3^2(t)}, \qquad (m) \tag{AIV.1}$$

$$\begin{aligned} sat_{rangerate}(t) &= \overline{v}_{sat,tcs}(t) \cdot \overline{u}_{sat,tcs}(t) \\ &= v_1(t)u_1(t) + v_2(t)u_2(t) + v_3(t)u_3(t), \qquad (m/s) \end{aligned} \tag{AIV.2}$$

where the unit vector $\overline{u}_{sat,tcs}(t)$ is defined as

$$\begin{aligned} \overline{u}_{sat,tcs}(t) &= [u_1(t), u_2(t), u_3(t)] \\ &= \overline{x}_{sat,tcs}(t) \big/ sat_{range}(t) \end{aligned} \tag{AIV.3}$$

- ***Satellite elevation and azimuth angles***

Using $\overline{x}_{sat,tcs}(t)$, the elevation and azimuth angles are obtained from

$$sat_{elevation}(t) = \arctan\left(\frac{x_3(t)}{\sqrt{x_1^2(t) + x_2^2(t)}}\right), \qquad (\text{deg}) \tag{AIV.4}$$

$$sat_{azimuth}(t) = \arctan\left(\frac{x_2(t)}{x_1(t)}\right), \qquad (\text{deg}) \tag{AIV.5}$$

- ***IPPs position and range to the ground station***

Ionospheric Pierce Point (IPP) or the satellite signal penetration point is the intersection point between the satellite-receiver line-of-sight and the ionosphere shell (nominally taken as 350 km).

IPP location $\bar{x}_{IPP,llh}(t)=[\phi_{IPP},\lambda_{IPP},h_{IPP}]$ can be computed in the geodetic coordinate system via [Skone, 2009]

$$\begin{aligned}\phi_{IPP}(t) &= \phi_r(t)+\psi\cos(sat_{azimuth}(t))\\ \lambda_{IPP}(t) &= \lambda_r(t)+\psi\frac{\sin(sat_{azimuth}(t))}{\cos(\phi_{IPP}(t))}\\ h_{IPP}(t) &= h\end{aligned} \qquad \text{(AIV.6)}$$

in which

$$\psi=\cos^{-1}\left(\left(\frac{R_E}{R_E+h}\right)\cos(sat_{elevation}(t))\right)-sat_{elevation}(t) \qquad \text{(AIV.7)}$$

where h represents the phase screen height ($h=350\,\text{km}$), R_E represents the mean radius of the spherical Earth ($R_E=6371\,\text{km}$) and (ϕ_r,λ_r) represent the receiver latitude and longitude.

The scintillation wave field is initiated at phase screen height and then propagated towards the ground station. The calculation of the propagation reference coordinate system (x_p, y_p, z_p) for the IPP point to the receiving antenna is done in two steps. First, the coordinates of the receiver $rec_{llh}(t)=[\phi_r(t),\lambda_r(t),h_r(t)]$ are calculated in a TCS system centered on the IPP point. With these TCS coordinates $(x_{tcs}, y_{tcs}, z_{tcs})$, the propagation system coordinates (x_p, y_p, z_p) are obtained via

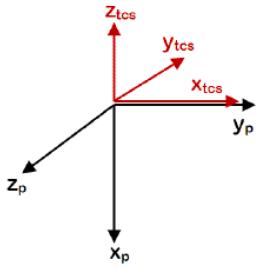

$$\begin{aligned} x_p(t) &= -z_{tcs}(t) \\ y_p(t) &= \ \ x_{tcs}(t) \\ z_p(t) &= -y_{tcs}(t) \end{aligned} \tag{AIV.8}$$

From this equation, the IPP range to the ground station is derived as

$$IPP_{range}(t) = \sqrt{x_p^2(t) + y_p^2(t) + z_p^2(t)}, \qquad (m) \tag{AIV.9}$$

- ***Propagation angles***

Using Equation (AIV.8), the propagation angles can be calculated via

$$\theta_p(t) = \arctan\left(\frac{\sqrt{y_p^2(t) + z_p^2(t)}}{x_p(t)}\right), \qquad (\text{deg}) \tag{AIV.10}$$

$$\phi_p(t) = \arctan\left(\frac{z_p(t)}{y_p(t)}\right), \qquad (\text{deg}) \tag{AIV.11}$$

- ***Signal penetration point velocity***

From $\bar{v}_{sat,tcs}(t) = [v_1(t), v_2(t), v_3(t)]$, the penetration point velocity components can be achieved via

$$\begin{aligned} v_{px}(t) &= -v_3(t)\cdot v_{SF} \\ v_{py}(t) &= \ \ v_1(t)\cdot v_{SF} \qquad\qquad (m/s) \\ v_{pz}(t) &= -v_2(t)\cdot v_{SF} \end{aligned} \tag{AIV.12}$$

where the scale factor is defined as

$$v_{SF} = \frac{IPP_{range}(t)}{sat_{range}(t)} \tag{AIV.13}$$

- ***Apparent velocities in the measurement plane***

Finally, the apparent velocity in the measurement plane is obtained via

$$\begin{aligned} v_{k\_east}(t) &= -v_{py}(t) + \tan(\theta_p(t))\cdot\cos(\phi_p(t))\cdot v_{px}(t) \\ v_{k\_south}(t) &= -v_{pz}(t) + \tan(\theta_p(t))\cdot\sin(\phi_p(t))\cdot v_{px}(t) \end{aligned} \tag{AIV.14}$$

Appendix V: Scintillation indices with geometric and anisotropy correction

The intensity scintillation index (S_4), and phase scintillation variance (σ_ϕ^2) given in Section 2.3.3 are two commonly used measures of the strength of scintillation activity when the wave field propagates *normally* in an *isotropic* medium. To accommodate oblique propagations in an anisotropic medium, both intensity and phase scintillation index terms should be modified. Assuming the x-axis as the principal propagation axis, for given propagation directions θ_p and ϕ_p, and anisotropic parameters a, b, A, B and C at each IPP points, the so-called intensity and phase indices are modified as follows [Rino, 2011]:

$$S_4 = \left[k^2 l_p C_s \rho_F^{(2\nu-1)} \sec\theta_p \frac{\Gamma\left((2.5-\nu)/2\right)\varpi}{2^{\nu+1/2}\sqrt{\pi}\ (\nu-0.5)\ \Gamma\left((0.5+\nu)/2\right)} \right]^{1/2} \tag{AV.1}$$

$$\sigma_\phi^2 = \left\langle \delta\phi^2 \right\rangle = k^2 l_p C_s \sec\theta_p \frac{\Gamma(\nu-1/2)\vartheta}{4\pi\ \Gamma(\nu+1/2)\ q_o^{2\nu-1}} \tag{AV.2}$$

in which $\rho_F = \sqrt{x\ \sec(\theta_p)/k}$,

$$\vartheta = \frac{ab}{\sqrt{AC - B^2/4}\ \cos\theta_p} \tag{AV.3}$$

and

$$\varpi = \begin{cases} abF\left(\nu+1/2, 1/2; 1; \dfrac{A''-C''}{A''}\right) A''^{-(\nu+1/2)} & \text{if } A'' > C'' \\ abF\left(\nu+1/2, 1/2; 1; \dfrac{C''-A''}{C''}\right) C''^{-(\nu+1/2)} & \text{if } A'' < C'' \end{cases} \tag{AV.4}$$

In Equation (AV.4) [**after modification from** Rino, 2011]

$$A'' = (A' + C' + D')/2$$
$$C'' = (A' + C' - D')/2 \qquad \text{(AV.5)}$$

with

$$A' = \left(A\cos^2\phi_p + B\sin\phi_p\cos\phi_p + C\sin^2\phi_p\right)\cos^2\theta_p$$
$$B' = \left(B\cos 2\phi_p + (C-A)\sin 2\phi_p\right)\cos\theta_p$$
$$C' = A\sin^2\phi_p - B\sin\phi_p\cos\phi_p + C\sin^2\phi_p \qquad \text{(AV.6)}$$
$$D' = \sqrt{(C'-A') - B'^2}$$

and the *hyper-geometric* function is defined for $|q_4| < 1$ by

$$F(q_1, q_2; q_3; q_4) = \sum_{n=0}^{\infty} \frac{(q_1)_n (q_2)_n}{(q_3)_n} \frac{q_4^n}{n!}, \qquad (n \approx 100) \qquad \text{(AV.7)}$$

provided that q_3 is not 0, −1, −2, ….

In Equation (AV.7), the *Pochhammer* symbol is calculated via

$$(q)_n = \begin{cases} 1 & if\ \ n = 0 \\ q(q+1)...(q+n-1) & if\ \ n > 0 \end{cases} \qquad \text{(AV.8)}$$